Thesis submitted for the Degree of Doctor of Philosophy

in the University of Oxford

BODLEIAN LIBRARY OXFORD
DEPOSITED
THESIS
25-7-79

# METAMORPHIC STUDIES

# IN THE SOUTH-EAST TAUERN WINDOW, AUSTRIA

by

Giles Timothy Reinhart Droop

VOLUME II - FIGURES, TABLES AND MAPS

St. Edmund Hall

and

Department of Geology and Mineralogy

Oxford University

1979

# LIST OF FIGURES

CHAPTER 1 Pages 1 to 5

1.1 Sketch map of the Eastern Alps.

1.2 Schematic cross-section through the Eastern Alps.

1.3 Metamorphic events in the Eastern Alps.

1.4 Sketch map of the south-east Tauern Window.

1.5 The areas mapped in this thesis in relation to areas mapped by other workers.

CHAPTER 2 Pages 7 to 33

2.1 Finely banded gneiss, Riekengraben.

2.2 Quartzo-feldspathic gneiss with amphibolite lenses.

2.3 Finely banded eclogitic amphibolite.

2.4 Garnet, rutile, quartz, and omphacite in eclogitic amphibolite.

2.5 Coronas of garnet around relict omphacite.

2.6 Albite poikiloblast enclosing hornblende and garnet.

2.7 Fine-grained symplectitic clinpyroxene+albite intergrowth garnets and albite poikiloblast.

2.8 Garnet porphyroblasts with reaction rims of plagioclase.

2.9 Hornblende poikiloblasts and two generations of garnet.

2.10 Ophitic metagabbro-pegmatite.

2.11 Metabasalt-amphibolite.

2.12 Concordant band of granite-gneiss within mica-schists.

2.13 Granular plagioclase apparently in equilibrium with micas.

2.14 Textures in and adjacent to the quartz+garnet vein.

2.15 Inner Schieferhülle mica schist with large garnet porphyroblasts.

2.16 Large zoned garnet porphyroblast and "pin prick" garnets in Inner Schieferhülle mica-schist.

2.17 Twinned grain of staurolite and kyanite.

2.18 Staurolite enclosing garnet and cutting across mats of fine-grained kyanite.

2.19 Euhedral staurolite porphyroblasts cutting across schistosity.

2.20 Oligoclase porphyroblast replacing paragonite and enclosing staurolite.

2.21 Chlorite enclosing garnet and kyanite.

2.22 Kyanite, partially altered to muscovite.

2.23 Myrmekitic intergrowth of plagioclase and quartz replacing orthoclase.

2.24 Recrystallised biotite, epidote and muscovite in augen-gneiss.

2.25 Plot of meta-granite bulk compositions.

2.26 Poorly deformed syenite-gneiss with pseudomorphs after ?hornblende.

2.27 Well recrystallised biotite, epidote and clinopyroxene forming a pseudomorph in syenite gneiss.

2.28 Albite, biotite and clinopyroxene in GD 1234b.

2.29 Dyke of biotite-epidote-feldspar-schist in syenite-gneiss.

2.30 Brown hornblende enclosing patches of actinolite in optical continuity.

2.31 Euhedral hornblende overgrowing aligned epidote granules and cutting across schistose chlorite in epidote-amphibolite.

2.32 Zoned amphiboles with chlorite and albite in meta-gabbro.

2.33 Tremolite-talc-dolomite-schist.

2.34 The thrust-zone on the south slope of Sicker Kopf.

2.35 Localised reaction rims of talc between tremolite and antigorite in serpentinite.

2.36 Tremolite, calcite and quartz in siliceous dolomite.

2.37 Tremolite-rich band next to tremolite-poor band in siliceous dolomite.

2.38 Coarse-grained chloritoid-schist, with porphyroblasts of chloritoid, garnet and albite.

2.39 Garnet, hornblende and chloritoid porphyroblasts in coarse-grained chloritoid-schist.

2.40 Garnet and hornblende porphyroblasts in garbenschiefer.

2.41 Zones of alteration in garnet-amphibolite adjacent to a chlorite+ albite vein.

2.42 Pseudotachylite band and associated microfractures in banded gneiss.

2.43 Thin section of pseudotachylite.

CHAPTER 3 Pages 34 to 73

3.1 Structural subareas in the two map areas.

3.2 $S_a^1$ compositional banding in clacareous quartzite.

3.3 Interbanded calc-schists and marble overlying pelitic mica-schists and biotite-epidote-feldspar-schist.

3.4 $F_a^2$ chevron-folds deforming an $S_a^1$ foliation containing a small $F_a^1$ isocline in quartz-muscovite-schist.

3.5 $S_a^1$ banding deformed by $F_a^2$ folds in calcareous quartzite.

3.6 Enlargement of the area marked in Fig. 3.5 showing a refolded $F_a^1$ isocline.

3.7 $F_a^1$ isocline refolded by open $F_a^2$ folds in calcareous quartzite.

3.8 Interferencepattern produced by the superposition of $F_a^1$ and $F_a^2$ folds in calc-schist.

3.9 Tremolite-talc-schist showing tremolite needles bent round an $F_a^2$ fold.

3.10 Tight $F_a^1$ folds deforming previously flattened quartz veins in graphitic quartzite.

3.11 Structural elements in the Bösеck subarea.

3.12 Structural elements in the Romate subarea.

3.13 Subvertical $S_a^1$ compositional banding and shallower $S_a^2$ schistosity in calc-schists.

3.14 Large, tight, asymmetric 'Z' folds in calc-schists in the upper limb of the Mallnitzer Mulde.

3.15 Feldsee Kopf, viewed from the south-east.

3.16 View north-west from Oschenik Scharte showing foliation in augen-gneisses.

3.17 Steeply dipping foliation in augen-gneisses close to the north-eastern margin of the Sonnblick Kern.

3.18 Tight $F_a^2$ folds in calcareous quartzite.

3.19 Refolded $F_a^1$ isocline in mica-schist.

3.20 South face of Geisel Kopf, showing cascade of large asymmetric $F_a^2$ folds.

3.21 $D_a^1$ lineations folded round an open $F_a^2$ in pelitic mica-schist.

3.22 Refolded $F_a^1$ isocline in micaceous marble.

3.23 Contact between mica-schists of the Woisgen Zone and underlying augen gneisses.

3.24 Steeply plunging $F_a^2$ fold axes in mica-schists.

3.25 Structural elements in the Auernig subarea.

3.26 Rotation of $S_a^1$ foliation on the east slope of Hindenburg Höhe.

3.27 Tight $F_a^2$ folds in graphitic mica-schists.

3.28 Diagram and stereogram illustrating structures at a locality near Mallnitz.

3.29 Variation in the relative intensity of $S_a^1$ and $S_a^2$ in mica-schists.

3.30 $F_a^3$ buckle-fold in epidote-amphibolite.

3.31 Intersecting lineations in epidote-amphibolite.

3.32 Décollement structure in epidote amphibolite.

3.33 Structural elements in the Kaponig subarea.

3.34 Structural elements in the Sickerkopf subarea.

3.35 Relationship of $S_a^1$ to $S_a^2$ in the Sonnblick Kern and Sonnblick gneiss-lamella.

3.36 Isoclinal $F_a^2$ folds in calc-schists.

3.37 Structural elements in the Dösener subarea.

CHAPTER 4 Pages 76 to 92

4.1 (a) Textures of matrix platy and prismatic minerals.

4.1 (b) Textures of porphyroblast minerals.

4.2 Variscan garnet porphyroblast containing discordant inclusion trails.

4.3 Zoned garnet porphyroblast in Inner Schieferhülle mica-schist.

4.4 Kyanite pseudomorphs after sillimanite in migmatitic mica-schist.

4.5 Kyanite pseudomorphs after sillimanite in large Variscan muscovite.

4.6 Biotite showing vermiform texture.

4.7 Corona of garnets surrounding a mosaic of recrystallised biotite in migmatitic mica-schist.

4.8 Rotated post-$S_a^1$ albite porphyroblasts in greenschist.

4.9 Rotated post-$S_a^1$ albite porphyroblast enclosing aligned actinolite and epidote prisms.

4.10 Rotated post-$S_a^1$ albite porphyroblast, with rim of oligoclase replacing muscovite.

4.11 Rotated post-$S_a^1$ albite porphyroblast.

4.12 Euhedral pre-$F_a^2$ garnet porphyroblast in mica-schist.

4.13 Zoned garnet porphyroblast in graphitic mica-schist.

4.14 Spherical aggregate of chloritoid+chlorite, possibly pseudomorphing garnet.

4.15 Pseudomorph of clinozoisite, margarite and quartz after lawsonite in garnet.

4.16 Calculated chemical composition of the lawsonite-pseudomorph plotted in ternary $CaO-Al_2O_3-SiO_2$.

4.17 Sigmoidal garnet in pelitic mica-schist.

4.18 Rolled hornblende in garbenschiefer.

4.19 Euhedral porphyroblasts of garnet and staurolite cutting across $F_a^2$ microfolds.

4.20 Porphyroblasts of garnet and staurolite cutting across an $S_a^2$ schistosity.

4.21 Euhedral garnet porphyroblast overgrowing a crenulated $S_a^1$ muscovite +?ilmenite fabric.

4.22 Interlocking flakes of biotite and chlorite.

4.23 "Pin prick" garnets and butterfly-twinned kyanite overgrowing an $S_a^2$ schistosity.

CHAPTER 5 Pages 94 to 110

5.1 Compositions of garnets from Inner Schieferhülle eclogitic amphibolites.

5.2 Compositions of garnets from Inner Schieferhülle metasediments.

5.3 Compositions of garnets from Peripheral Schieferhülle metasediments.

5.4 Zoning half-profiles across an $M_a$ garnet in Inner Schieferhülle paragneiss.

5.5 Zoning half-profiles across three garnets.

5.6 Zoning profile across a post-$S_a^2$ garnet in Peripheral Schieferhülle pelite in a direction perpendicular to the schistosity.

5.7 Zoning profiles across a flat post-$S_a^2$ garnet in a Peripheral Schieferhülle pelite.

5.8 Clinopyroxene compositions in terms of jadeite, acmite and augite.

5.9 Plot of Na versus Ca for amphiboles.

5.10 Plot of $Al^{VI}$ versus $Al^{IV}$ for amphiboles.

5.11 Plots showing the degree of ($R^{3+}$ + $R^{2+}$ + = Mg replacement as a function of $Al^{IV}$ and $Al^{VI}$ in metabasite amphiboles.

5.12 Epidote compositions plotted in terms of $Fe^{3+}$ versus Al - 4.0.

5.13 Histogram of plagioclase compositions.

5.14 Compositions of white micas.

5.15 Muscovite compositions plotted in the SAF diagram of Lambert (1959).

5.16 SAF diagram of biotite compositions.

5.17 Chlorite compositions.

5.18 Carbonate compositions plotted in ternary Ca-Mg-Fe.

CHAPTER 6 Pages 111 to 129

6.1 Schematic Thompson AFM diagrams showing compatibility relationships between high-variance pelite assemblages.

6.2 Schreinemaker's bundle for the AFM invariant assemblage gt+st+ctd+ biot+chl.

6.3 Garnet overgrowing plates of chloritoid.

6.4 Post-$S_a^2$ chloritoid in equilibrium with biotite.

6.5 Mg/Mg + fe zoning profiles across garnets in Peripheral Schieferhülle pelites.

6.6 Schematic representation of a garnet-forming reaction.

6.7 Thompson AFM diagram for pelites from the chloritoid+biotite zone.

6.8 Staurolite and chlorite growing at the expense of chloritoid.

6.9 Staurolite and chlorite growing at the expense of chloritoid partially enclosed by garnet.

6.10 Thompson AFM diagram for pelites from the garnet+staurolite+chlorite subzone.

6.11 Thompson AFM diagram for the staurolite+biotite zone pelite GD 18.

6.12 Thompson AFM diagram for the staurolite+biotite zone pelite GD 209b.

6.13 Thompson AFM diagram for the staurolite+biotite zone pelite GD 465b.

6.14 Staurolite and kyanite surrounding garnet in pelitic mica-schist.

6.15 Schematic T-X (Fe-Mg) sections for pelites of the north-west and south-east Mölltal.

6.16 The north-east Mölltal and south-west Mölltal facies series in relation to the preferred topology of the pelite petrogenetic grid.

6.17 $M_a$ metamorphic zones in the eastern Tauern Window.

6.18 Schematic map of the Mölltal region showing the relationship between isotherms, isobars and isograds.

6.19 A hypothetical section through the eastern Tauern Window showing the angular relationship between the staurolite+biotite isograd and the basement-cover interface.

6.20 Isobaric T-$X_{CO_2}$ diagram for quartz+plagioclase bearing metabasites.

6.21 Calcic amphibole, epidote, chlorite and plagioclase compatibility.

6.22 AFM diagram of two Peripheral Schieferhülle metabasite.

6.23 Calcite and plagioclase replacing epidote.

CHAPTER 7 Pages 130 to 155

7.1 Pre-Alpine metamorphic conditions.

7.2 Experimentally determined aluminosilicate equilibria.

7.3 Some experimentally reversed reaction and the calculated equilibrium positions of reaction (7.W).

7.4 The 2.07 kb muscovite-paragonite solvus of Eugster et al. (1972).

7.5 Muscovite and paragonite compositions in aluminous pelites.

7.6 Calculated equilibrium curves and experimental reversals for reactions involving FASH phases.

7.7 Calculated and experimentally determined equilibrium curves for reactions involving CASH phases.

7.8 Calculated equilibrium curves for reaction (7.T).

7.9 Calculated equilibrium curves for reaction (7.D) at different values of $X_{H_2O}$.

7.10 5 kb T-$X_{CO_2}$ diagram showing equilibria relevant to syenite-gneisses.

7.11 Mineral compatibility relationships in quartz- and albite-bearing meta-granites and meta-syenites.

7.12 Calcite compositions plotted in the 5 kb thermometer of Bickle and Powell (1977).

7.13 Compositions of coexisting calcite and dolomite plotted in the 5 kb thermometer of Bickle and Powell (1977).

7.14 7 kb T-$X_{CO_2}$ diagram showing equilibria relevant to calc-schists.

7.15 6 kb T-$X_{CO_2}$ diagram showing equilibria relevant to siliceous dolomites.

7.16 7 kb T-$X_{CO_2}$ diagram showing equilibria relevant to serpentinites.

7.17 6 kb T-$X_{CO_2}$ diagram for some reactions involving serpentine and other CMS minerals.

7.18 Estimated $M_a$ metamorphic conditions in the Romate subarea.

7.19 Estimated $M_a$ metamorphic conditions at the base of the Mölltal Schieferhülle.

7.20 Estimated $M_a$ metamorphic conditions $2\frac{1}{4}$ km below the basement-cover interface.

7.21 Estimated $M_a$ metamorphic conditions 3 to 4 km below the basement-cover interface.

7.22 Some possible early-Alpine P-T-time trajectories.

7.23 $\mu_{SiO_2}$ versus $\mu_{CaO}$ diagrams for serpentinites and talc-schists.

7.24 Replacement of muscovite by sodic plagioclase in pelites explained in terms of a gradient in $Na^+/H^+$.

CHAPTER 8 Pages 157 to 167

8.1 Graph of $\Delta O^{18}$ (mineral-water) vs. temperature for the calibrations used in the text.

8.2 Graph of $\Delta O^{18}$ (mineral-mineral) vs. temperature for the calibrations used in the text.

8.3 Fractionation vs. temperature plots and Javoy diagrams for isotopically well-equilibrated rocks.

8.4 Fractionation vs. temperature plot for Auernig vein samples.

8.5 Fractionation vs. temperature plots and Javoy diagrams for isotopically poorly-equilibrated mica schists.

8.6 Graph of $\Delta O^{18}$ (qz-biot) vs. $\Delta O^{18}$ (qz-musc).

8.7 Oxygen isotope sample localities.

CHAPTER 9 Pages 171 to 174

9.1 PVT diagram for $H_2O$.

9.2 Primary two-phase fluid inclusions in vein quartz.

9.3 Calibration curve for the Chaix-Meca microthermometry apparatus.

9.4 Estimated conditions of mineral growth in a $D_a^3$ vein.

CHAPTER 10 Pages 175 & 176

10.1 Pressure-temperature-time trajectory for the base of the Mölltal Schieferhülle.

10.2 Range of acceptable solutions to the thermal model.

# LIST OF TABLES

## CHAPTER 2


| | | page |
|---|---|---|
| 2.1 | Mineral abbreviations used in the text. | 6 |
| 2.2 | Modal analyses of quartz+garnet vein and host mica-schist. | 15 |
| 2.3 | Textural and mineralogical changes with increasing deformation in metagranites. | 21 |
| 2.4 | Chemical analyses of metagranites. | 23 |


## CHAPTER 3


| | | |
|---|---|---|
| 3.1 | Structural succession in the Mallnitzer Mulde. | 41 |
| 3.2 | Synopsis of the structural history of the south-east Tauern. | 74 |
| 3.3 | Correlation of deformation phases over the central and eastern Tauern. | 75 |


## CHAPTER 4


| | | |
|---|---|---|
| 4.1 | Mineral growth phases in eclogites and garnet-amphibolites. | 78 |
| 4.2 | Calculated modal and chemical composition of the lawsonite-pseudomorph. | 88 |
| 4.3 | Synopsis of the metamorphic history of the south-east Tauern. | 93 |

CHAPTER 7

page

7.1 Average Na/Na+K values and solvus-temperatures for muscovites and paragonites in aluminous pelites. 134

7.2 Some reactions involving FASH phases. 135

7.3 Thermodynamic data for the reactions listed in Table 7.2. 136

CHAPTER 8

8.1 Experimentally determined and calculated mineral-water fractionation curves. 156

8.2 Oxygen isotopic compositions of metamorphic waters. 168

8.3 Calculated oxygen isotopic compositions of waters in equilibrium with segregation quartz at various temperatures. 169

CHAPTER 9

9.1 Standards used in the calibration of the Chaix-Meca apparatus. 173

# LIST OF MAPS

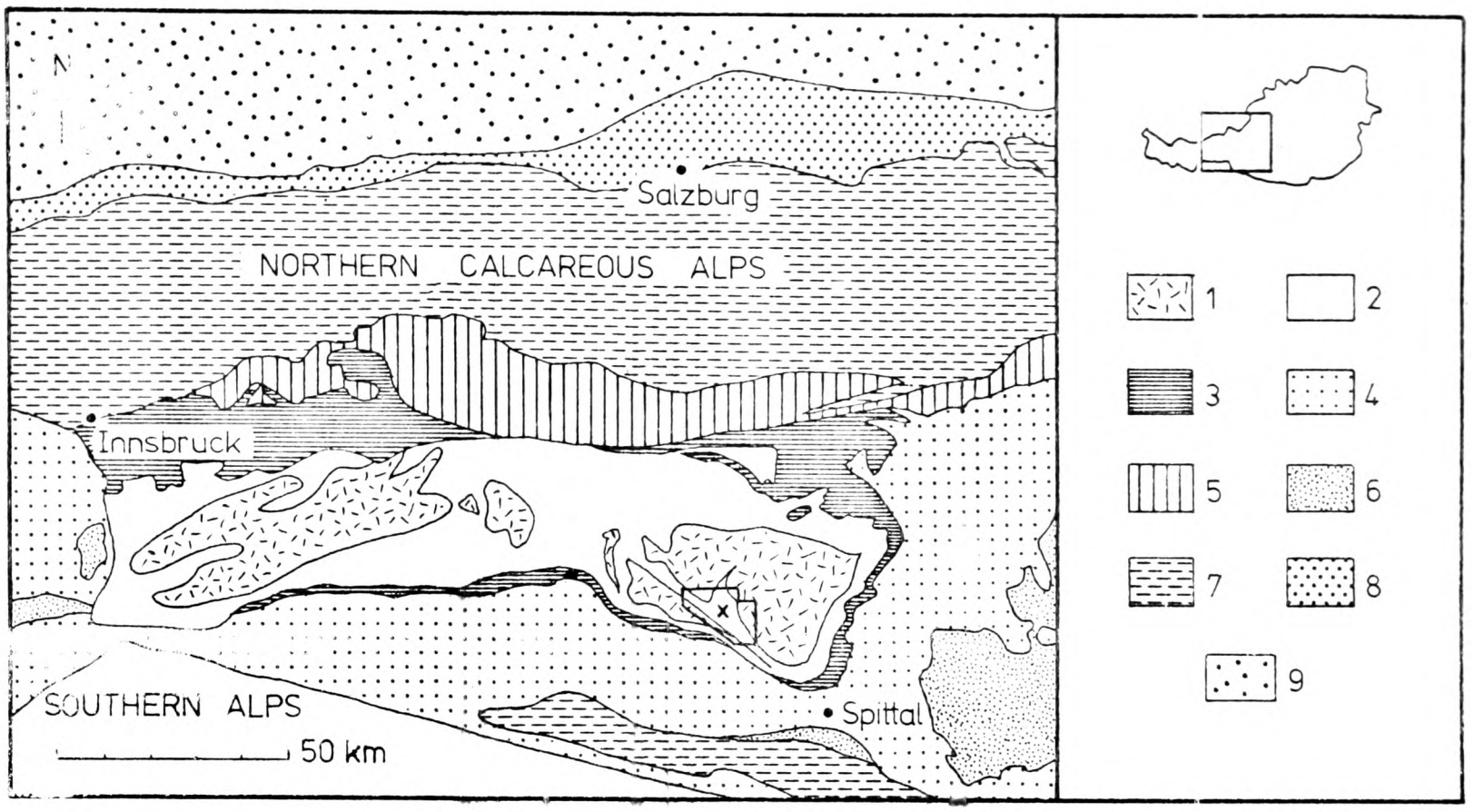
Map 1 Geological map of the area around Kaponigtal, Mölltal, Austria.

Map 2 Geological map of the area around Mallnitz, Austria.

Map 2A Cross-sections of the area covered by Map 2.

Map 3 Metamorphic zonation.

Maps 1, 2, 2A and 3 are folded inside the back cover of this volume.




1. Pennine basement complex

2. Peripheral Schieferhülle

3. Lower East Alpine sheet

4. Altkristallin

5. Grauwackenzone

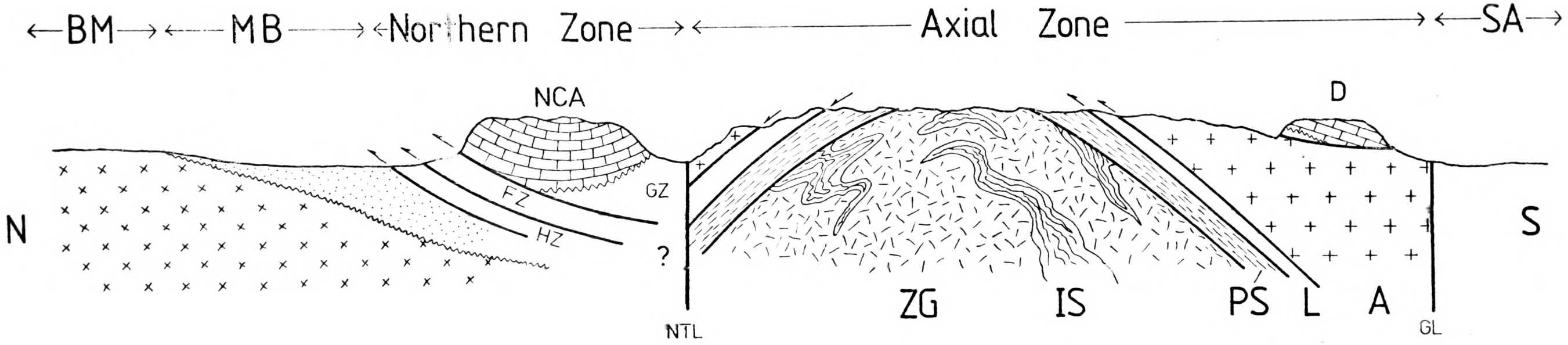
6,7. Sedimentary cover of the Altkristallin sheet

8. Flysch and Helvetic zones

9. Molasse

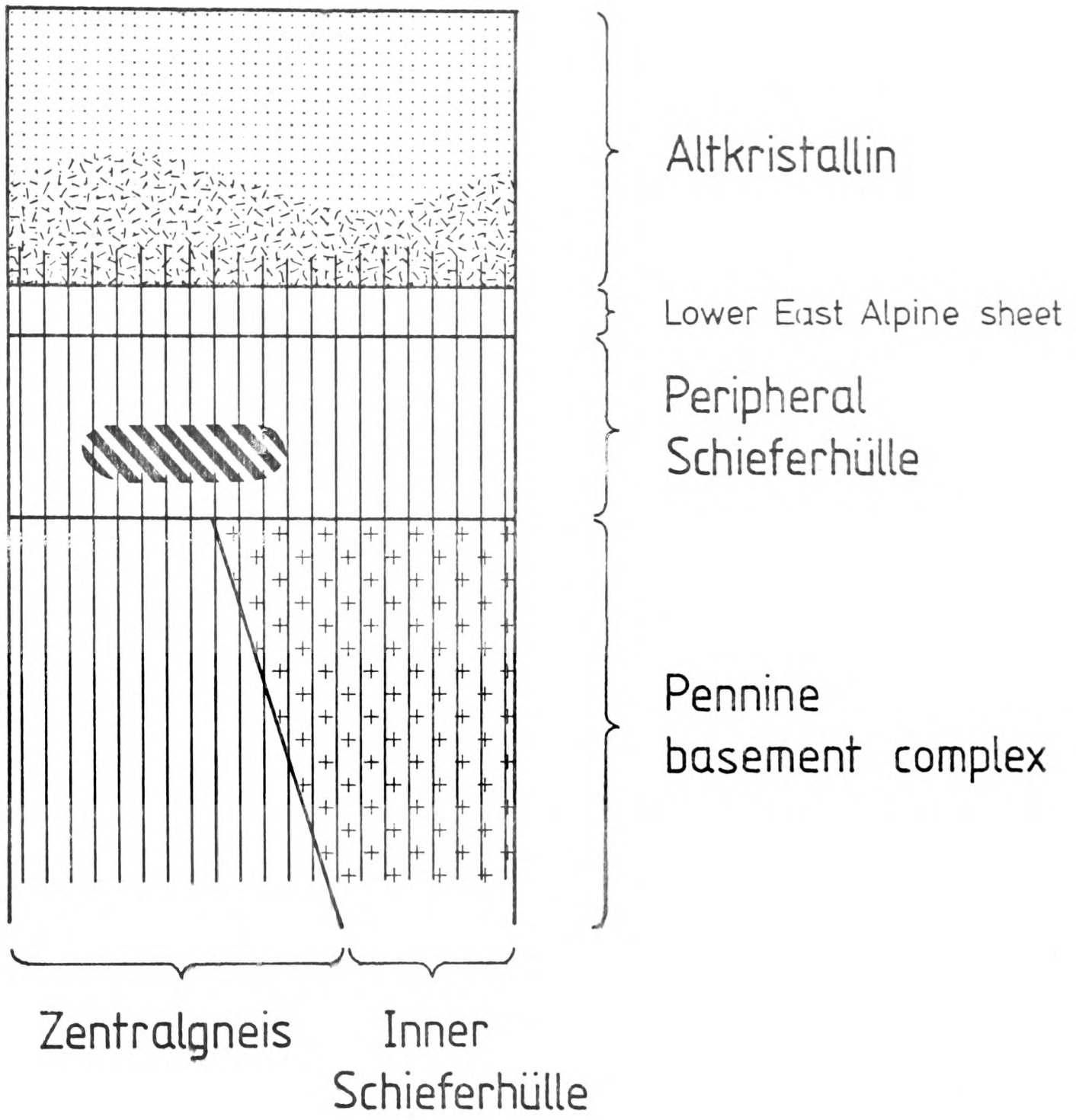
x Area mapped in this thesis

Fig. 1.1 Sketch map of the Eastern Alps.




| | | | | | |
|---|---|---|---|---|---|
| A | Altkristallin | GZ | Grauwackenzone | NCA | Northern Calcareous Alps |
| BM | Bohemian Massif | HZ | Helvetic Zone | NTL | North Tauern Line |
| D | Drauzug | IS | Inner Schieferhulle | PS | Peripheral Schieferhulle |
| FZ | Flysch Zone | L | Lower East Alpine sheet | SA | Southern Alps |
| GL | Gailtal Line | MB | Molasse Basin | ZG | Zentralgneis |

Fig. 1.2 Schematic cross-section through the Eastern Alps.




A. 35-40 mybp amphibolite facies metamorphism

B. Eo-Alpine blueschist facies metamorphism

C. 100 mybp low-pressure amphibolite facies metamorphism

D. 380-400 mybp amphibolite facies metamorphism

E. Variscan and possibly older metamorphic events

Fig. 1.3 Metamorphic events in the Eastern Alps.

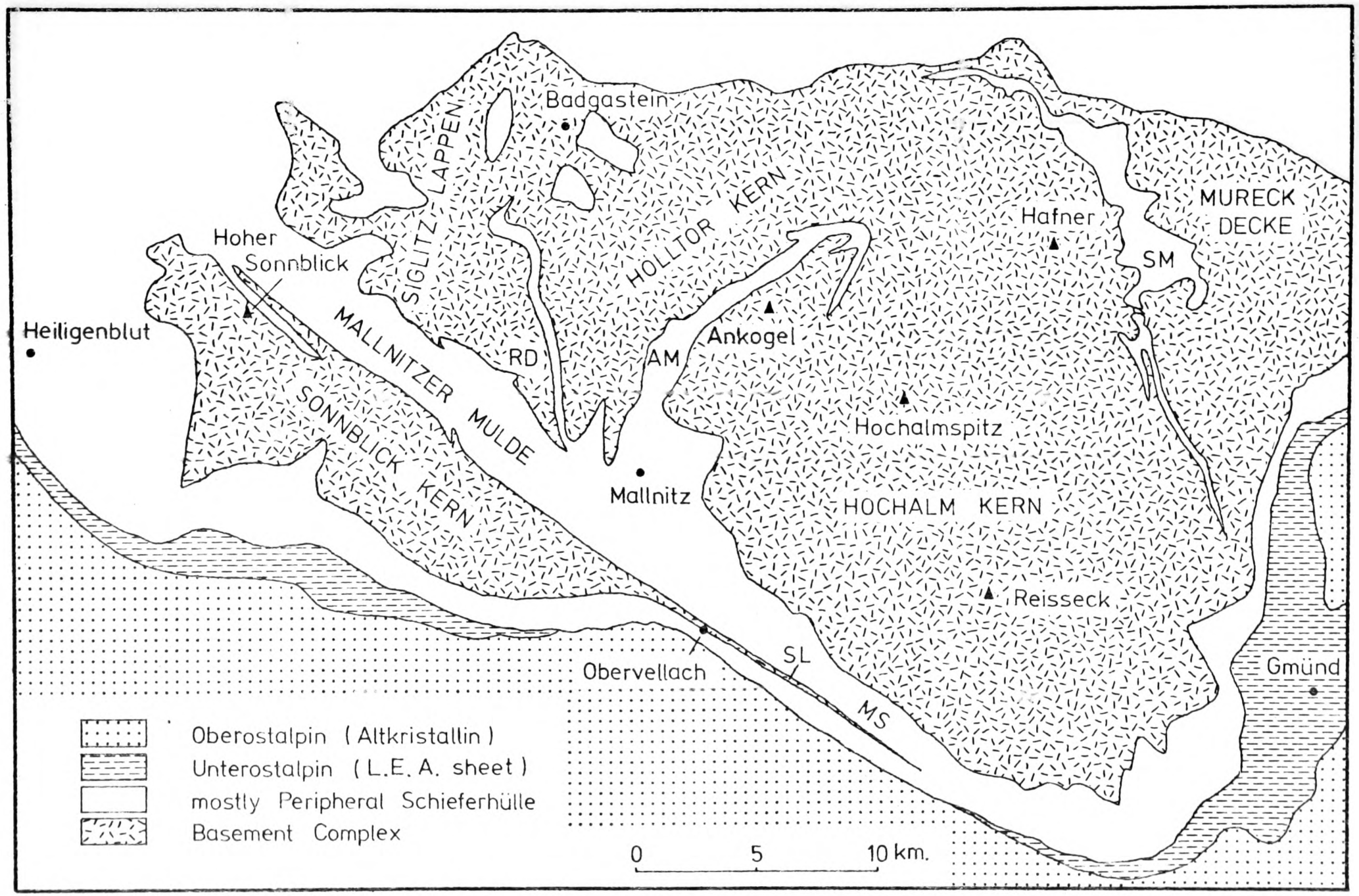



Fig. 1.4 Sketch map of the south east Tauern Window.

SM Silbereck Mulde

AM Ankogel Mulde MS Möltal Schieferhülle RD Romate-decke SL Sonnblick Lamella

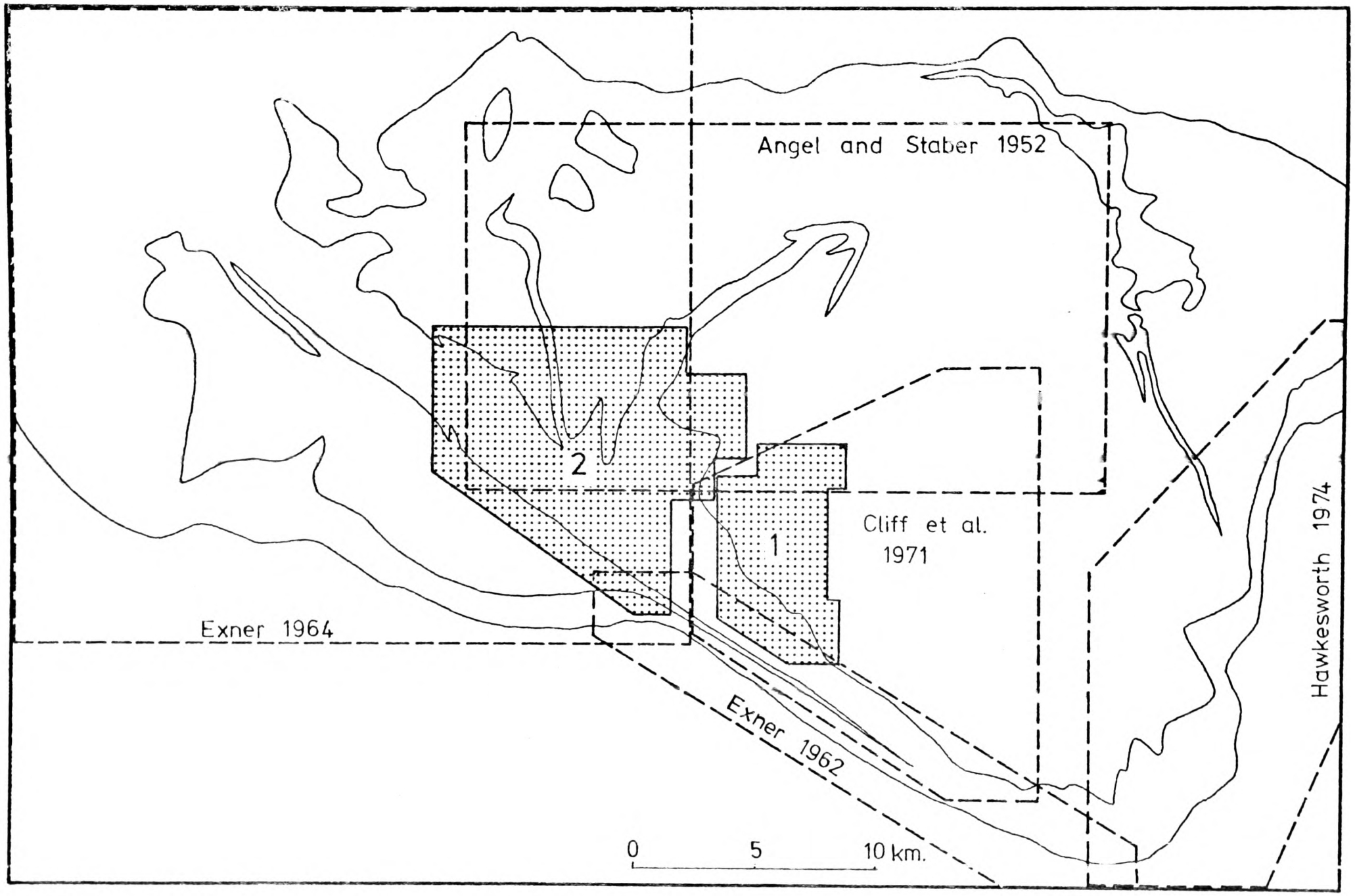



Fig. 1.5 The areas mapped in this thesis (stippled) in relation to areas mapped by other workers.

Table 2.1 Mineral abbreviations used in the text.

| | |
|---|---|
| ab | albite |
| acm | acmite |
| act | actinolite |
| all | allanite |
| alm | almandine |
| amph | calcic amphibole |
| an | anorthite |
| and | andalusite |
| andr | andradite |
| ank | ankerite |
| ann | annite |
| anth | anthophyllite |
| antig | antigorite |
| ap | apatite |
| aug | augite |
| biot | biotite |
| bruc | brucite |
| CaTs | calcium Tschermak's pyroxene |
| cc | calcite |
| celad | celadonite |
| chl | chlorite |
| chr | chromite |
| clin | clinochlore |
| cord | cordierite |
| cpx | clinopyroxene |
| ctd | chloritoid |
| czo | clinozoisite |
| di | diopside |
| dol | dolomite |
| east | eastonite |
| ed | edenite |
| en | enstatite |
| ep | epidote |
| fa | fayalite |
| Fe-cord | iron cordierite |
| Fe-ctd | iron chloritoid |
| Fe-st | iron staurolite |
| fo | forsterite |
| glauc | glaucophane |
| graph | graphite |
| gross | grossular |
| gt | garnet |
| hast | hastingsite |
| hbl | hornblende |
| hem | haematite |
| ilm | ilmenite |
| jd | jadeite |
| jo | johannsenite |
| ksp | potassium feldspar |
| ky | kyanite |
| laws | lawsonite |
| mag | magnesite |
| marg | margarite |
| Mg-cord | magnesium cordierite |
| mt | magnetite |
| musc | muscovite |
| or | orthoclase |
| ore | magnetite or ilmenite |
| parag | paragonite |
| parg | pargasite |
| pheng | phengite |
| phlog | phlogopite |
| plag | plagioclase |
| pyr | pyrite |
| pyroph | pyrophyllite |
| pyrp | pyrope |
| qz | quartz |
| rut | rutile |
| serp | serpentine |
| sid | siderophyllite |
| sill | sillimanite |
| spess | spessartine |
| sph | sphene |
| st | staurolite |
| tc | talc |
| tour | tourmaline |
| trem | tremolite |
| tsch | tschermakite |
| woll | wollastonite |
| zirc | zircon |
| zo | zoisite |

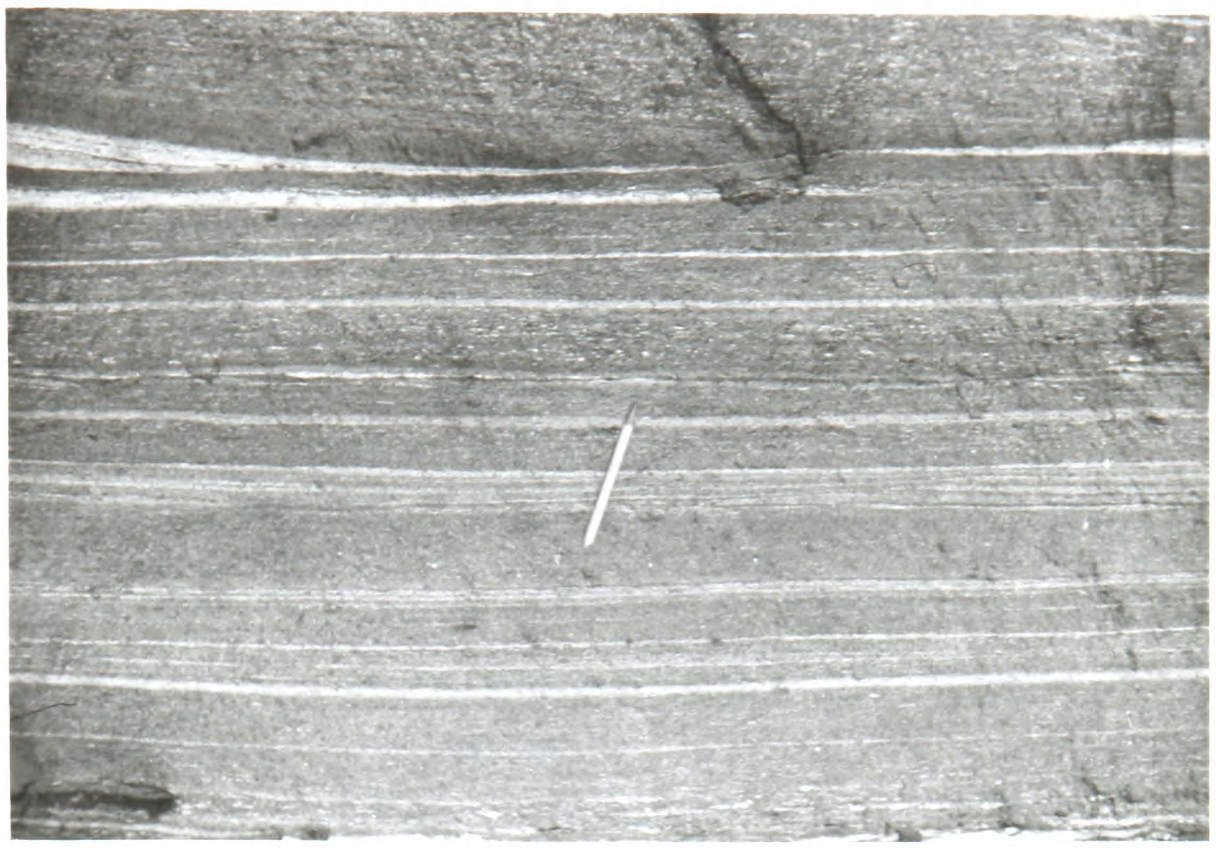


Fig. 2.1 Finely banded gneiss, Riekengraben



Fig. 2.2 Quartzo-feldspathic gneiss (pale) with amphibolite lenses (dark). North-east ridge of Böseck.




Fig. 2.3 Finely banded eclogitic amphibolite. White spots are albite poikiloblasts.

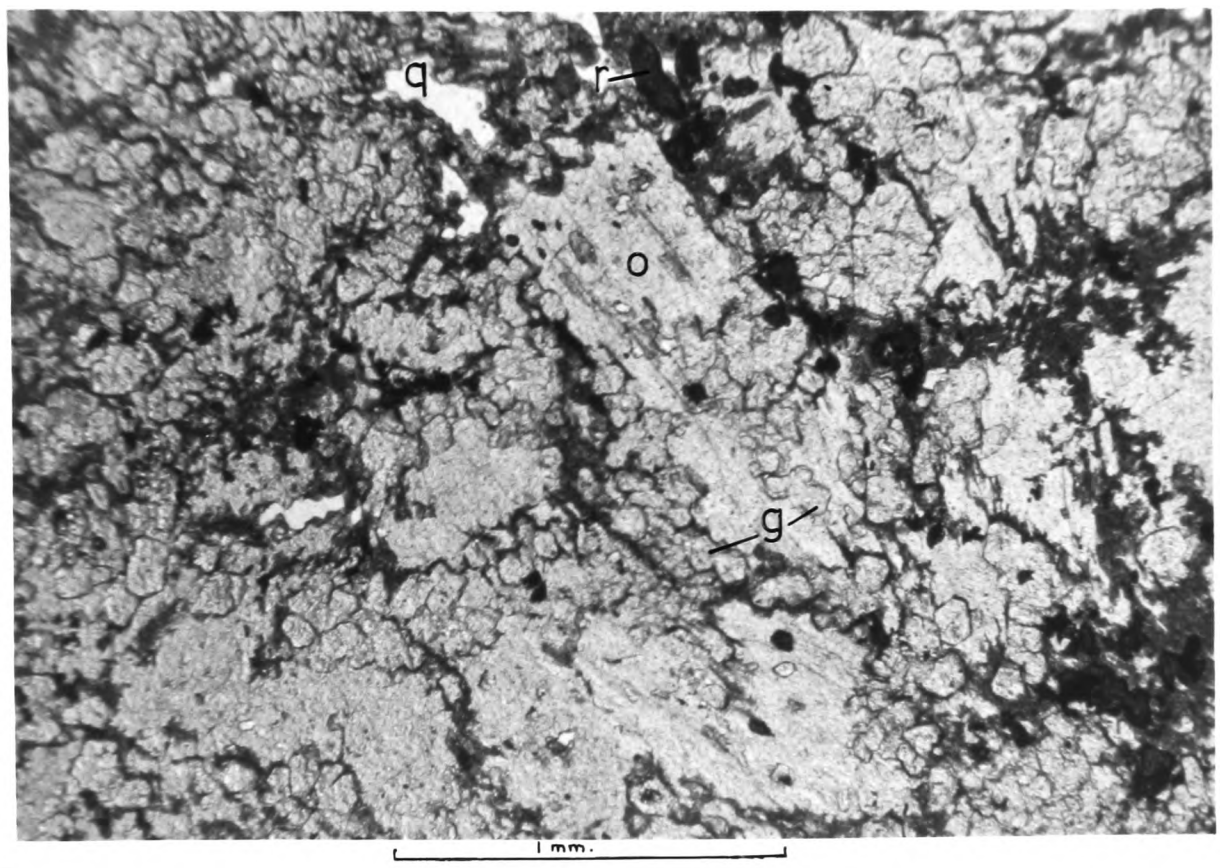



Fig. 2.4 Tiny garnets (g), rutile (r) and quartz (q) enclosed by poikiloblastic omphacite (o), slightly altered along grain boundaries, in fresh eclogite patch in eclogitic amphibolite GD 136a. Plane polarised light.

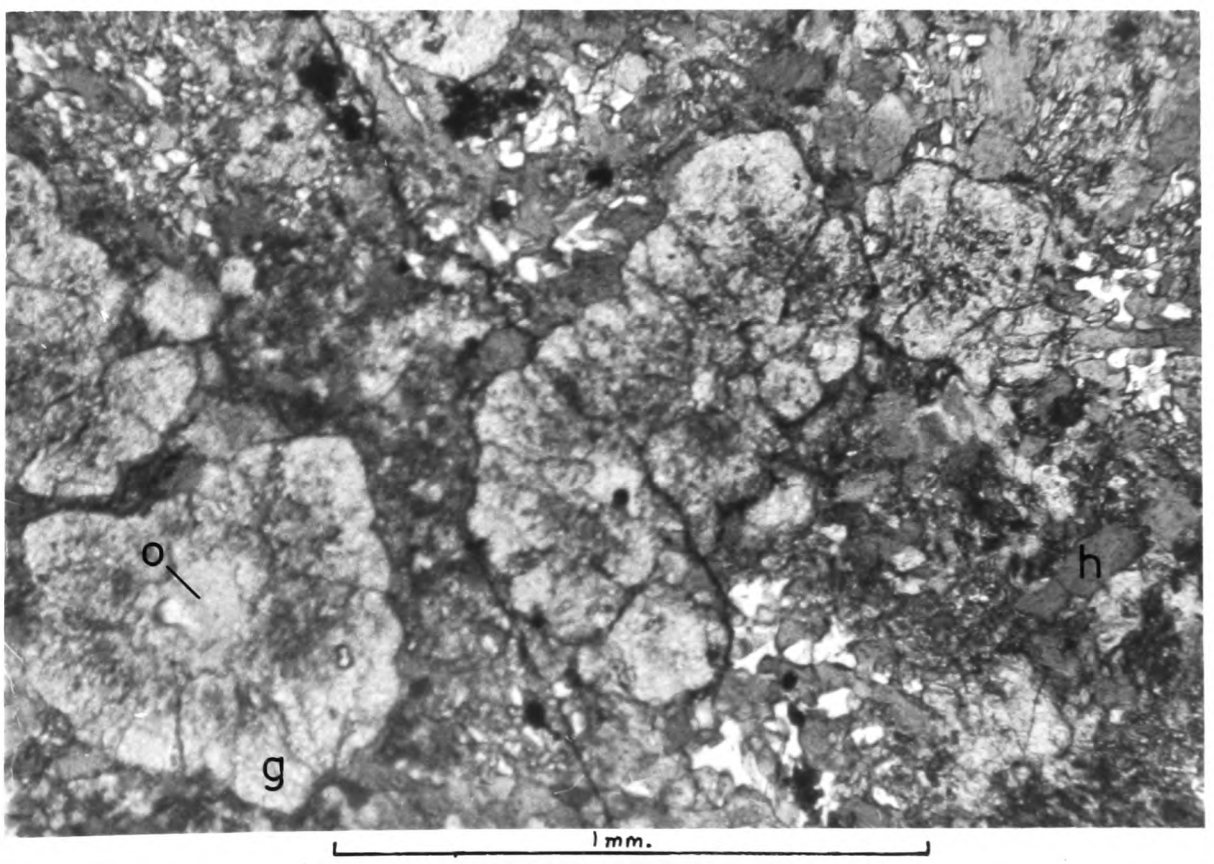



Fig. 2.5 Coronas of garnet (g) around relict omphacite (o), in a matrix of hornblende (h) locally intergrown with albite. GD 136a. Plane polarised light.

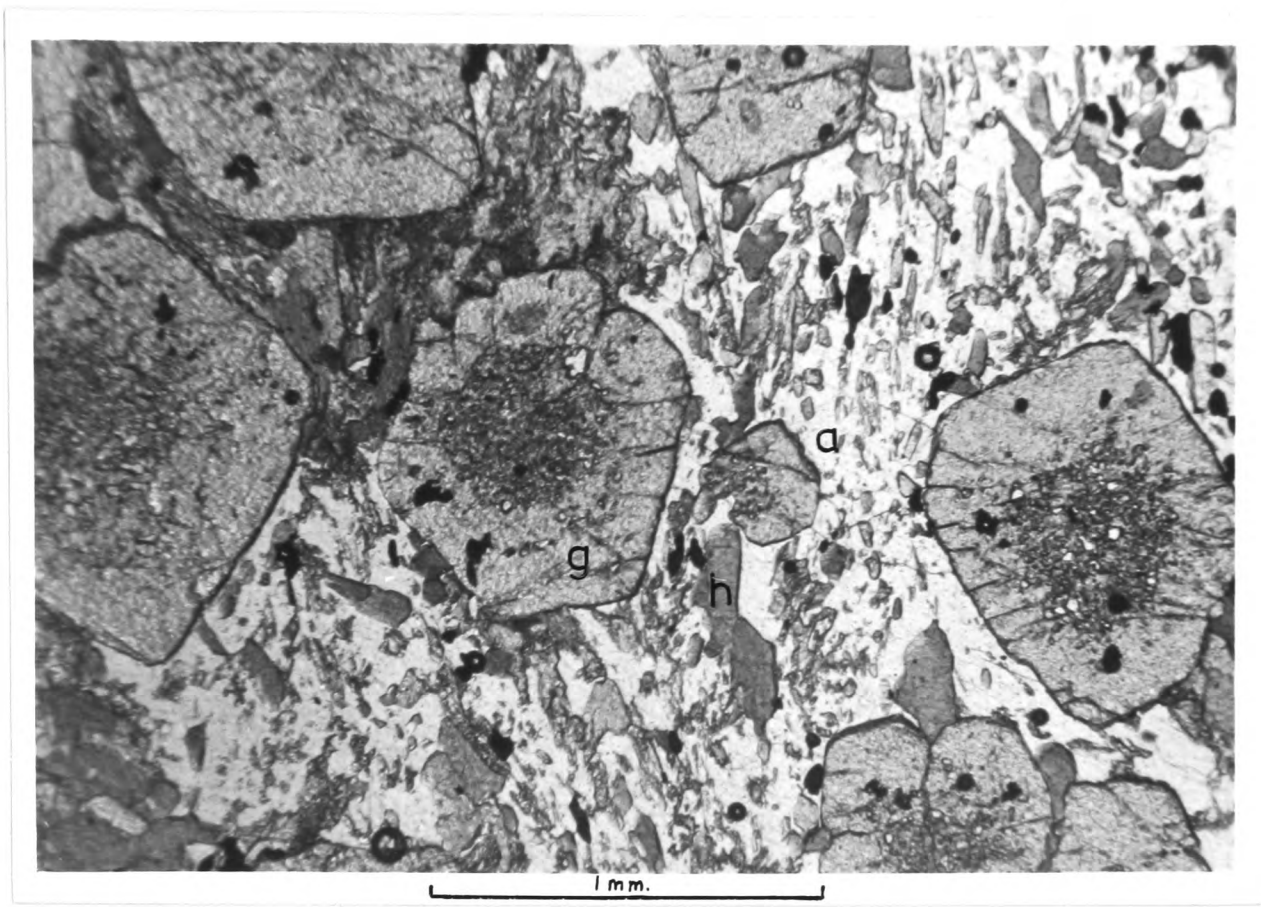



Fig. 2.6 Albite poikiloblast (a) enclosing hornblende (h) and large subhedral garnets with spongy cores (g) in eclogitic amphibolite GD 13c. Plane polarised light.

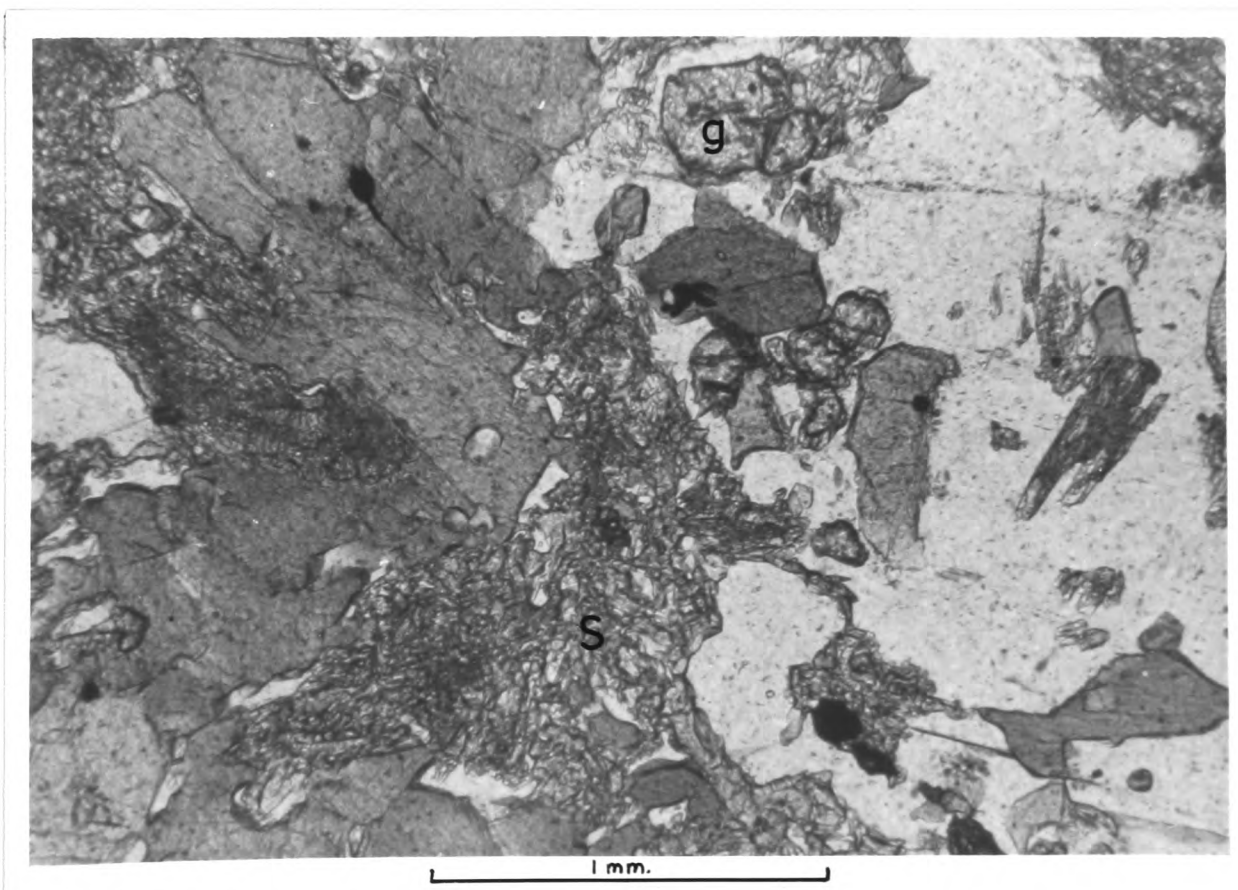



Fig. 2.7 Fine-grained symplectitic clinopyroxene + albite intergrowth (S), garnets (g) and albite poikiloblast in eclogitic amphibolite GD 13d. Plane polarised light.

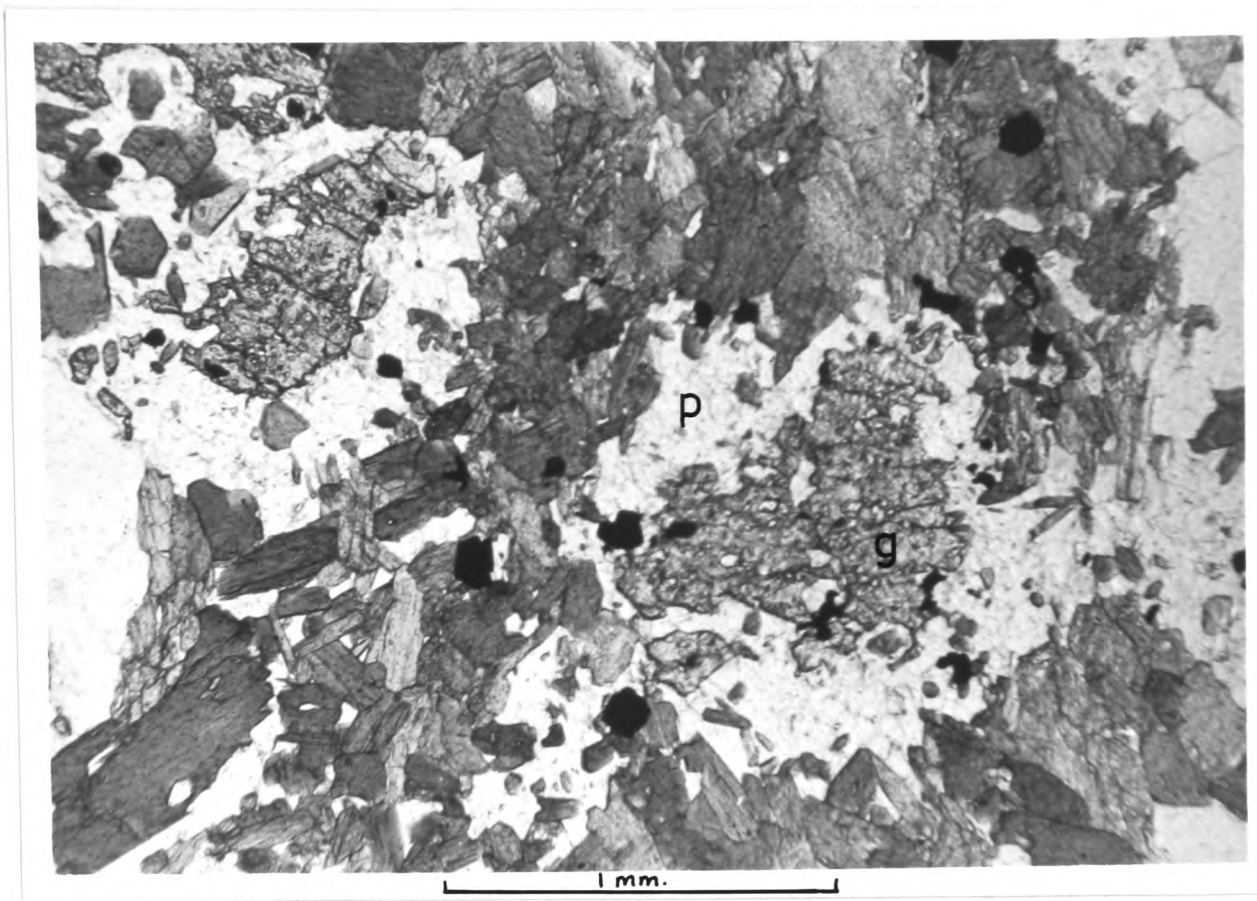



Fig. 2.8 Garnet porphyroblasts (g) with reaction rims of plagioclase (p) in garnet-amphibolite GD 135. Plane polarised light.

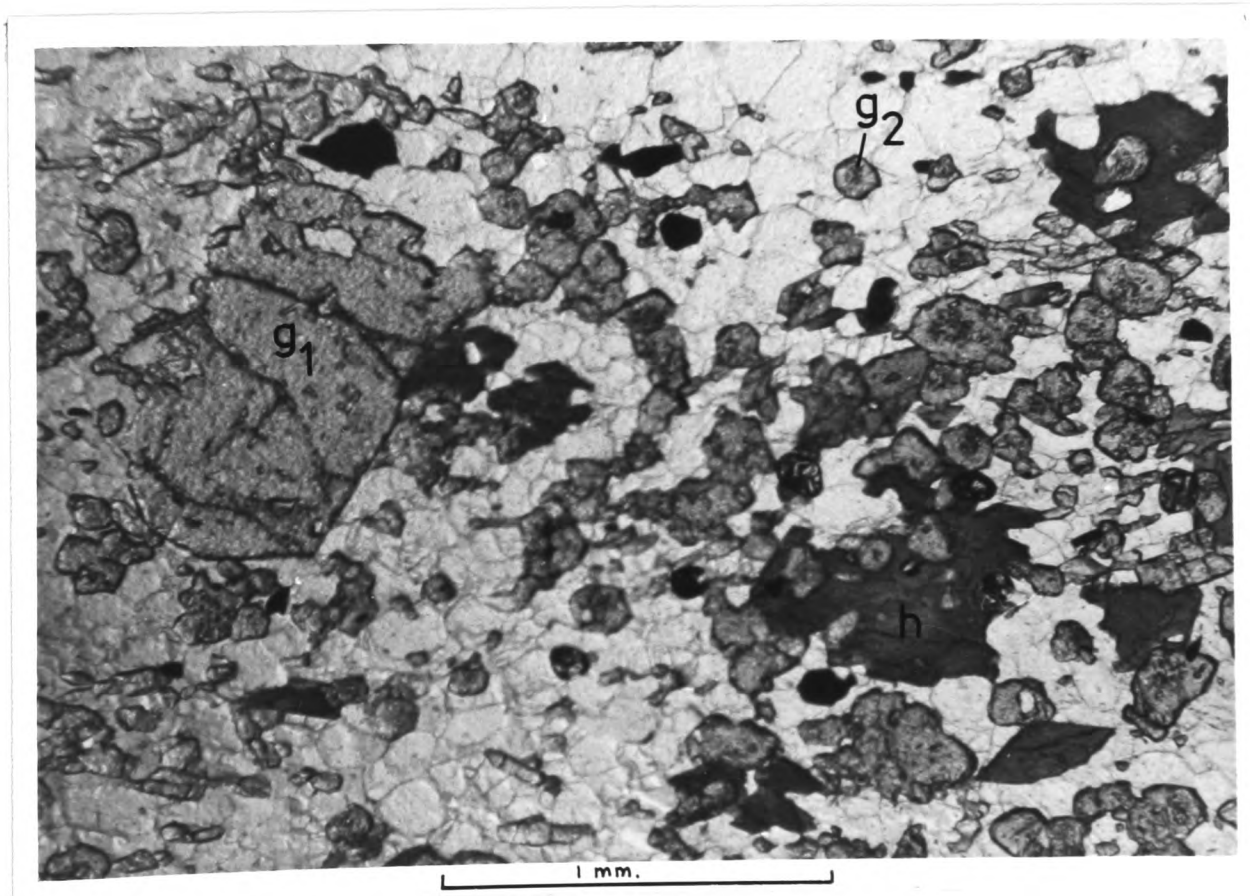



Fig. 2.9 Hornblende poikiloblasts (h) and two generations of garnet ($g_1$, $g_2$) in garnetiferous leucoamphibolite GD 98. Plane polarised light.







Fig. 2.10 Ophitic metagabbro-pegmatite, GD 94. (a)Above: Hand specimen.

(b) Below: thin section (plane polarised light) showing hornblende (h) pseudomorphing pyroxene, and saussuritised plagioclase (p).

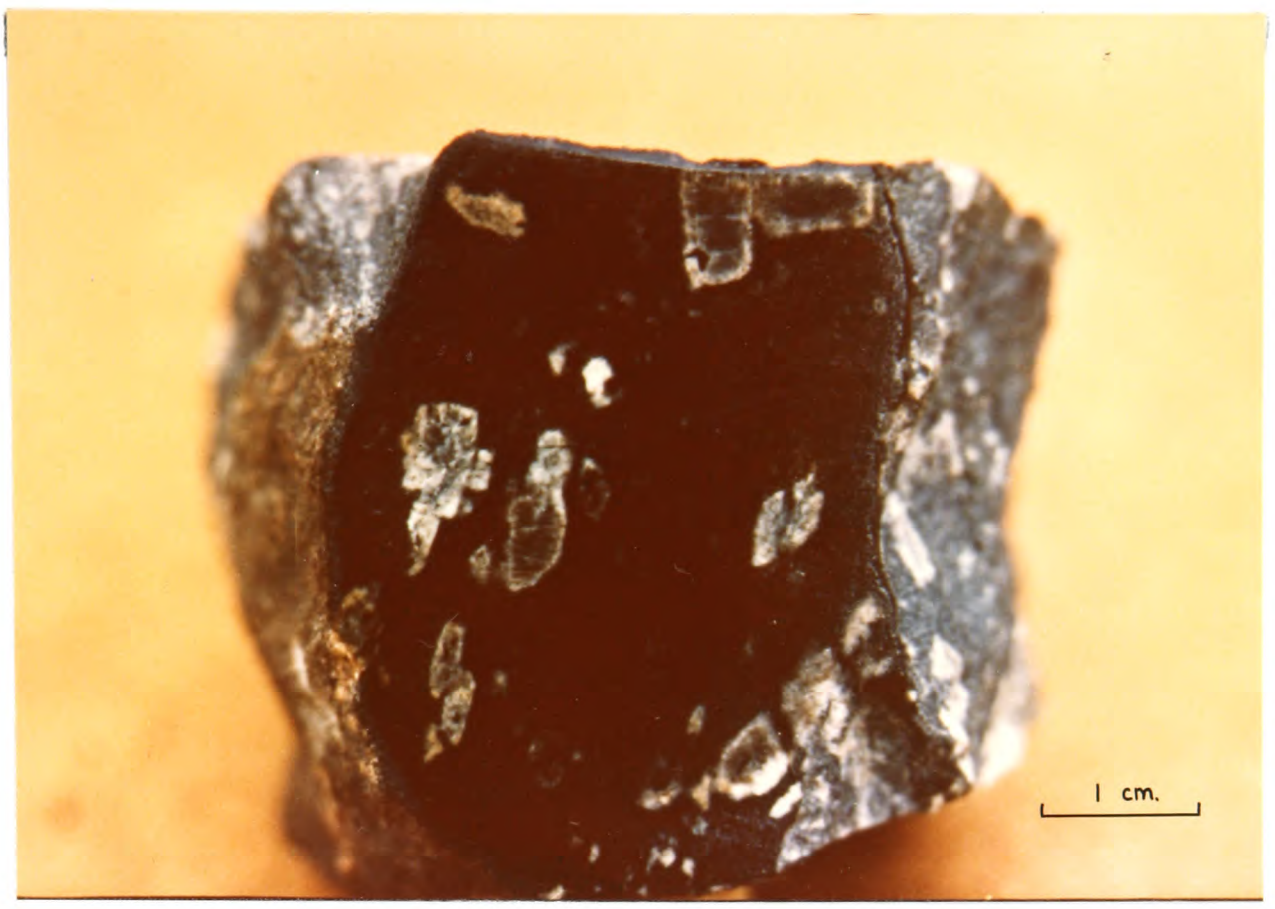



Fig. 2.11 Metabasalt-amphibolite, GD 96. (a) Above: hand specimen, showing porphyritic texture. (b) Below: thin section (plane polarised light) showing recrystallised margins (r) and saussuritised interiors (s) of relict plagioclase phenocrysts.



Fig. 2.12 Concordant band of granite-gneiss (pale) within mica-schists. Near Ankogelbahn car-park, Seebachtal.

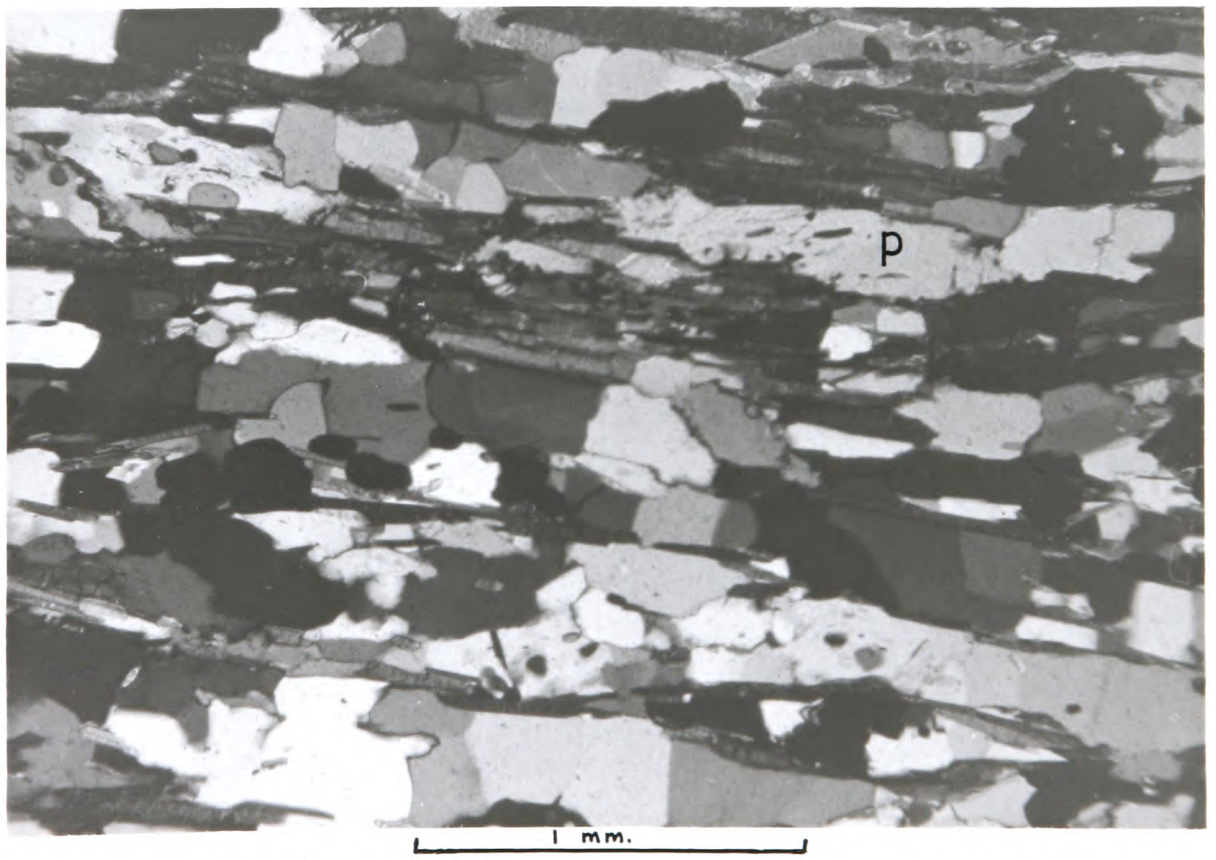



Fig. 2.13 Granular plagioclase (p) apparently in equilibrium with micas in mica-schist GD 1230a. Crossed polars.

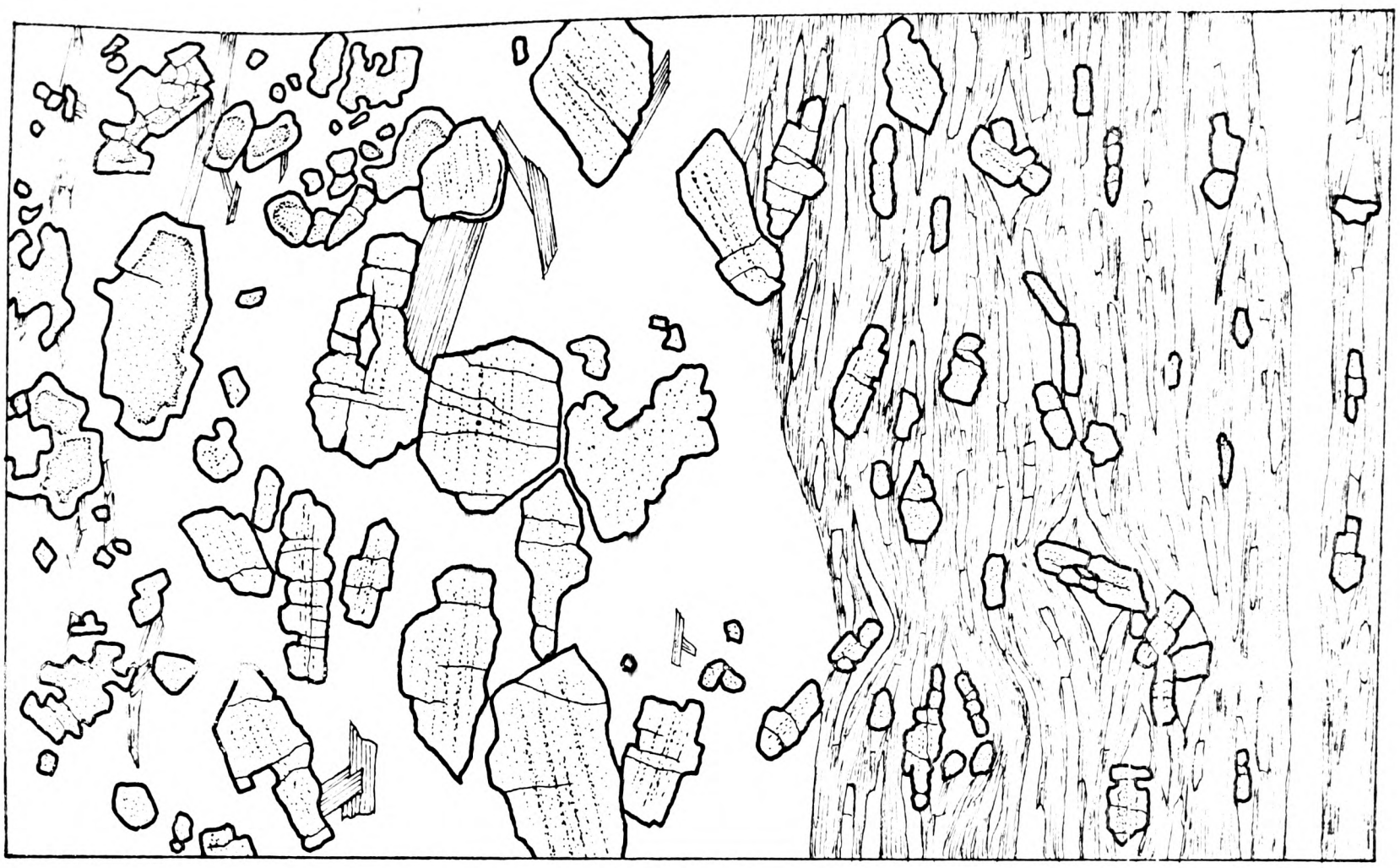


Fig. 2.14 Textures in and adjacent to the quartz and garnet vein in mica-schist GD 1230b. (Stipple : garnet; lined : muscovite and chlorite; clear areas : quartz.)

Table 2.2 Modal analyses of quartz + garnet vein and host mica-schist, GD 1230b.

| | GD 1230b rock | GD 1230b vein |
|---|---|---|
| GT. | 19 | 33 |
| BIOT. | 1 | 0 |
| CHL. | 7 | 4 |
| MUSC. | 39 | 6 |
| QZ | 33 | 57 |
| RUT | 1 | 0 |




Fig. 2.15 Inner Schieferhülle mica-schist GD 450, with large garnet porphyroblasts.

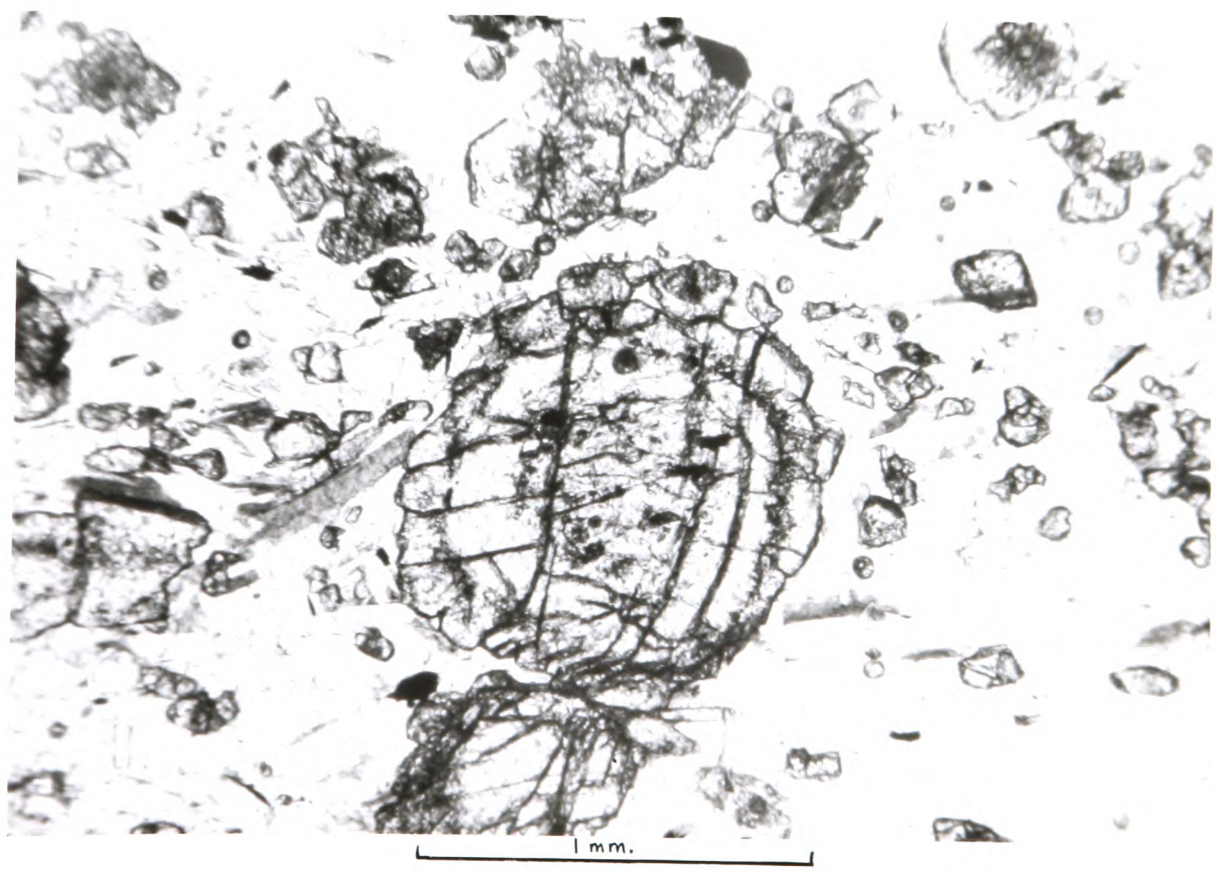



Fig. 2.16 Large zoned garnet porphyroblast and "pin-prick" garnets in Inner Schieferhülle mica-schist GD 209a. Plane polarised light.

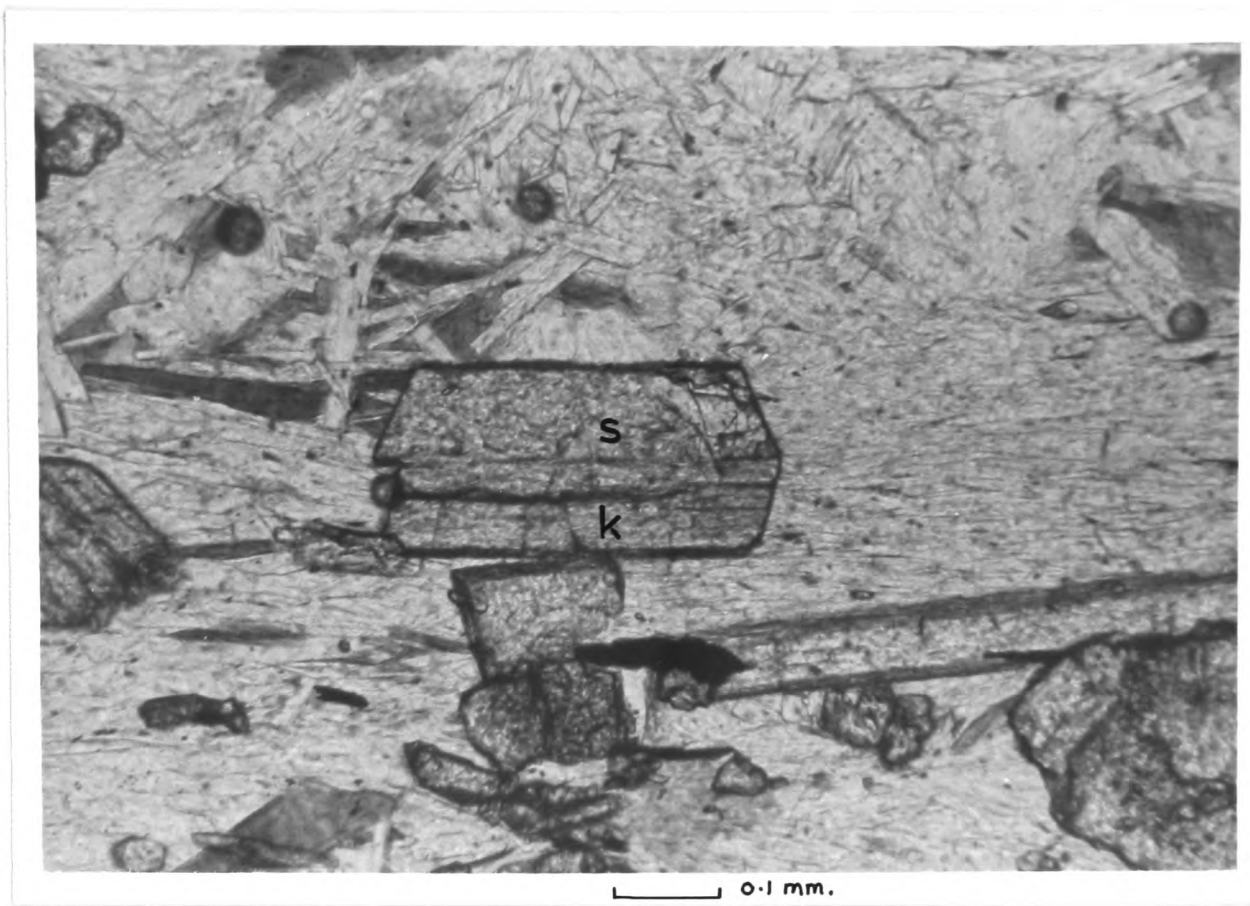



Fig. 2.17 Twinned grain of staurolite (s) and kyanite (k) in GD 209a. Plane polarised light.

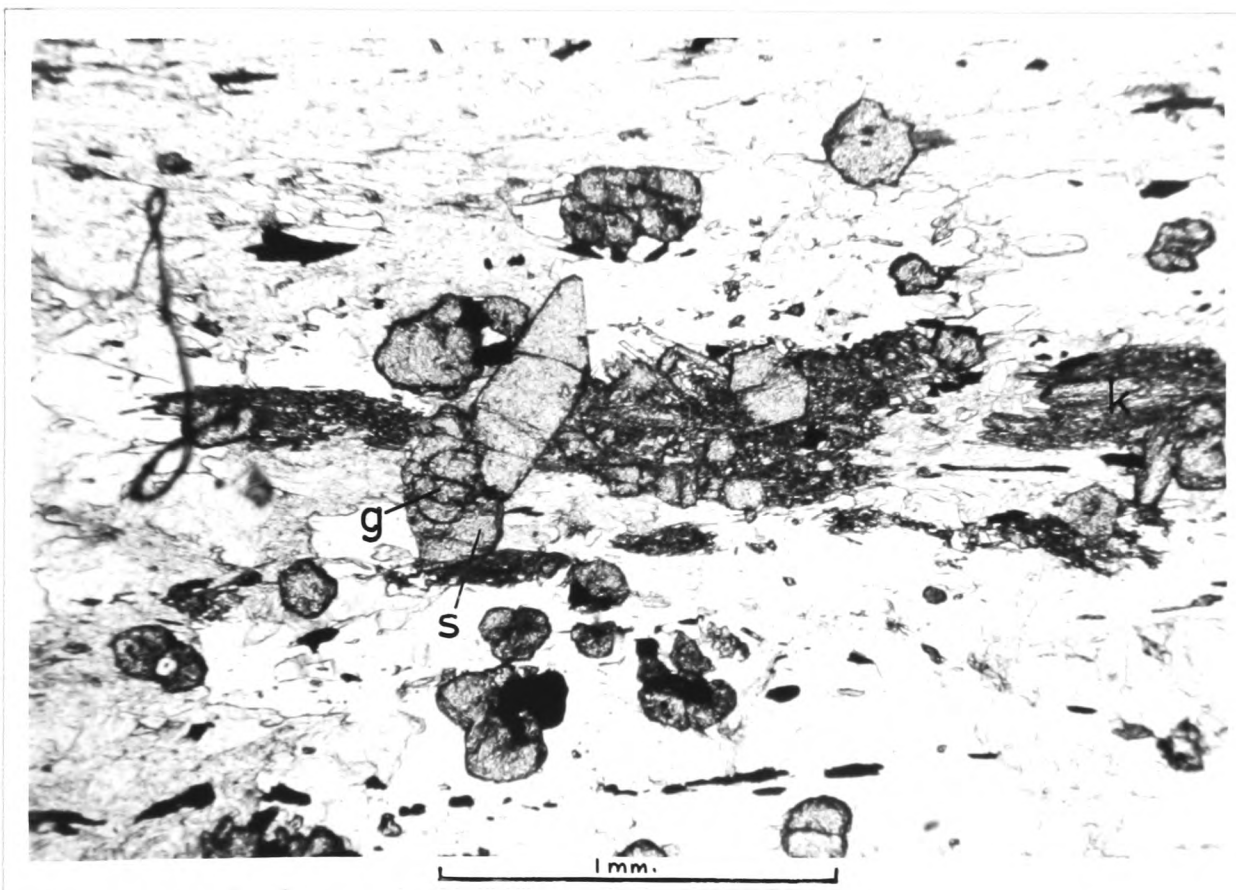



Fig. 2.18 Staurolite (s) enclosing garnet (g) and cutting across mats of fine-grained kyanite (k) in Inner Schieferhülle mica-schist GD 208d. Plane polarised light.

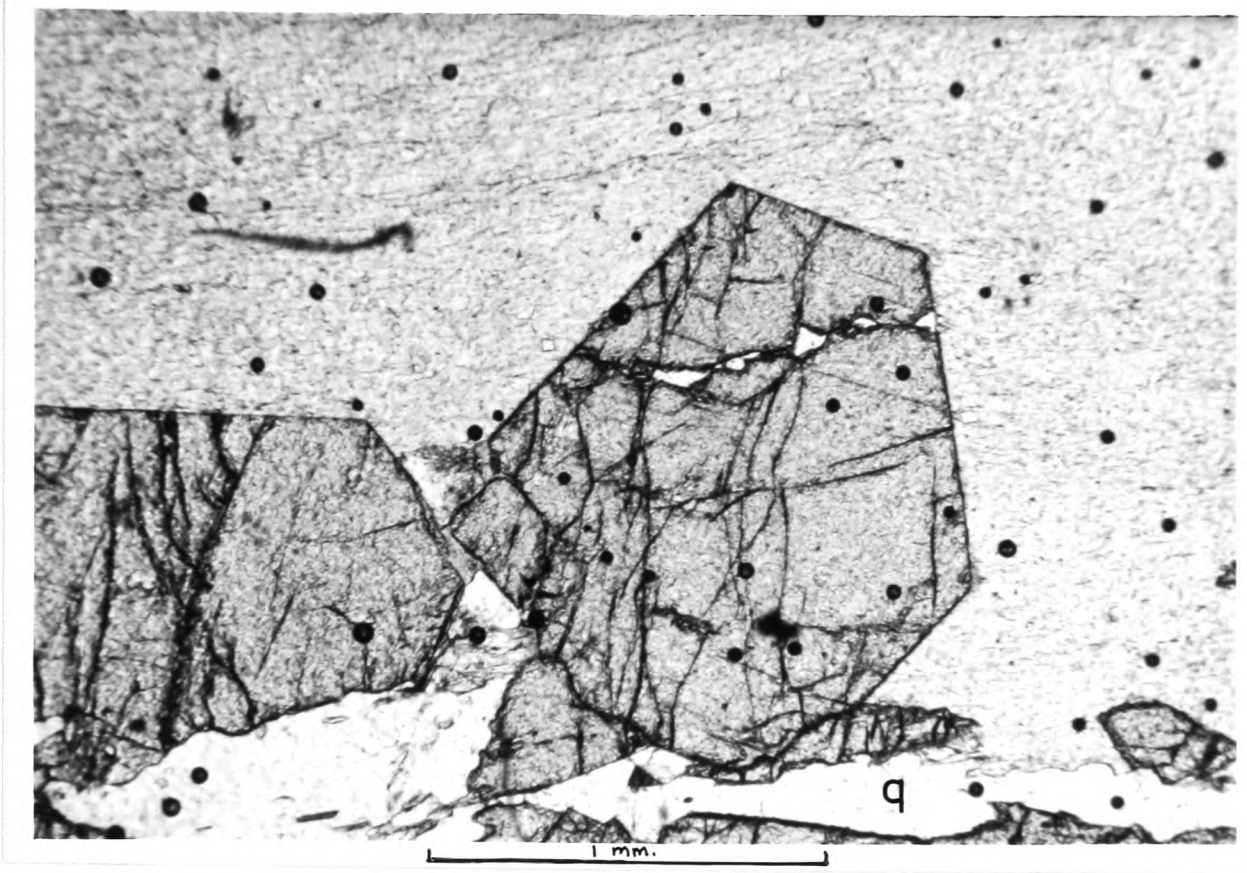



Fig. 2.19 Euhedral staurolite porphyroblasts cutting across schistosity in fine-grained monomineralic paragonite which locally contacts quartz (q). GD 209a. (Black spots are bubbles in the mounting medium.) Plane polarised light.

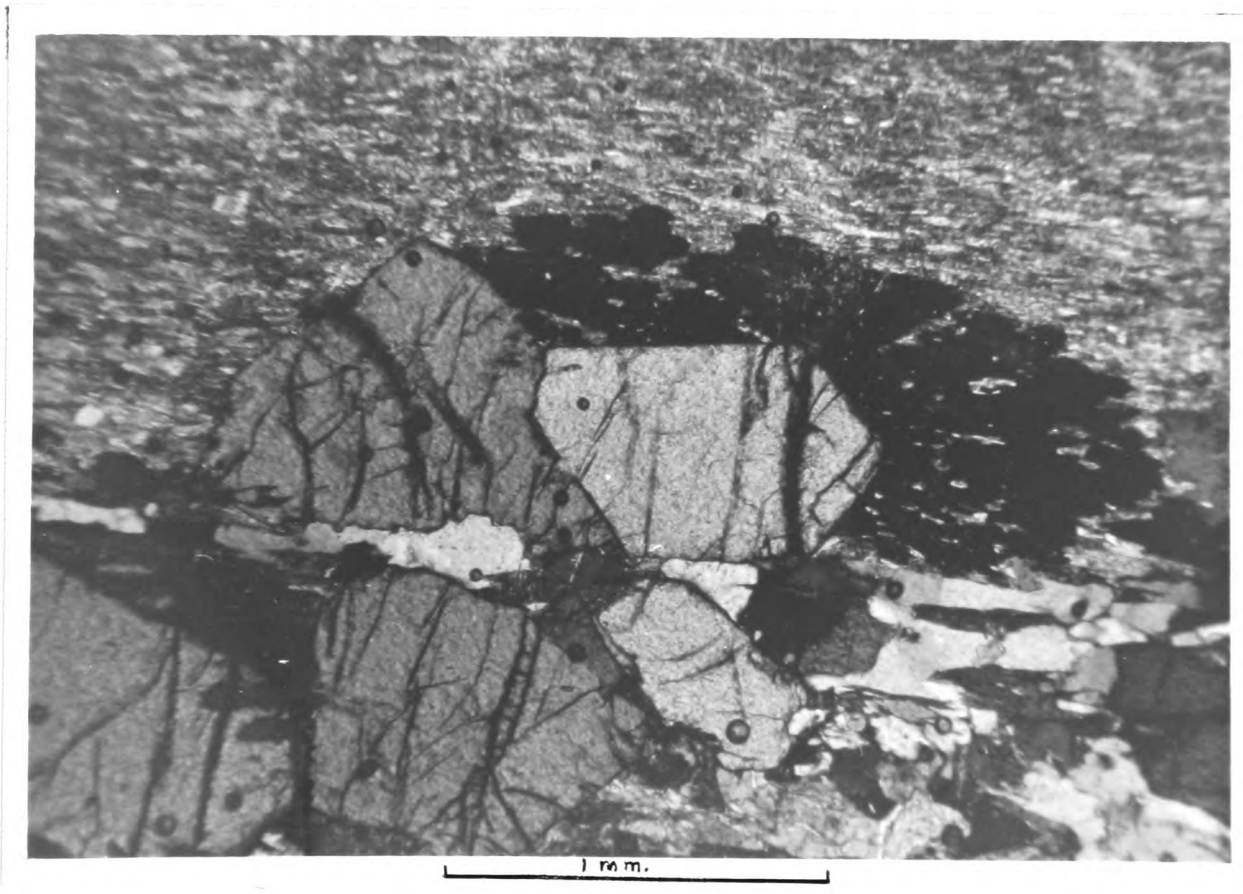



Fig. 2.20 Oligoclase porphyroblast (in extinction) replacing paragonite and enclosing staurolite in GD 209a. Crossed polars.

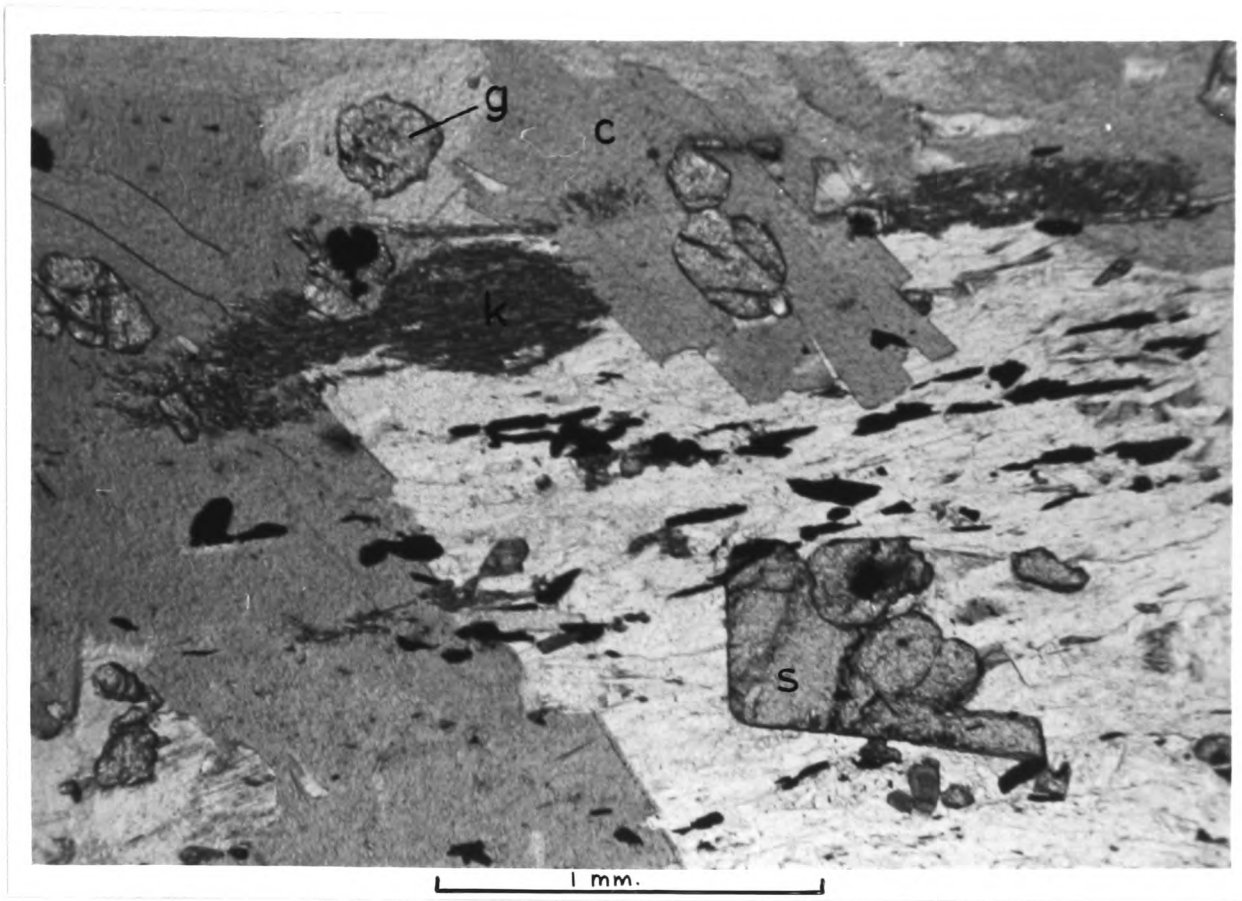



Fig. 2.21 Part of a large spray of chlorite (c) enclosing garnet (g) and kyanite (k) in GD 208d. Note also euhedral staurolite (s) nucleating on garnets. Plane polarised light.

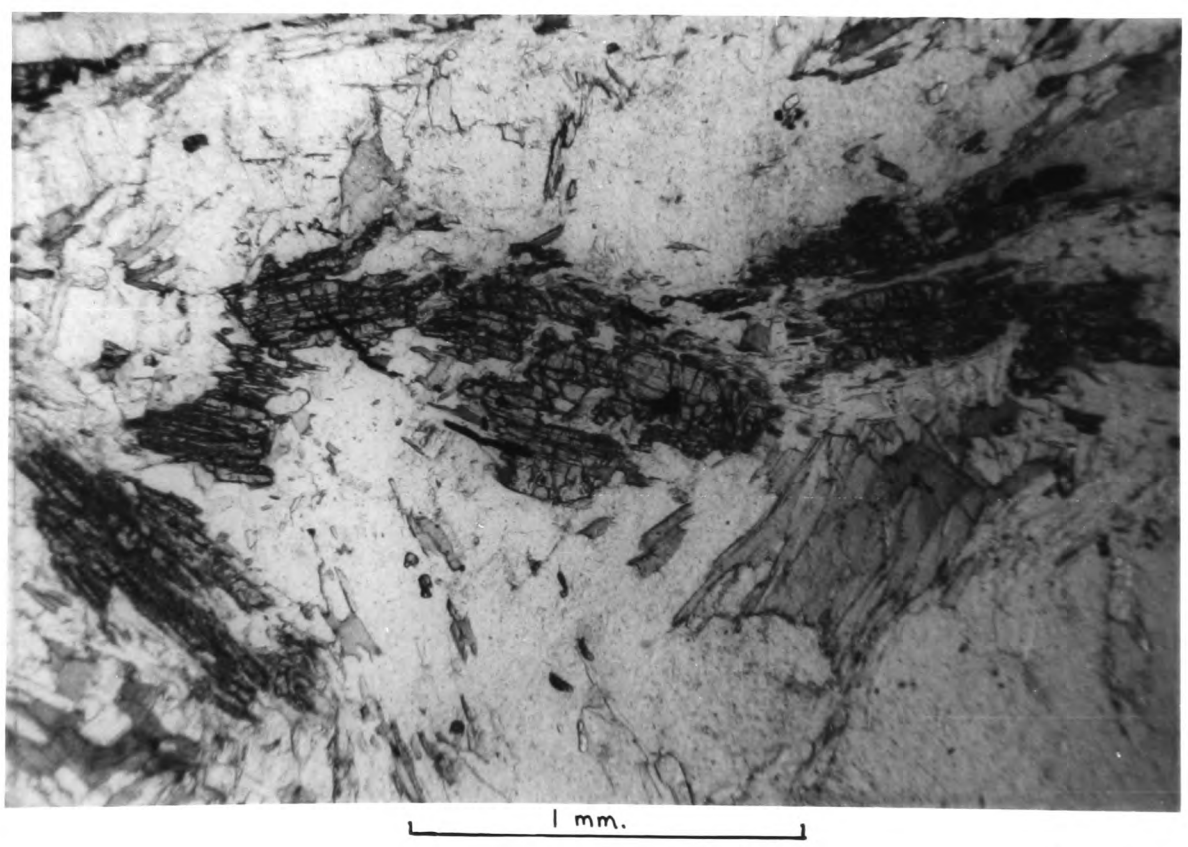



Fig. 2.22 Kyanite, partially altered to muscovite, in GD 652. Plane polarised light.

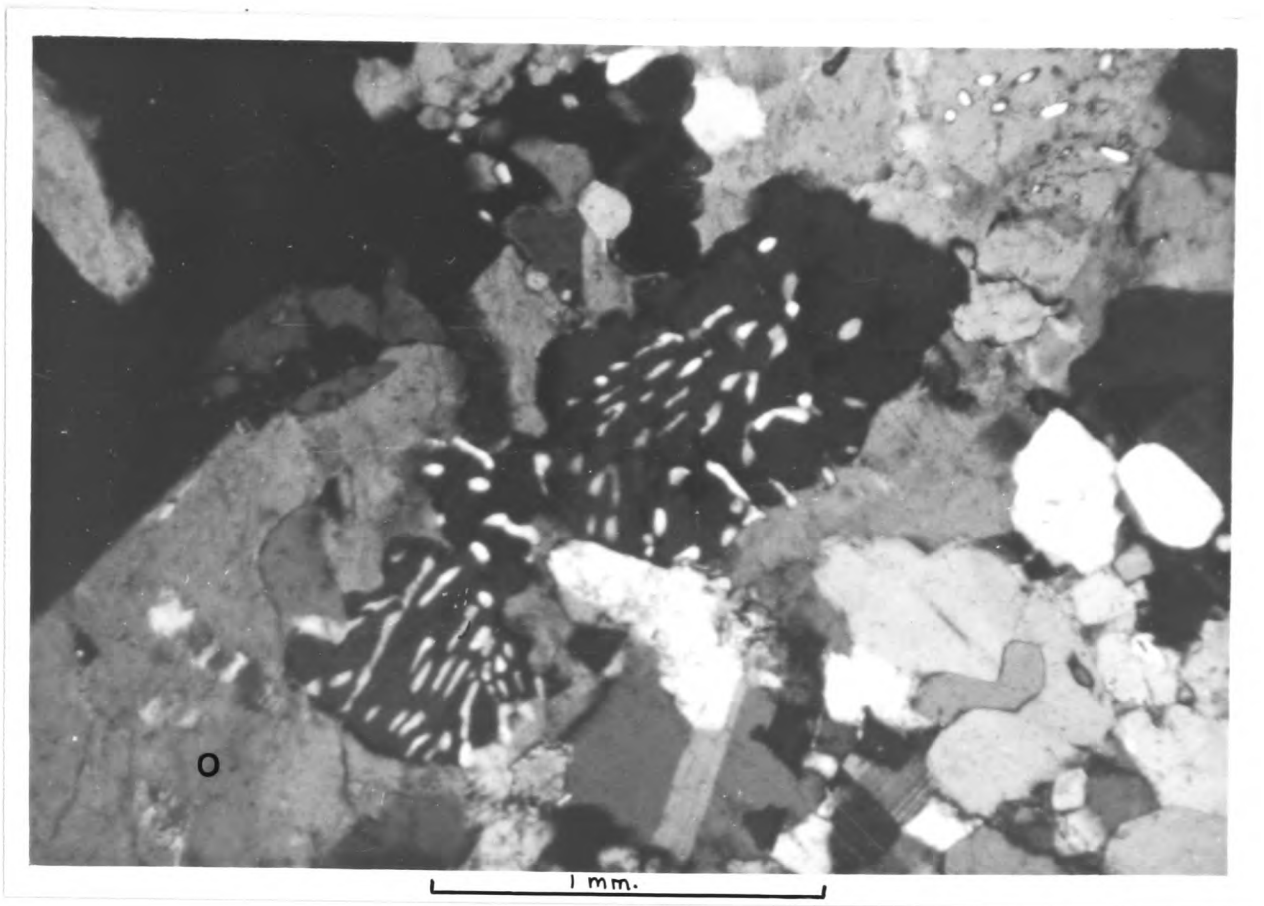



Fig. 2.23 Myrmekitic intergrowth of plagioclase (in extinctcn) and quartz replacing orthoclase (o) in leucogranite GD 468. Crossed polars.

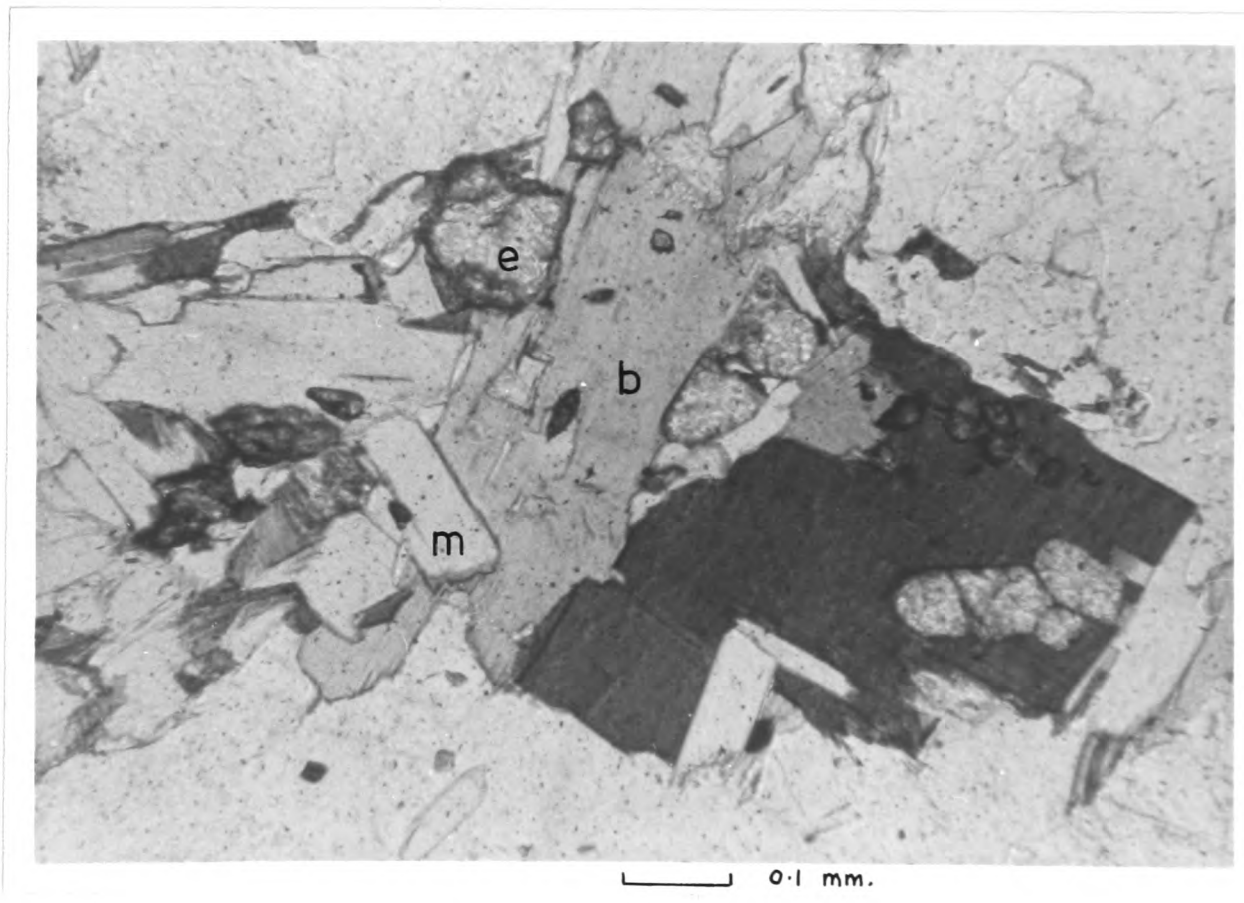



Fig. 2.24 Recrystallised biotite (b), epidote (e) and muscovite (m) in augen-gneiss GD 595. Plane polarised light.

Table 2.3 Textural and mineralogical changes with increasing deformation in six metagranites.

| SAMPLE | MG1 | MG2 | MG3 | MG4 | MG5 | MG6 |
|---|---|---|---|---|---|---|
| LITHOLOGY | granite-gneiss | augen-gneiss | augen-gneiss | quartz-phengite-schist | pale bands in quartz-phengite-schist | dark bands in quartz-phengite-schist |
| LOCALITY | ├---- SONNBLICK KERN ----┤ | | | ├--- GNEISS LAMELLA 4 ------┤ | | |
| MODES BIOT. | 4 | 5 | 4 | 0 | 0 | 0 |
| " PHENG. | 8 | 8 | 9 | 23 | 33 | 48 |
| " QZ. | 27 | 31 | 29 | 37 | 45 | 49 |
| " KSP. | 24 | 18 | 20 | 30 | 15 | 2 |
| " PLAG. | 29 | 31 | 29 | 7 | 5 | 0 |
| " EP. | 7 | 5 | 5 | 0 | 0 | 0 |
| " CC. | 0 | 1 | 1 | 1 | 0 | 0 |
| " ACC. | 1 | 1 | 3 | 2 | 2 | 1 |
| MATRIX GRAINSIZE | coarse | medium -coarse | medium -coarse | medium -fine | fine | medium |
| KSP. AUGEN | +++ | +++ | ++ | ++ | + | - |
| KSP. GRAINSIZE | >1 cm. | 1-2 cm. | 1-2 cm. | 2-3 mm. | 1-2 mm. | <1mm. |
| SCHISTOSITY | + | ++ | ++ | ++ | ++ | + |
| cm.-SCALE BANDING | - | - | - | + | ++ | +++ |
| QZ. FABRIC | reX'd | reX'd | reX'd | strained | strained | reX'd |
| INCREASING DEFORMATION | ⟶ | | | | | |

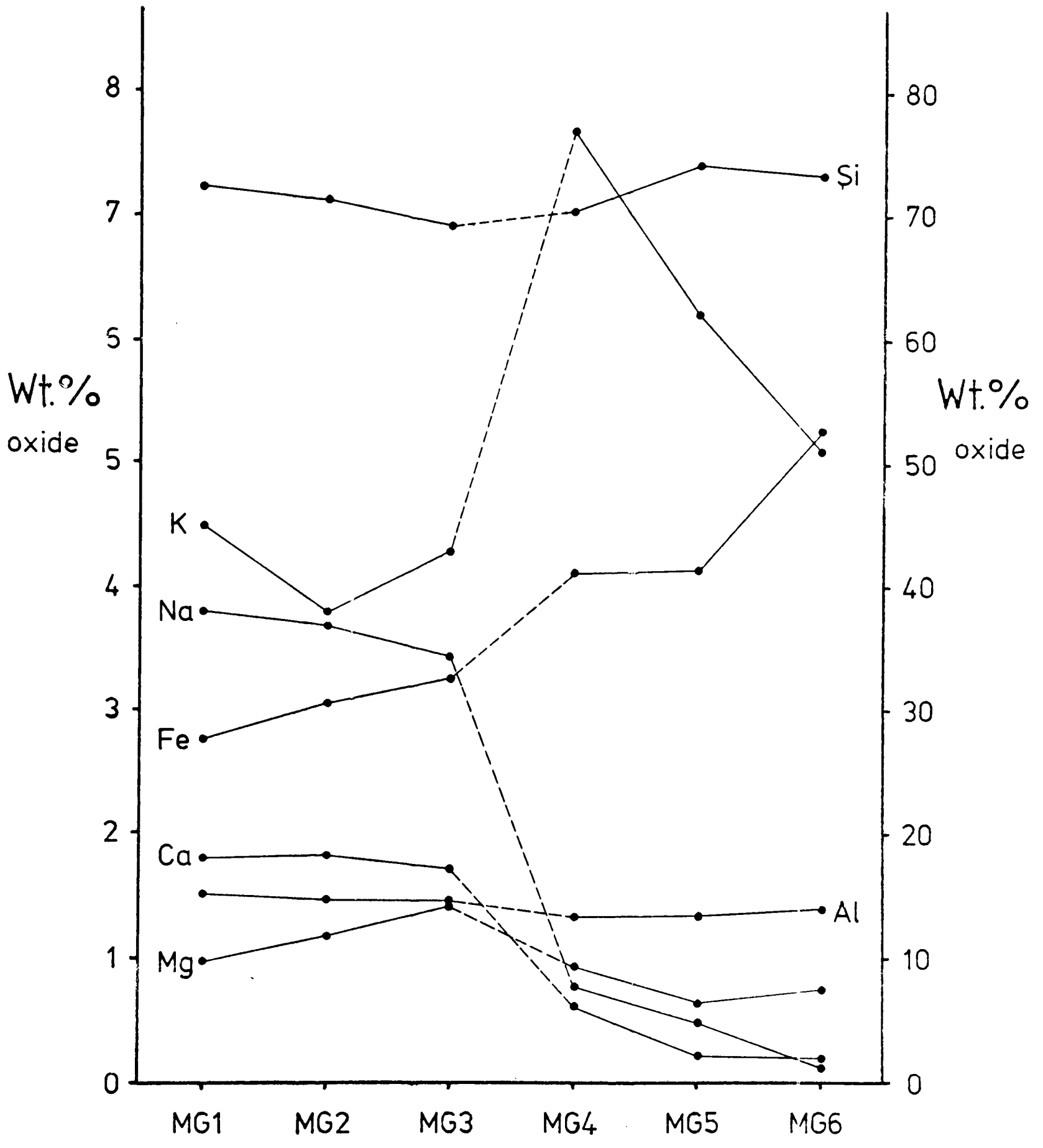



Fig. 2.25 Plot of meta-granite bulk compositions (cf. table 2.3).

Table 2.4 Chemical analyses of six metagranites.

AD = average composition of 135 adamellites

GR = average composition of 2485 granites (from Le Maitre, 1976).

| | MG1 | MG2 | MG3 | MG4 | MG5 | MG6 | AD. | GR. |
|---|---|---|---|---|---|---|---|---|
| $SiO_2$ | 72.379 | 71.421 | 69.291 | 70.594 | 74.222 | 73.160 | 69.51 | 72.04 |
| $Al_2O_3$ | 15.023 | 14.526 | 14.448 | 13.126 | 13.239 | 13.860 | 14.76 | 14.42 |
| $TiO_2$ | 0.285 | 0.312 | 0.355 | 0.402 | 0.552 | 0.561 | 0.54 | 0.30 |
| $Fe_2O_3$ | 2.753 | 3.044 | 3.243 | 4.105 | 4.121 | 5.264 | 4.21 | 3.09 |
| MgO | 0.973 | 1.172 | 1.408 | 0.901 | 0.636 | 0.743 | 1.11 | 0.71 |
| CaO | 1.794 | 1.813 | 1.719 | 0.606 | 0.213 | 0.204 | 2.55 | 1.82 |
| $K_2O$ | 4.480 | 3.780 | 4.294 | 7.708 | 6.216 | 5.094 | 4.14 | 4.12 |
| MnO | 0.040 | 0.053 | 0.047 | 0.022 | 0.005 | 0.008 | - | - |
| $P_2O_5$ | 0.102 | 0.129 | 0.157 | 0.103 | 0.151 | 0.150 | - | - |
| $Na_2O$ | 3.790 | 3.670 | 3.420 | 0.770 | 0.470 | 0.140 | 3.51 | 3.69 |
| VOL. | 1.514 | 1.919 | 2.324 | 2.410 | 1.599 | 2.260 | - | - |
| Rb(ppm.) | 188 | 162 | 190 | 224 | 159 | 158 | - | - |
| Sr(ppm.) | 415 | 377 | 569 | 73 | 67 | 19 | - | - |
| TOTAL | 103.132 | 101.839 | 100.706 | 100.745 | 101.425 | 101.444 | 100.33 | 100.19 |

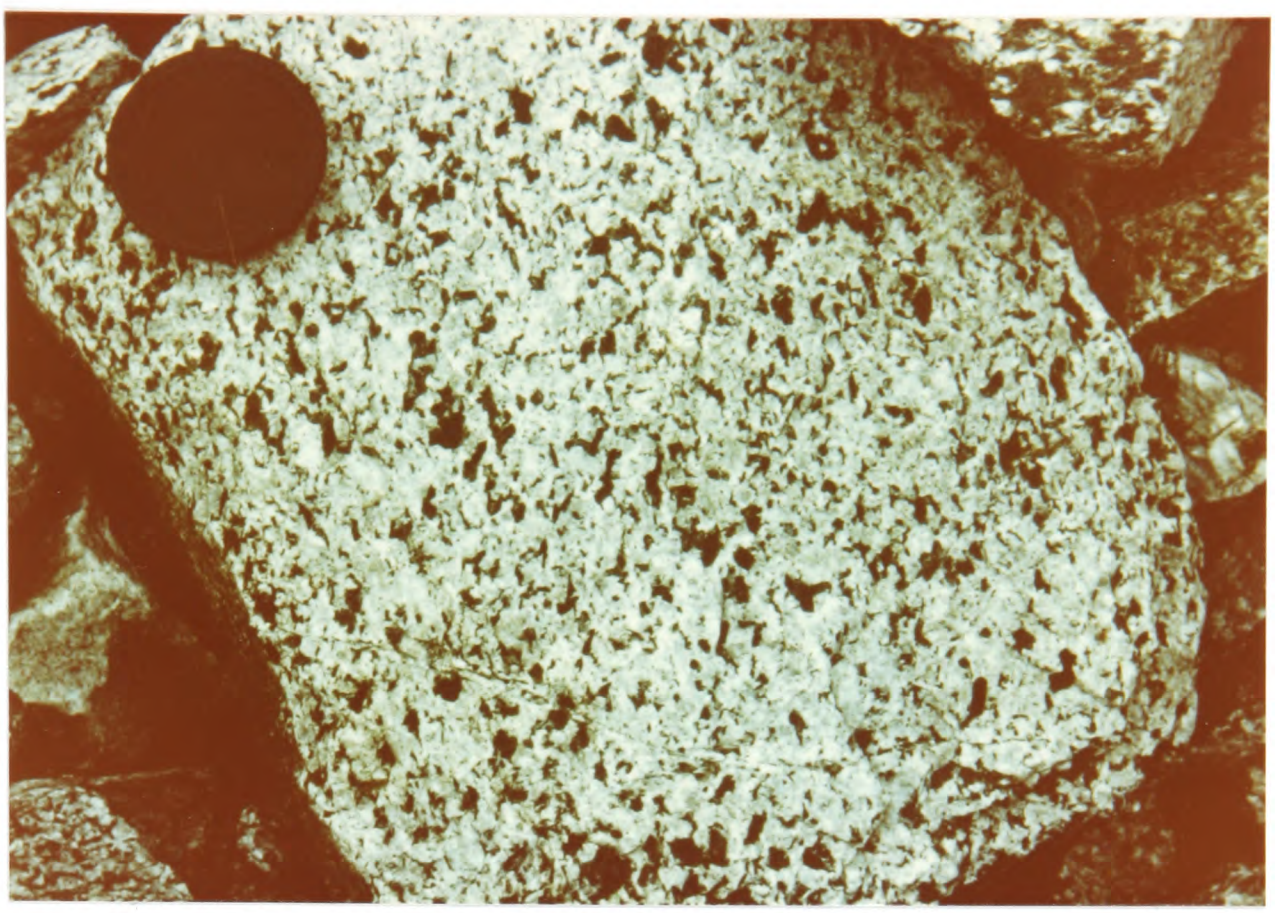


Fig. 2.26 Poorly deformed syenite-gneiss with pseudomorphs after ? hornblende.

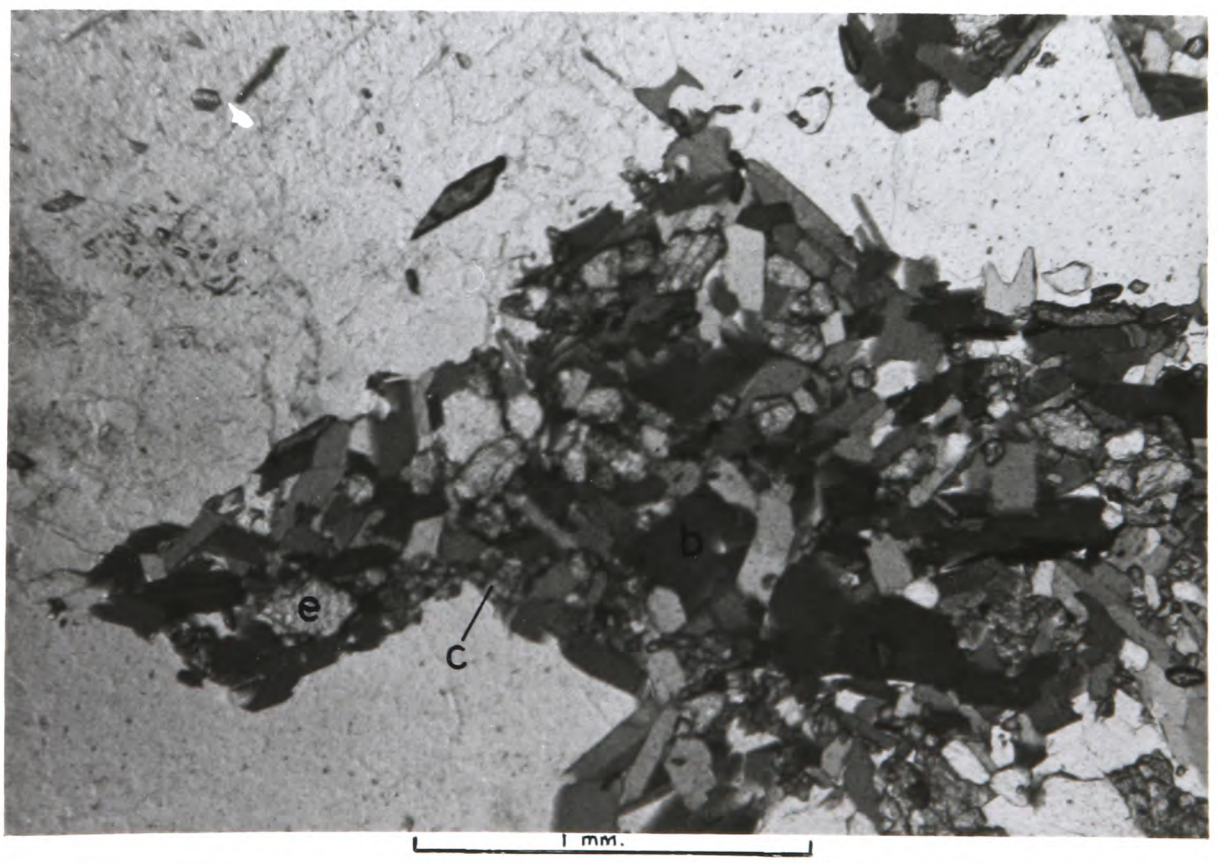



Fig. 2.27 Well recrystallised biotite(b) epidote (e) and clinopyroxene (c) forming a pseudomorph in syenite gneiss GD 1234a.
Plane polarised light.

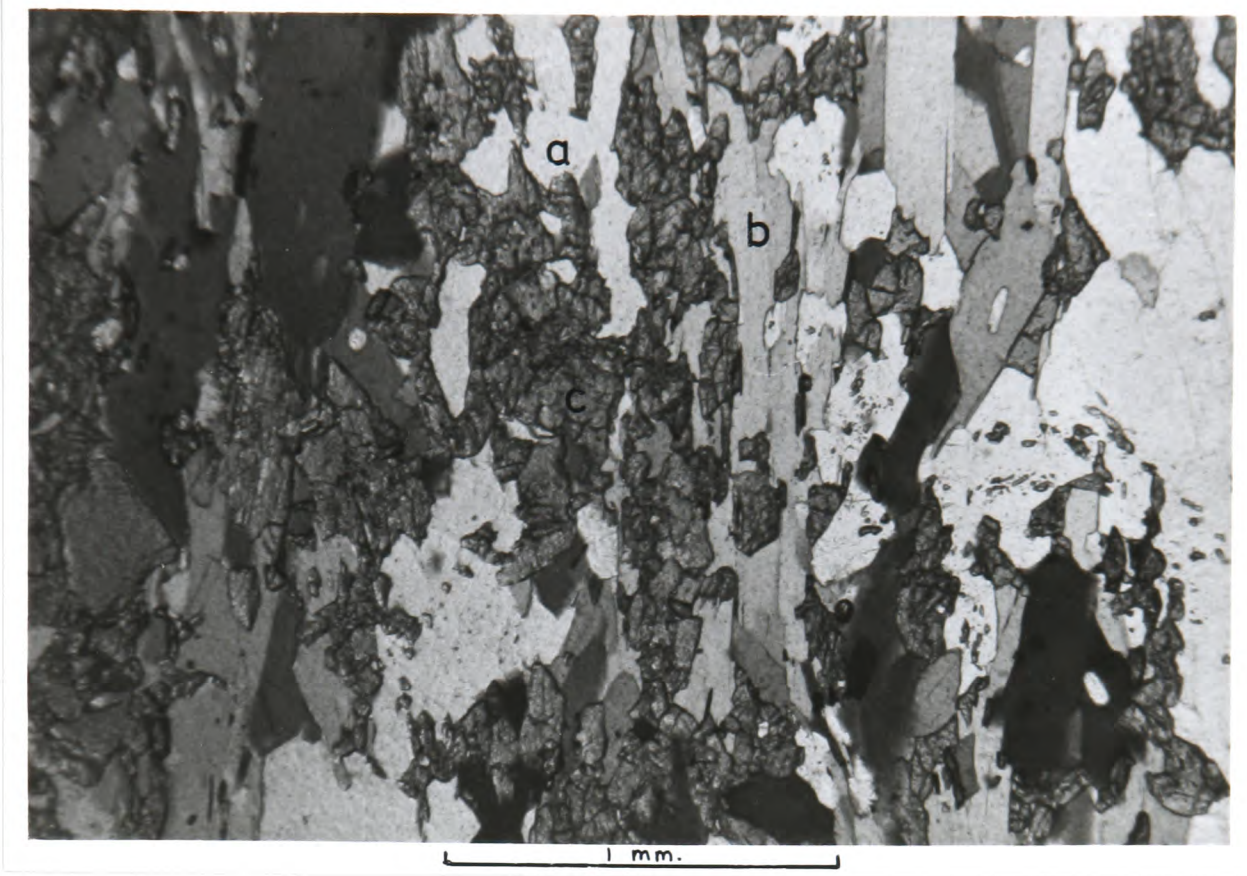



Fig. 2.28 Albite (a), biotite (b) and clinopyroxene (c) in GD 1234b. Plane polarised light.



Fig. 2.29 Dyke of biotite-epidote-feldspar-schist in syenite-gneiss. Jamnig Alm road section. Contacts are arrowed.

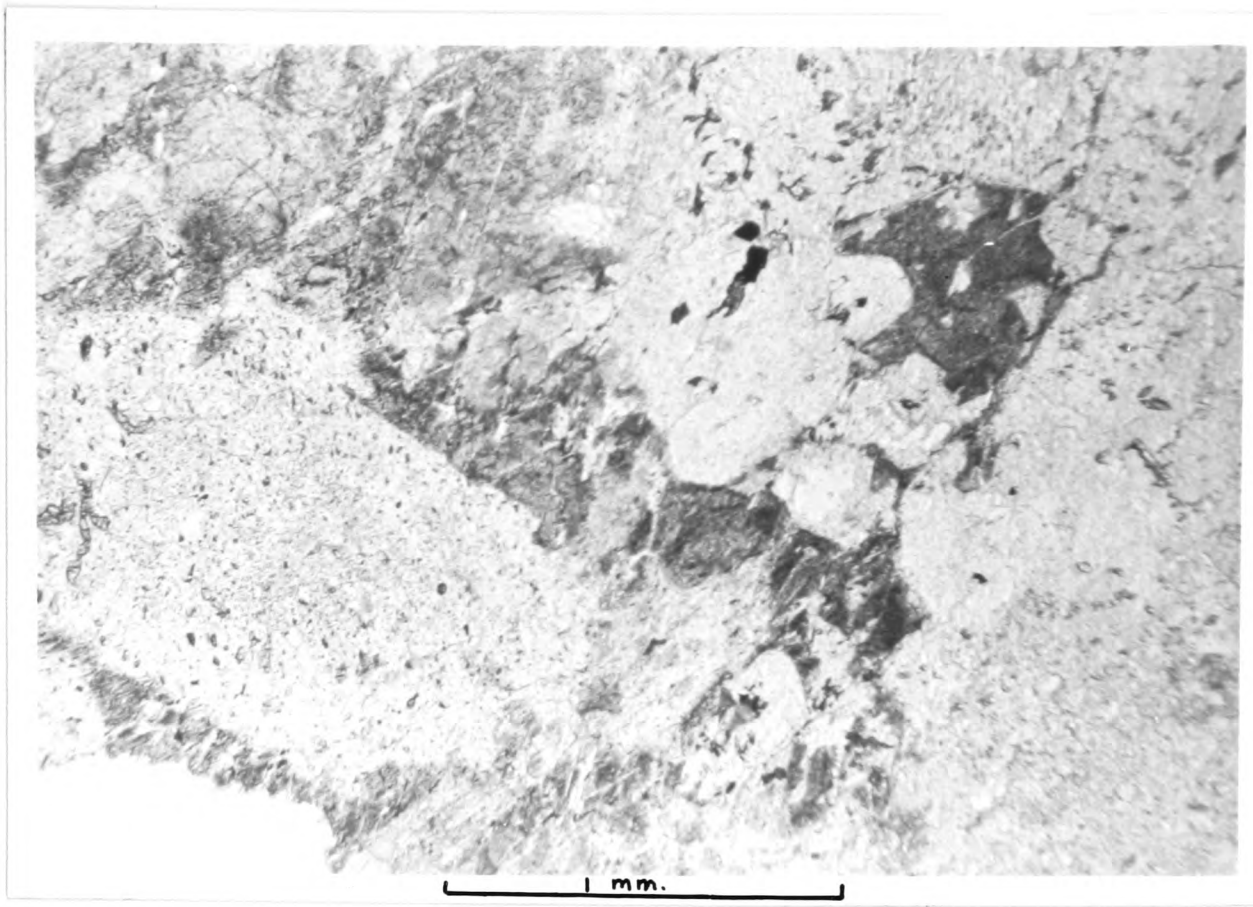



Fig. 2.30 Brown hornblende enclosing patches of actinolite in optical continuity. Hornblendite GD 918. Plane polarised light.

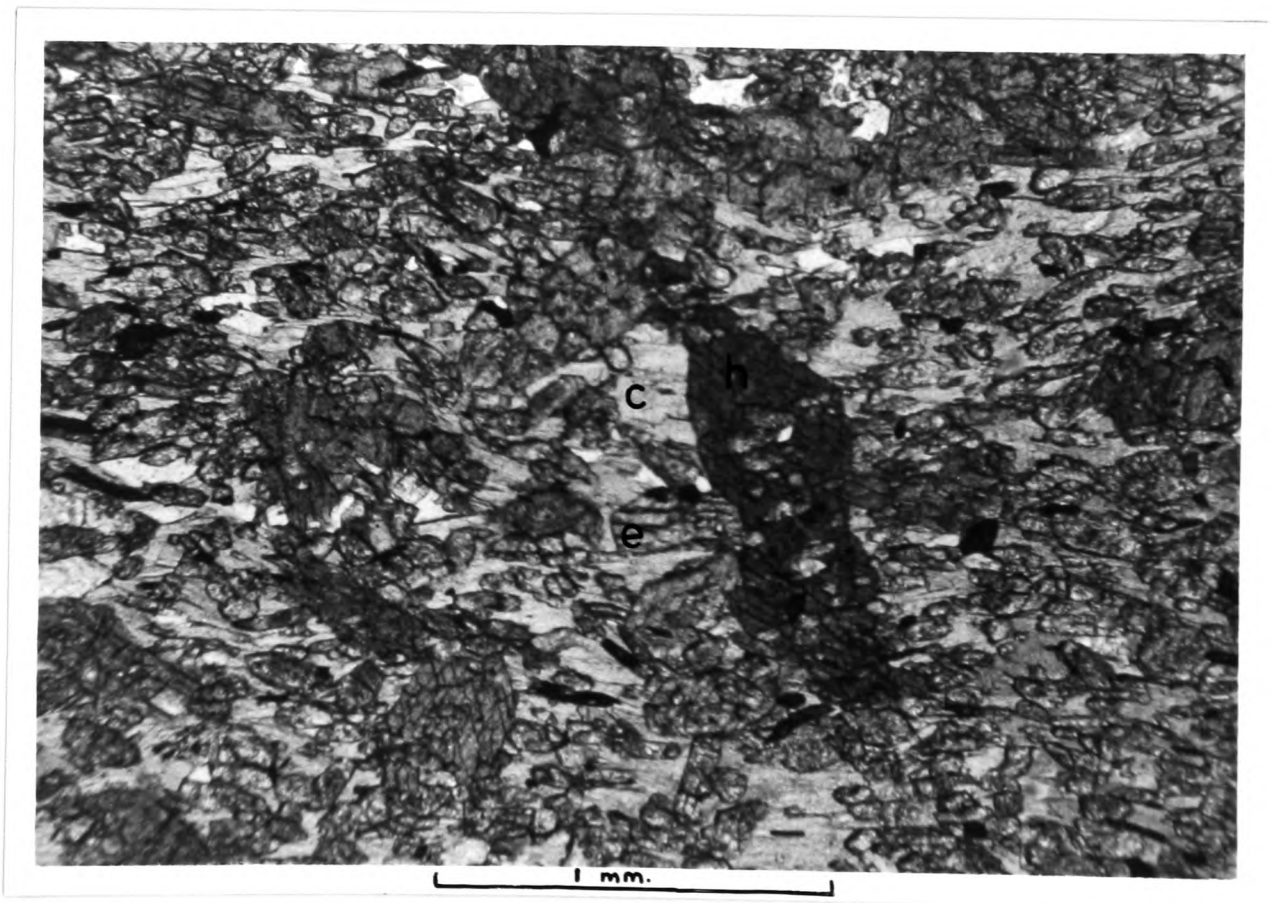



Fig. 2.31 Euhedral hornblende (h) overgrowing aligned epidote granules (e) and cutting across schistose chlorite (c) in epidote-amphibolite GD 193. Plane polarised light.




Fig. 2.32 Zoned amphiboles (actinolite cores, hornblende rims) with chlorite and albite in meta-gabbro GD 179c.
Plane polarised light.



Fig. 2.33 Tremolite-talc-dolomite-schist. Böseck-Törl Kopf ridge.

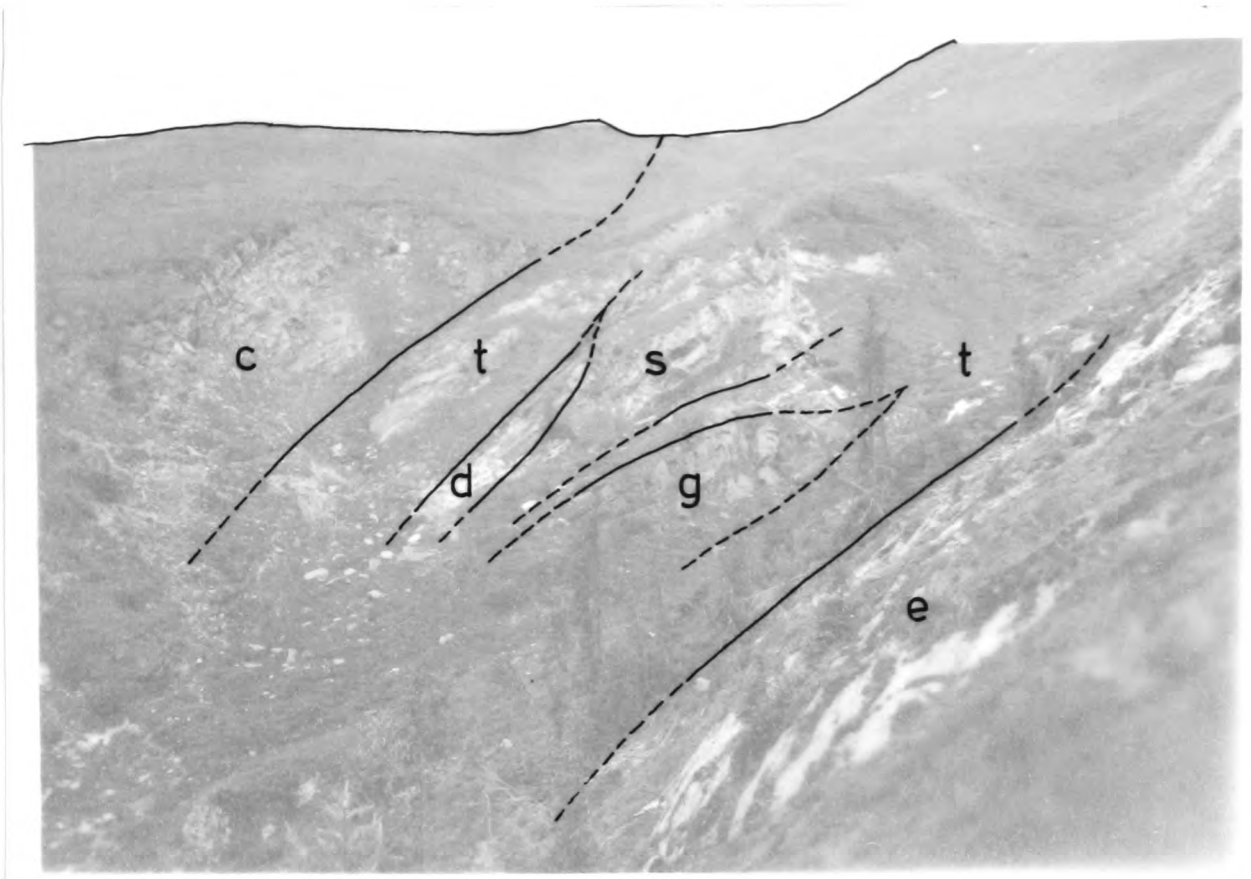



Fig. 2.34 The thrust-zone on the south slope of Sicker Kopf, viewed along strike.

c : calc schist
d : siliceous dolomite
e : epidote-amphibolite
g : meta-gabbro
s : serpentine
t : talc-schist

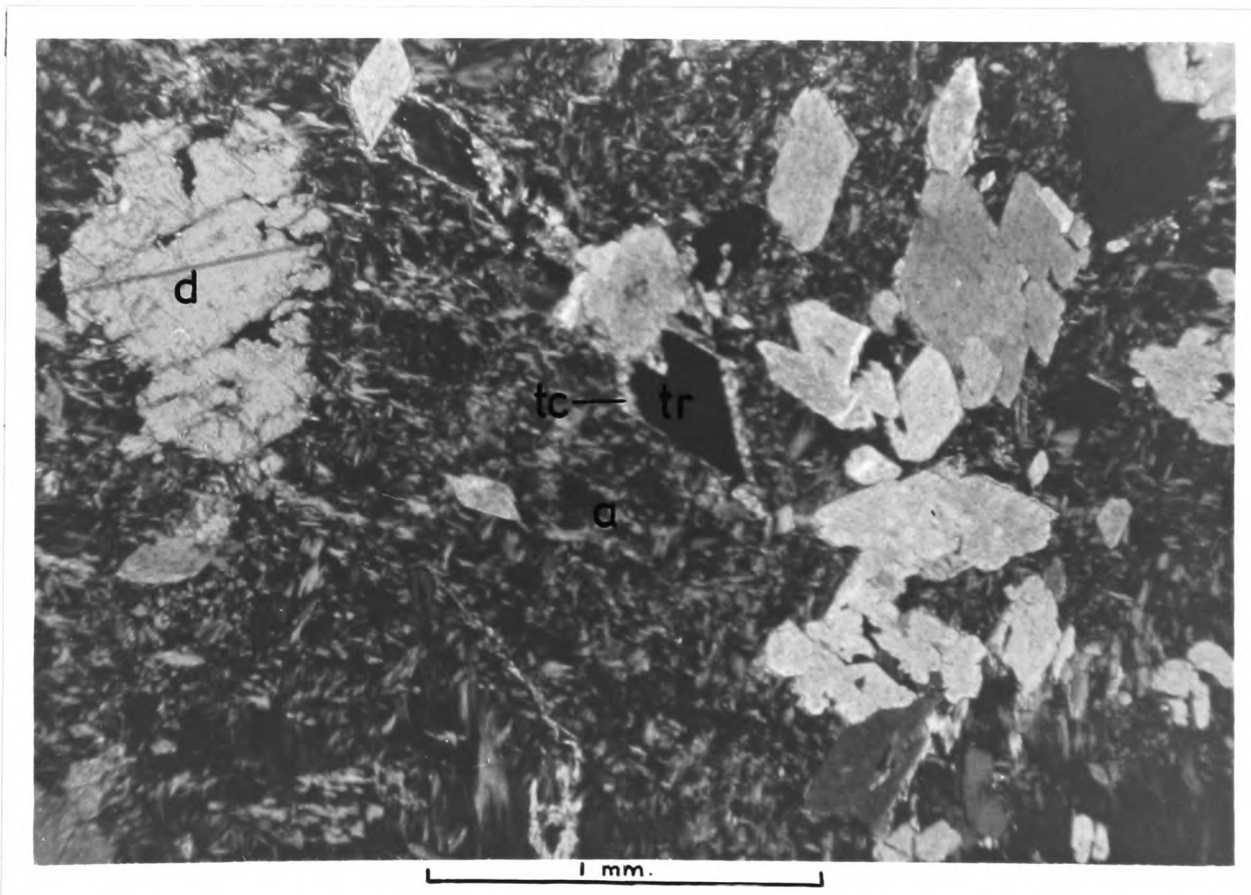



Fig. 2.35 Localised reaction rims of talc (tc) between euhedral tremolite (tr) and fine-grained antigorite matrix (a) in serpentinite GD 868. Some dolomite (d) is also present. Crossed polars.



Fig. 2.34 The thrust-zone on the south slope of Sicker Kopf, viewed along strike.

c : calc schist
d : siliceous dolomite
e : epidote-amphibolite
g : meta-gabbro
s : serpentine
t : talc-schist

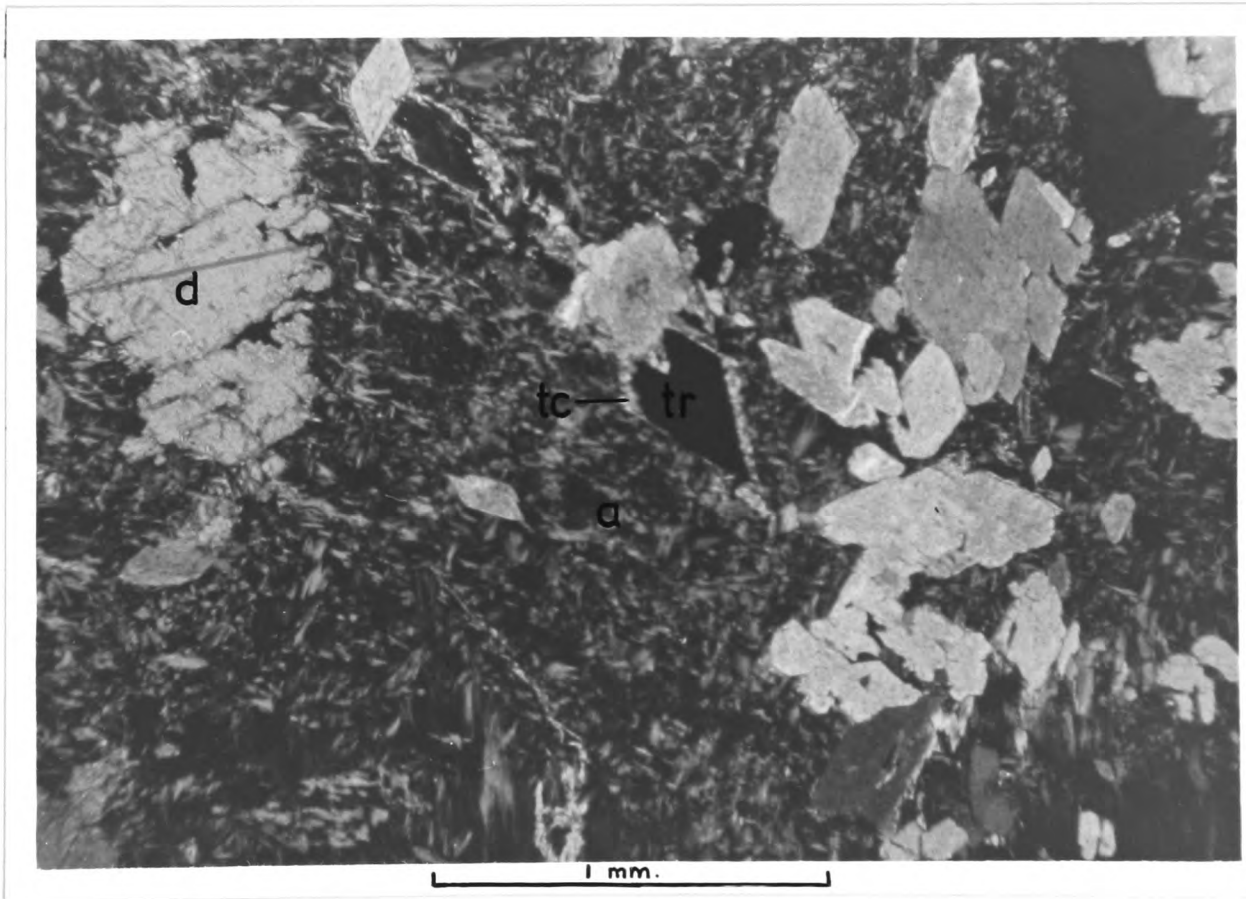



Fig. 2.35 Localised reaction rims of talc (tc) between euhedral tremolite (tr) and fine-grained antigorite matrix (a) in serpentinite GD 868. Some dolomite (d) is also present. Crossed polars.

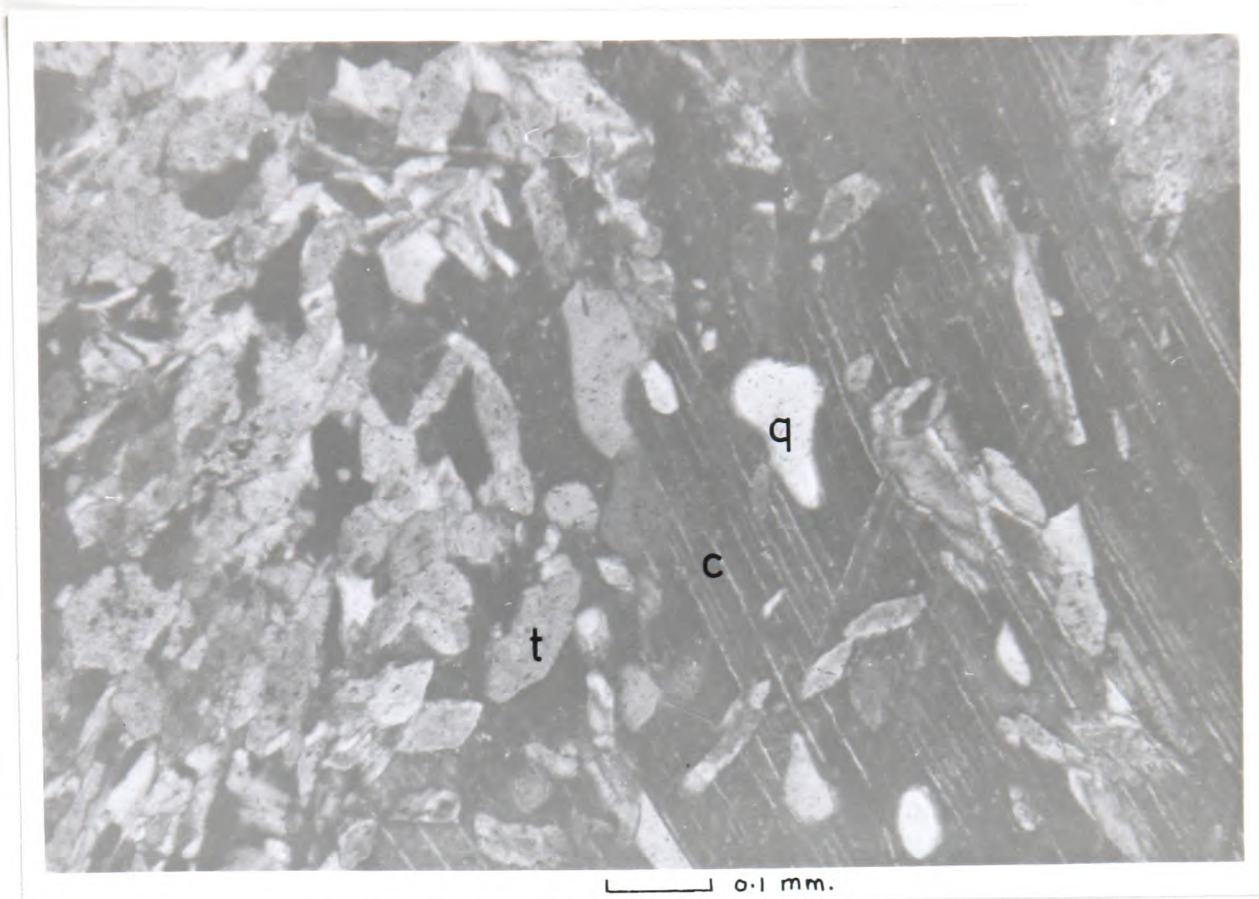



Fig. 2.36 Tremolite (t), calcite (c) and quartz (q), apparently in equilibrium, in siliceous dolomite GD 556. Crossed polars.




Fig. 2.37 Tremolite-rich band (pale green) containing the assemblage trem + dol + qz next to tremolite-poor band (bluish) with the assemblage trem + cc + qz in siliceous dolomite GD 233.

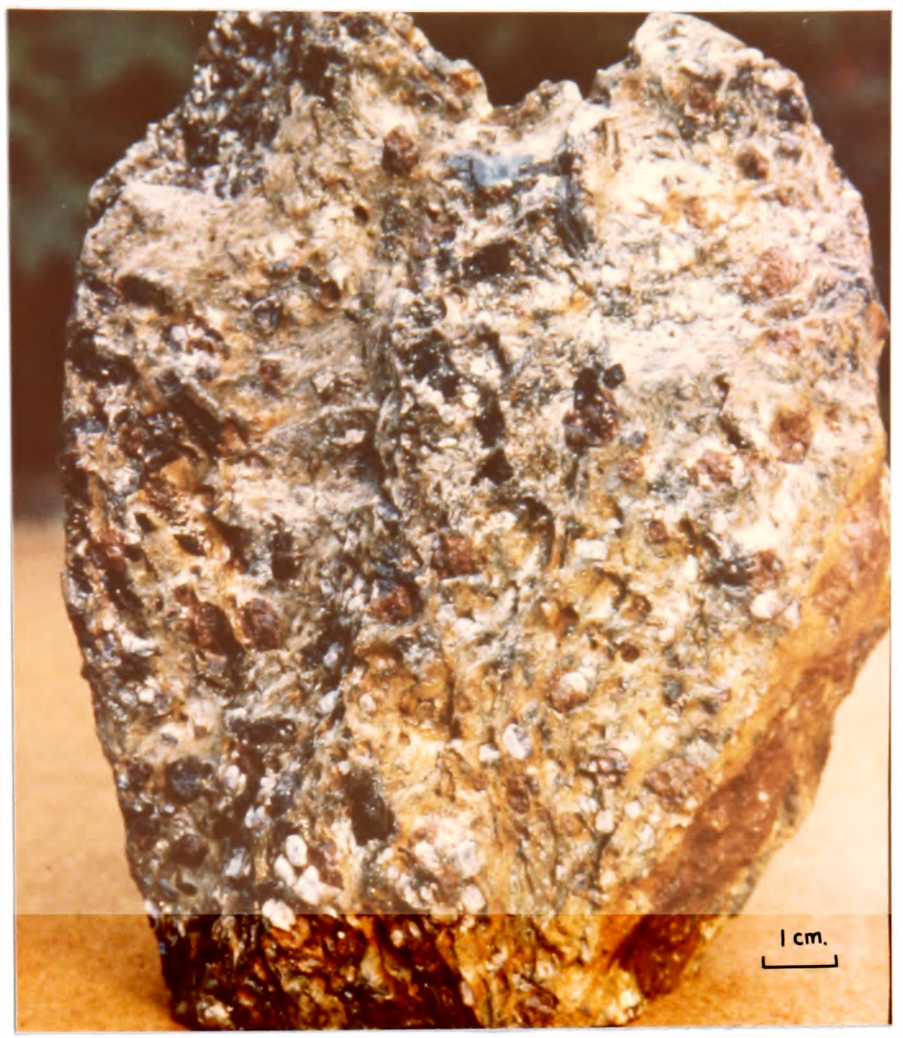



Fig. 2.38 Coarse-grained chloritoid-schist, with porphyroblasts of chloritoid, garnet and albite.



Fig. 2.39 Garnet, hornblende and chloritoid porphyroblasts in coarse-grained chloritoid-schist.




Fig. 2.40 Garnet and hornblende porphyroblasts in the margarite-bearing garbenschiefer GD 480.

Fig. 2.41 Zones of alteration in Inner Schieferhülle garnet-amphibolite GD 476 adjacent to a chlorite + albite vein.

| Zone | A | | B | | C |
|---|---|---|---|---|---|
| Assemblage: | GT + HBL + EP + PLAG + QZ + ILM (+ BIOT + CHL + CC) | | GT + BIOT + EP + PLAG + QZ + RUT + CC (+ SPH + ILM + AP) | | CHL + PLAG + QZ + CC + SPH |
| Textures: | Fine-grained GT-amphibolite with good $S_A^2$ HBL-schistosity. (Country rock) | Sharp front | Fine-grained BIOT-rich rock. BIOT's are aligned in $S_A^2$. | Gradual transition | Alternating bands rich in CHL and PLAG give rise to colour banding. Individual mineral grains not preferentially orientated. |
| Garnet: | 1-2mm. pre-$S_A^2$ Mv porphyroblasts being replaced by PLAG + QZ ± CC. | | As for A, except much less abundant. | | - |
| Other mafic minerals: | Blue-green HBL abundant, apparently in equilibrium with rare BIOT. | | Abundant ragged flakes of orange BIOT, some altering to CHL near C. | | Rosettes of CHL with anomalous brown interference colour. |
| Plagioclase: | Oligoclase. Clear polygonal grains replacing GT, and in matrix. | | ? Texture as in A except finer-grained. | | Albite. Abundant, medium-grained, turbid grains, in part altering from BIOT. |
| Ti-rich phase: | ILM plates aligned in $S_A^2$ | | Numerous small RUT granules, locally rimmed by SPH. | | Occasional euhedral SPH grains. |

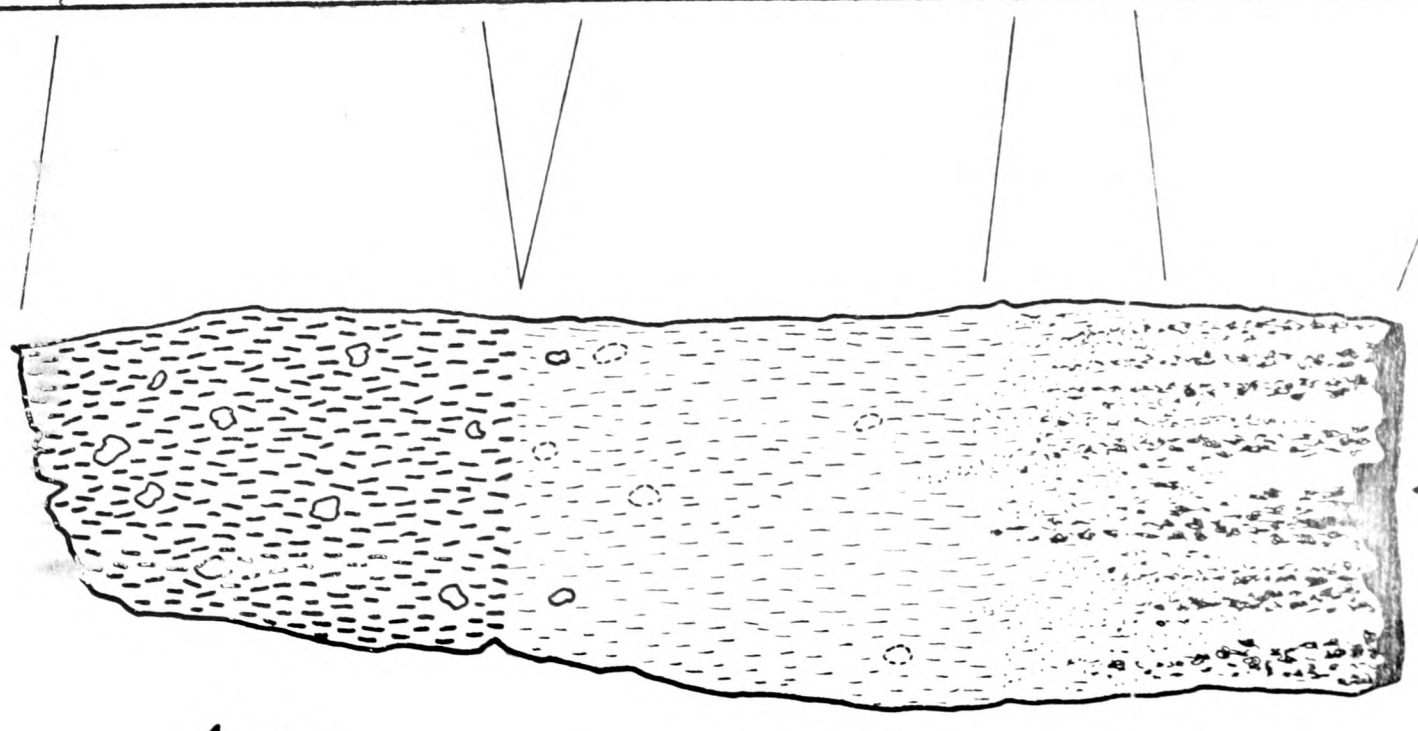





Fig. 2.42 Pseudotachylite band (arrowed) and associated microfractures in banded gneiss.

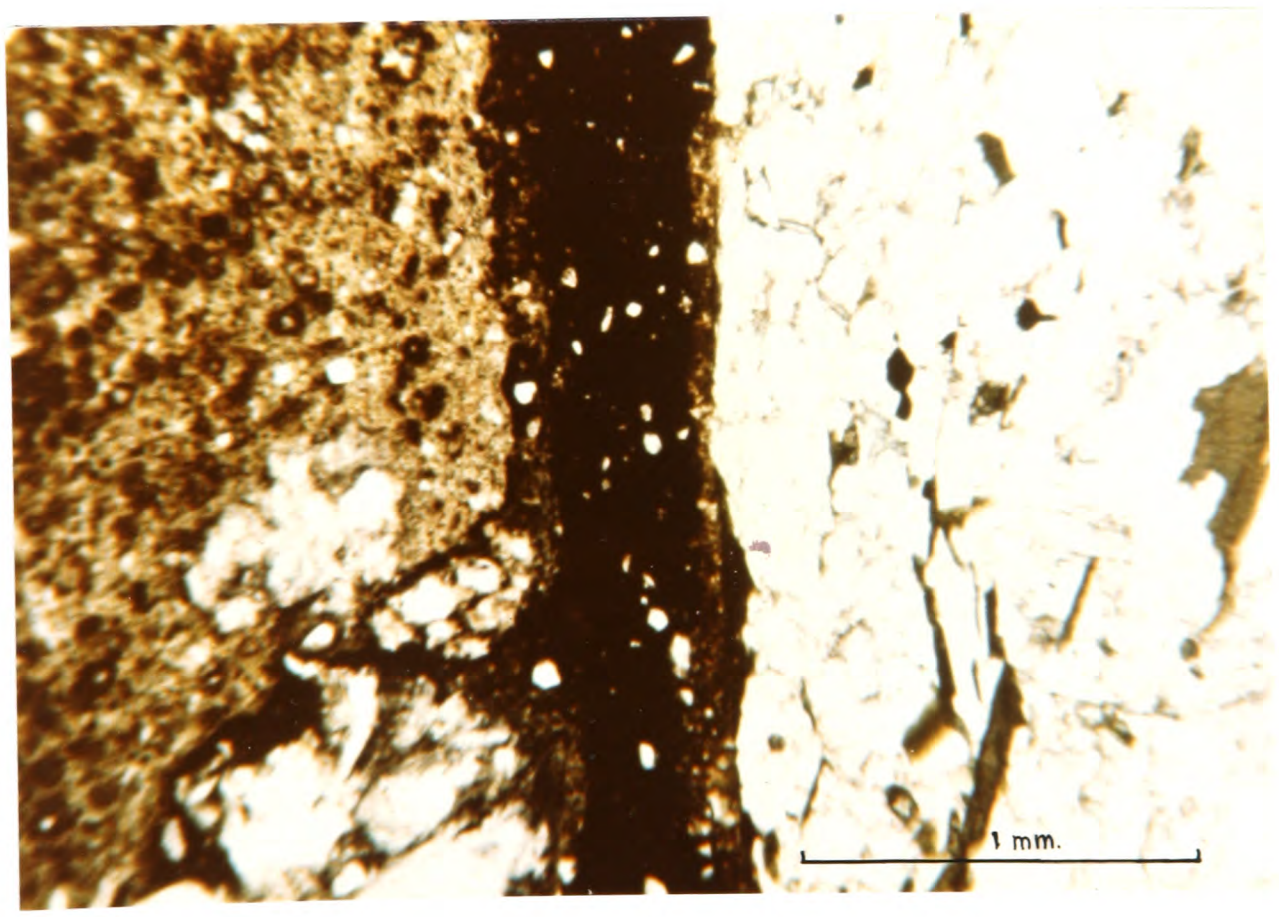



Fig. 2.43 Thin section of pseudotachylite showing black glassy margin and brown ? devitrified centre.

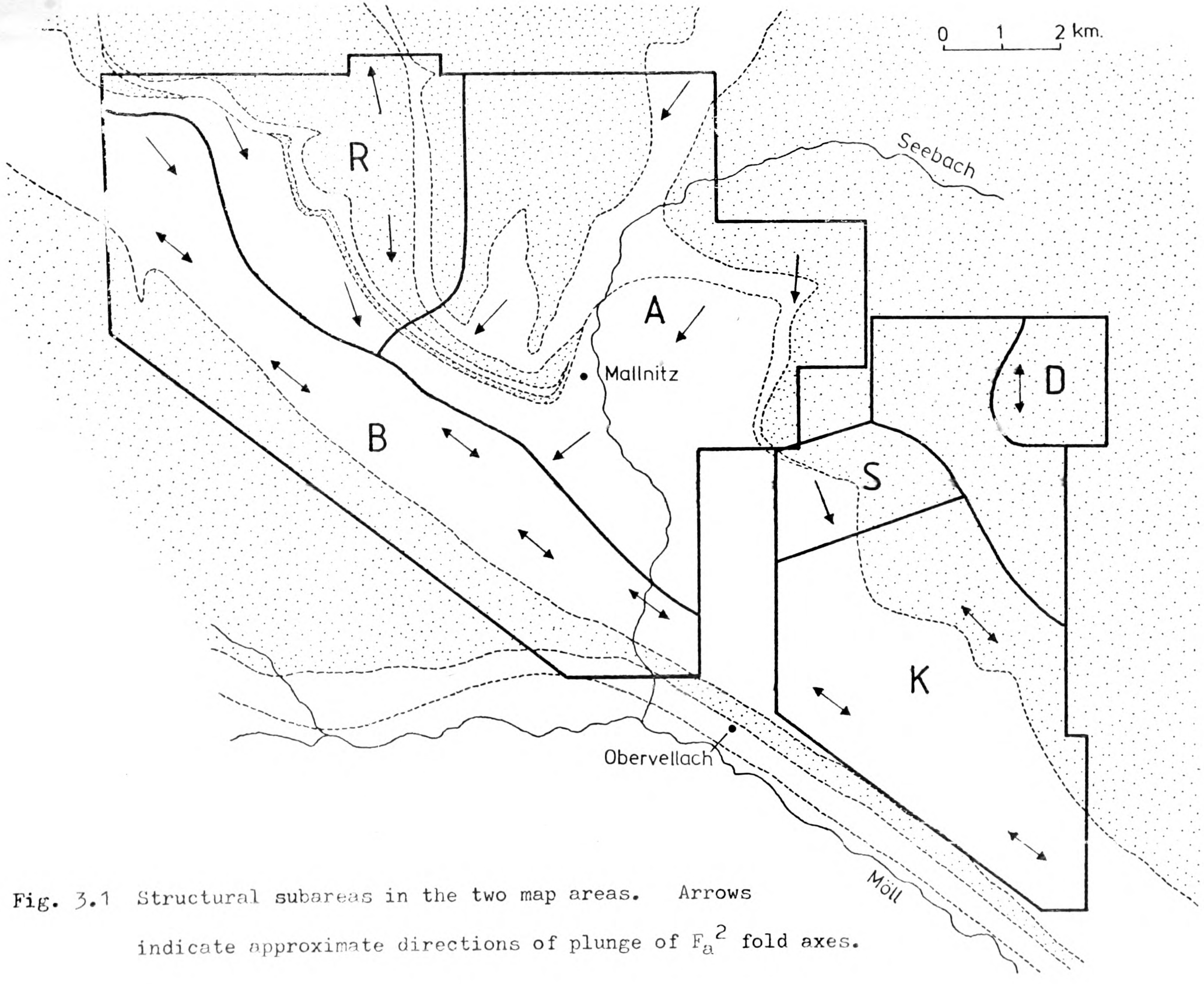



Fig. 3.1 Structural subareas in the two map areas. Arrows indicate approximate directions of plunge of $F_a^2$ fold axes.



Fig. 3.2 $S_a^1$ compositional banding in calcareous quartzite north of Mauternitz Scharte.



Fig. 3.3 Interbanded calc-schists (brown) and marble (white) overlying pelitic mica-schists and biotite-epidote-feldspar-schist (grey). The boundary is offset by a reverse fault. 1 km. north of Jamnig Alm.

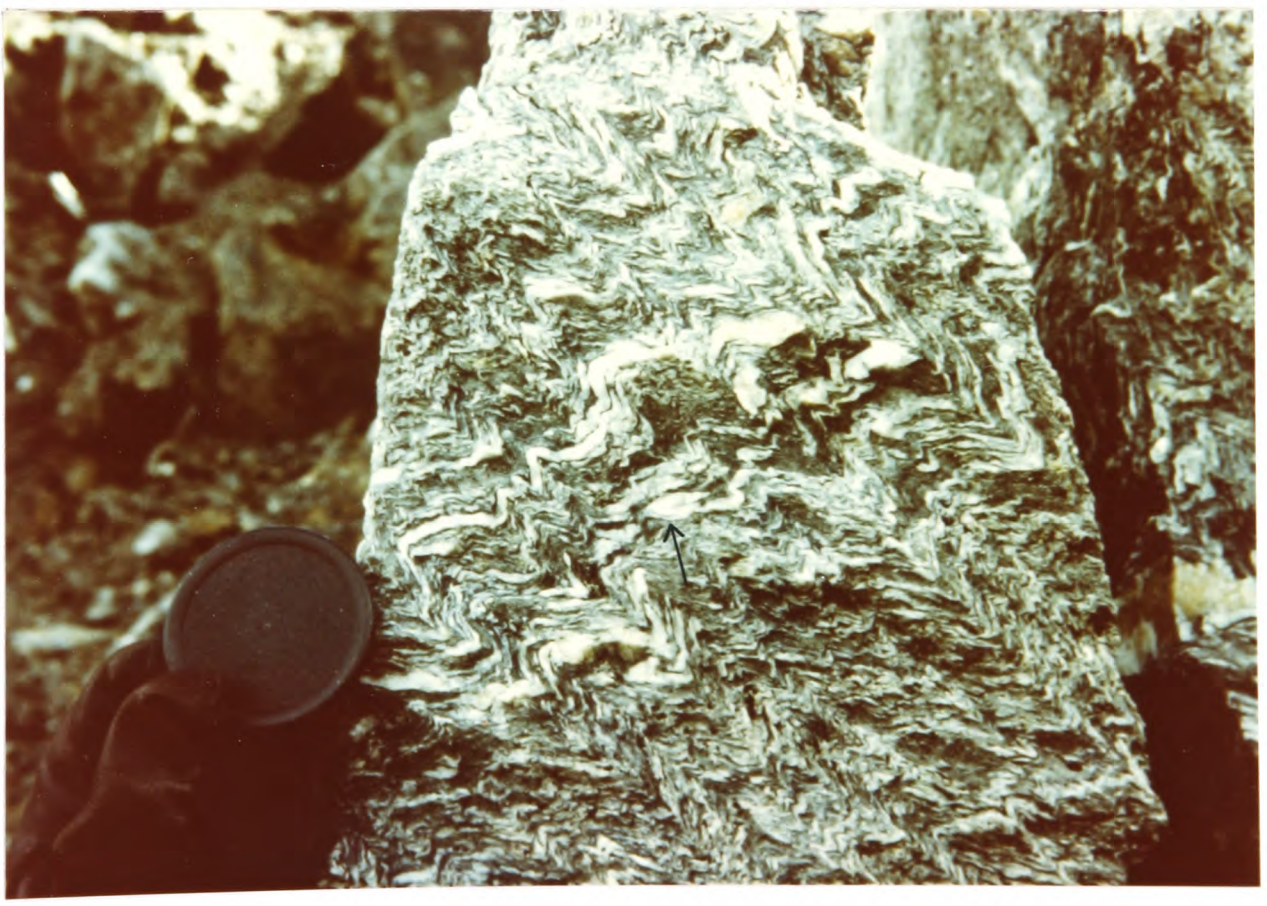


Fig. 3.4 $Fa^2$ chevron-folds deform an $Sa^1$ foliation containing a small $Fa^1$ isocline (arrowed) in quartz-muscovite-schist. North-east ridge of Böseck.



Fig. 3.5 $S_a^1$ banding deformed by $F_a^2$ folds in calcareous quartzite, Törl Kopf - Rissieck ridge.



Fig. 3.6 Enlargement of the area marked in fig. 3.5 showing a refolded $F_a^1$ isocline (arrowed).



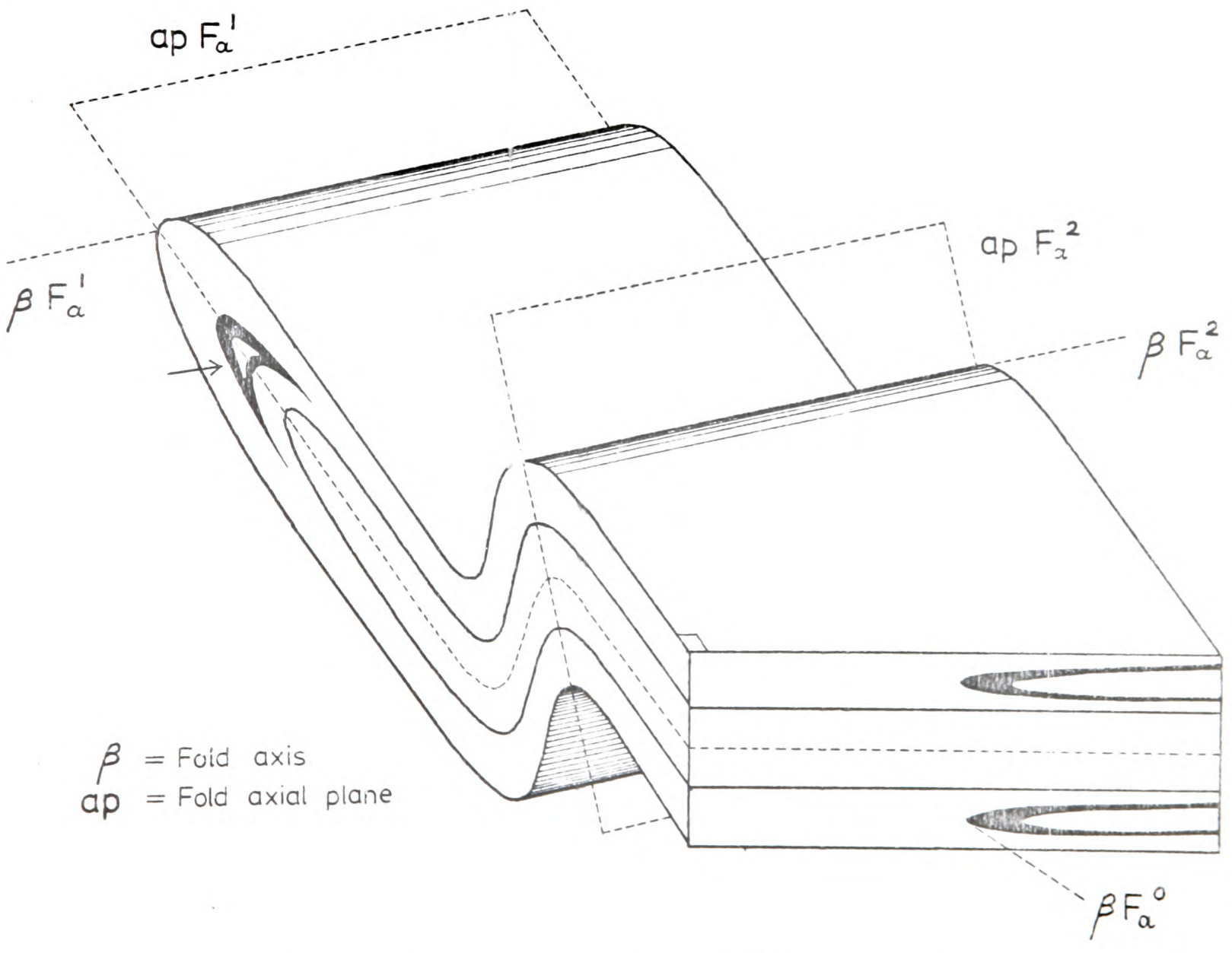
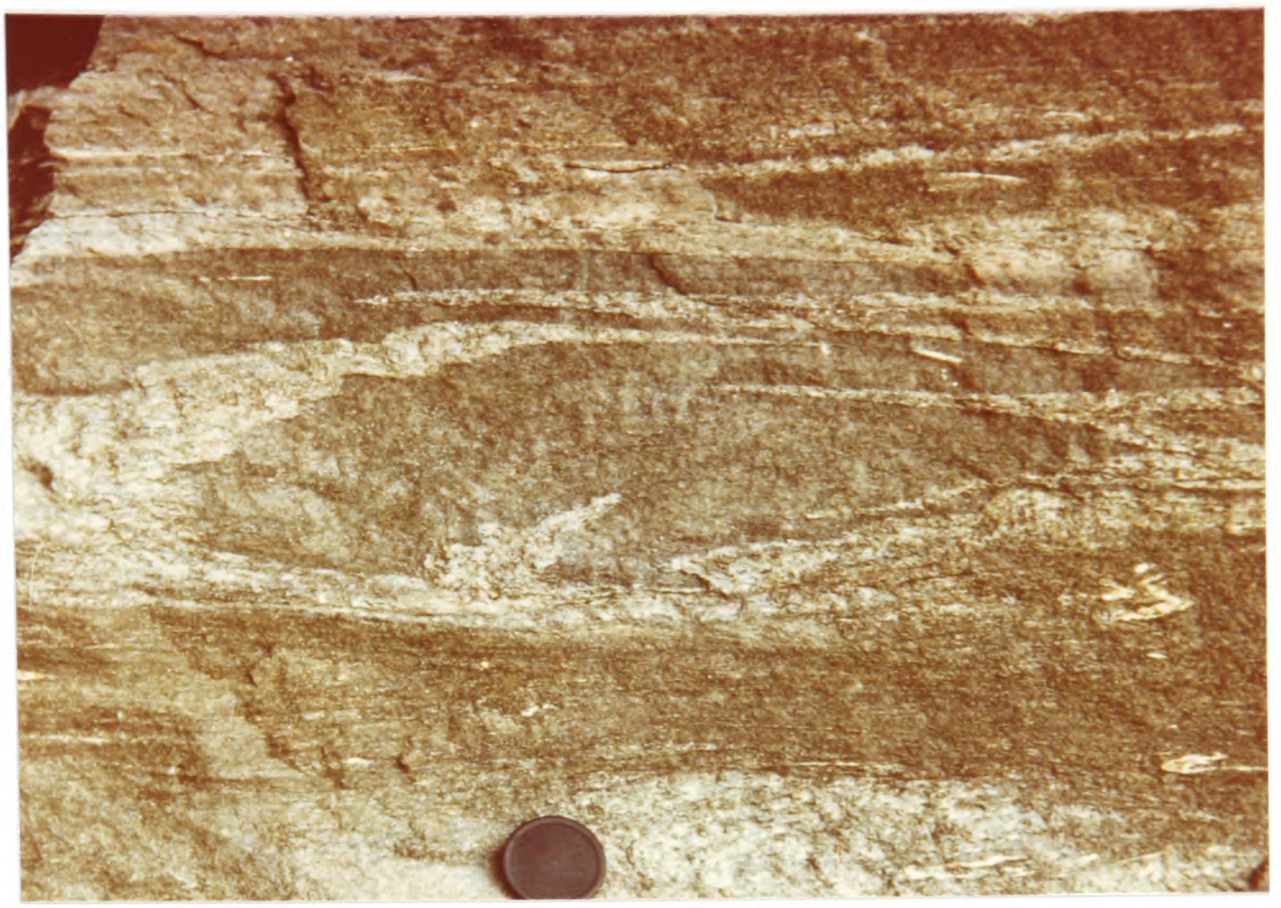



Fig. 3.7 $F_a^1$ isocline refolded by open $F_a^2$ folds in calcareous quartzite, Geisel Kopf. Possible "boomerang" type interference pattern (arrowed) in the $F_a^1$ fold nose.



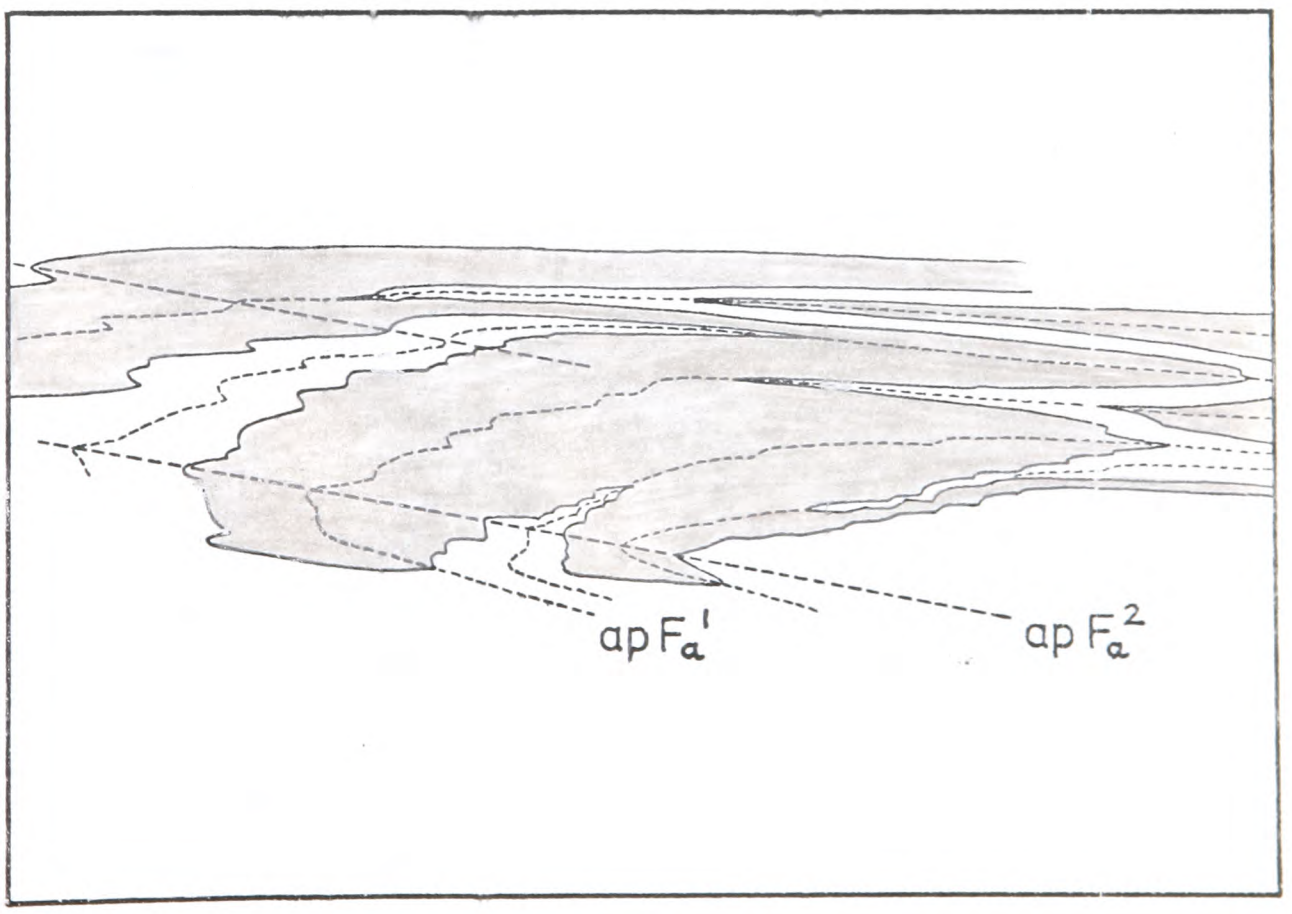



Fig. 3.8 Interference pattern produced by the superposition of $F_a^1$ and $F_a^2$ folds in calc schist, Geisel Kopf.




Fig. 3.9 Tremolite-talc-schist from Geisel Kopf, showing tremolite needles bent round an $F_a^2$ fold.

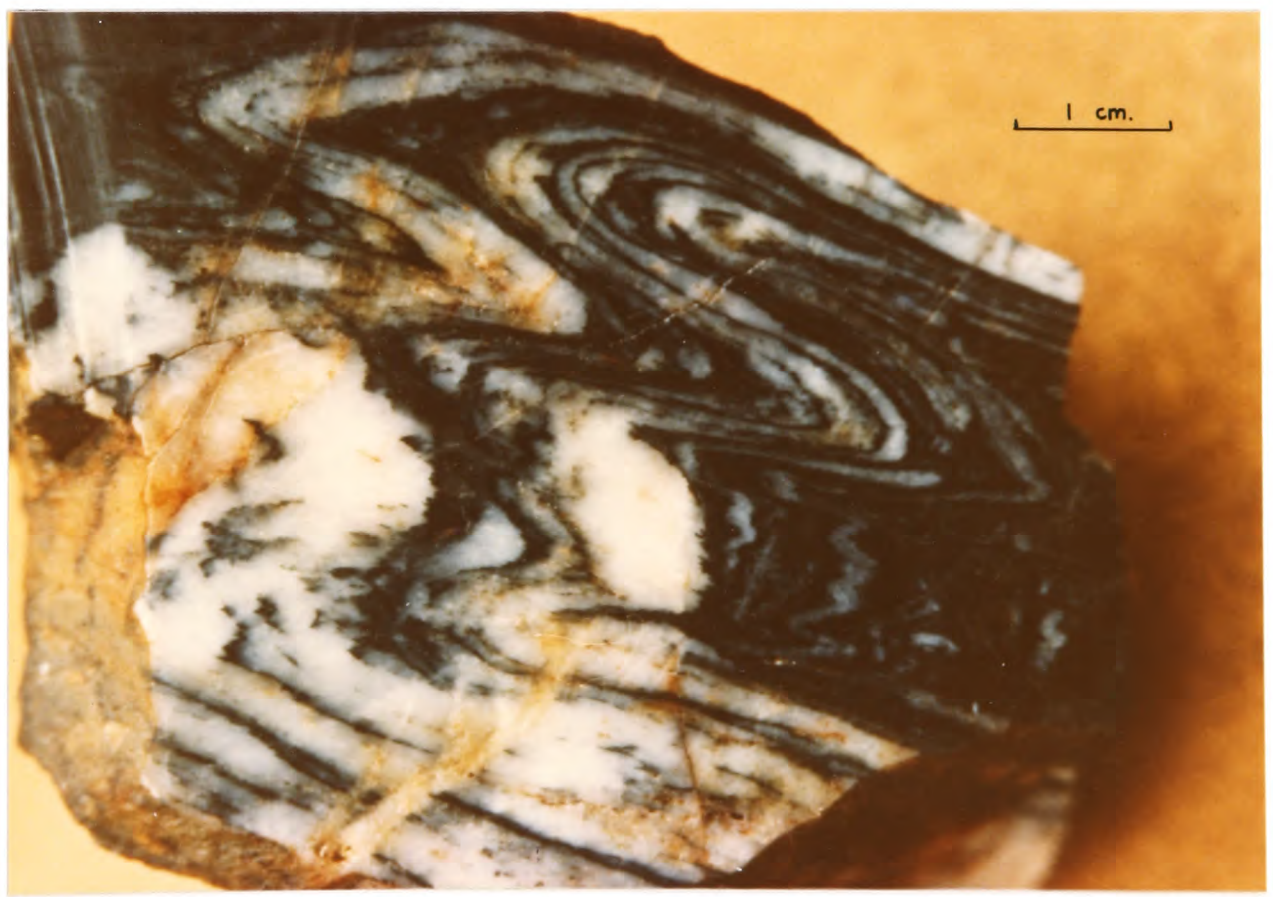
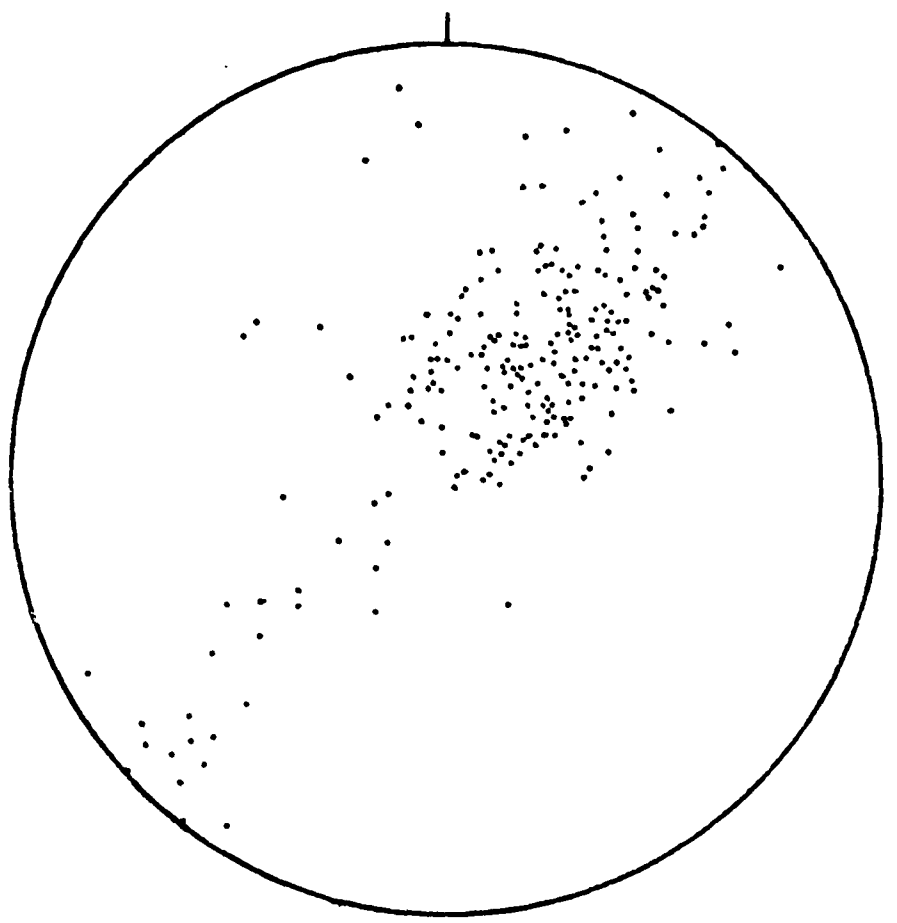



Fig. 3.10 Tight $F_a^1$ folds deforming previously flattened quartz veins in graphitic quartzite.

Table 3.1 Structural succession in the Mallnitzer Mulde, showing definite and tentative correlations (solid and dashed lines respectively).

| | South-west (=upper) limb | North-east (=lower) limb | |
|---|---|---|---|
| 400+ m. | Main calc-schist unit with greenschists, serpentinites and calcareous quartzites. | | 400+ m. |
| ~40 m. | Calcareous quartzite<br>Gneiss lamella<br>Graphitic mica-schist or calc-schist<br>Calcareous quartzite | Calcareous quartzite<br>Gneiss lamella<br>Graphitic mica-schist or calc-schist<br>Calcareous quartzite | ~100 m. |
| 150-300 m. | Main graphitic mica-schist containing abundant calc-schists, quartzites and marbles to S. of area. | Main graphitic mica-schist unit | ~300 m. |
| | Törl Kopf-Rissieck ridge: Pelitic mica-schist<br>Gneiss lamella --?-- Gneiss lamella<br>Quartzite and graphitic mica-schist (S. of area)<br>Calc-schists ----?-- Calc schists (S. of area)<br>Pelitic mica-schists (N. of area) | | 0-300 m. |
| | Marble or calc-schist -----?- | Marbles and calc-schists with localised epidote-amphibolites. (Marbles predominate to N. of area) | 20-100+ m. |
| | | Pelitic mica-schists | 100 m. |
| Böseck lenticle zone | COVER<br>***?*****?****?********** | | |
| 100-200 m. | BASEMENT<br>Gneiss lamella or epidote-rich metabasite ----?- | Biotite-epidote-feldspar-schist. (Feldwand lamella) | 100-200 m. |
| | Mica schists ----------?- | Mica-schists, paragneisses and graphitic quartzites of the Randgneis. (Some may be Peripheral Schieferhülle) | |
| | Dark biotite-schist and quartzo-feldspathic gneiss with amphibolite lenses. "Schollenmigmatit" -?- | Syenite-gneiss. (Romate decke) | 200-500+ m. |
| | Graphitic mica-schist -----?- | Various crystalline mica-schists and paragneisses of the Randgneis. (Woisgen zone) | 100+ m. |
| | Augen-gneisses (Sonnblick Kern) | Augen-gneisses and granite gneisses. (Hölltor Kern) | |

(a) Poles to principal foliation, $S_a^1$.



(b) $D_a^1$ lineations and $F_a^1$ fold axes.

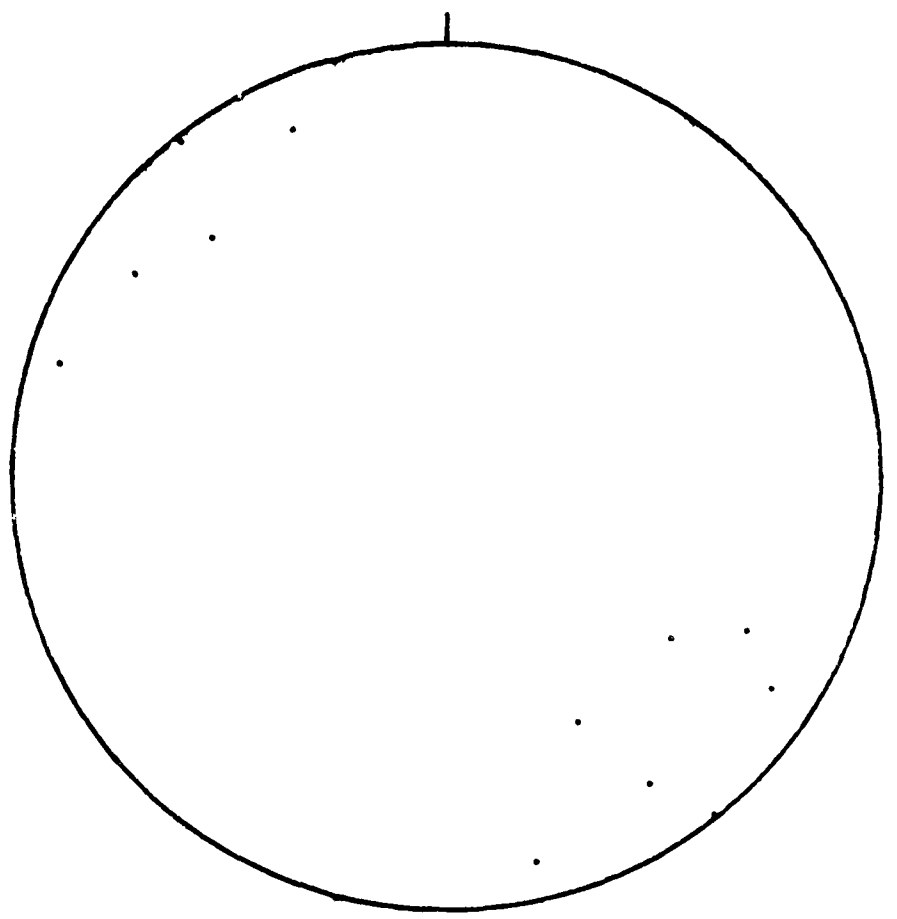
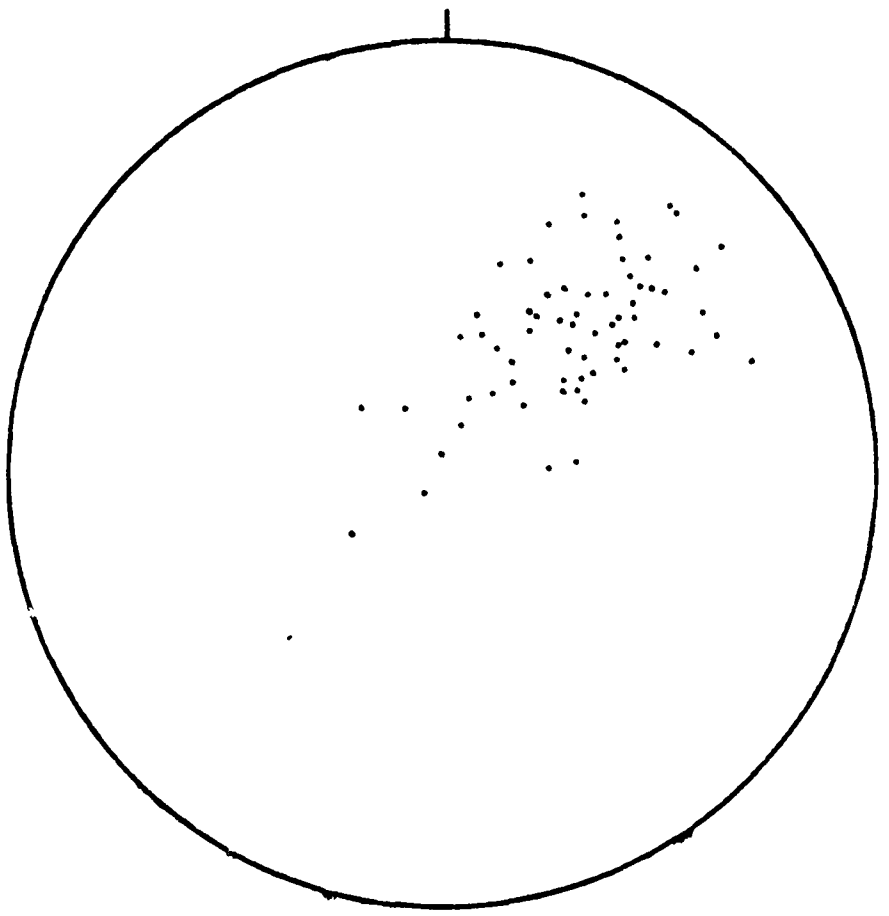


Fig. 3.11 Structural elements in the Böseck subarea.

(c) Poles to $S_a^2$ schistosity and $F_a^2$ axial planes.



(d) $D_a^2$ lineations and $F_a^2$ fold axes.

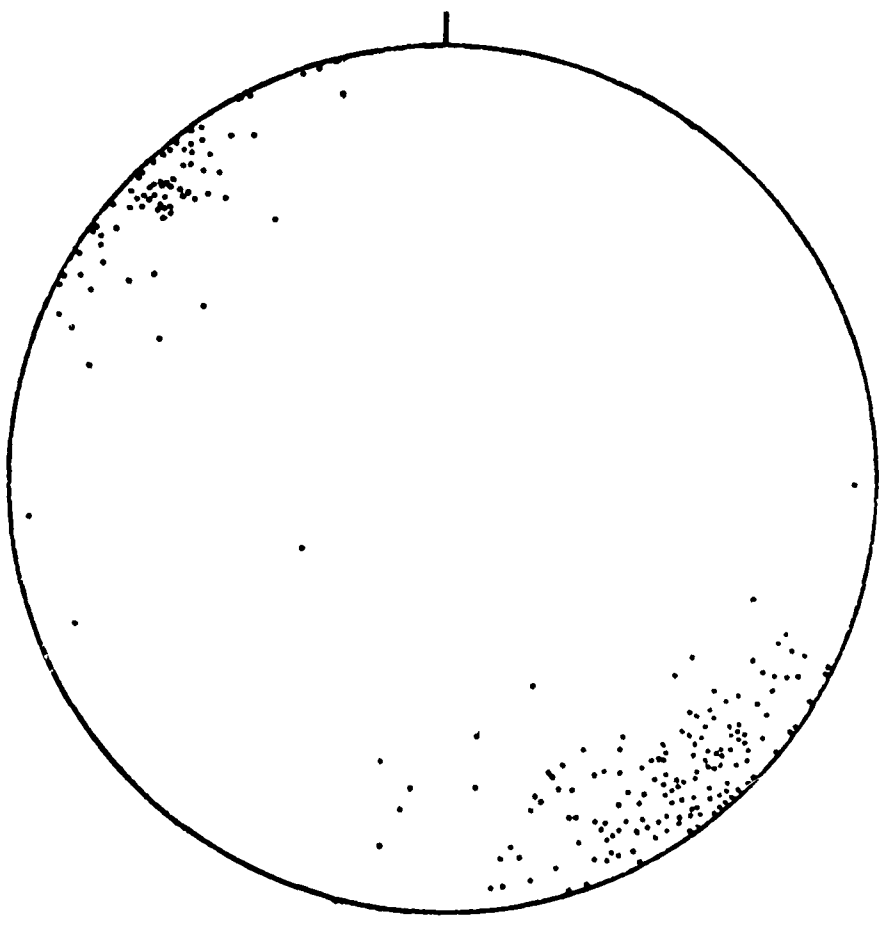
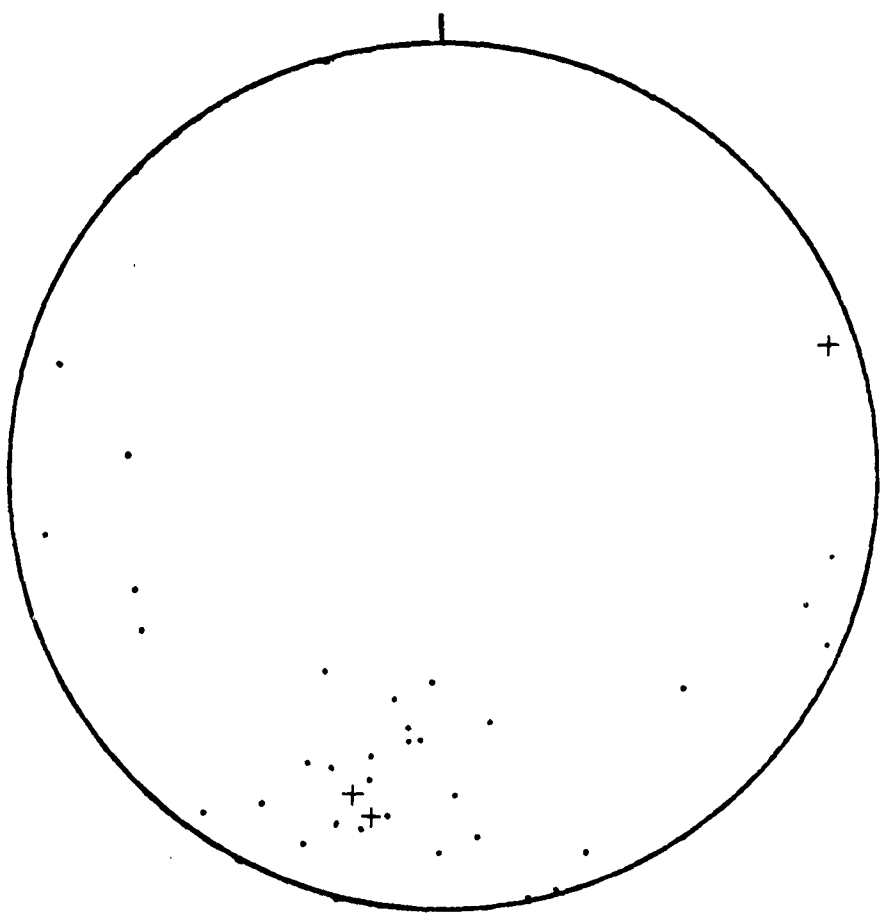


Fig. 3.11 Structural elements in the Böseck subarea (cont'd).

(e) $D_a^3$ lineations and buckle-fold axes (dots) and boudin axes (crosses).



(f) $F_a^3$ kink axes.

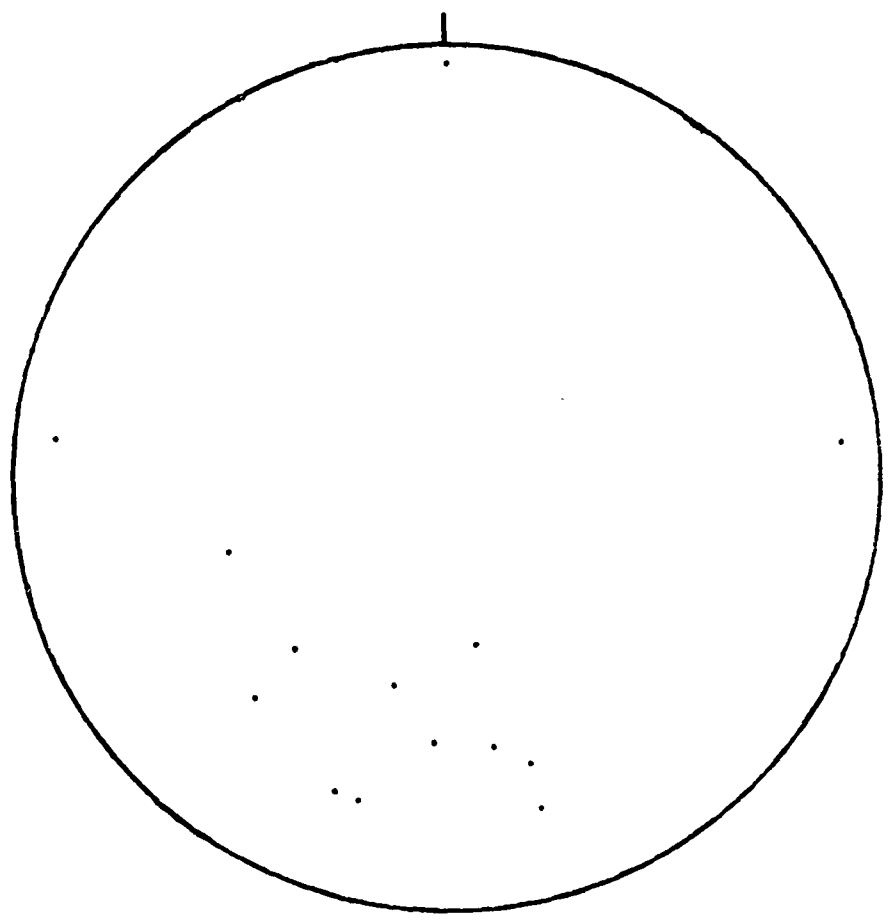
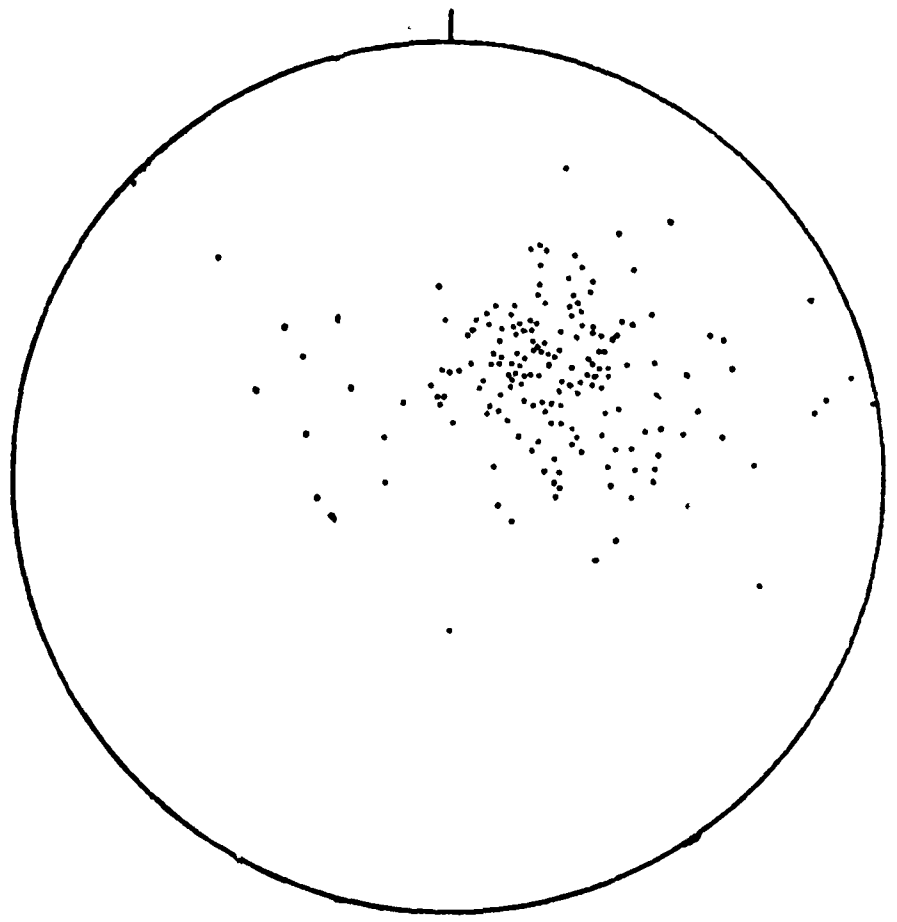


Fig. 3.11 Structural elements in the Böseck subarea (cont'd.).

(a) Poles to principal foliation, $S_a^1$.



(b) $D_a^1$ lineations and $F_a^1$ fold axes.

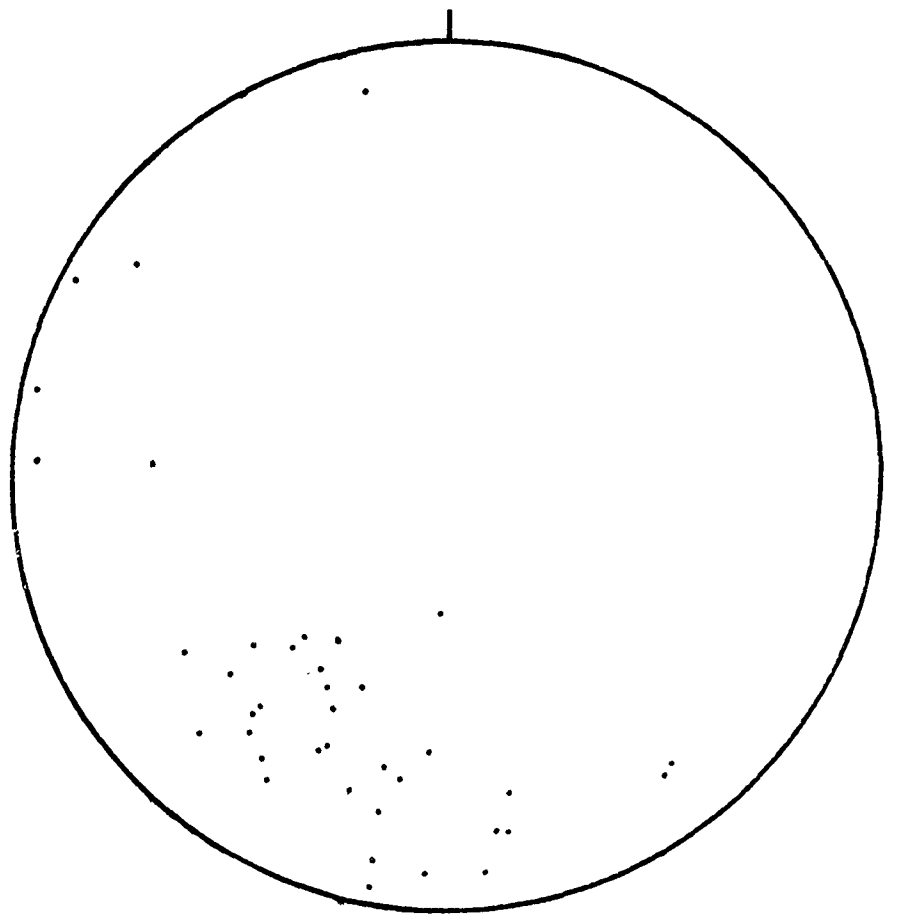
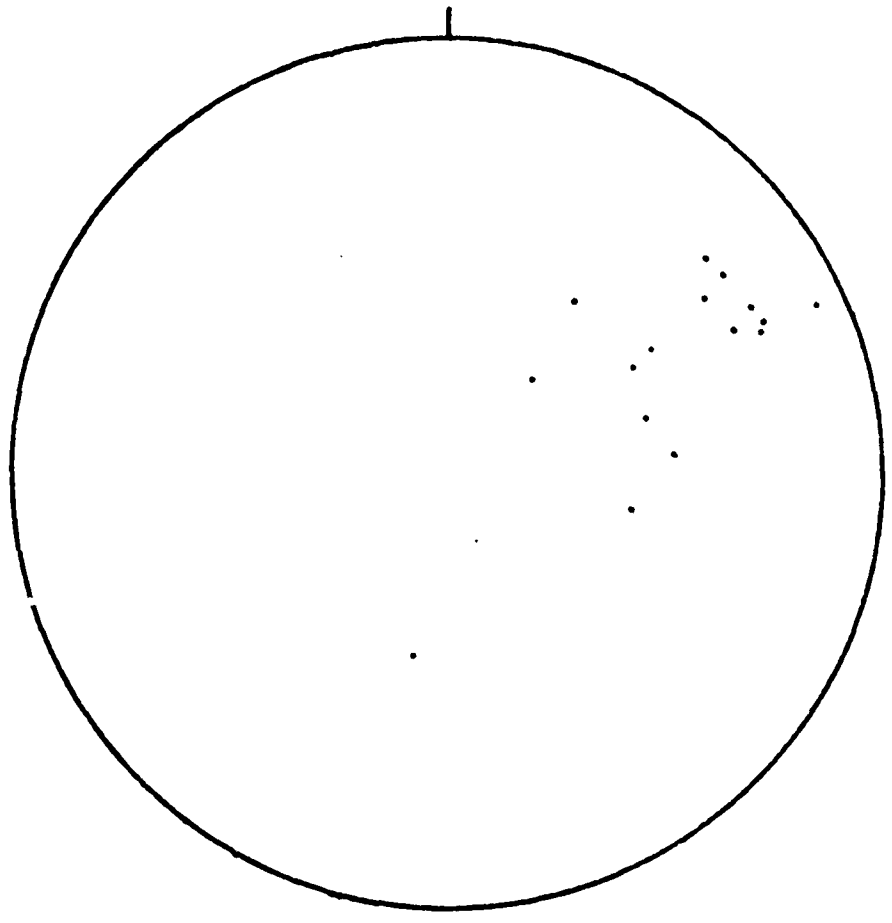


Fig. 3.12 Structural elements in the Romate subarea.

(c) Poles to $S_a^2$ schistosity and $F_a^2$ axial planes.



(d) $D_a^2$ lineations and $F_a^2$ fold axes.

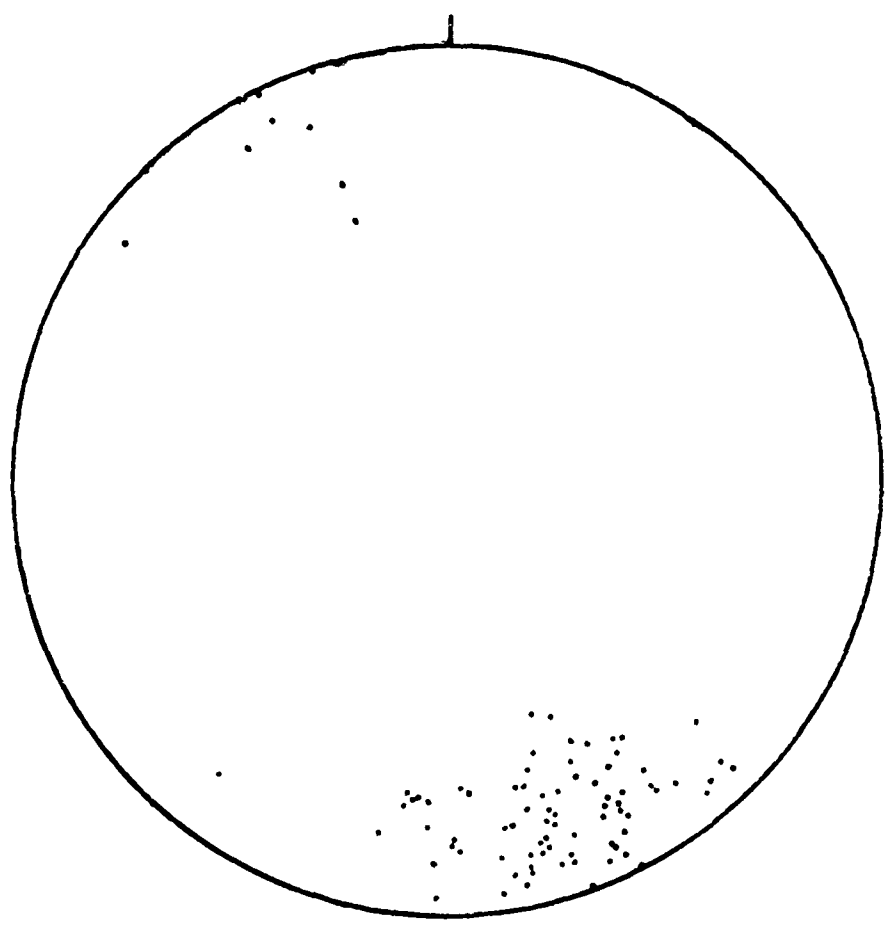
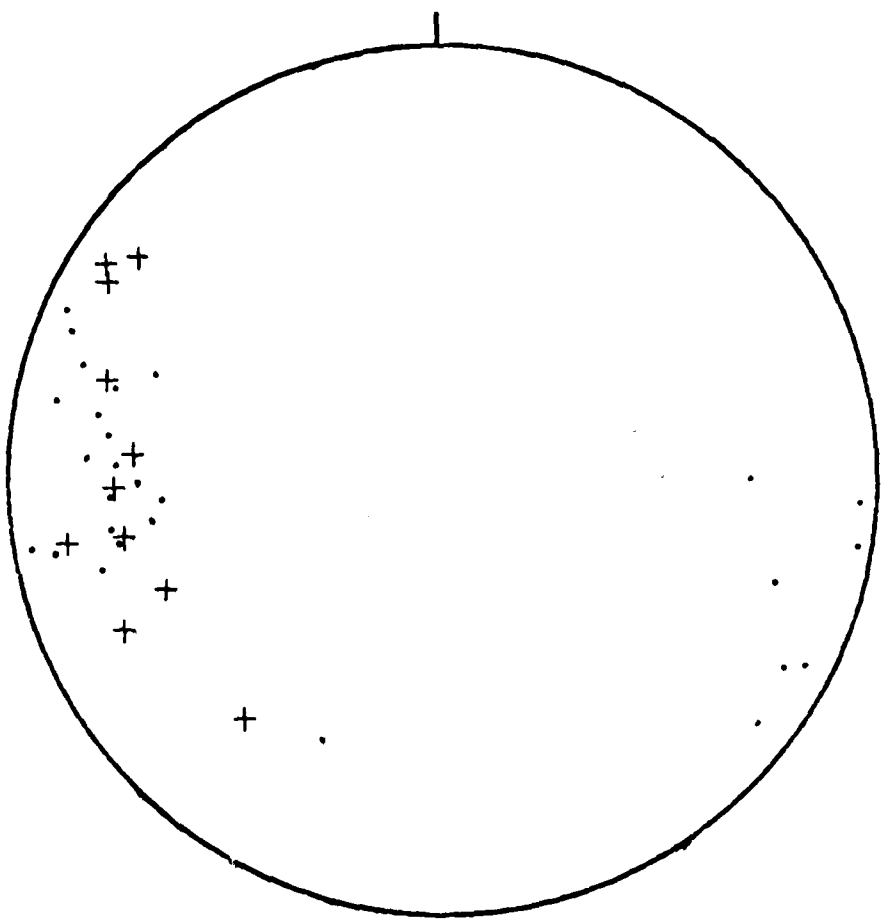


Fig. 3.12 Structural elements in the Romate subarea (cont'd.).

(e) $D_a^3$ lineations and buckle-fold axes (dots) and boudin axes (crosses).



(f) $F_a^3$ kink axes.

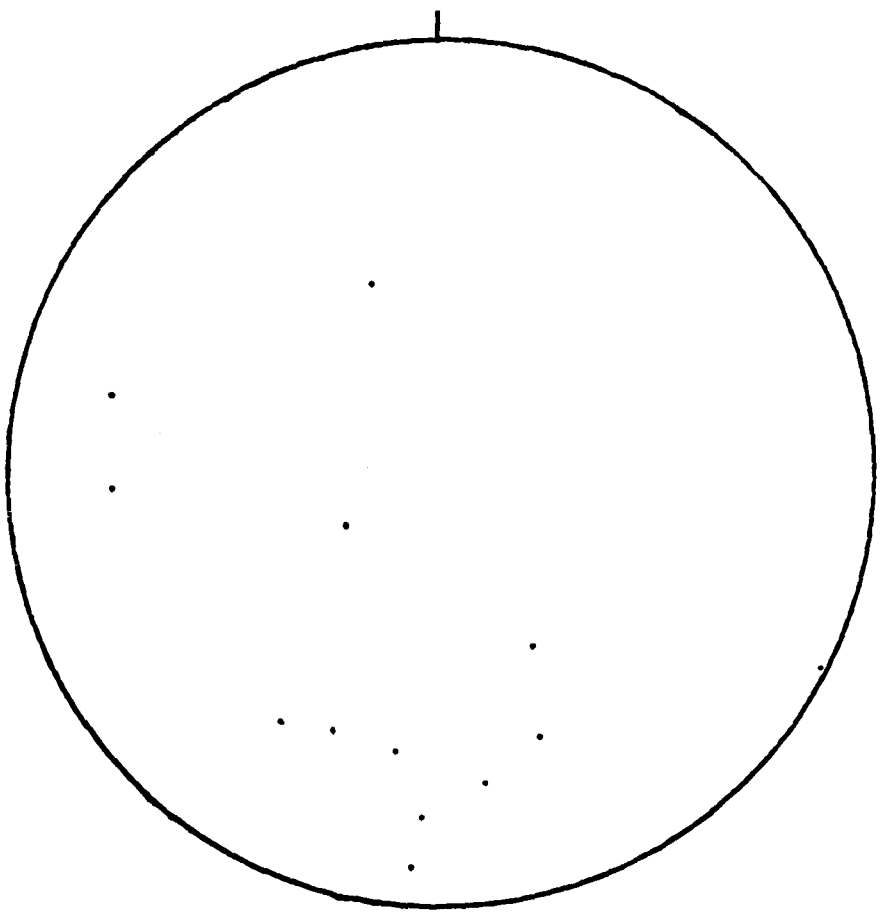


Fig. 3.12 Structural elements in the Romate subarea (cont'd.).




Fig. 3.13 Subvertical $S_a^1$ compositional banding and shallower $S_a^2$ schistosity in calc-schists. Törl Kopf - Lonza Köpfl ridge.



Fig. 3.14 Large, tight, asymmetric 'Z' folds in calc-schists in the upper limb of the Mallnitzer Mulde. Mauternitz Scharte.



Fig. 3.15 Feldsee Kopf, viewed from the south-east, showing graphitic mica-schists resting horizontally on top of augen-gneisses.



Fig. 3.16 Foliation in augen-gneisses of the Sonnblick Kern swinging from subvertical (extreme right) round to subhorizontal (left). View north-west from Oschenik Scharte.



Fig. 3.17 Steeply dipping foliation in augen-gneisses close to the north-eastern margin of the Sonnblick Kern.



Fig. 3.18 Tight $F_a^2$ folds in calcareous quartzite, Geisel Kopf.



Fig. 3.19 Refolded $F_a^1$ isocline in mica-schist north-west of Hochalmblick.

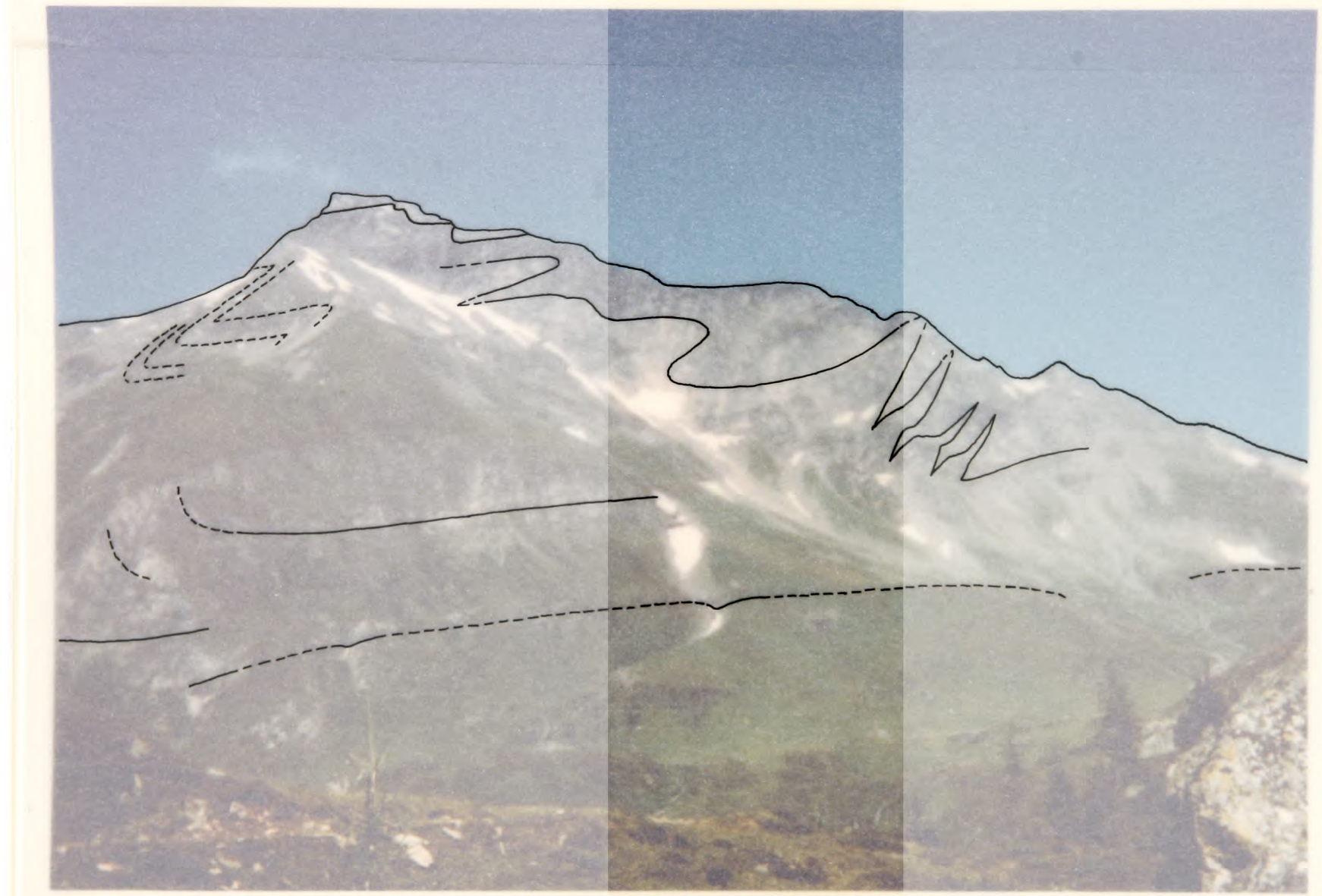


Fig. 3.20 South face of Geisel Kopf, showing cascade of large asymmetric $F_a^2$ folds.



Fig. 3.20 South face of Geisel Kopf, showing cascade of large asymmetric $F_a^2$ folds.



Fig. 3.21 $D_a^1$ lineations folded round an open $F_a^2$ fold in pelitic mica-schist. An $F_a^2$ axial crenulation is also present. Jamnig Alm road section.



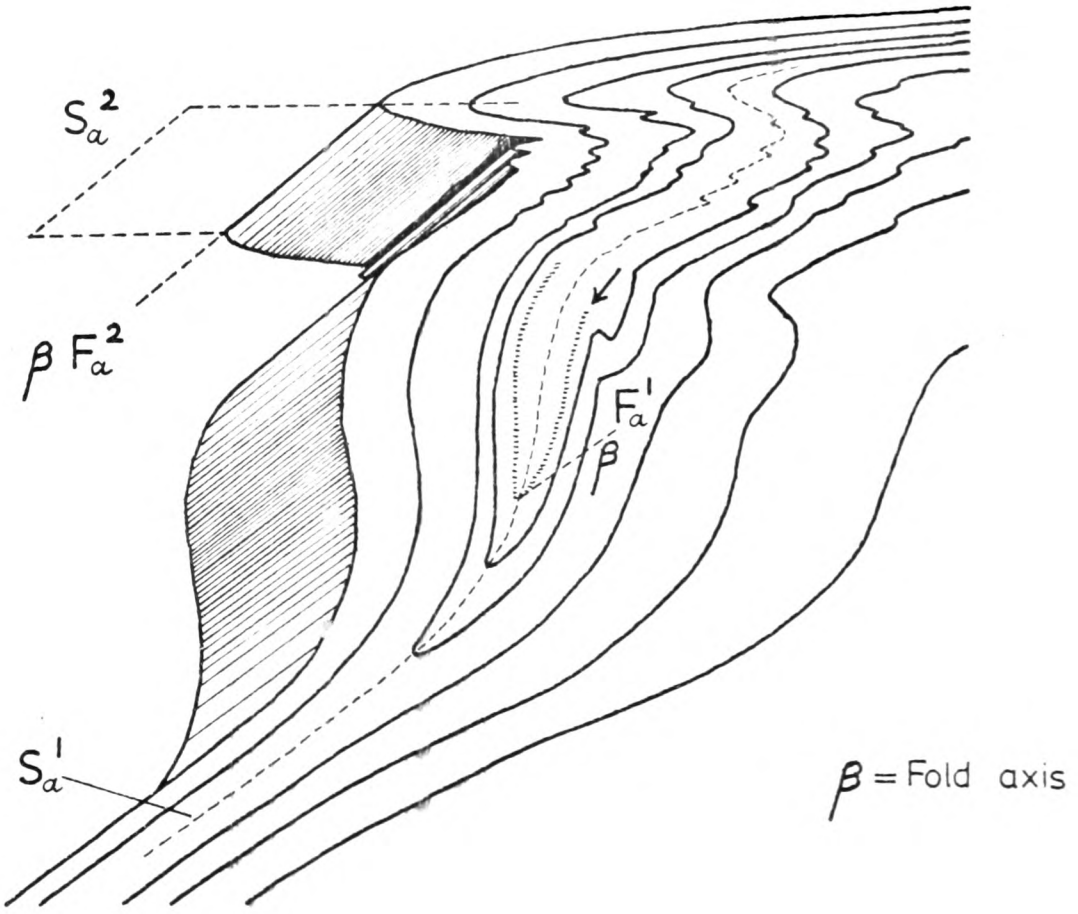



Fig. 3.22 Refolded $F_a^1$ isocline in micaceous marble, 600 m. E.S.E. Häusler Alm. One band (arrowed) is ornamented to show muscovite flakes aligned in $S_a^2$.

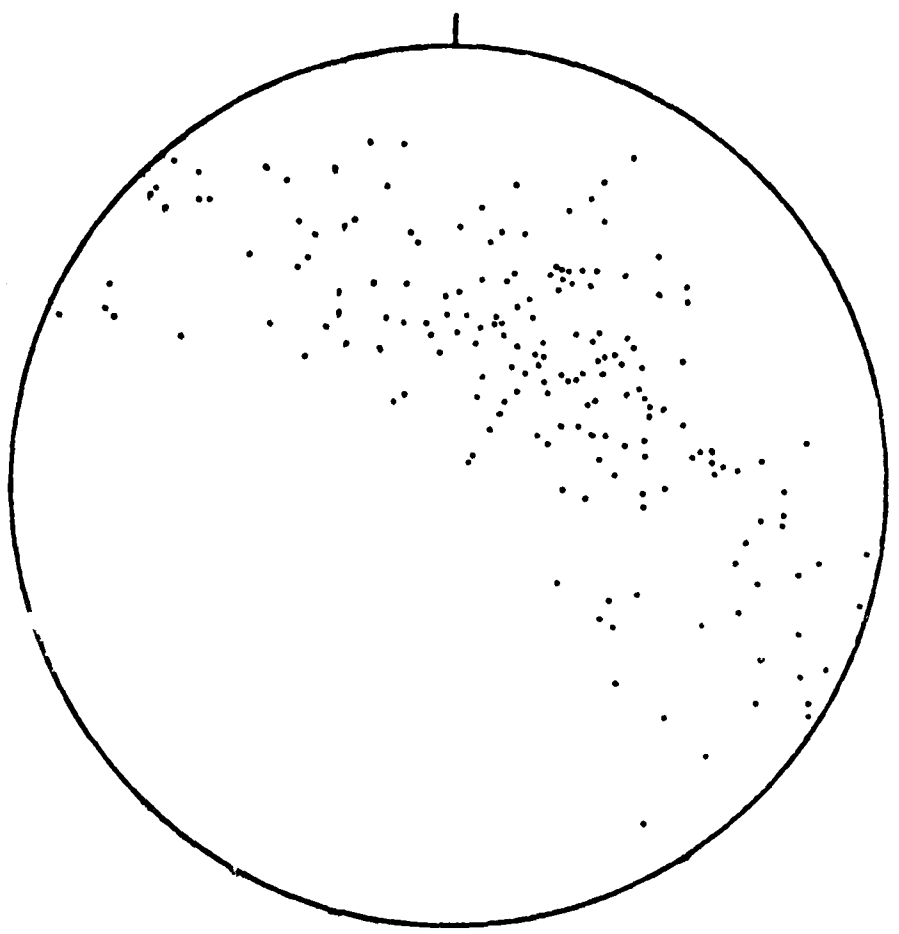


Fig. 3.23 Contact between mica-schists of the Woisgen Zone and underlying augen-gneisses exposed on the west face of Lisgele Spitze.



Fig. 3.24 Steeply plunging $F_a^2$ fold axes in mica-schists, Mallnitz.

(a) Poles to principal foliation, $S_a^1$.



(b) $D_a^1$ lineations and $F_a^1$ fold axes.

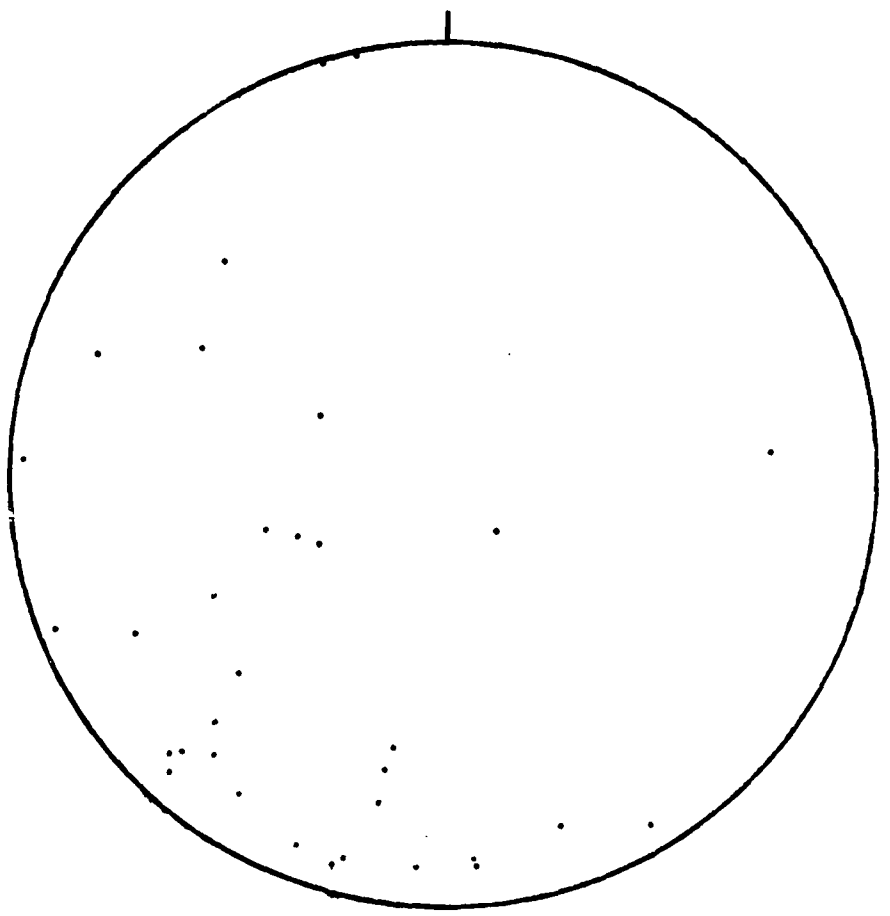
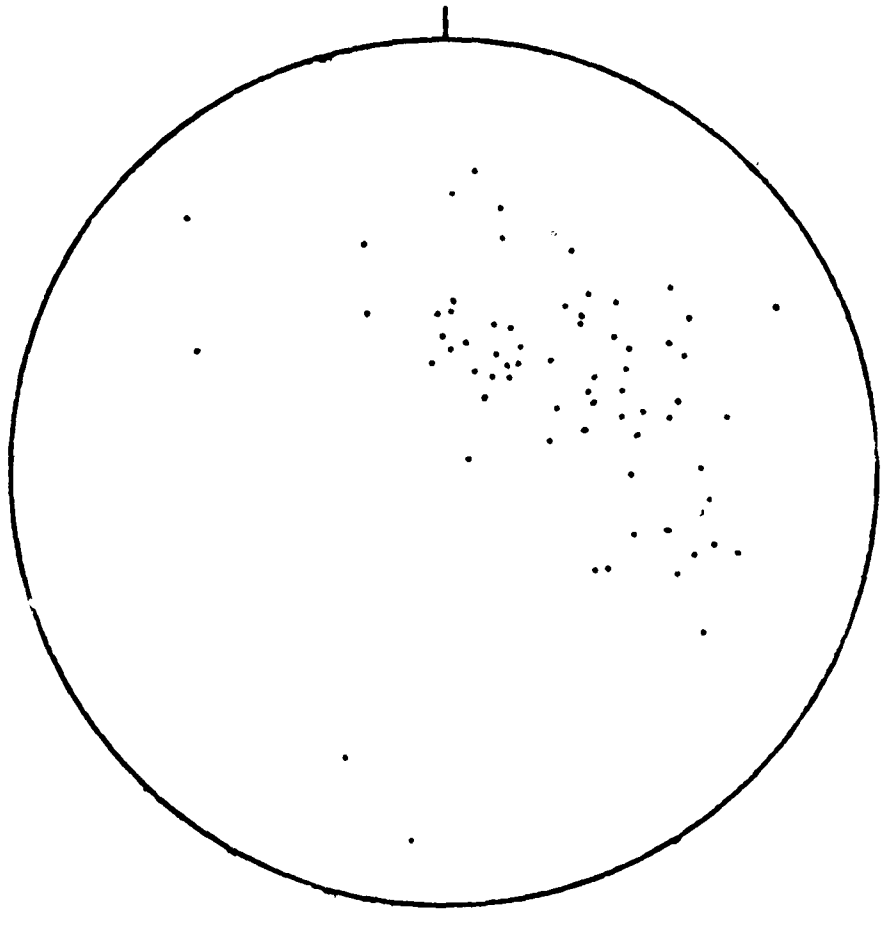


Fig. 3.25 Structural elements in the Auernig subarea.

(c) Poles to $S_a^2$ schistosity and $F_a^2$ axial planes.



(d) $D_a^2$ lineations and $F_a^2$ fold axes.

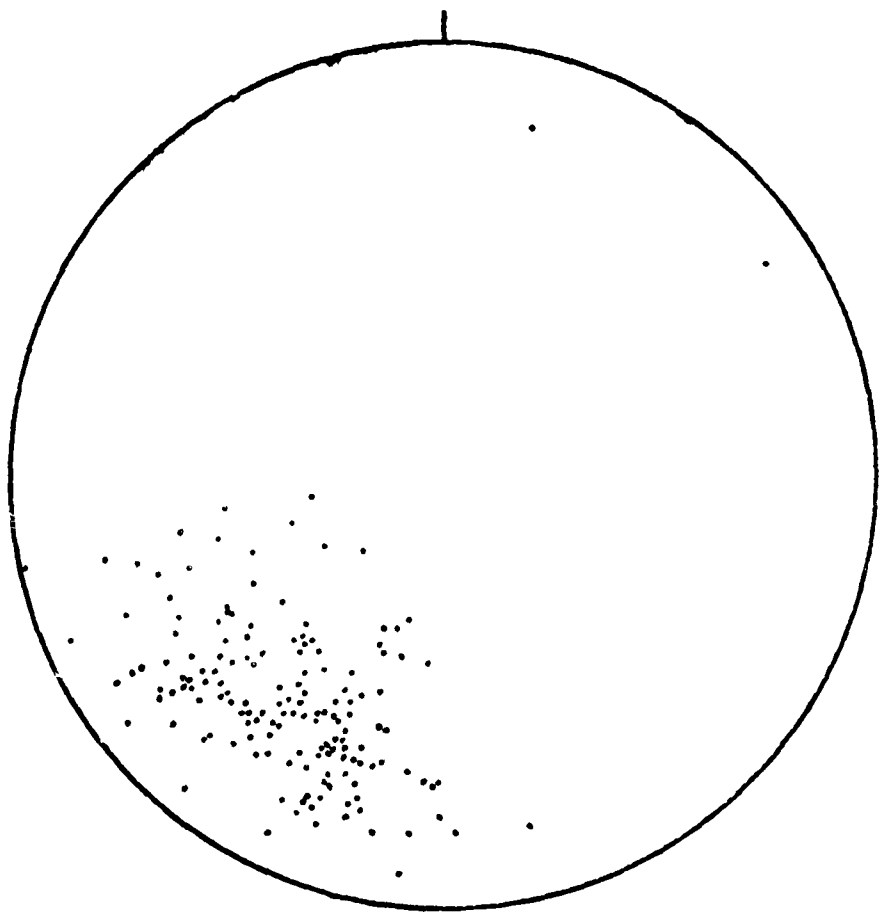
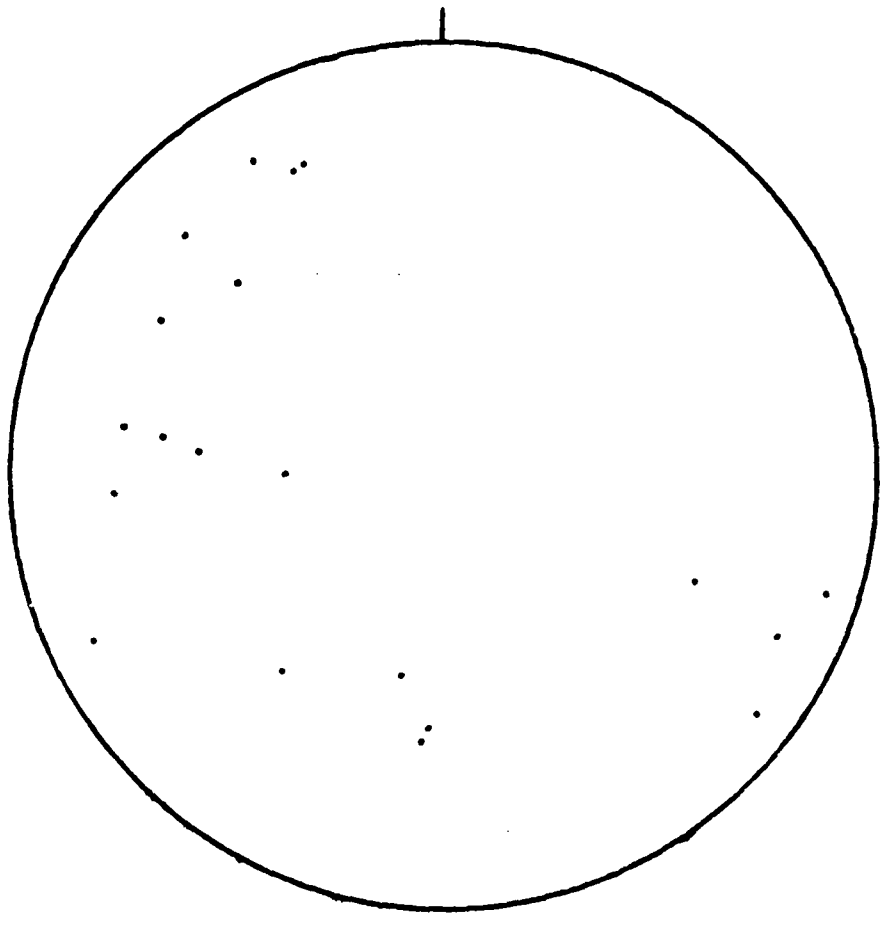


Fig. 3.25 Structural elements in the Auernig subarea (cont'd.).

(e) $D_a^3$ lineations and buckle-fold axes (dots) and boudin axes (crosses).



(f) $F_a^3$ kink axes.

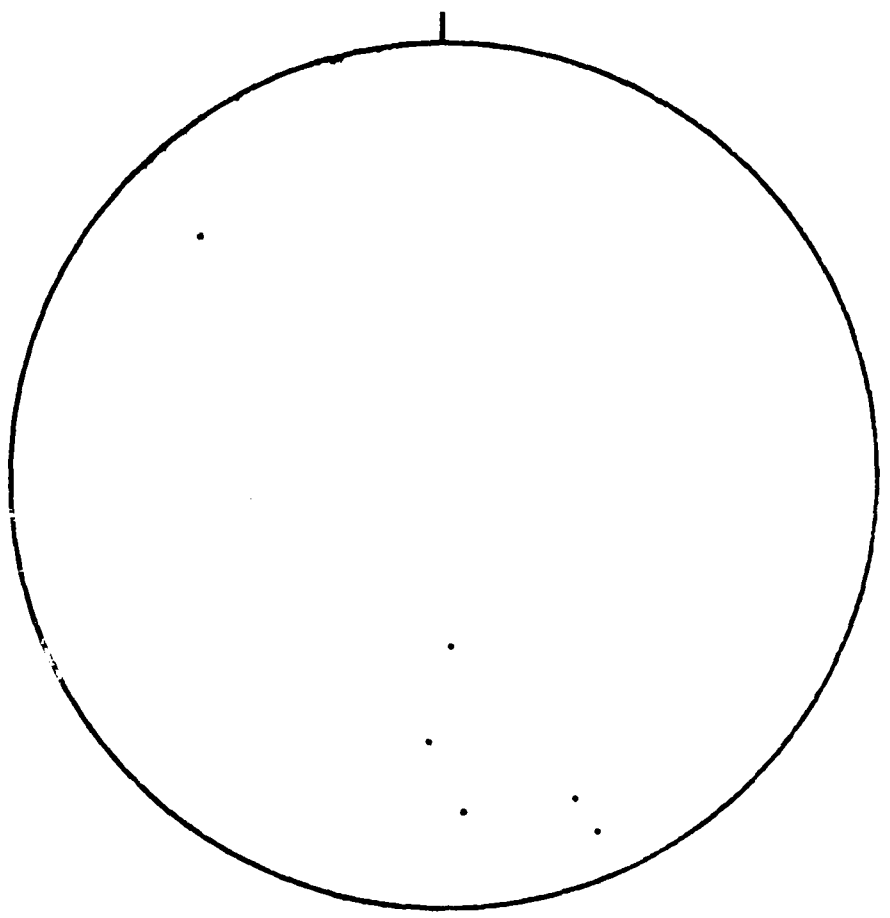


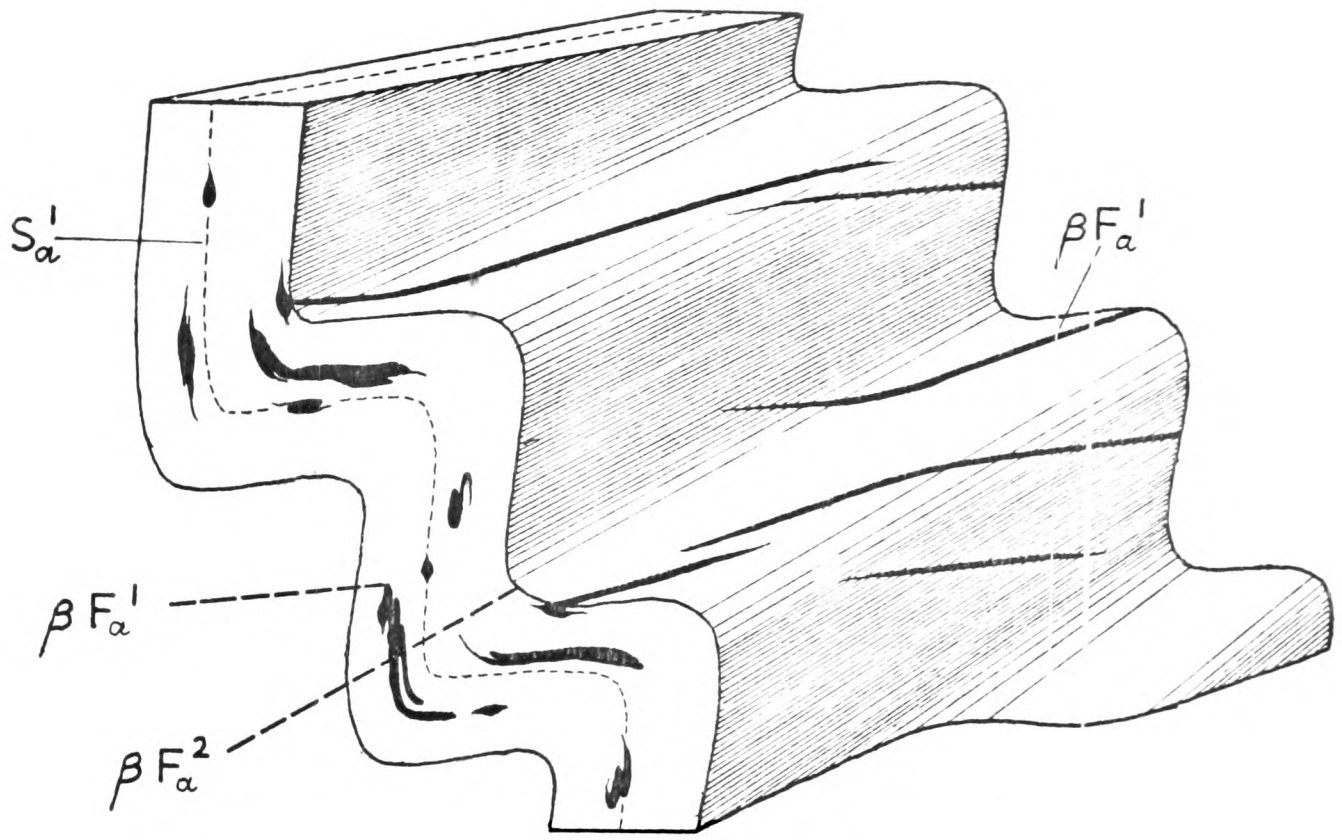
Fig. 3.25 Structural elements in the Auernig subarea (cont'd.).



Fig. 3.26 Rotation of $S_a^1$ foliation on the east slope of Hindenburg Höhe.



Fig. 3.27 Tight $F_a^2$ folds in graphitic mica-schists, Seebachtal.




$\beta$ = Fold axis

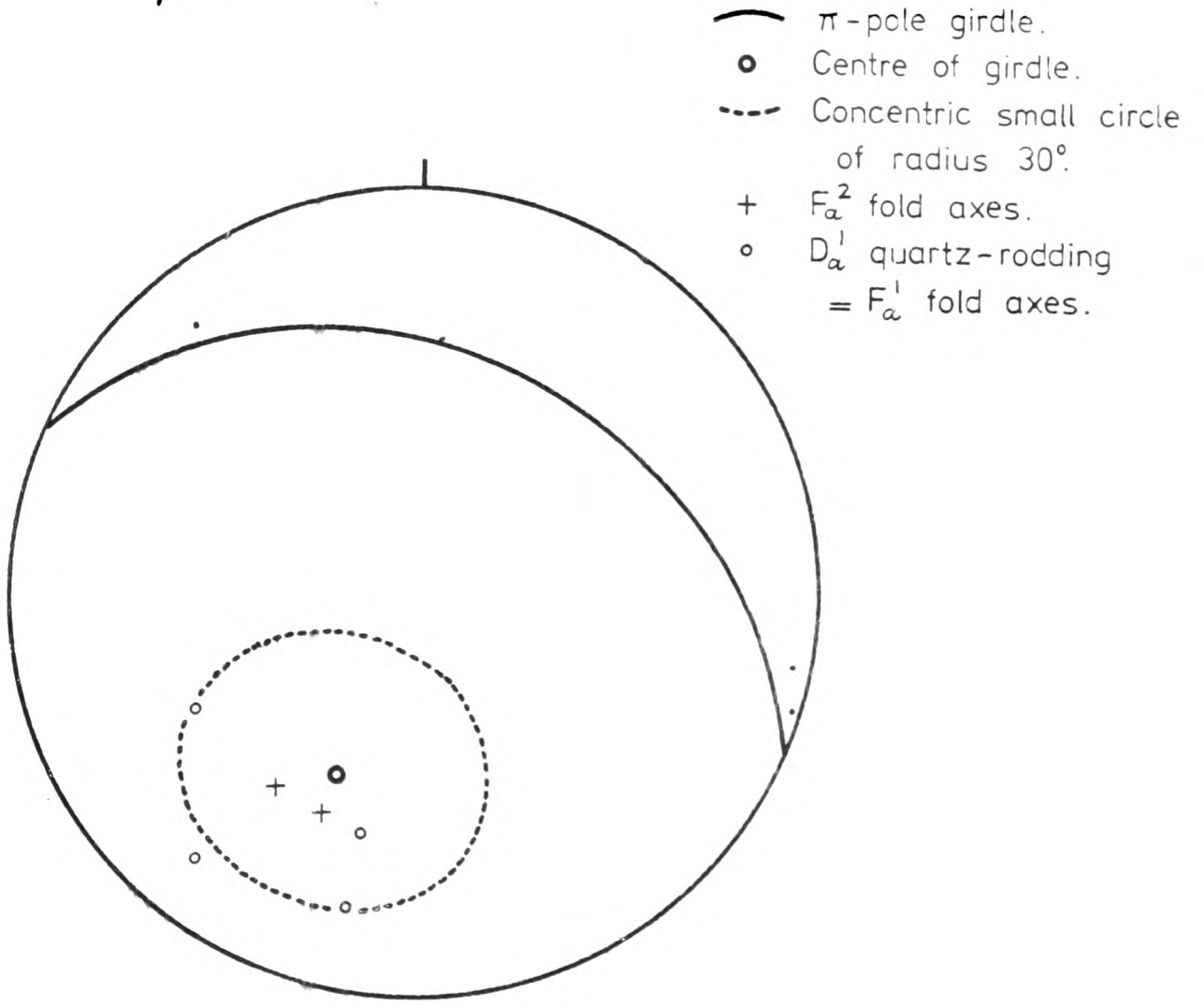



Fig. 3.28 Diagram and stereogram illustrating structures at locality 657, near Mallnitz.

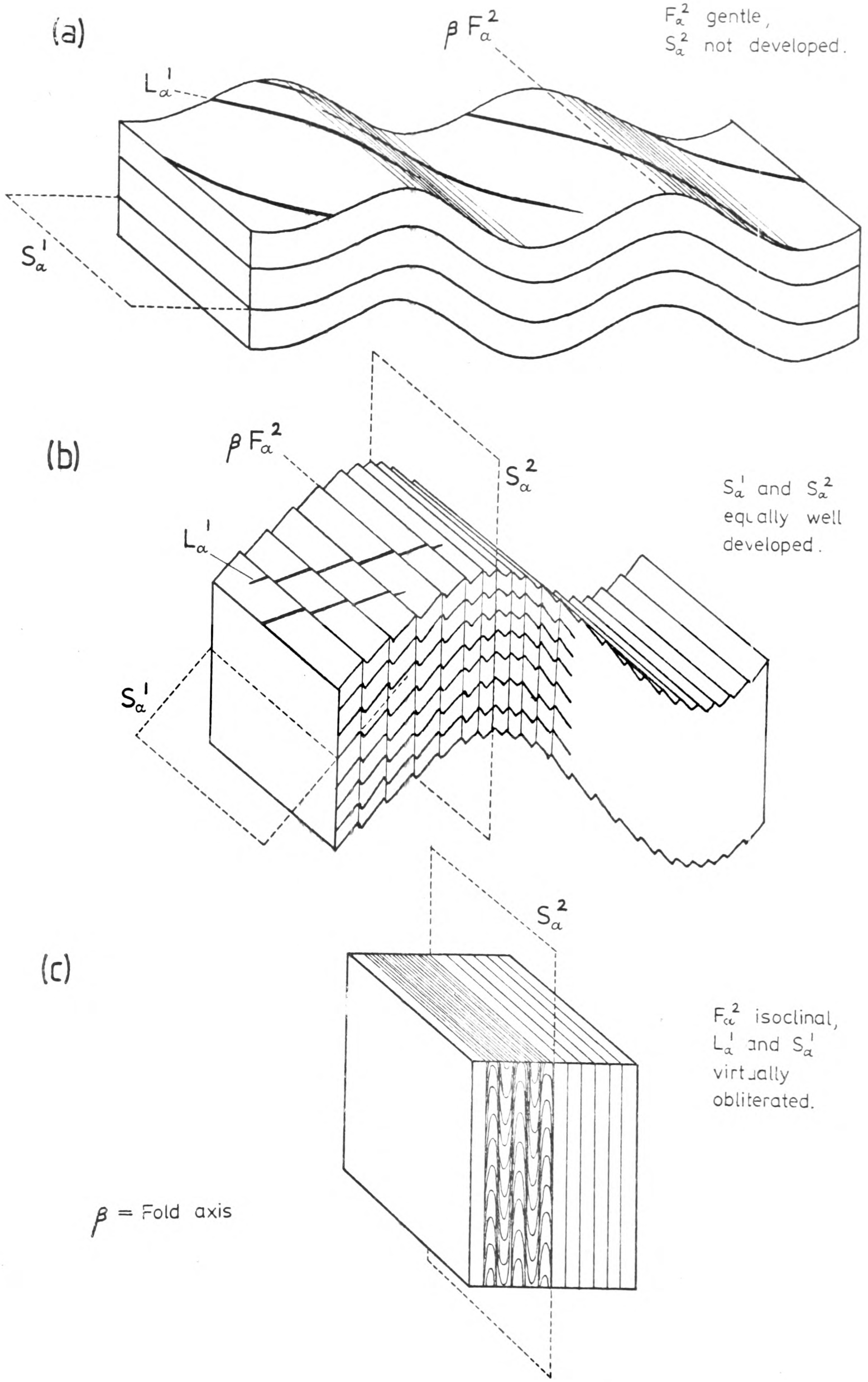



Fig. 3.29 Variation in the relative intensity of $S_a^1$ and $S_a^2$ encountered in mica-schists.

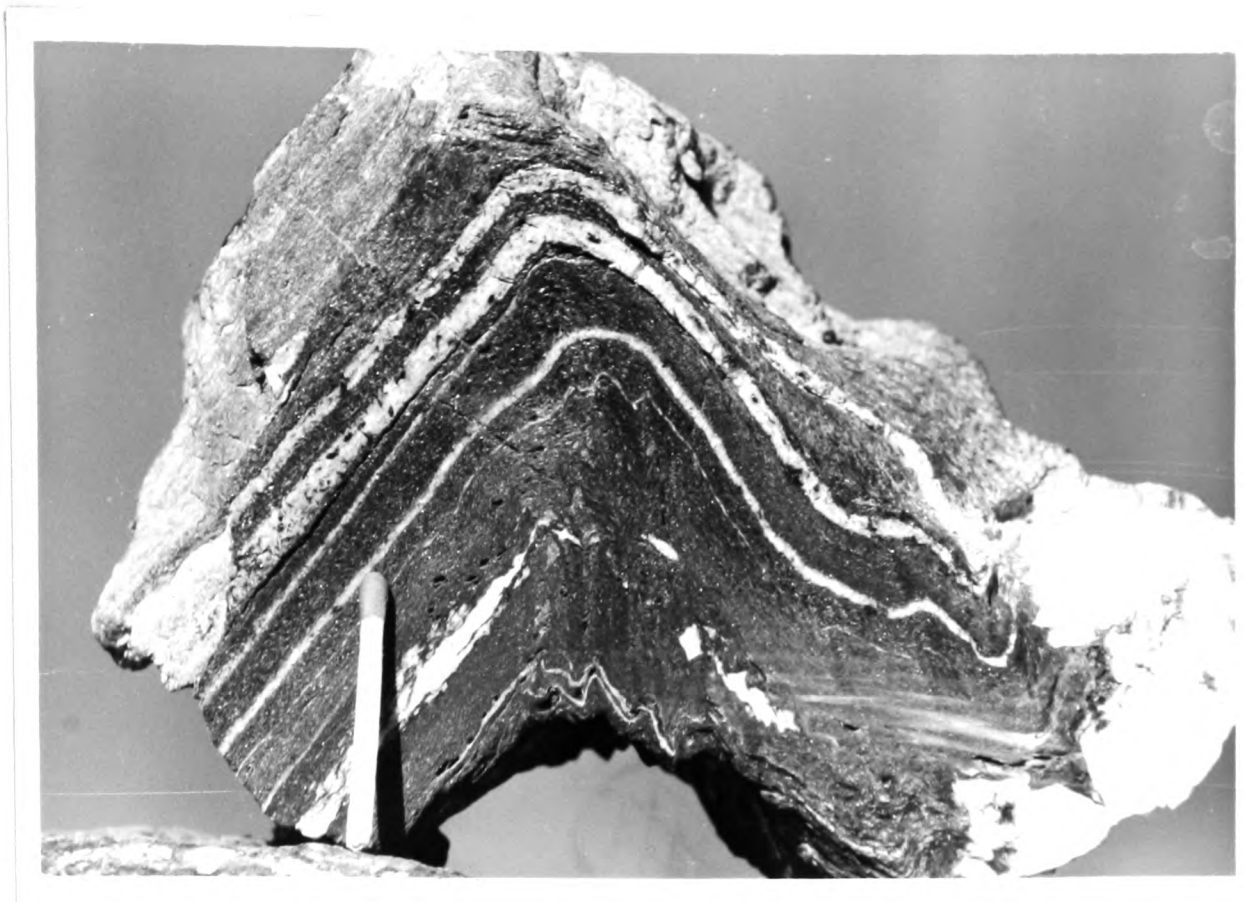


Fig. 3.30 $F_a^3$ buckle-fold in epidote-amphibolite from Auernig. Note albite vein at edge of specimen.

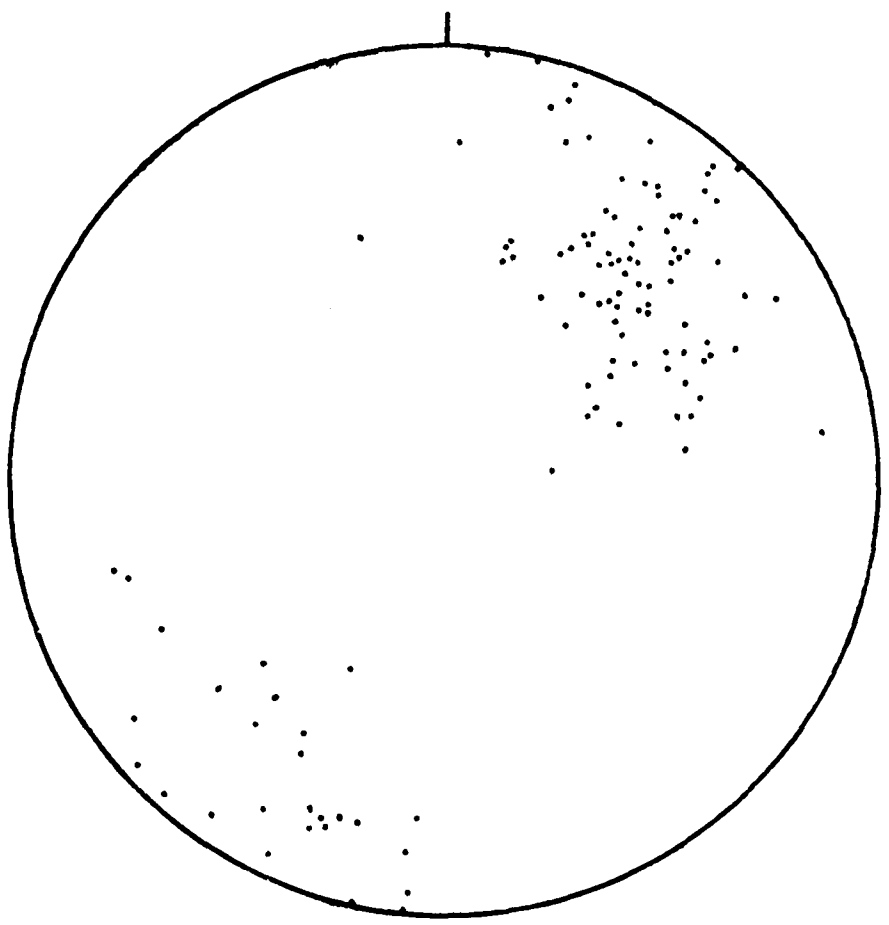


Fig. 3.31 Intersecting lineations ($D_a^2$ shallow, $D_a^3$ steep) in epidote-amphibolite. Mallnitz.



Fig. 3.32 Décollement structure in loose block of epidote-amphibolite, demonstrating the spatial and temporal association between albite + chlorite veins and $D_a^3$ deformation.

(a) Poles to principal foliation, $S_a^1$.



(b) $D_a^1$ tremolite lineations at locality 233.

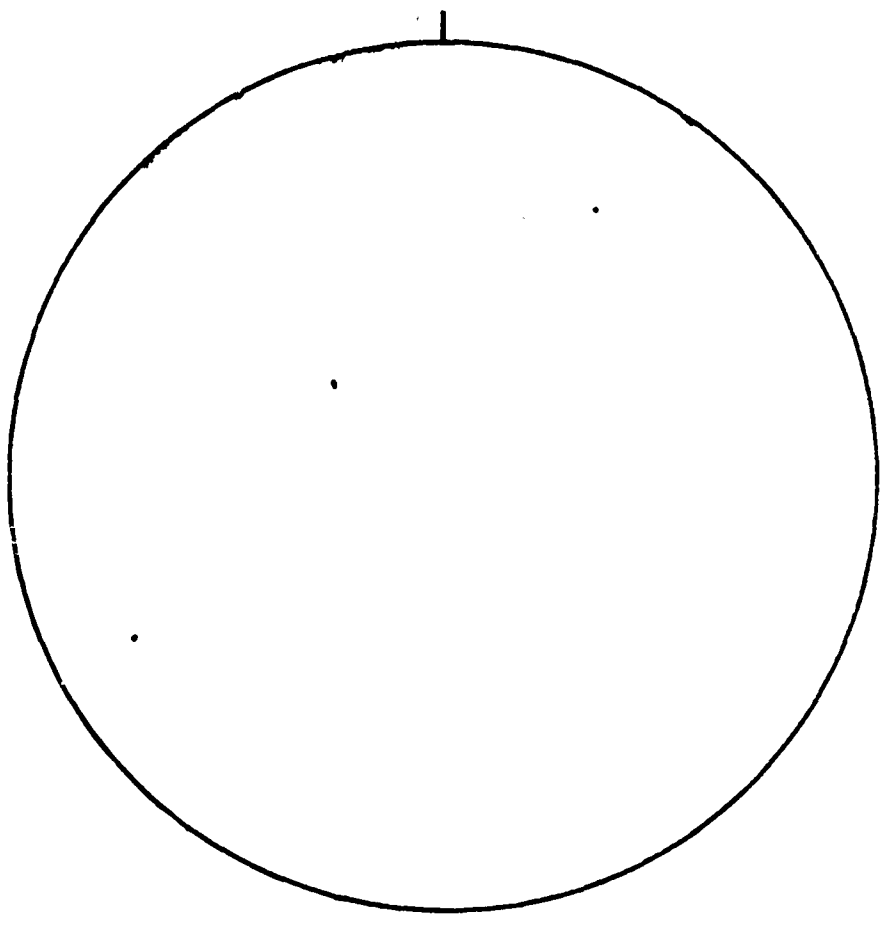
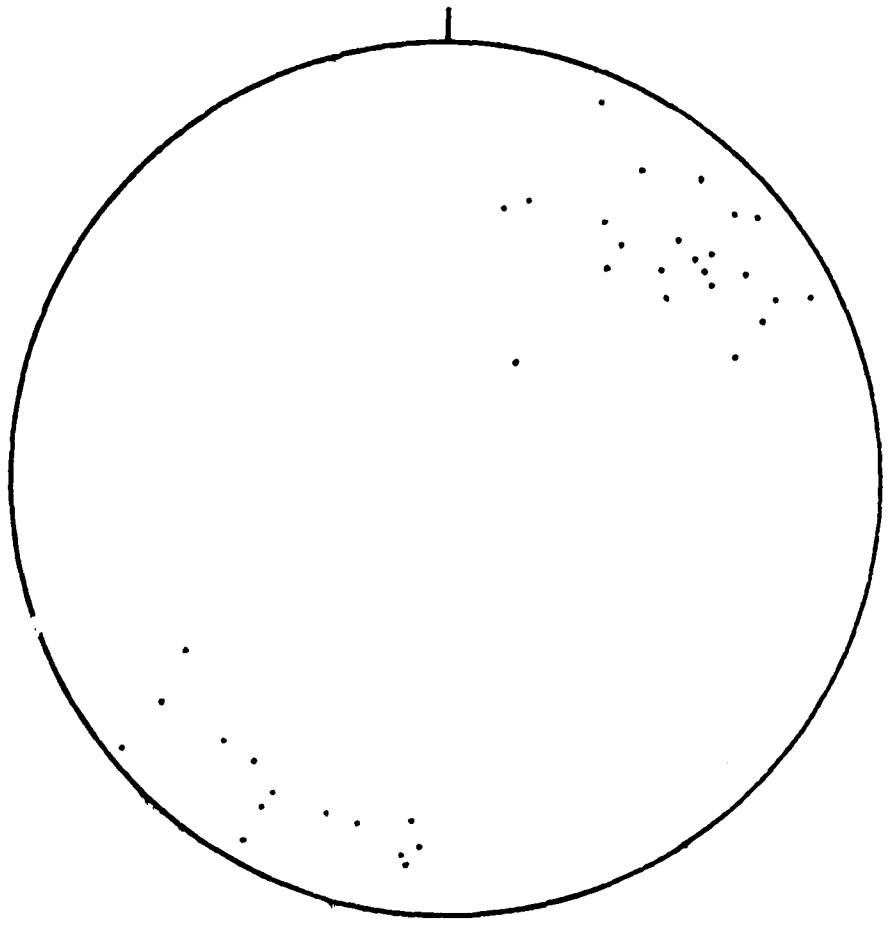


Fig. 3.33 Structural elements in the Kaponig subarea.

(c) Poles to $S_a^2$ schistosity and $F_a^2$ axial planes where demonstrably different from (a).



(d) $D_a^2$ lineations and $F_a^2$ fold axes.

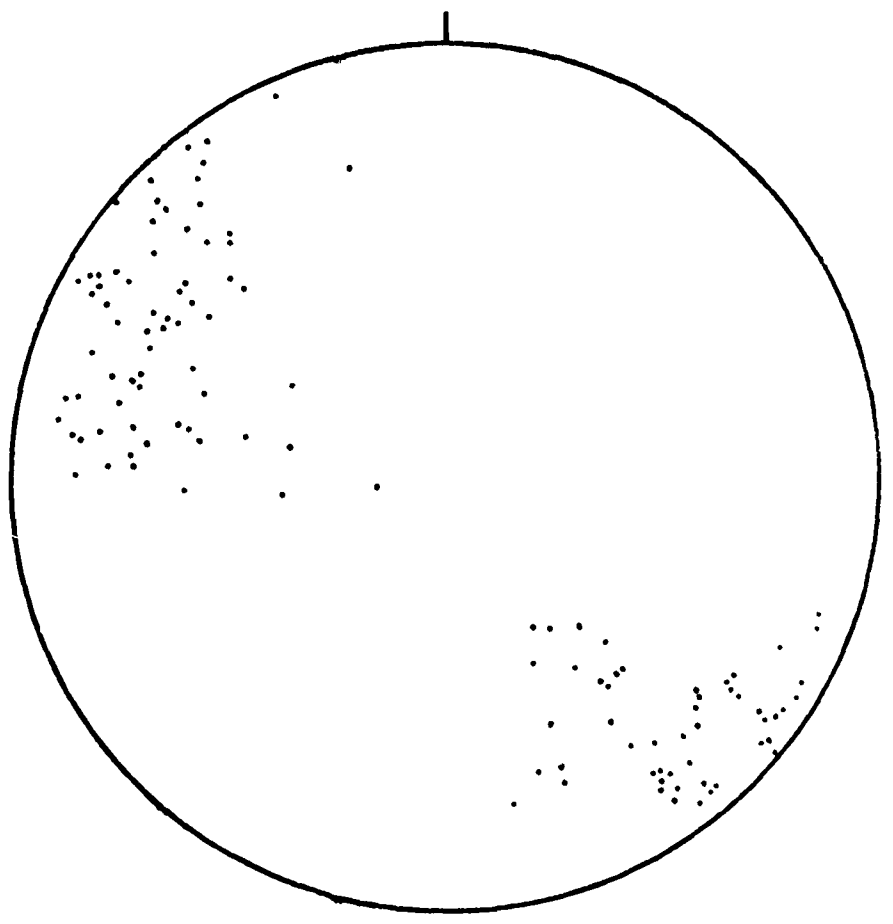
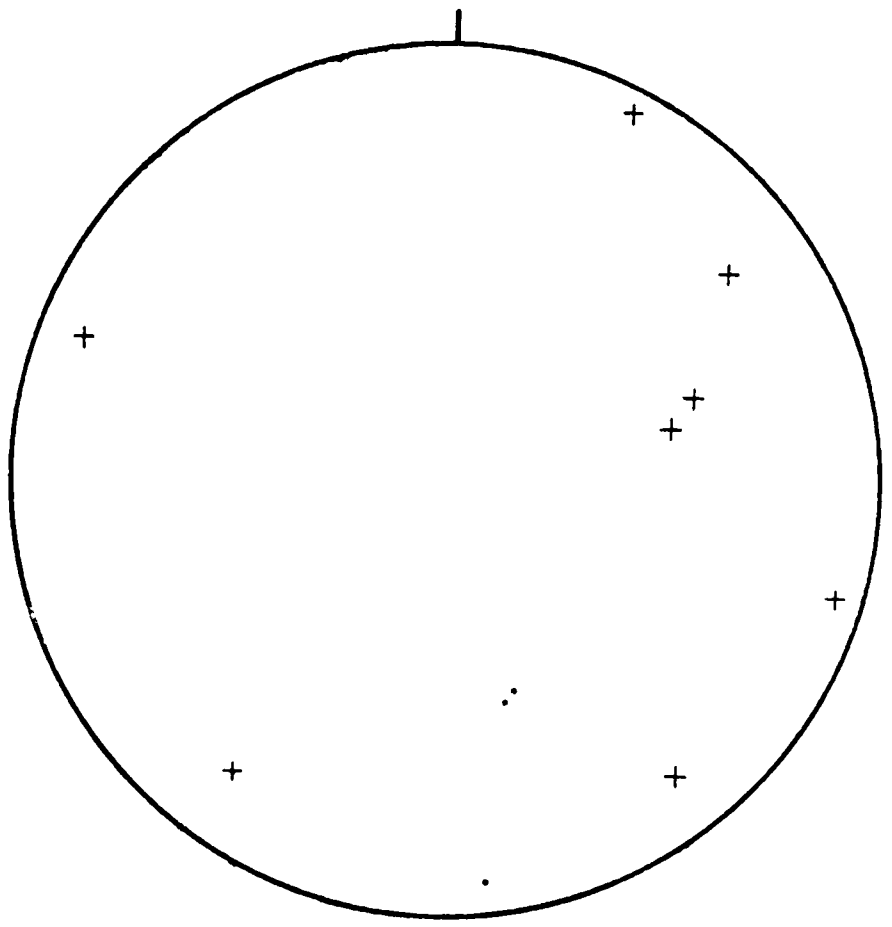


Fig. 3.33 Structural elements in the Kaponig subarea (cont'd.).

(e) $D_a^3$ lineations and buckle-fold axes (dots) and boudin axes (crosses).



(f) $F_a^3$ kink axes.

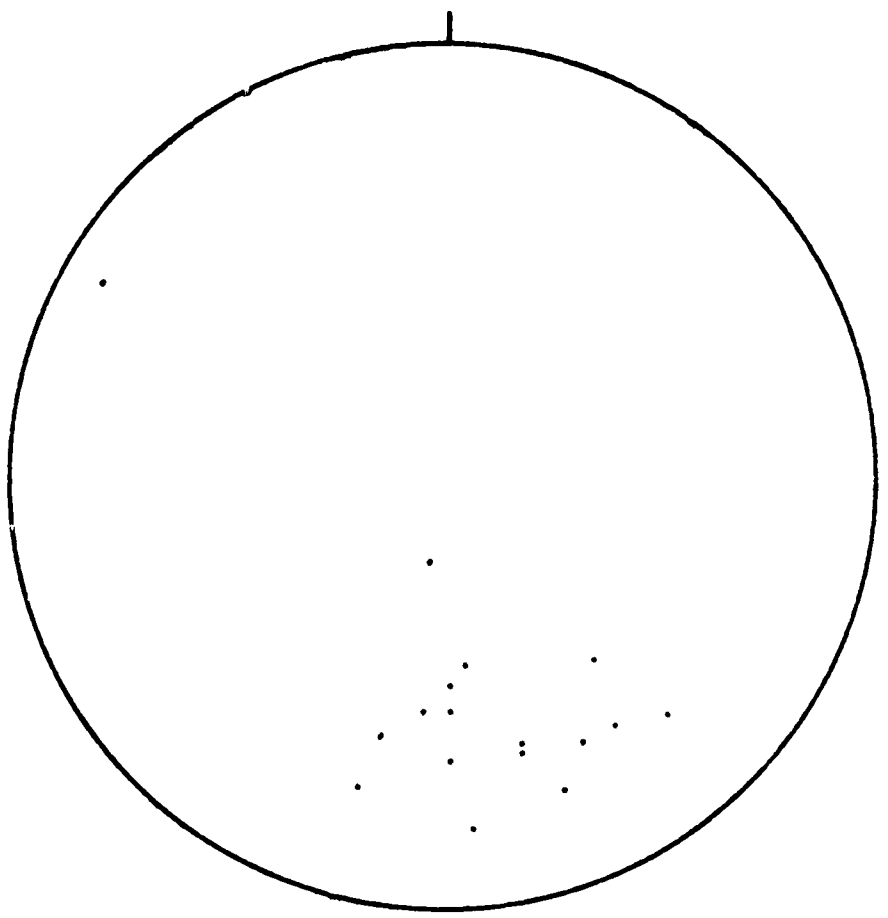
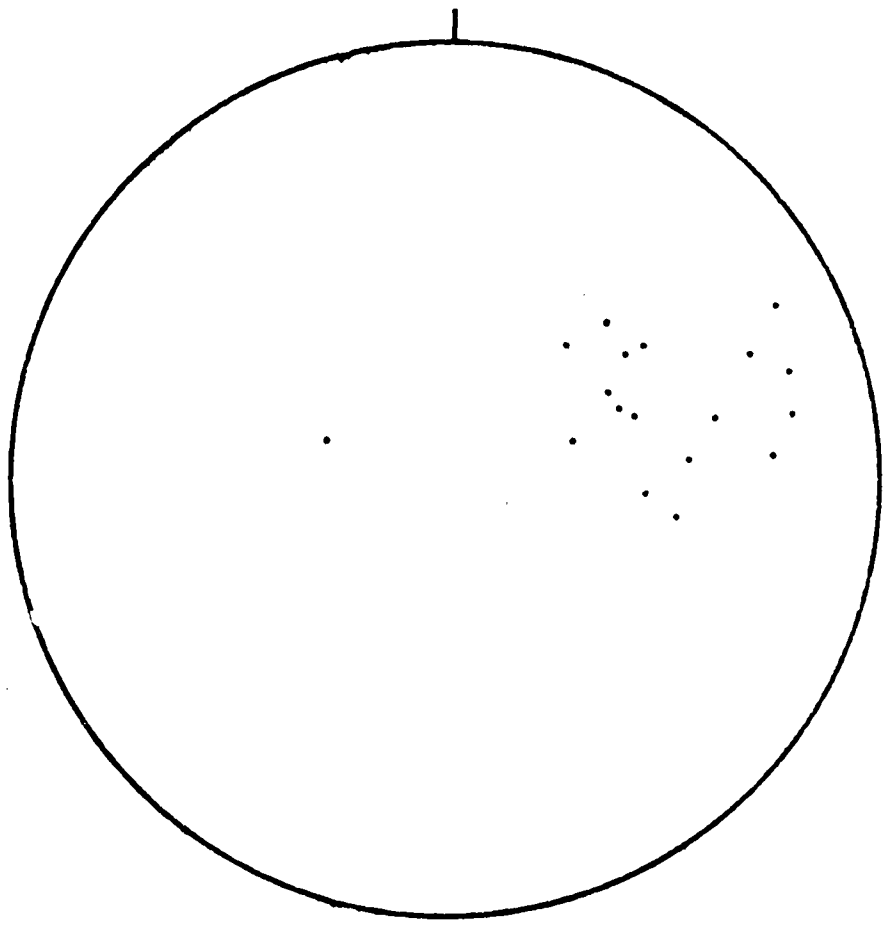


Fig. 3.33 Structural elements in the Kaponig subarea (cont'd.).

(a) Poles to principal foliation surfaces.



(b) $D_v$ lineations.

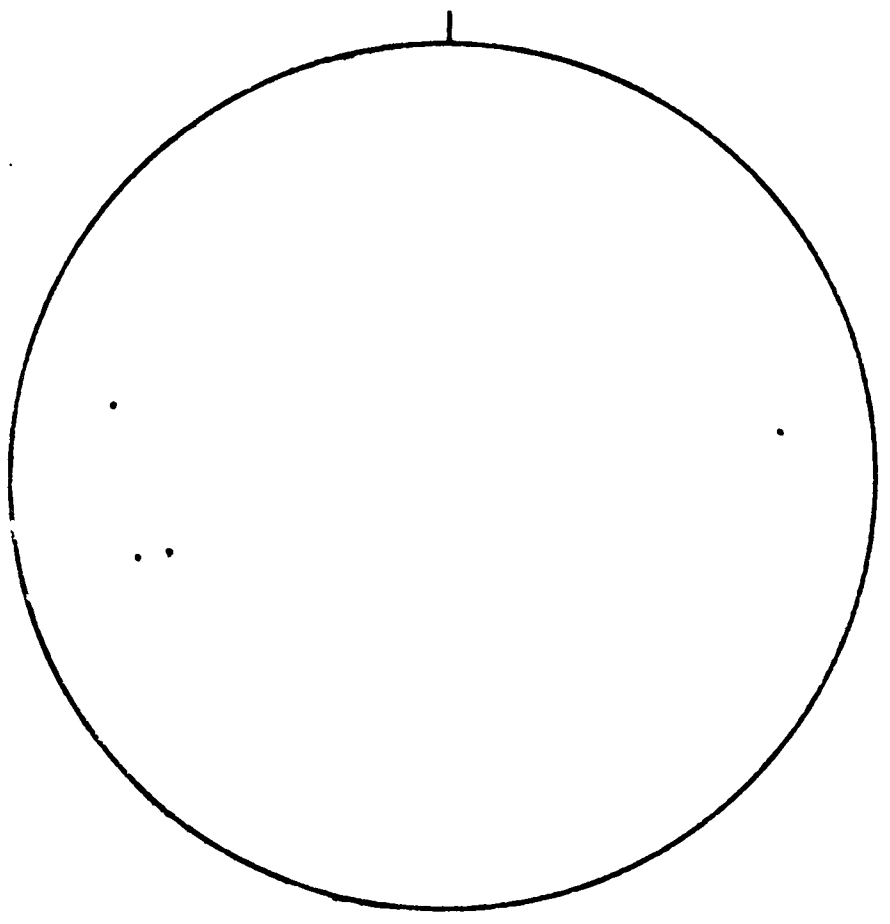
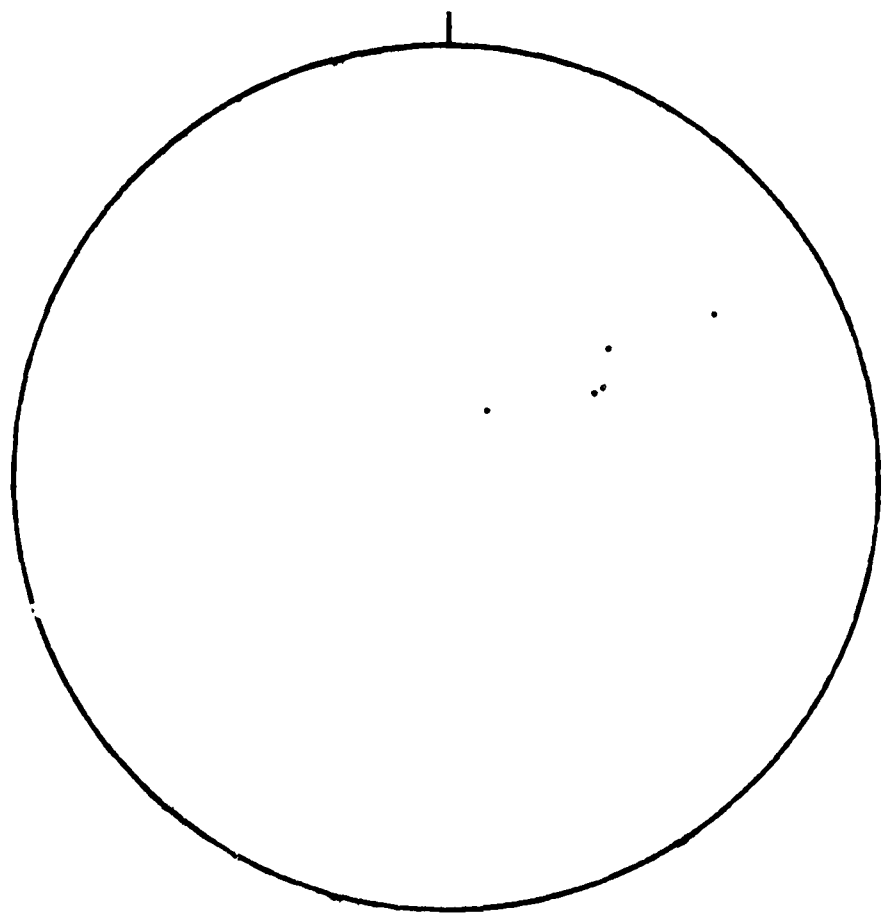


Fig. 3.34 Structural elements in the Sickerkopf subarea.

(c) Poles to $S_a^2$ schistosity and $F_a^2$ axial planes where demonstrably different from (a).



(d) $D_a^2$ lineations and $F_a^2$ fold axes.

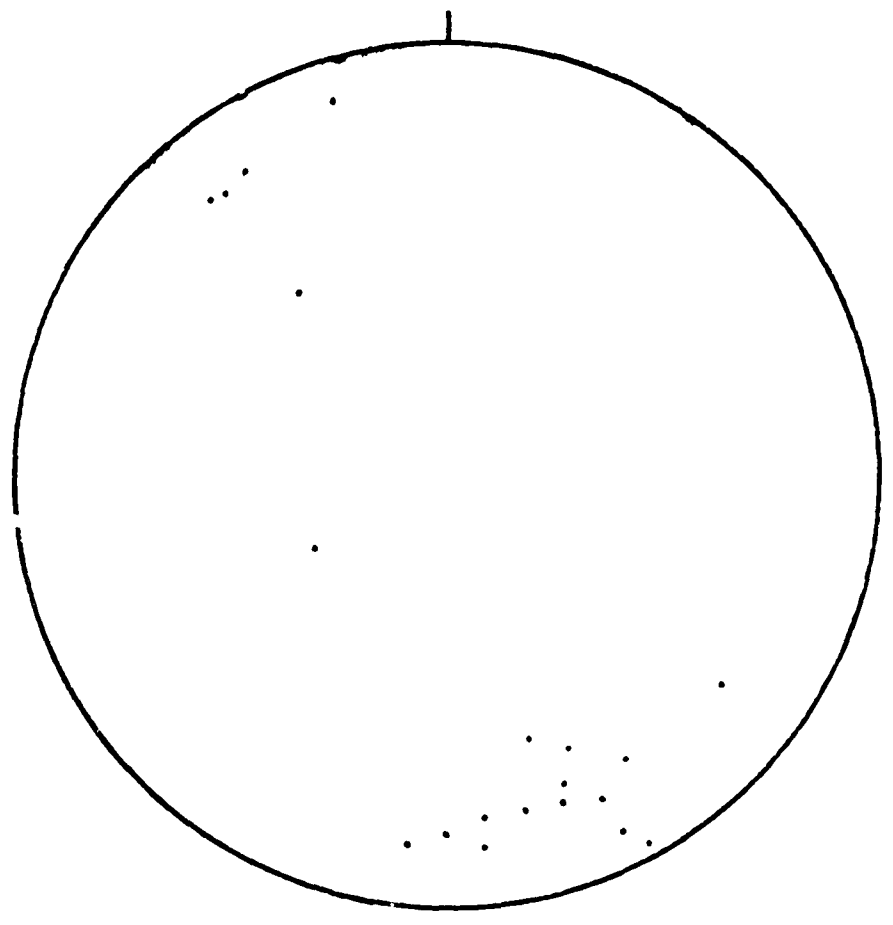
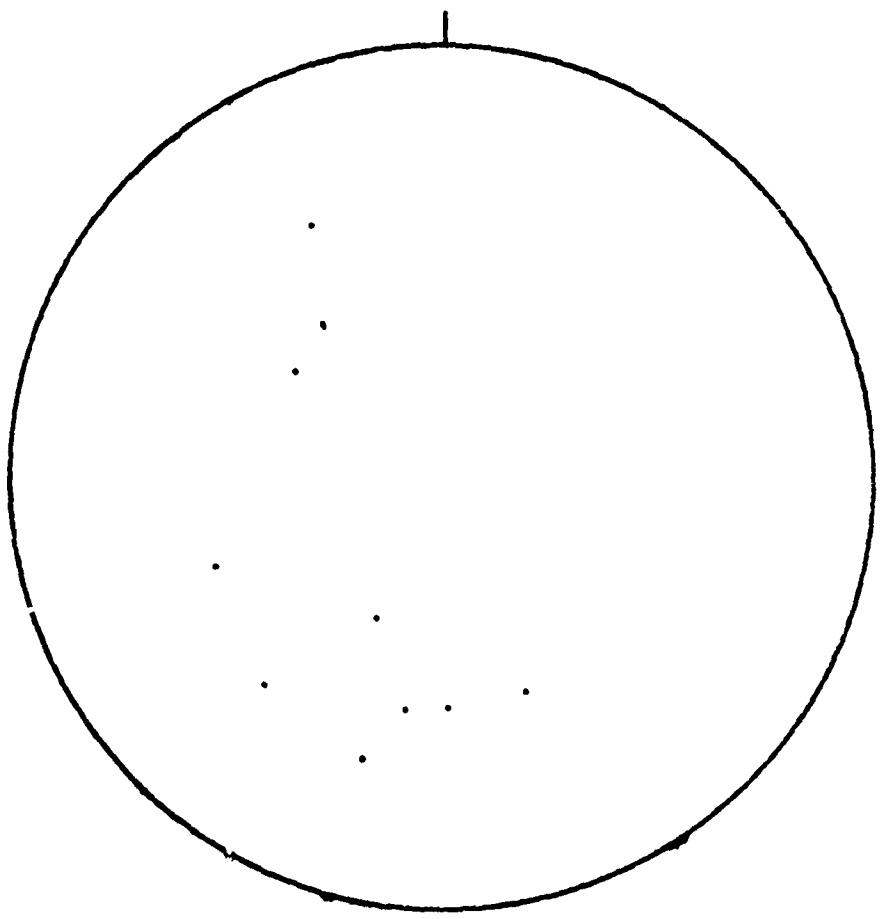


Fig. 3.34 Structural elements in the Sickerkopf subarea (cont'd.).

(e) $D_a^3$ lineations and buckle-fold axes (dots) and boudin axes (crosses).



(f) $F_a^3$ kink axes.

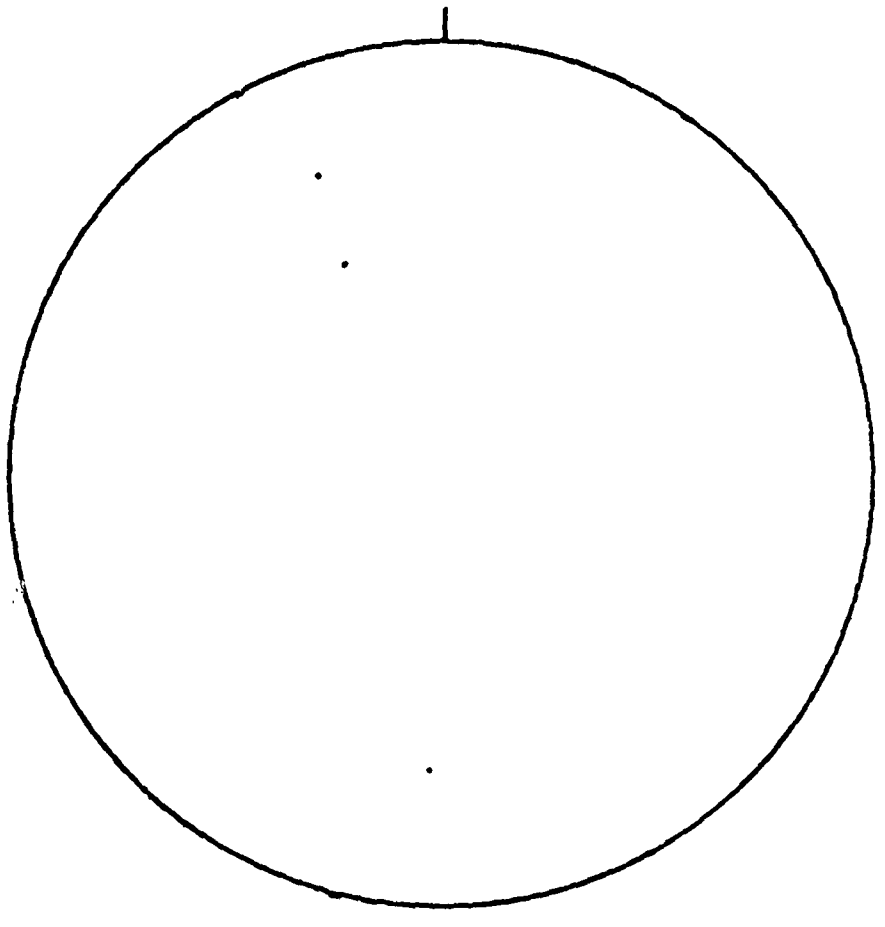


Fig. 3.34 Structural elements in the Sickerkopf subarea (cont'd.).

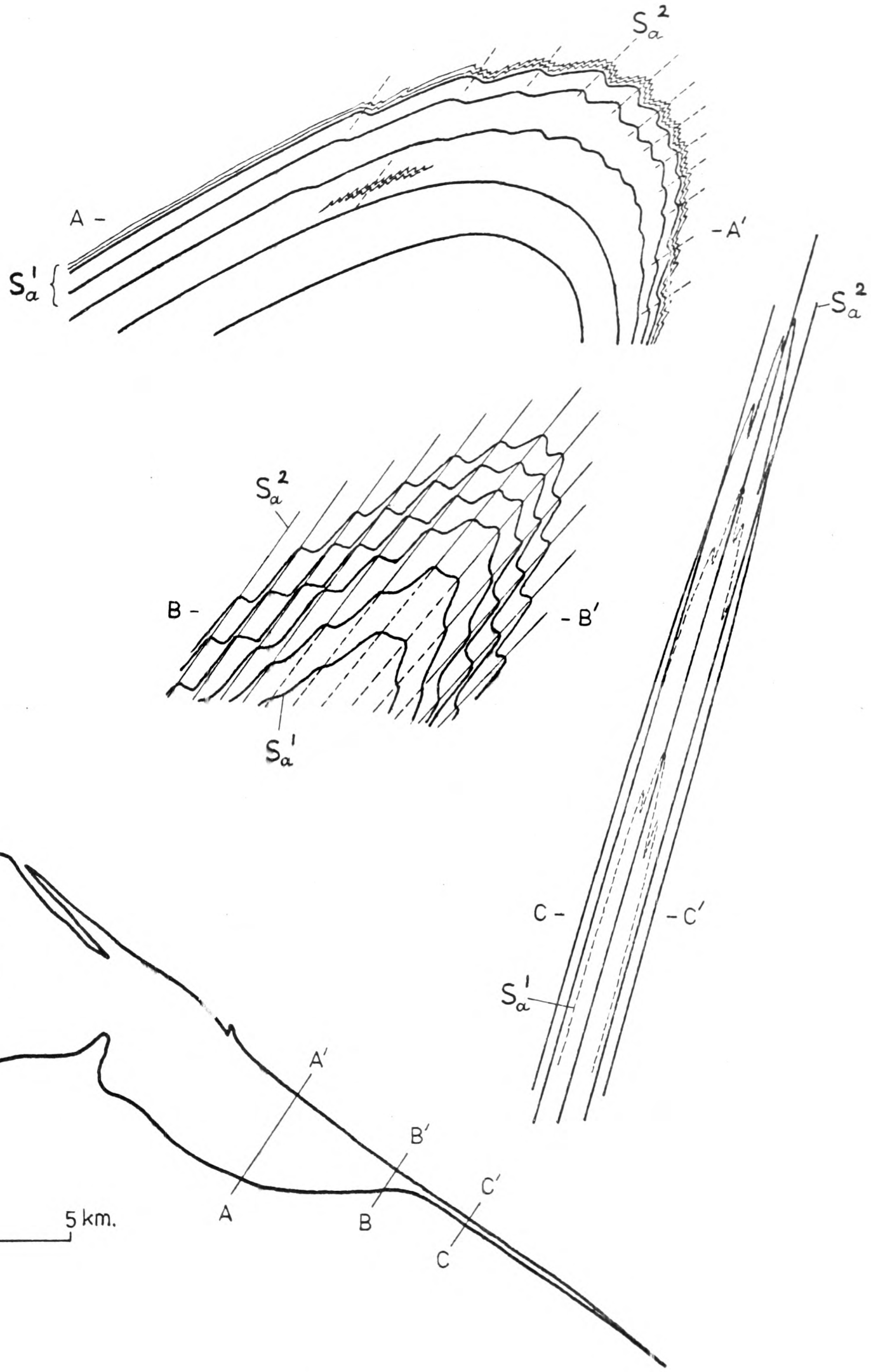



Fig. 3.35 Relationship of $S_a^1$ to $S_a^2$ in the Sonnblick Kern and Sonnblick gneiss-lamella.

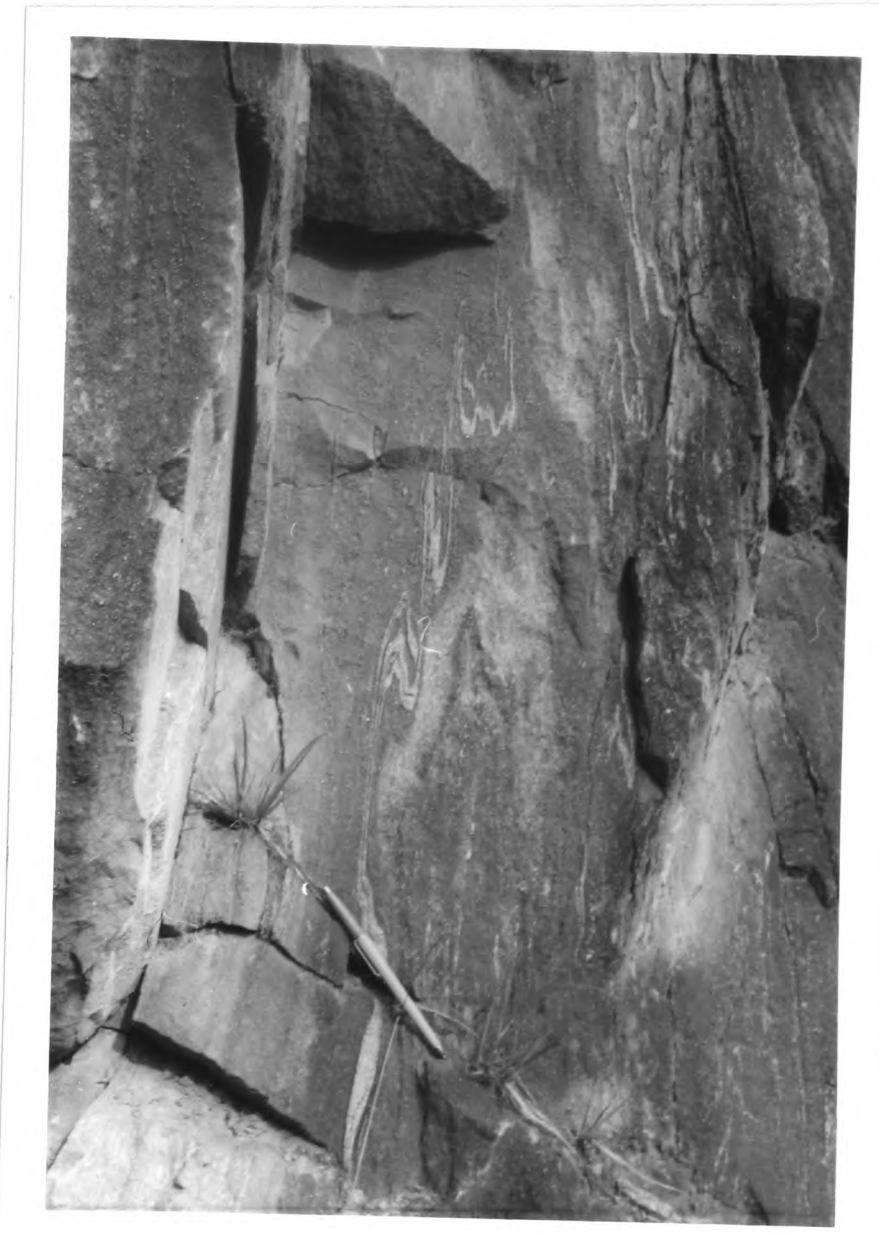
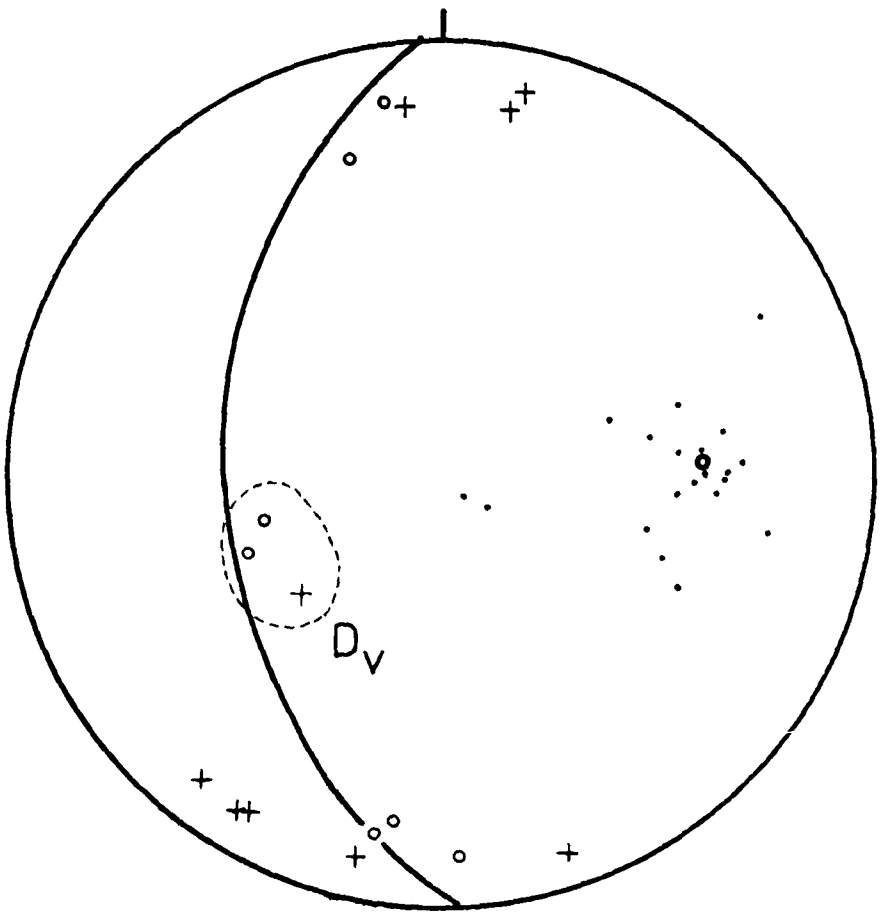


Fig. 3.36 Isoclinal $F_a^2$ folds in calc-schists south of Gröneck.




- Poles to schistosity.
- π-pole girdle.
- Centre of girdle.
- Fold axes.
- Mineral lineations.

Fig. 3.37 Structural elements in the Dösener subarea.

Table 3.2 Synopsis of the structural history of the south-east Tauern.

| Area covered by Map 2. | | | | Area covered by Map 1. | | | |
|---|---|---|---|---|---|---|---|
| MACROSCOPIC | MESOSCOPIC | | | MACROSCOPIC | MESOSCOPIC | | |
| | PERIPHERAL SCHIEFERHULLE | ZENTRALGNEIS | INNER SCHIEFERHULLE | | PERIPHERAL SCHIEFERHULLE | ZENTRALGNEIS | INNER SCHIEFERHULLE |
| Regional updoming | Kinks, joints and faults. Non-penetrative, semi-brittle deformation. Localised boudinage, buckles, microripples. Chlorite + Albite veins | | | Regional updoming. Rotation of foliation to subvertical along Mölltal line. | Kinks, fractures, faults, pseudotachylites, buckles, microripples, chlorite + albite veins. | | |
| Large, asymmetric folds (kern and mulde structures). Tongue-like proto-nappes with cores of basement. | Penetrative deformation. Open, tight and isoclinal asymmetric folds. Axial planar schistosity only locally developed (mostly in calcareous rocks). Crenulations. Rodding. | Asymmetric open to gentle folds. Crenulations. Mineral lineation. | Penetrative deformation. Asymmetric folds. Localised axial planar schistosity. | Large-scale tight folding. Sonnblick lamella. | Intense penetrative deformation. Tight to isoclinal folds. Strong axial planar schistosity and rodding. Mineral lineation. Floating fold hinges. | Penetrative deformation. Schistosity. Mineral lineation. | Tightening of $D_v$ structures. Asymmetric tight to open folds. |
| Large-scale lithological banding. | Intense penetrative deformation. Schistosity. Isoclinal folds. Rodding. | Penetrative deformation only intense at high structural levels. Schistosity. | Intense penetrative deformation. Destruction of angular discordances. Schistosity. Strong rodding. Isoclinal folds. | Large-scale lithological banding. (not confirmed). | Flattened pebbles. Schistosity. (rarely preserved) | | |
| Thrusting. Allochthonous sheets include precursors of gneiss-lamellae, Romate-decke?, Feldwand-lamella?, serpentinites, etc. | | Localised shear-zones at low levels. | | Thrusting of cover over basement? Shear-zones within cover? Introduction of ophiolites? (not confirmed). | | Localised shear-zones? (not confirmed) | Not recognised. |
| Deposition of P.S. Uplift & erosion. | Primary compositional banding. | - | - | Deposition of Peripheral Schieferhülle. Uplift and erosion. | Primary compositional banding. | - | - |
| Intrusion of Zentralgneis | - | Intrusive contacts. Very rarely preserved. | Truncation of $D_v$ structures?? | Intrusion of Zentralgneis | - | Intrusive contacts. Discordant aplites. | Truncation of $D_v$ structures. |
| ? | - | - | Penetrative deformation. Isoclinal folding. (Not confirmed). Only preserved in graphitic quartzites. | ? | - | - | Penetrative deformation. Banding. Mineral lineation in amphibolites. Polyphase isoclinal folding. |

Table 3.3 Correlation of deformation phases over the central and eastern Tauern.

| | This work | Norris et al (1971b) | Bickle (1973) | Hawkesworth (1974) | Holland (1977) |
|---|---|---|---|---|---|
| Peak of Alpine Metamor-phism. * | $D_a^3$ | $D_a^2$ | $D_a^5$, $D_a^4$, $D_a^3$ | $D_a^3$, $D_a^2$ | $D_a^3$ |
| | Not recognised | Not recognised | $D_a^2$ (N.S. crenulations in Glockner area) | Not recognised | Not recognised |
| | $D_a^2$ | $D_a^1$ | $D_a^1$ | $D_a^1$ | $D_a^2$ |
| | $D_a^1$ | Not recognised | $D_a^o$ | $D_a^o$ | $D_a^1$ |
| | Not confirmed | Not recognised | Not recognised | Not recognised | $D_a^o$ (confined to eclogites) |
| Intrusion of Zentral-gneiss | $D_v$ | $D_v$ | - | $D_v$ | $D_v$ |

* see chapter 4.

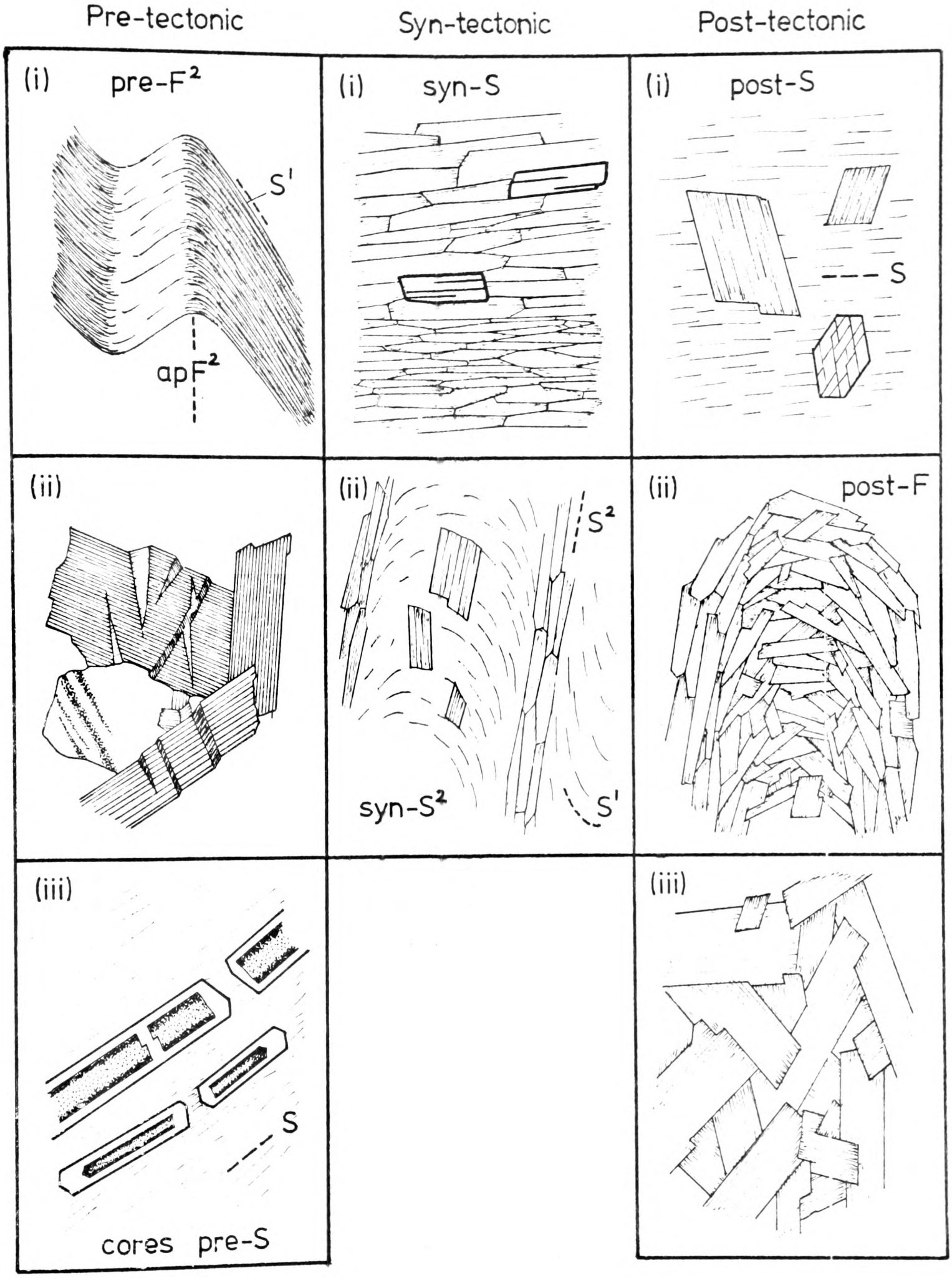



Fig. 4.1(a) Textures of matrix platy and prismatic minerals. (See text for explanation.)

Partly adapted from Spry (1969) and Misch (1969).

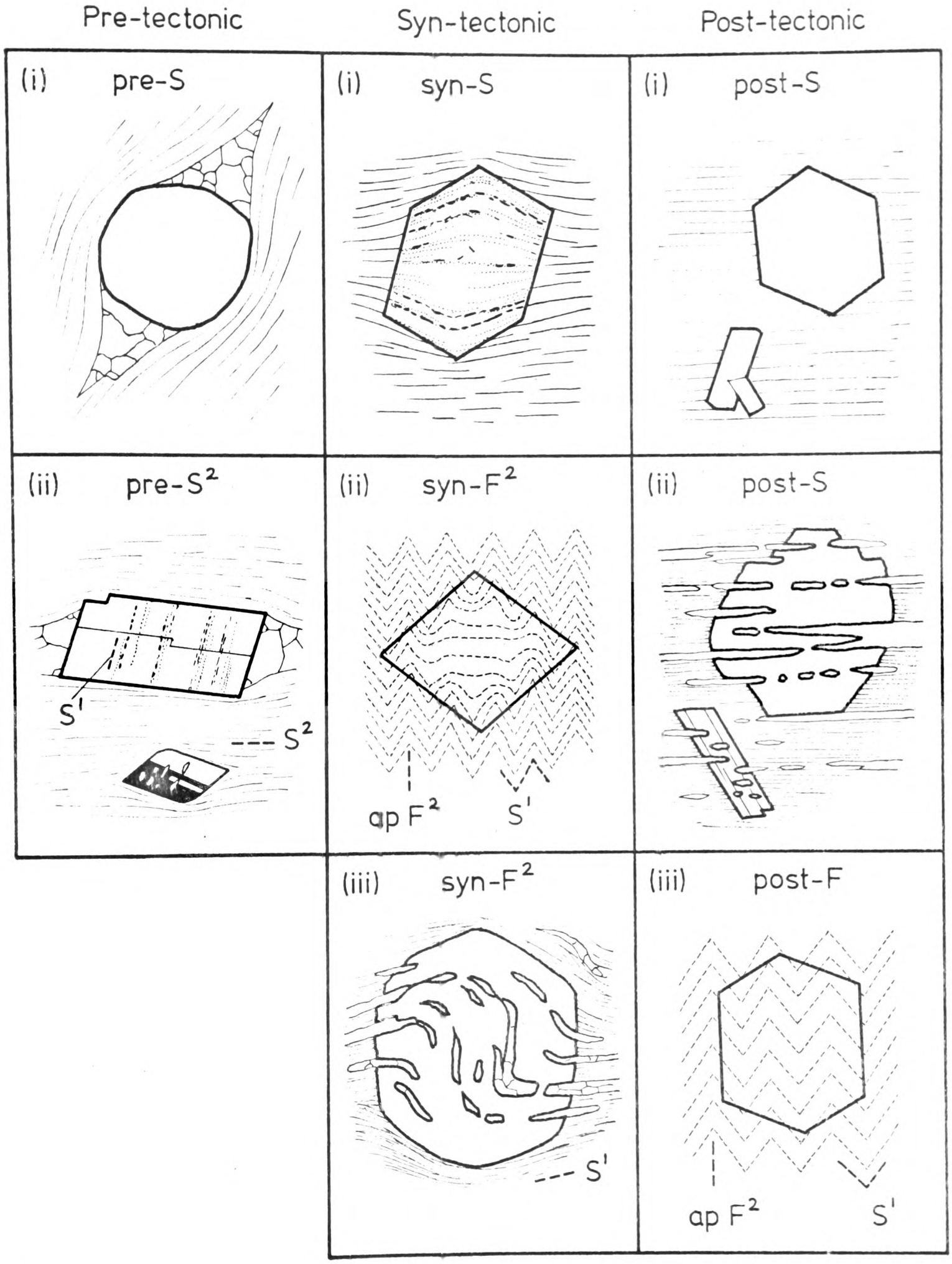



Fig. 4.1 (b) Textures of porphyroblast minerals. (See text for explanation.)

Partly adapted from Spry (1963, 1969) and Zwart (1962).

Table 4.1 Mineral growth phases in Dösener Tal eclogites and garnet amphibolites.

| | A. GD 136a | B. GD 136a | C. GD 13e | D. GD 135 |
|---|---|---|---|---|
| | Fresh patch of eclogite (GT + CPX + RUT + QZ + ORE) | Partly amphibolitised eclogite (assemblage 2) | Amphibolitised eclogite (assemblage 4) | Garnet amphibolite (assemblage 8) |
| CPX 1 (Omphacite) | Large (1mm.) random prisms, altered along grain boundaries. | Rare. Relicts enclosed within GT2. | - | - |
| GT 1 (dark) | Tiny (0.05-0.1mm.) partially interconnected euhedral orange-pink grains. | V. rare. Within CPX1 relicts. Texture as in A. | - | - |
| RUT | Tiny equant prisms. | As in A., but associated with abundant oxide. | Tiny granules associated with oxide. Both occ. rimmed by sphene. | |
| CPX 2 (Diopside rich) | - | Pale green. Symplectitically intergrown with albite (probably a breakdown product of CPX1). Associated with HBL. | Texture as in B. | - |
| GT 2 (pale) | - | Coronas round CPX1 relics, (growing at expense of CPX1), or as individual grains/clusters. Inner sides of coronas and cores of single grains darker than rims and full of quartz inclusions. | Large (1-2mm) euhedral crystals with cores full of quartz inclusions. | Large (1.5mm.) anhedral spongy grains with clear reaction rims of granulose plagioclase. |
| HBL (mostly pleochroic in greens) | - | Mostly as random anhedral grains but also in HBL + AB symplectitic intergrowth. Probably growing at expense of both CPX1 and CPX2. | Texture as in B. | Bluish green colour than in A,B,C. Granular. Poor schistosity. |
| PLAG | | Rare $\frac{1}{2}$mm. poikiloblasts enclosing HBL and CPX2. Albite. | Large 2-3mm. poikiloblasts enclosing HBL and GT2. Albite. | Clear untwinned granules rimming GT. A few poikiloblasts enclose align- |

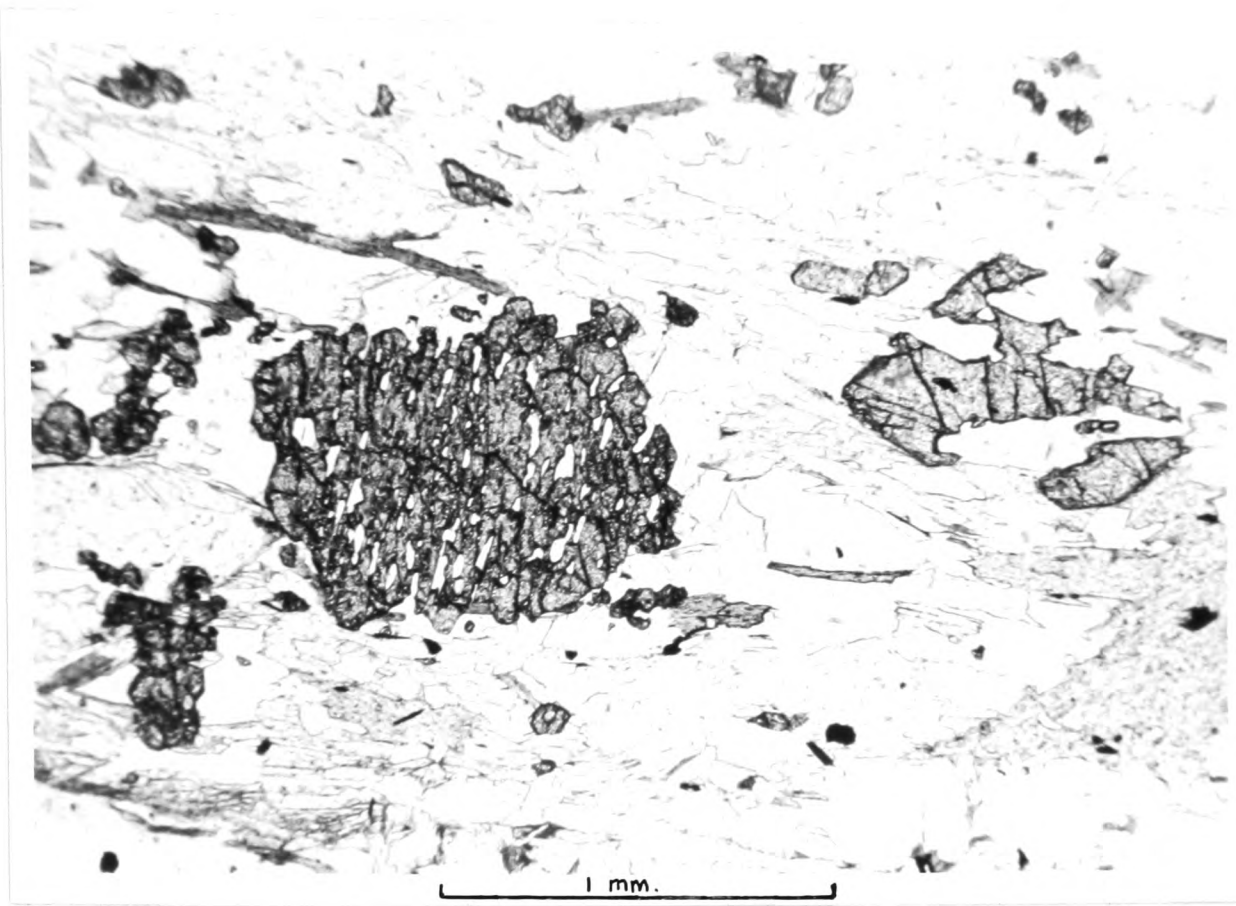



Fig. 4.2 Variscan garnet porphyroblast containing inclusion trails of quartz discordant to $S_a^2$ in the matrix. Inner Schieferhülle mica-schist GD 209b. Plane polarised light.

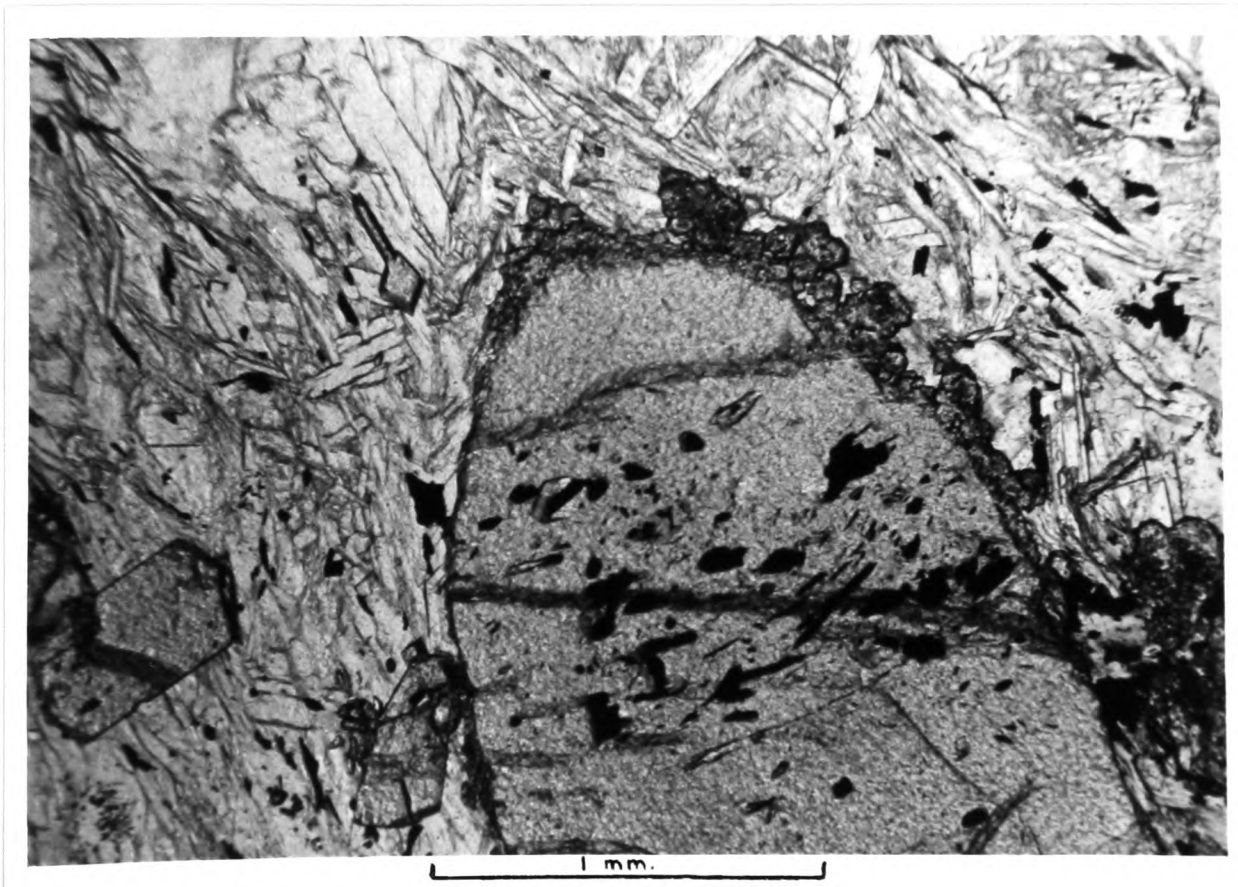
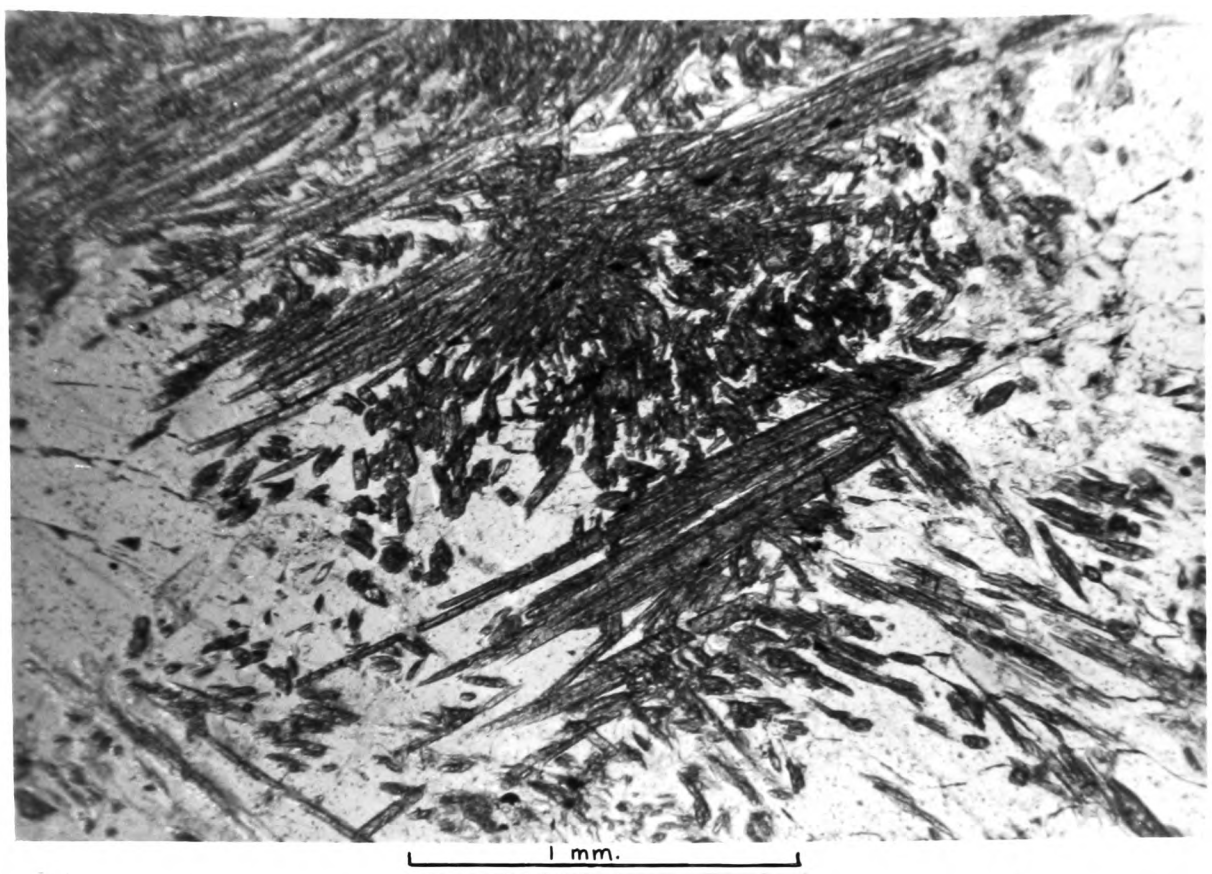



Fig. 4.3 Garnet porphyroblast in Inner Schieferhülle mica-schist GD 465a, showing rounded Variscan core with inclusion trails, and Alpine rim. Euhedral Alpine staurolites cut across recrystallised muscovites.



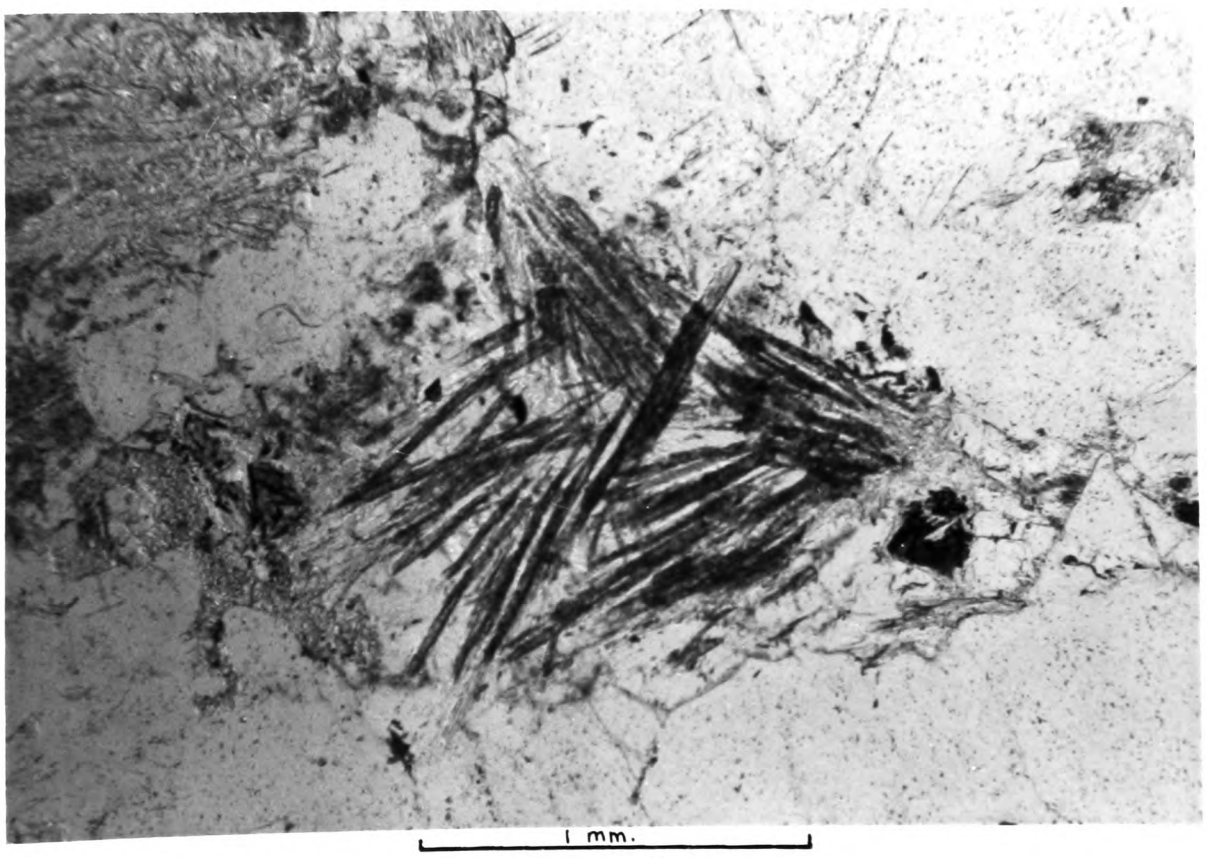
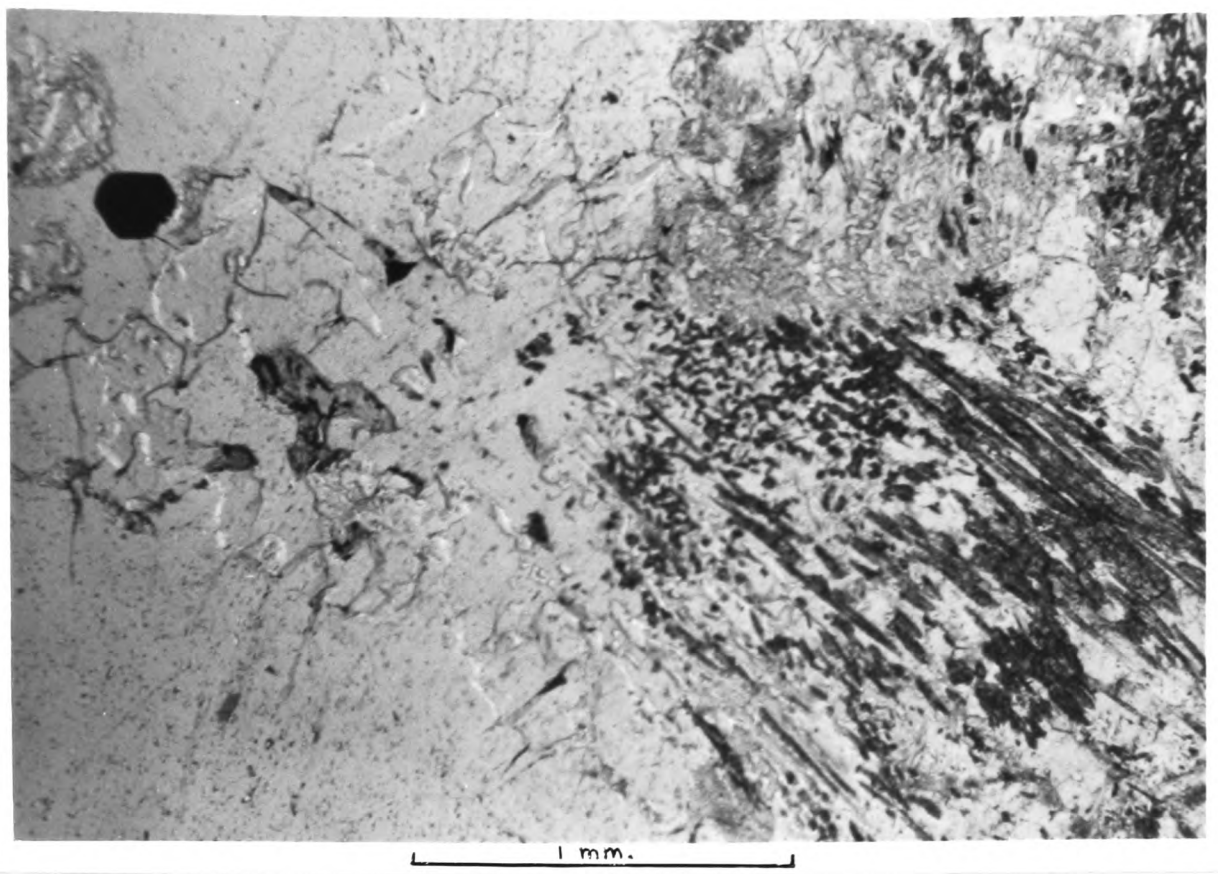




Fig. 4.4 Kyanite pseudomorphs after sillimanite in migmatitic mica-schist RN 247. Plane polarised light.



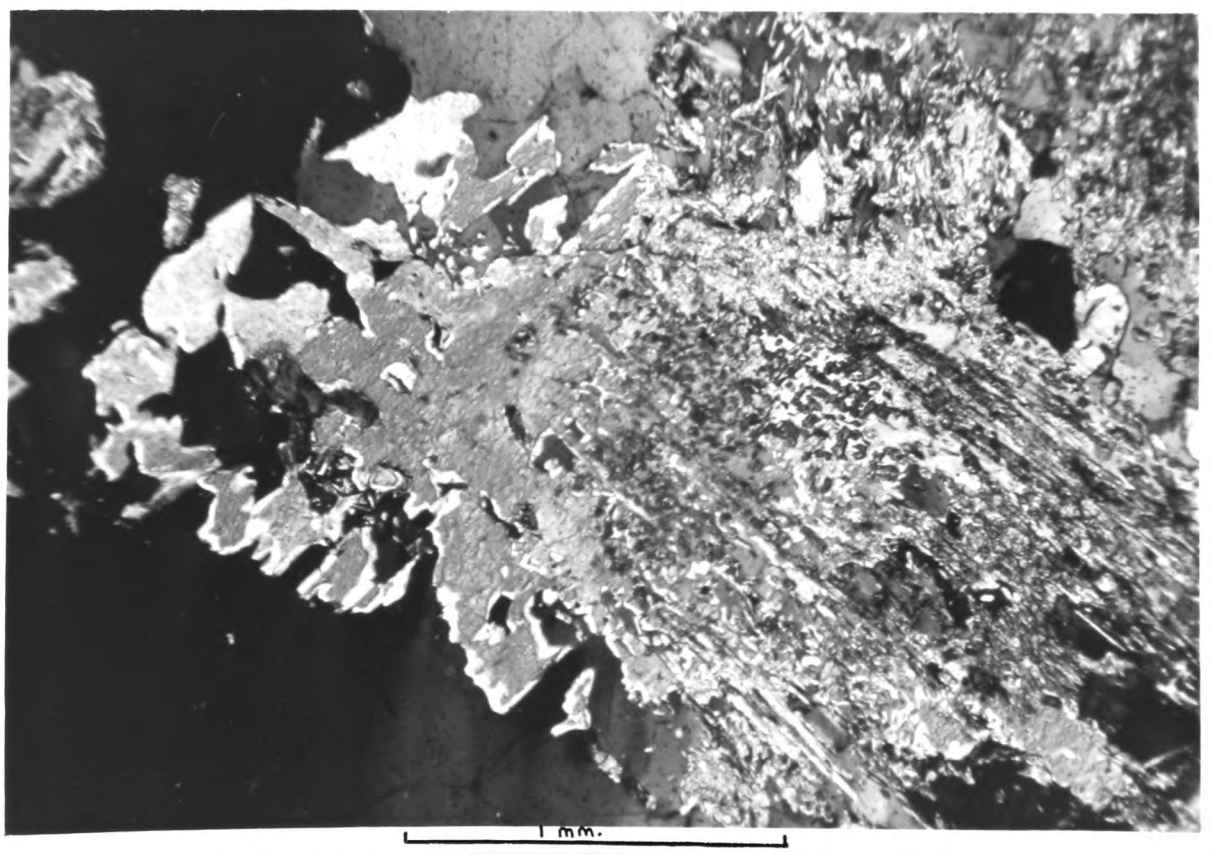




Fig. 4.5 Kyanite pseudomorphs after sillimanite in a large Variscan muscovite with a strongly embayed margin suggestive of partial melting. RN 247.

Above: Plane polarised light. Below: Crossed polars.




Fig. 4.6 Biotite in RN 247 showing vermiform texture possibly produced by partial melting. Plane polarised light.

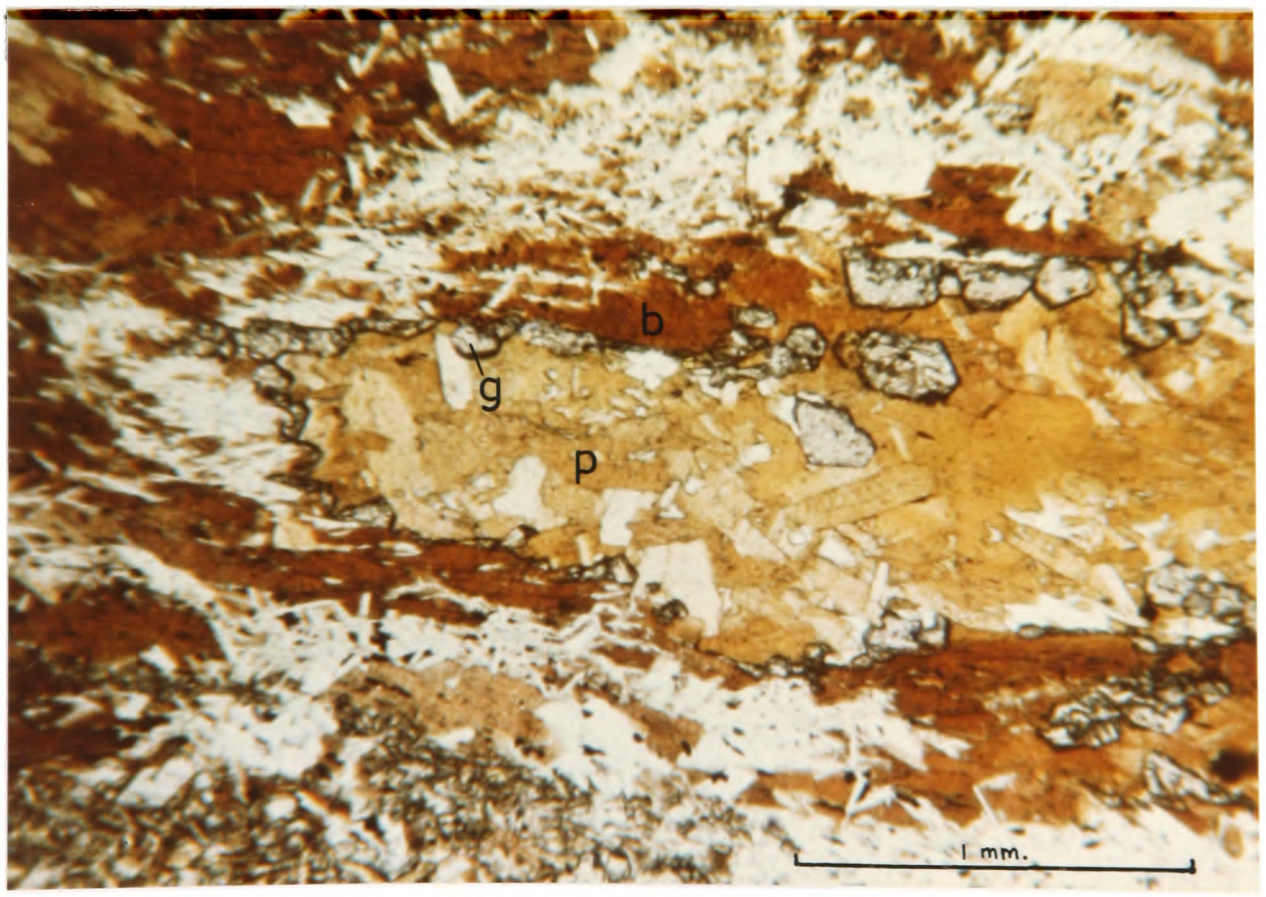



Fig. 4.7 Corona of garnets (g) surrounding a mosaic of recrystallised phlogopitic biotite (p) in migmatitic mica-schist GD 404. Matrix biotites (b) are more iron-rich. Plane polarised light.

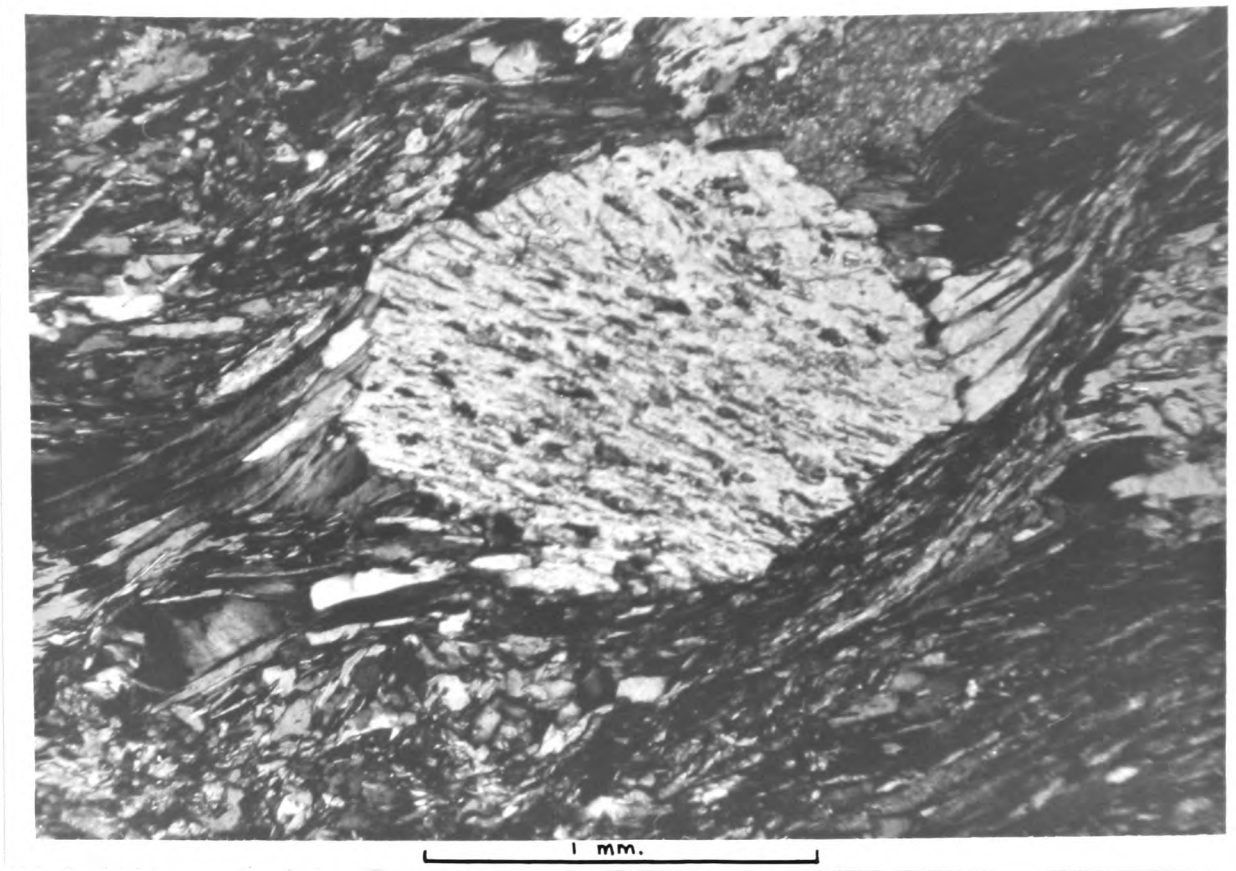



Fig. 4.8 Rotated post-$S_a^1$ albite porphyroblasts in greenschist GD 551. Crossed polars.

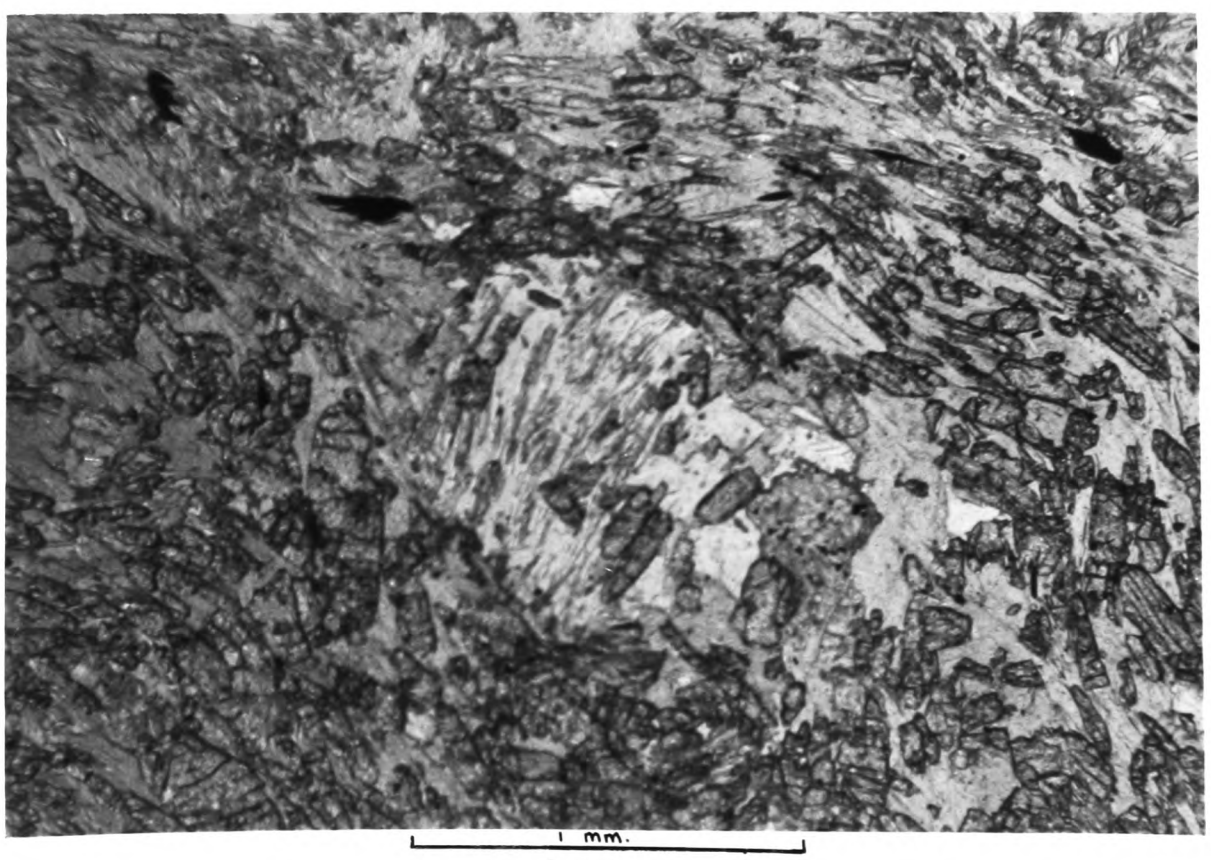



Fig. 4.9 Rotated post-$S_a^1$ albite porphyroblast enclosing aligned actinolite and epidote prisms. Greenschist GD 230i. Plane polarised light.

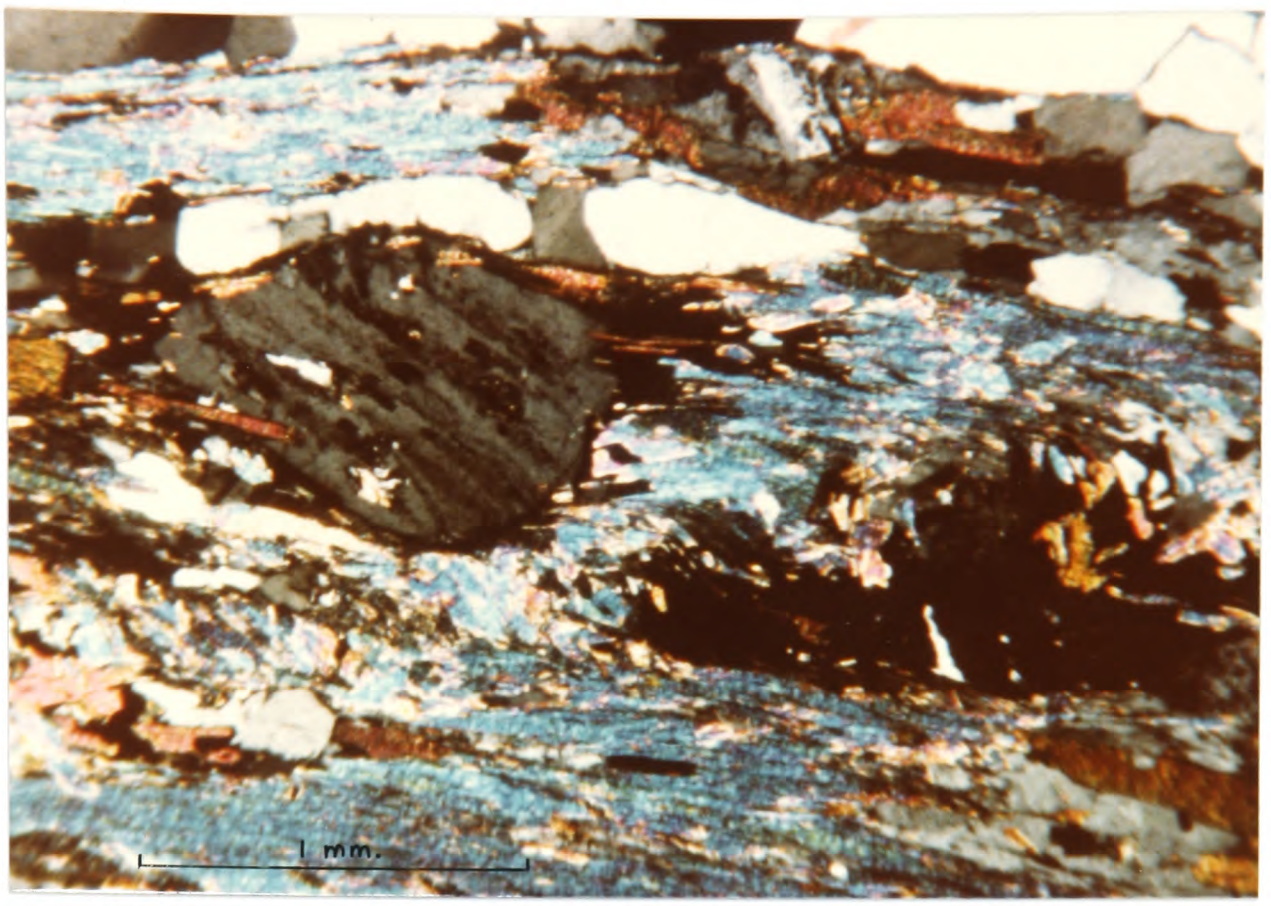



Fig. 4.10 Rotated post-$S_a^1$ albite porphyroblast (nearly in extinction), with ragged rim of oligoclase (in extinction, and in optical continuity with an adjacent patch) replacing muscovite aligned in $S_a^2$. Pelitic mica-schist GD 365. Crossed polars.

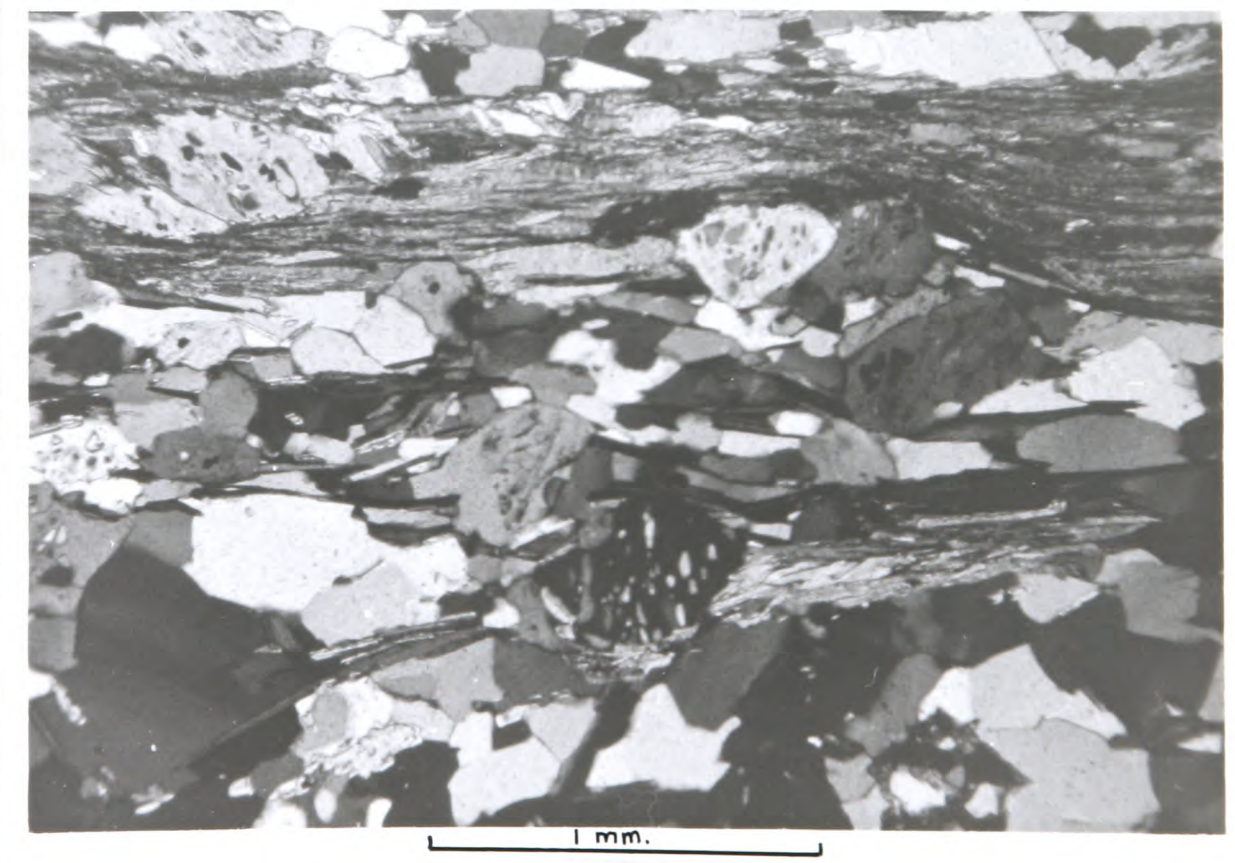
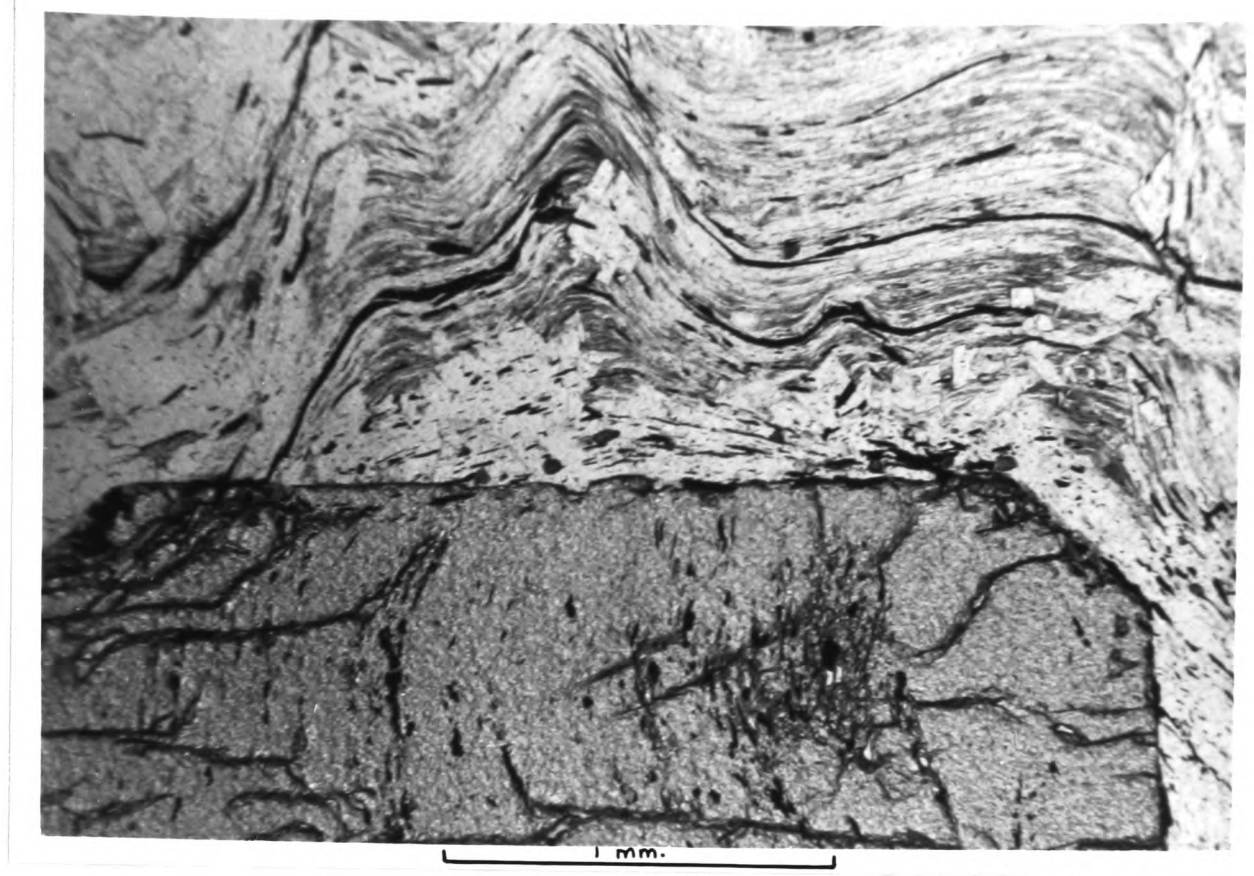



Fig. 4.11 Rotated post-$S_a^1$ albite porphyroblast. Pelitic mica-schist GD 479. Crossed polars.



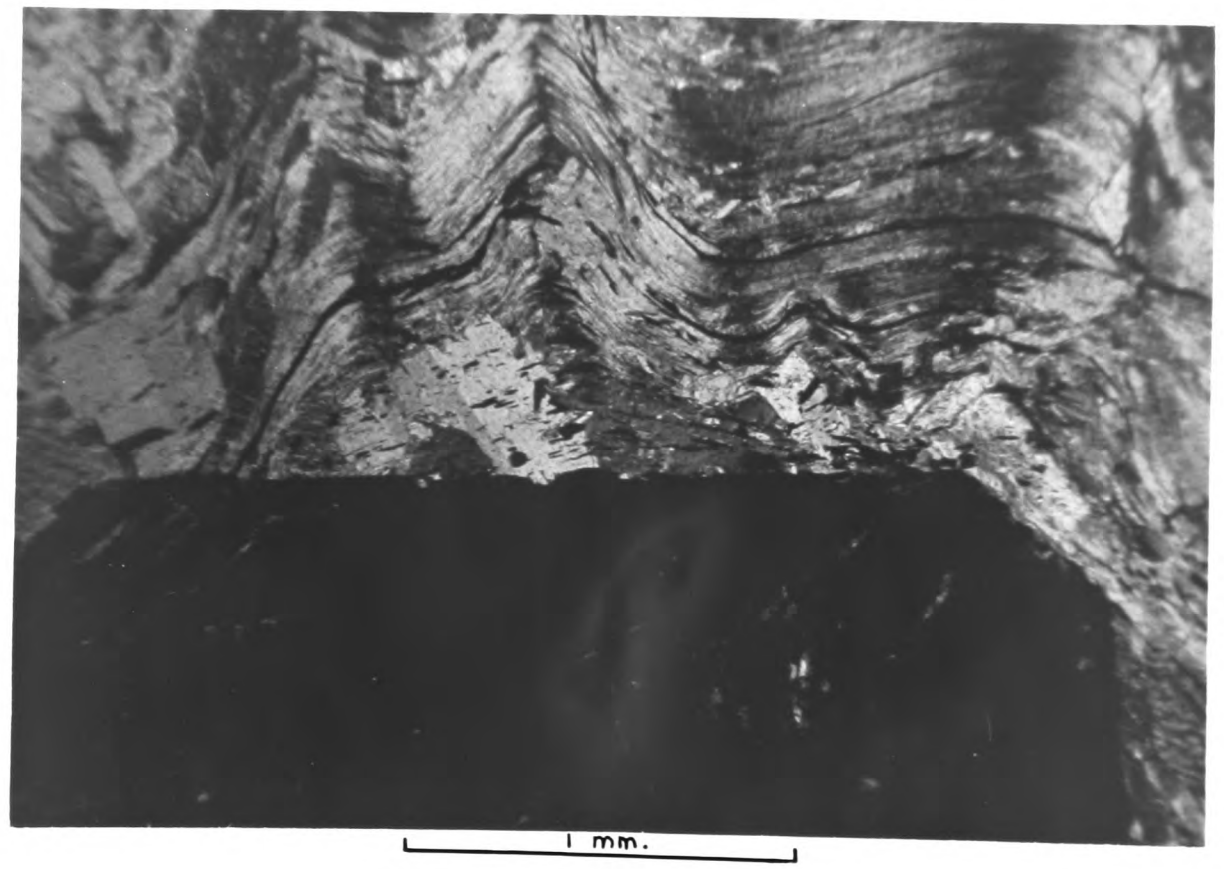




Fig. 4.12 Euhedral pre-$F_a^2$ garnet porphyroblast set in a matrix of muscovite mostly aligned in $S_a^1$ and folded by $F_a^2$. Pelitic mica-schist GD 561.

**Above: Plane polarised light. Below: Crossed polars.**

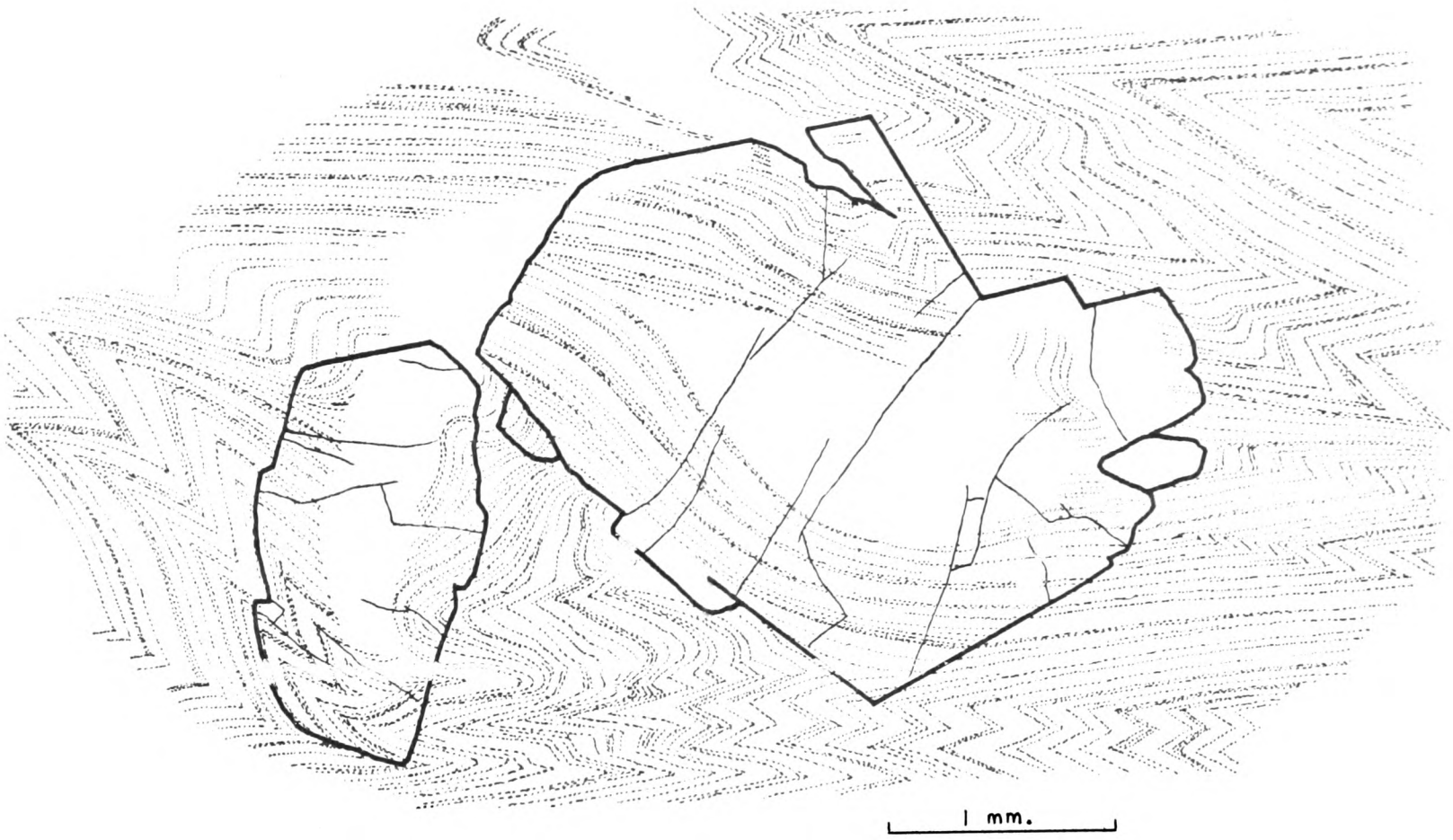



Fig. 4.13 Garnet porphyroblast in graphitic mica-schist GD 202 with inclusion-free pre-$F_a^2$ cores and inclusion-rich post $F_a^2$ rims.

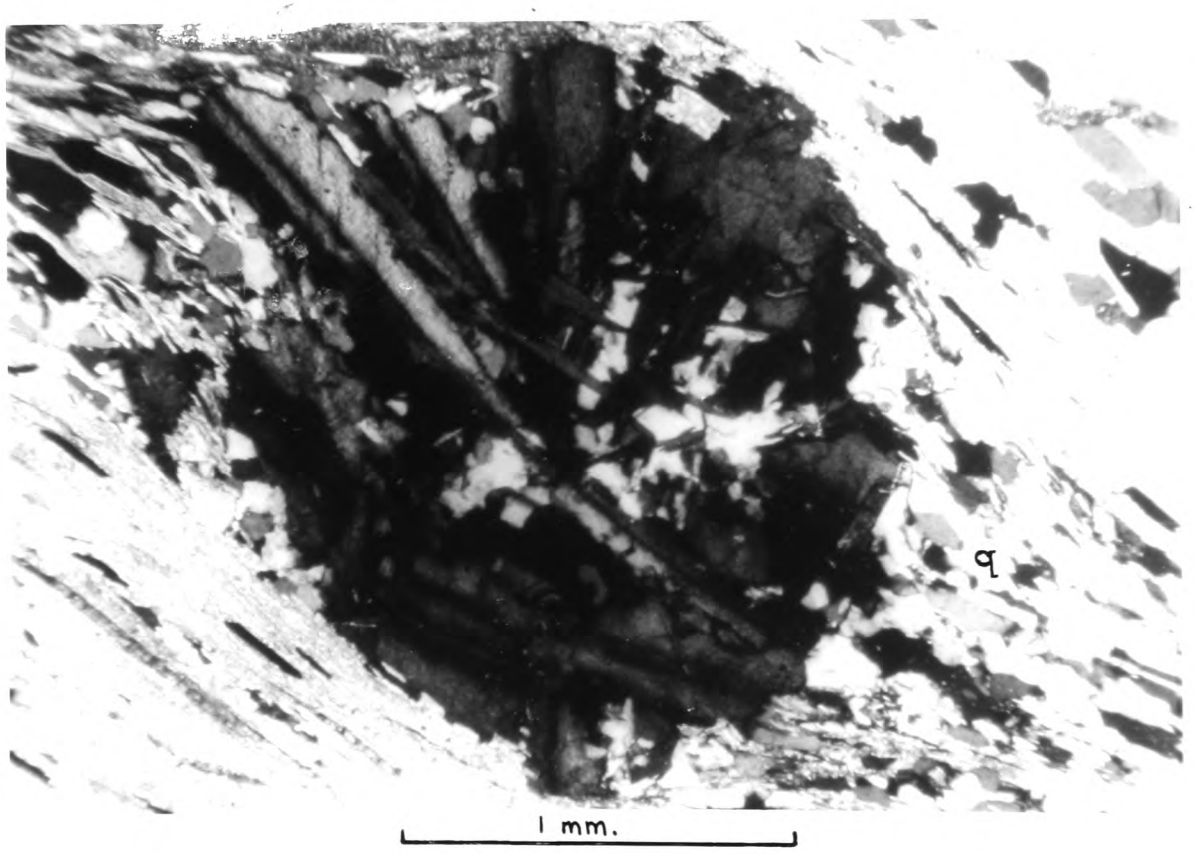



Fig. 4.14 Spherical aggregate of chloritoid + chlorite, possibly pseudomorphing garnet, in pelitic mica-schist GD 496. $S_a^2$ schistosity has been deflected round the ? pseudomorph and quartz pressure-shadows (q) have formed.

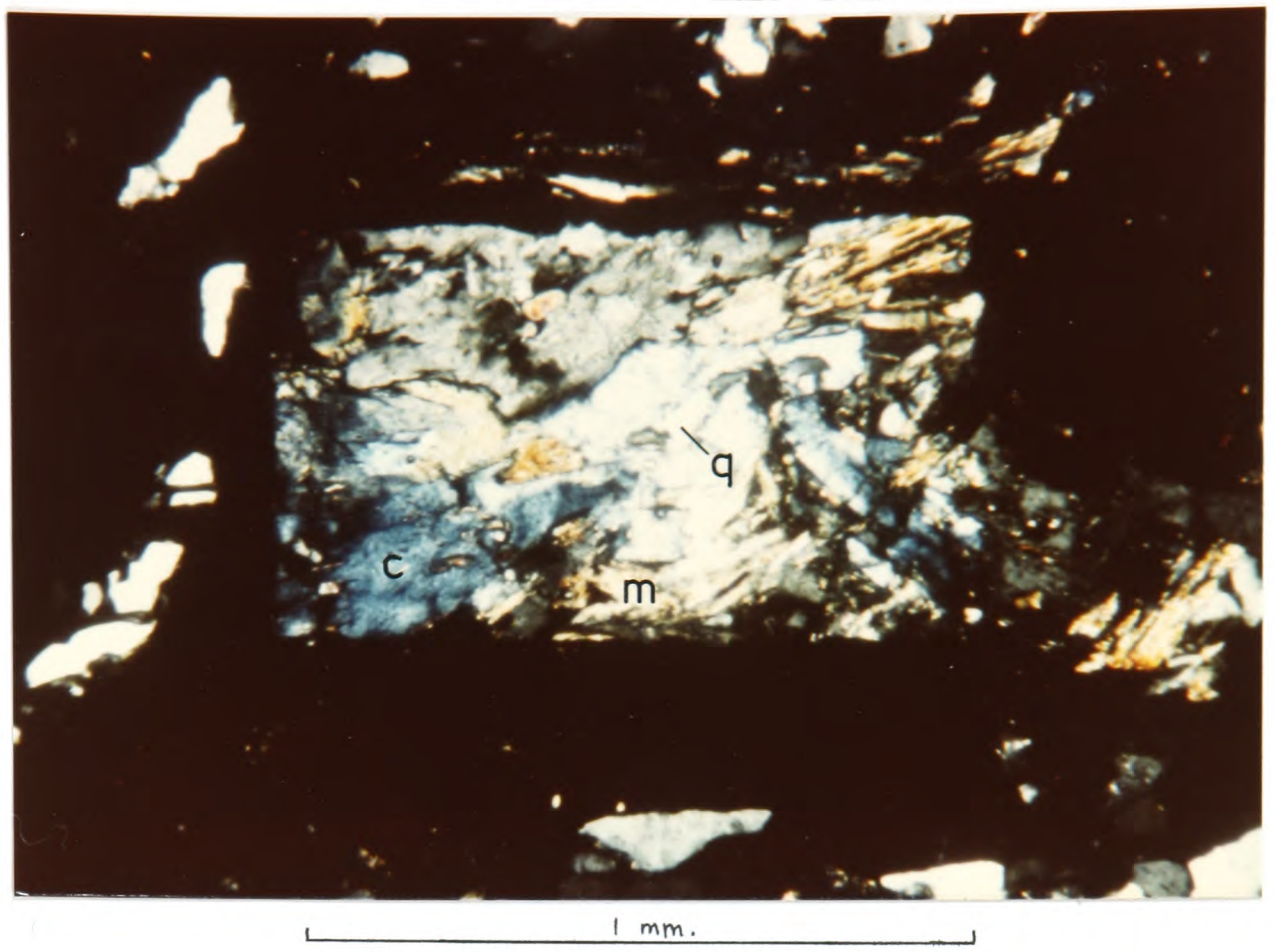



Fig. 4.15 Pseudomorph of clinozoisite (c), margarite (m) and quartz (q) after lawsonite in garnet (isotropic). GD 49. Crossed polars.

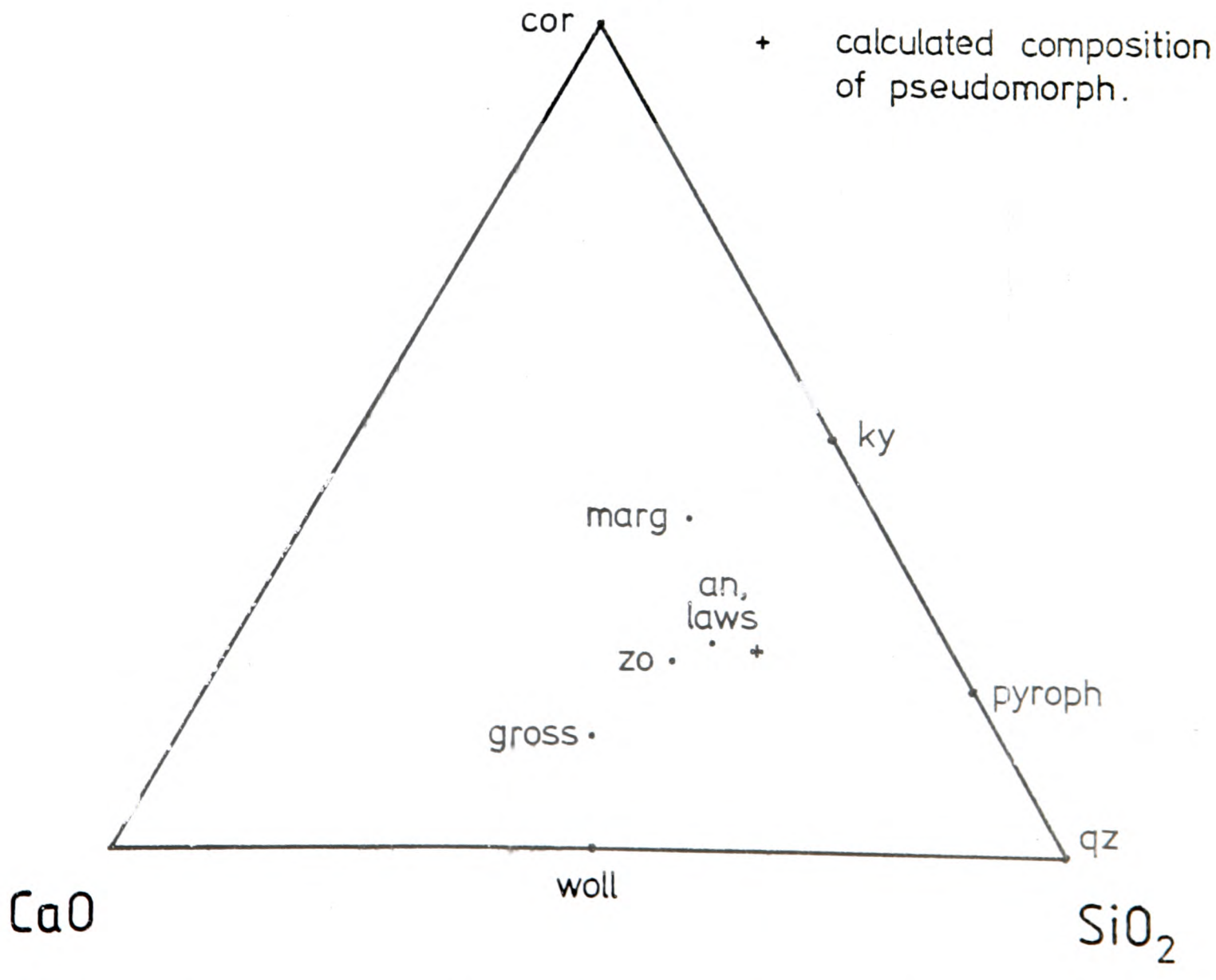



Fig. 4.16 Calculated chemical composition of the lawsonite-pseudomorph plotted in ternary $CaO$-$Al_2O_3$-$SiO_2$.

Table 4.2 Calculated modal and chemical composition of the lawsonite-pseudomorph in GD 49.

| | V. (cal/bar) | mode % | mole % | Proportional molar composition (anhydrous) | | |
|---|---|---|---|---|---|---|
| | | | | CaO | $Al_2O_3$ | $SiO_2$ |
| Margarite | 3.1093 | 0.402 | 0.336 | 0.067 | 0.134 | 0.134 |
| Clinozoisite | 3.2557 | 0.480 | 0.383 | 0.118 | 0.088 | 0.177 |
| Anorthite | 2.4043 | 0.076 | 0.083 | 0.021 | 0.021 | 0.042 |
| Quartz | 0.5412 | 0.041 | 0.198 | 0 | 0 | 0.198 |
| Pseudomorph | - | - | - | 0.206 | 0.243 | 0.551 |

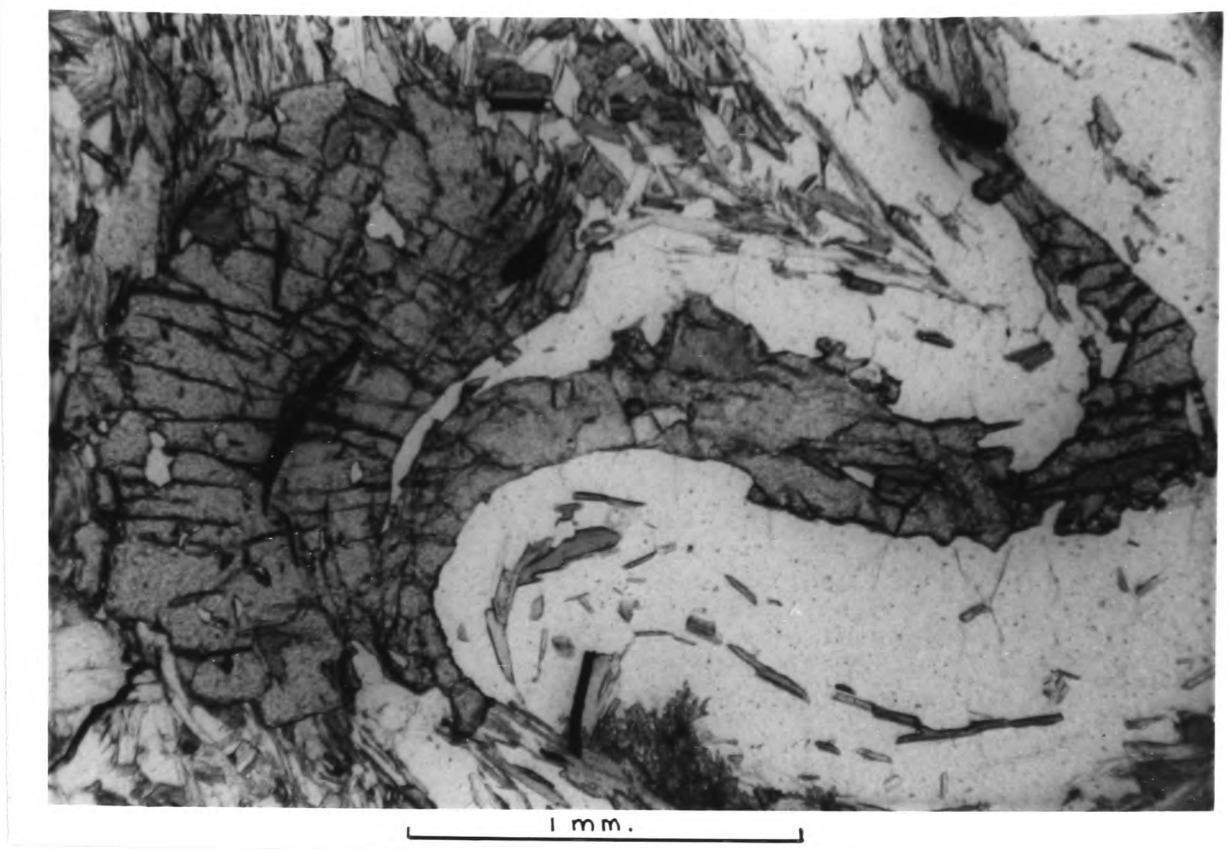



Fig. 4.17 Sigmoidal garnet in pelitic mica-schist GD 572. Plane polarised light.

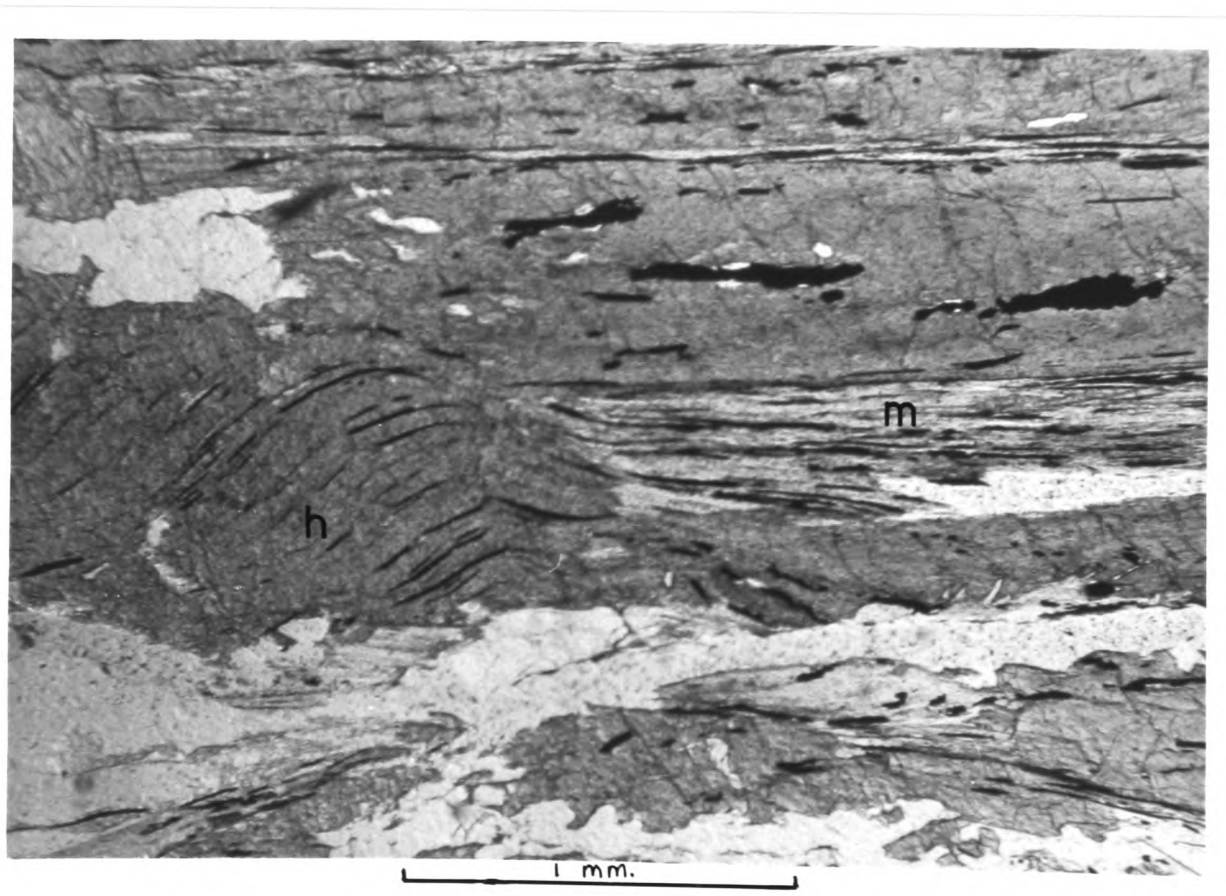
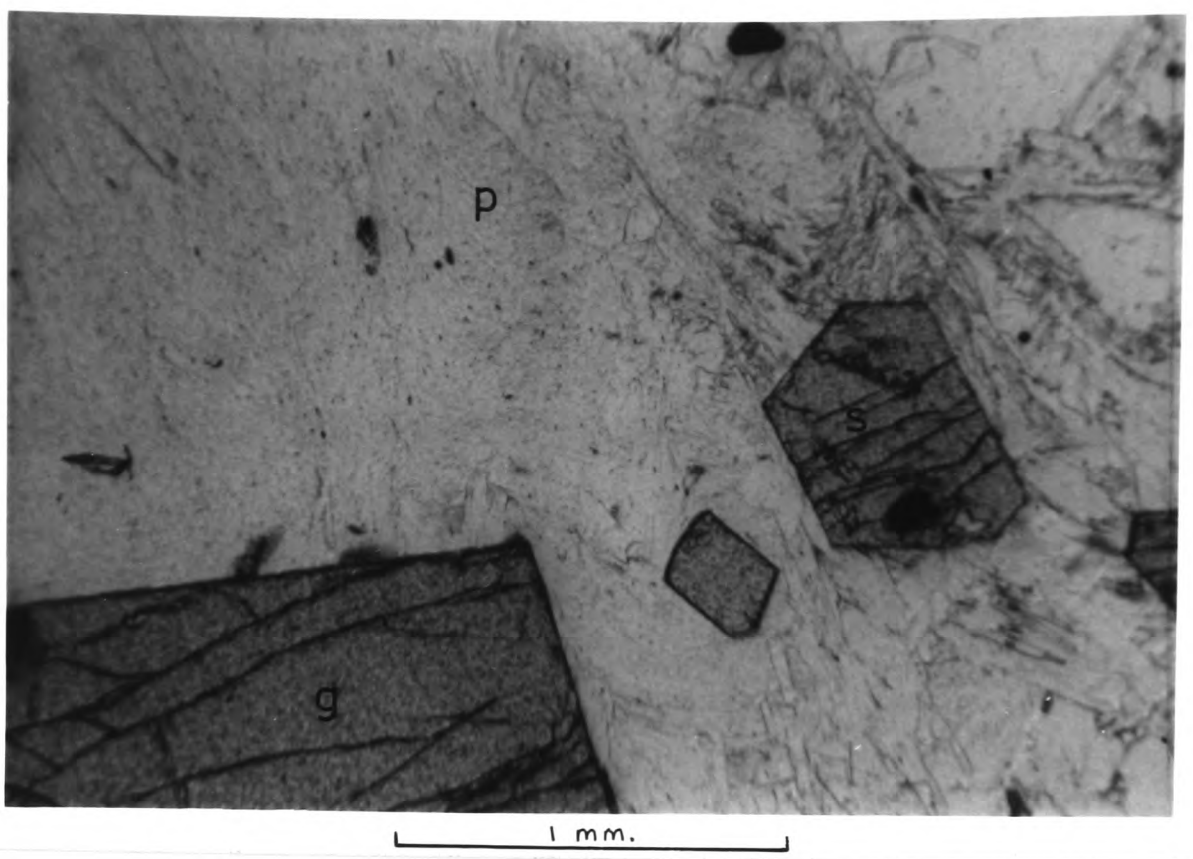



Fig. 4.18 Rolled hornblende (h) and schistose margarite (m) enclosing aligned ilmenite plates in garbenschiefer GD 480. Plane polarised light.



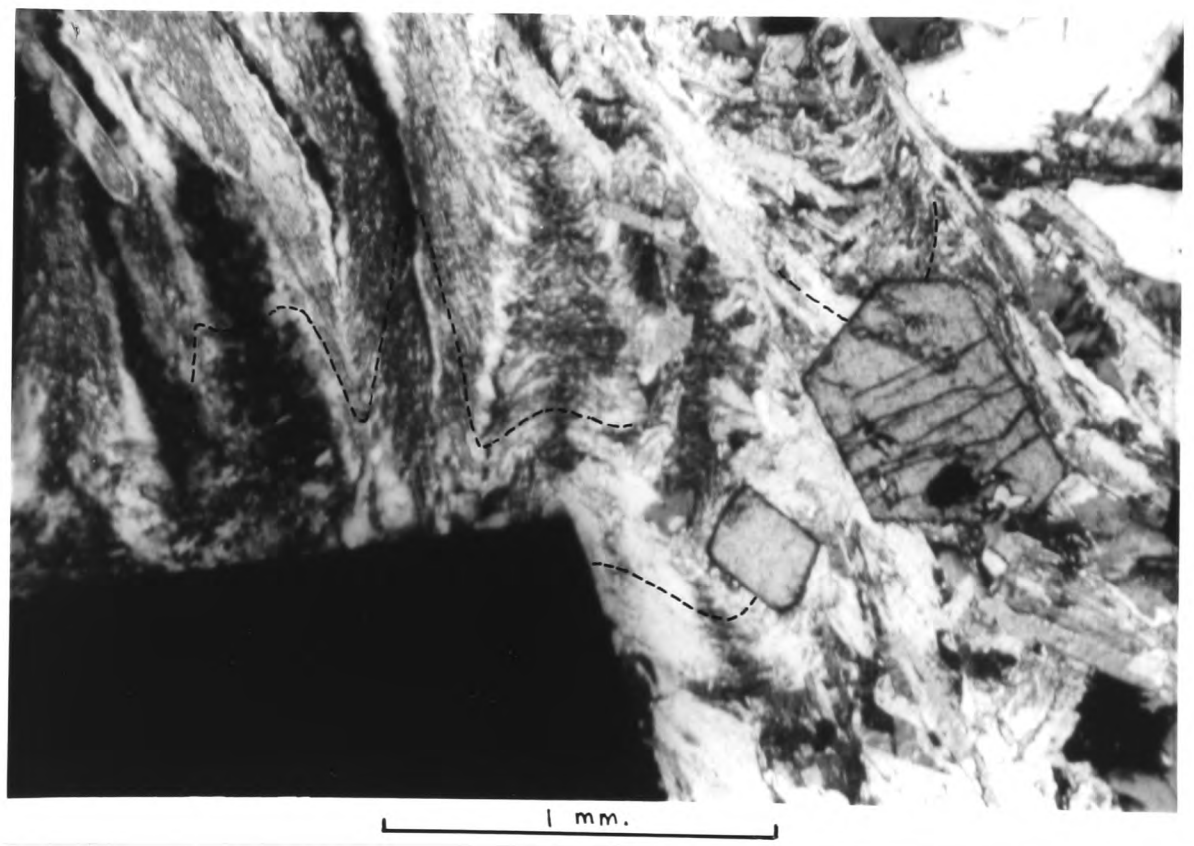




Fig. 4.19 Euhedral porphyroblasts of garnet (g) and staurolite (s) cutting across $F_a^2$ microfolds in fine-grained paragonite (p). Pelitic mica-schist GD 18.

Above: Plane polarised light. Below: Crossed polars.

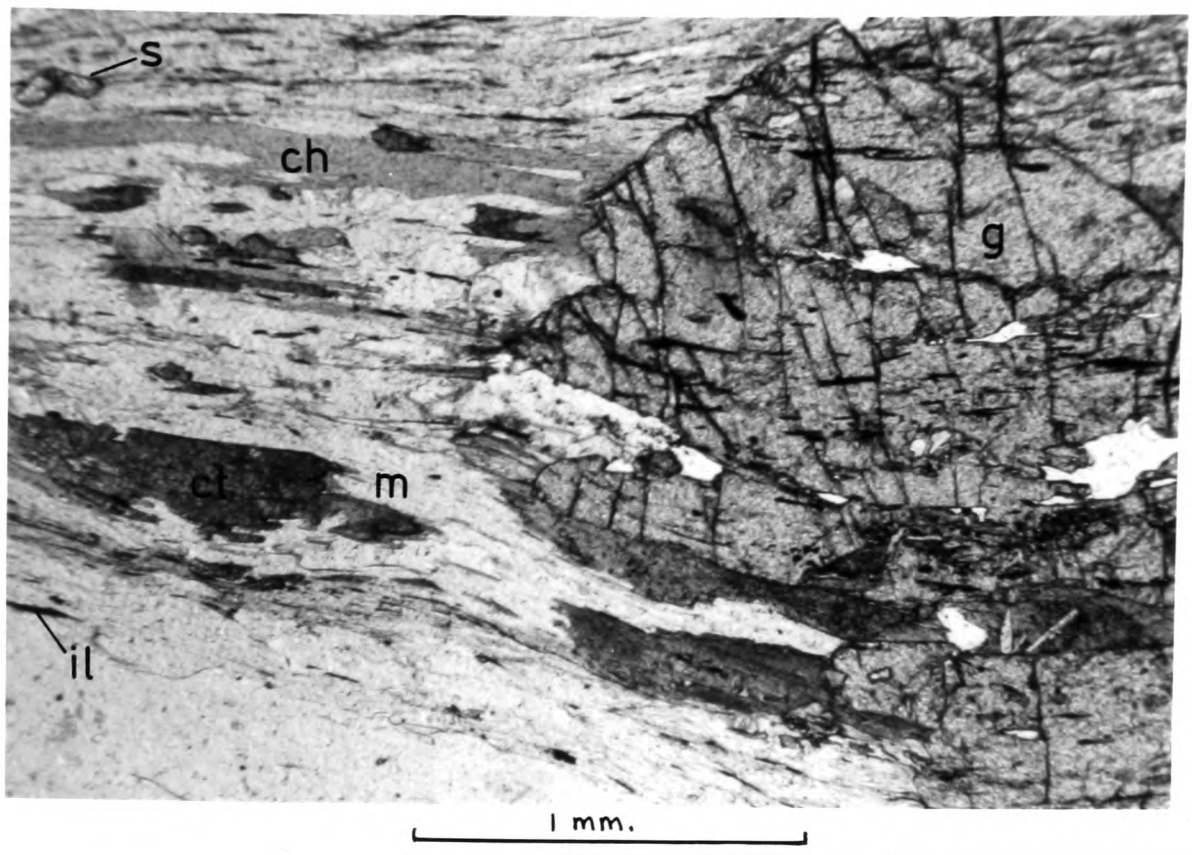



Fig. 4.20 Porphyroblasts of garnet (g) and knee-twinned staurolite (s) cutting across an $S_a^2$ schistosity defined by chloritoid (ct), chlorite (ch), muscovite (m) and ilmenite (il) in pelitic mica-schist GD 43b. Plane polarised light.

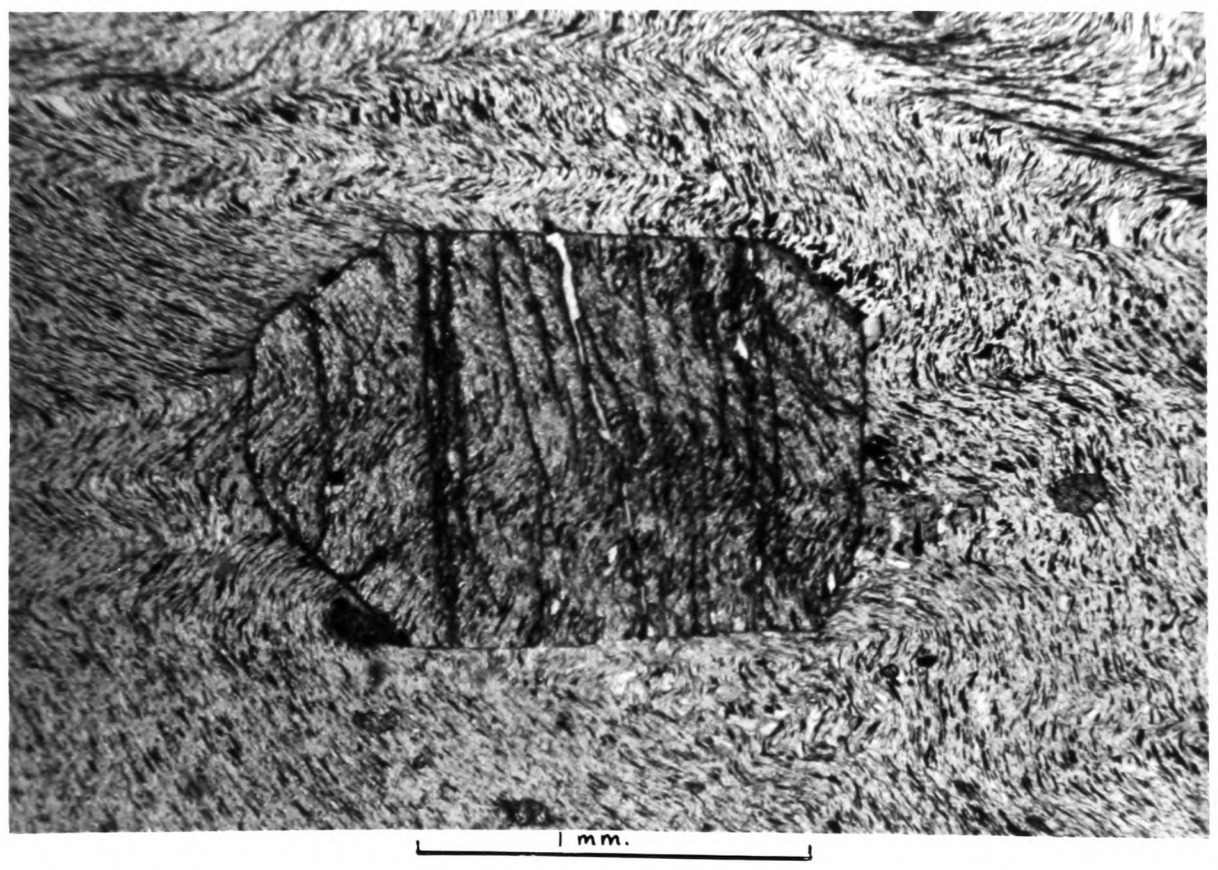



Fig. 4.21 Euhedral garnet porphyroblast overgrowing a crenulated $S_a^1$ muscovite + ? ilmenite fabric in pelitic mica-schist GD 492. Plane polarised light.

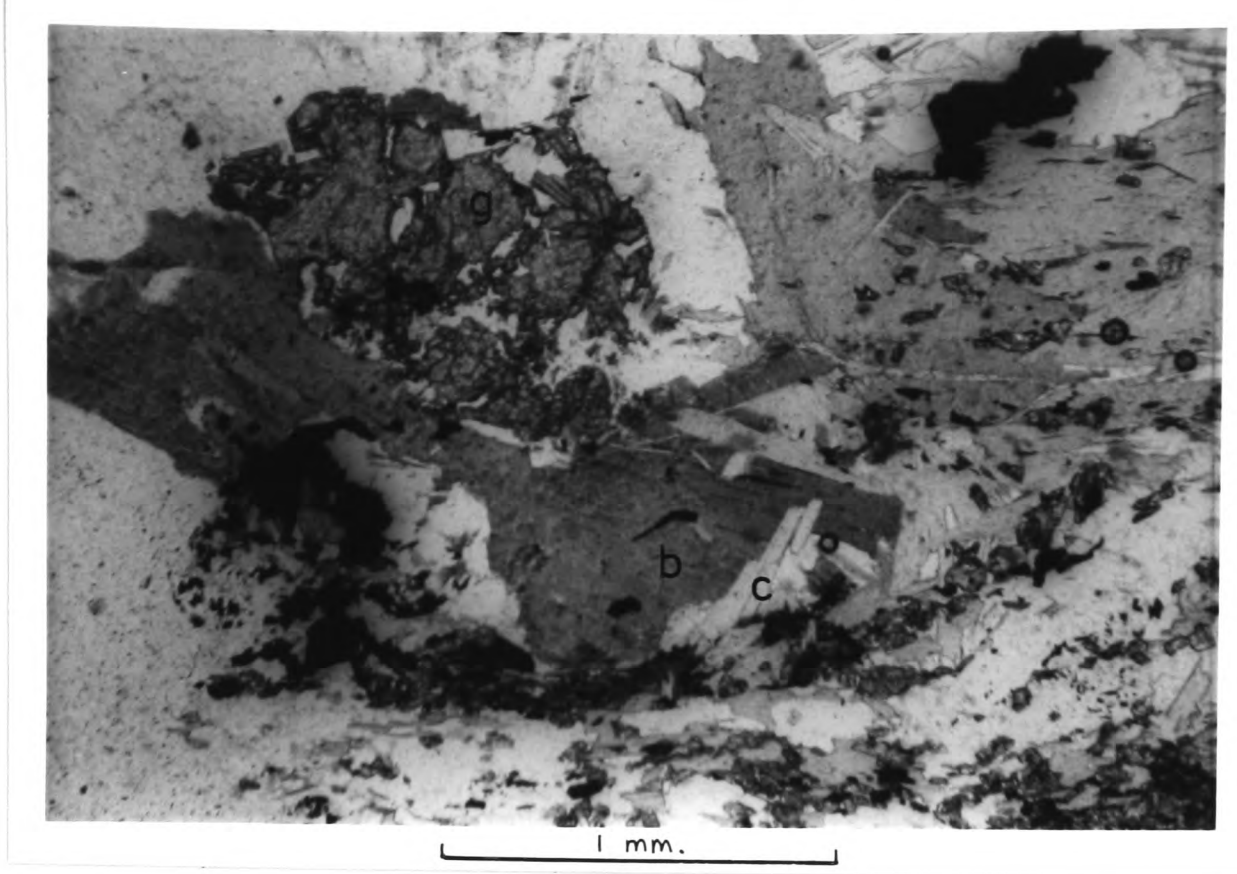



Fig. 4.22 Interlocking flakes of biotite (b) and chlorite (c) with corroded garnet (g) in pelitic mica-schist GD 43a. Plane polarised light.

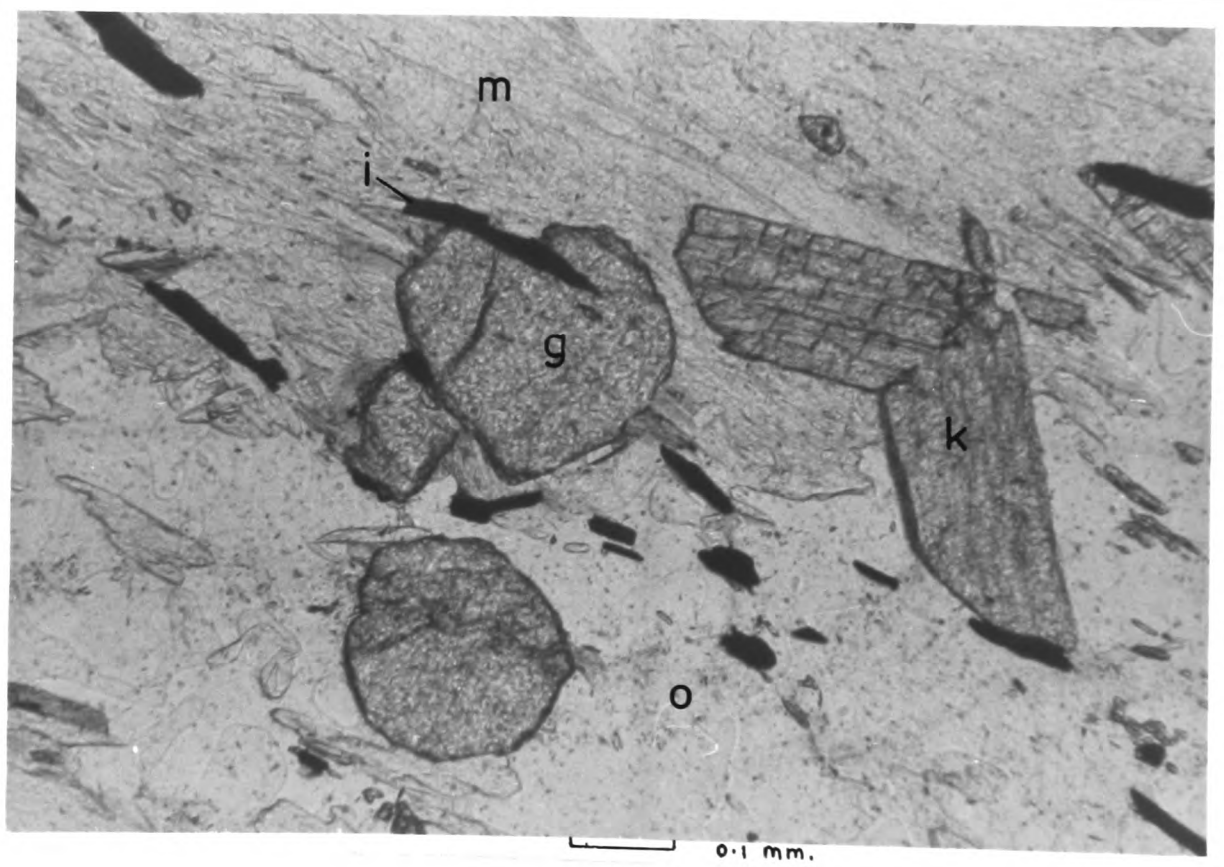
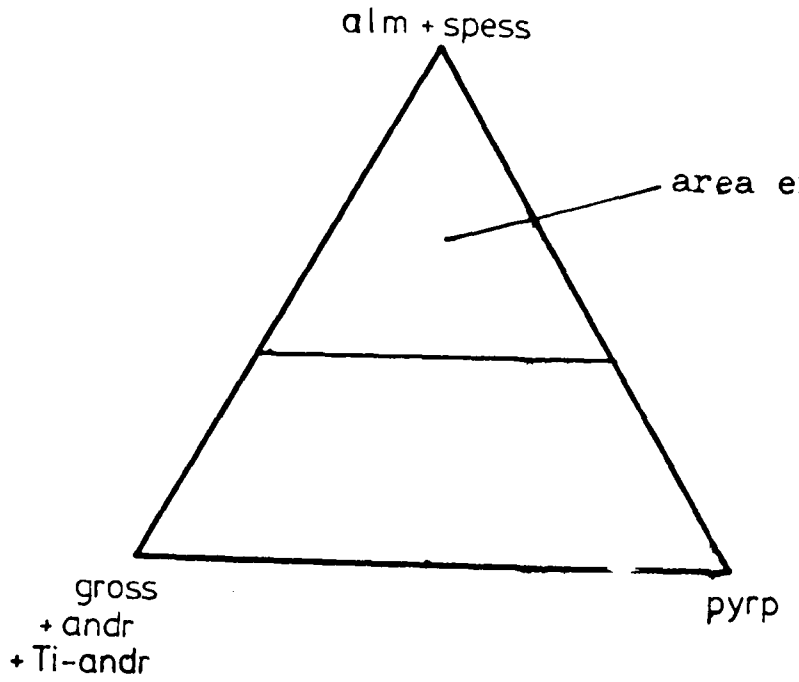



Fig. 4.23 "Pin-prick" garnets (g) and butterfly-twinned kyanite (k) overgrow an $S_a^2$ schistosity defined by muscovite (m) and ilmenite (i), but are themselves enclosed by a large patch of oligoclase (o) which has replaced some of the mica. GD 208d. Plane polarised light.

Table 4.3 Synopsis of the metamorphic history of the south-east Tauern, as exemplified by pelitic and basic rocks.

| EVENT | | INNER SCHIEFERHÜLLE | | PERIPHERAL SCHIEFERHÜLLE | |
|---|---|---|---|---|---|
| | | METABASITES | METAPELITES | METABASITES | METAPELITES |
| $D_a^3$ | | Retrogressive CHL. | Sprays of CHL Large PLAG porphyroblasts. | | Retrogressive CHL. PLAG porphyroblasts and rims. |
| | | | | PLAG rims on AB. | |
| ~35my. | REGIONAL $M_a$ PEAK | Some HBL, EP, BIOT, PLAG (range $An_0$-$An_{70}$). GT in leucoamphibolites only. | Cross-cutting ST, KY. Decussate MUSC, BIOT, PARAG. SILL pseudomorphed by KY. "Pinprick" GT. | Granular PLAG. Decussate HBL. HBL rims on ACT? | Cross-cutting porphyroblast of GT, CTD, BIOT, ST, KY. Recrystallise MICAS and QZ. |
| $D_a^2$ | | | Schistose MUSC, BIOT, ILM, PARAG. | Schistose HBL, CHL, EP, BIOT. HBL rims on ACT? | Sigmoidal GT. Axial planar MICAS, CHL, CTD. |
| $D_a^1$ ~65my. | | AB porphyroblasts (Randgneis only). Retrogressive CHL. (Randgneis only.) | Schistose MUSC, BIOT, CHL (Randgneis only). | AB porphyroblasts. ACT, CHL, EP. | GT, AB porphyroblasts. LAWSONITE? Schistose MICAS, CHL, CTD. LAWSONITE? |
| Deposition of Peripheral Schieferhülle | | | | | |
| Intrusion of Zentralgneis ~280my. | CONTACT $M_z$ | Effects not recognised. | BIOT, MUSC digested by melt. BIOT, MUSC rimmed by GT in remaining schist. MUSC broken down to SILL. | | |
| $D_v$ | REGIONAL $M_v$ | HBL porphyroblasts in garnet-free rocks. Garnet-amphibolite assemblage: $GT_2$ + HBL + PLAG? $CPX_2$ + PLAG symplectite. | Cores of large GT. Large MUSC, BIOT. Some KY, ST. | | |
| ?$D_e$ | REGIONAL $M_e$ | Eclogitic assemblage: $GT_1$ + CPX + RUT + QZ. | Effects not recognised. | | |




- • $M_e$ garnets, GD 136a.
- ▫ Inner rims of $M_v$ garnet coronas.
- ○ Outer rims of $M_v$ garnets.
- \+ $M_a$ garnet, GD 122

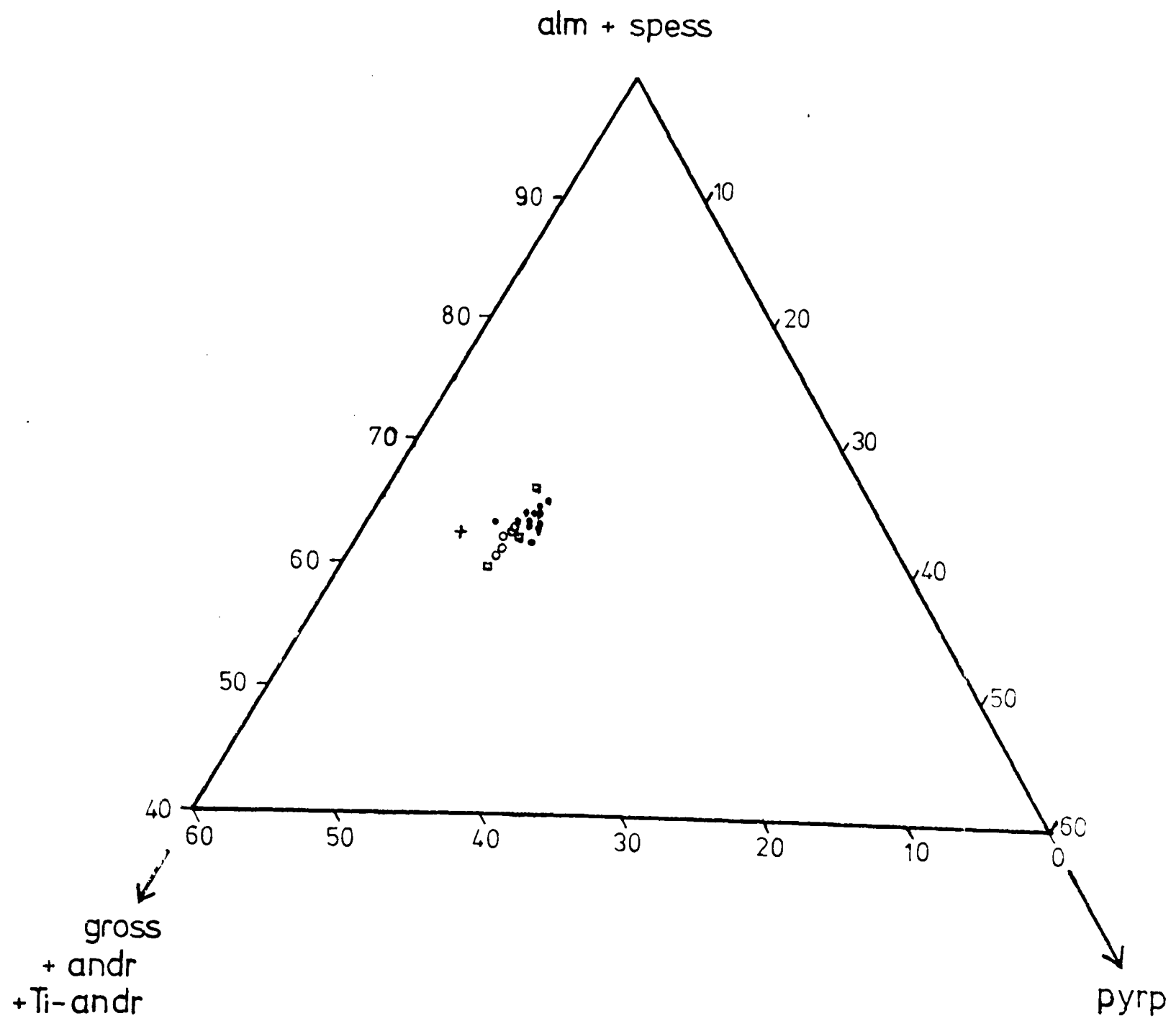



Fig. 5.1 Compositions of garnets from Inner Schieferhulle eclogitic amphibolites.

+ $M_a$ garnets, feldspathic paragneiss GD 145a.

o $M_v$ garnets )
) mica-schist GD 209b.
• $M_a$ garnets )

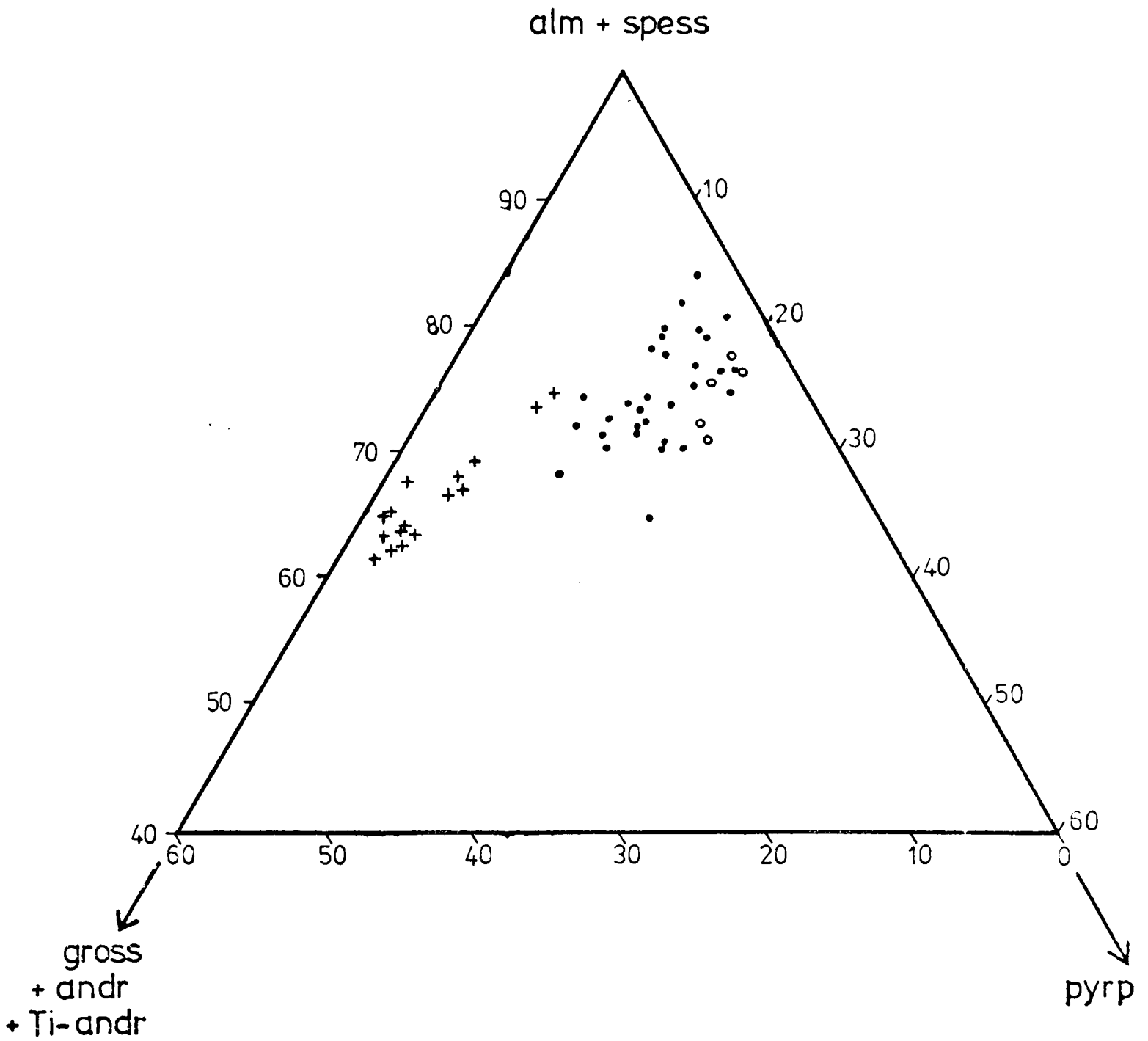



Fig. 5.2 Compositions of garnets from Inner Schieferhülle metasediments.

- • Pelitic mica-schists.
- o Hornblende-garbenschiefer GD 480a.
- \+ Coarse-grained chloritoid-schist GD 821d.

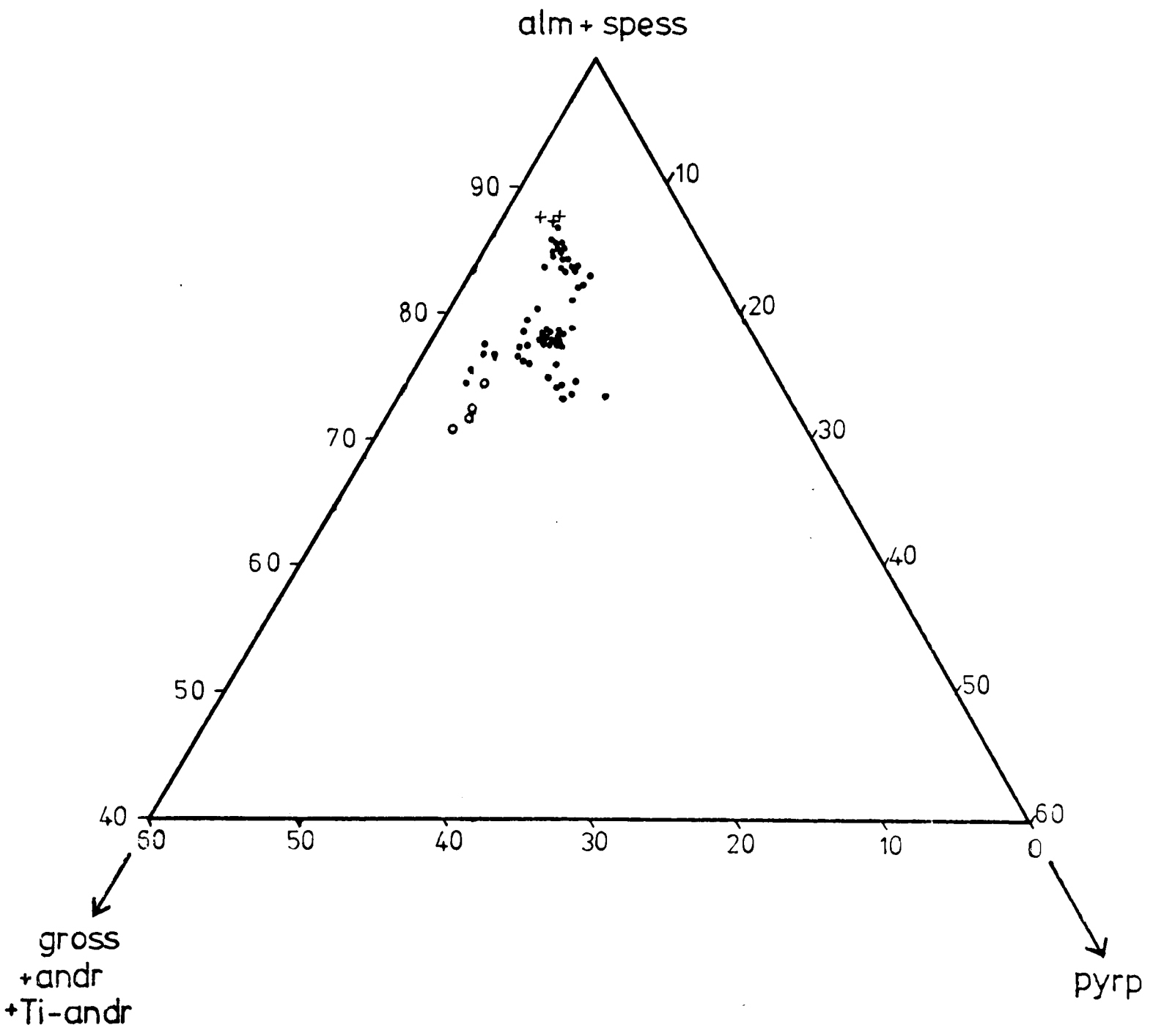



Fig. 5.3 Compositions of garnets from Peripheral Schieferhülle metasediments.

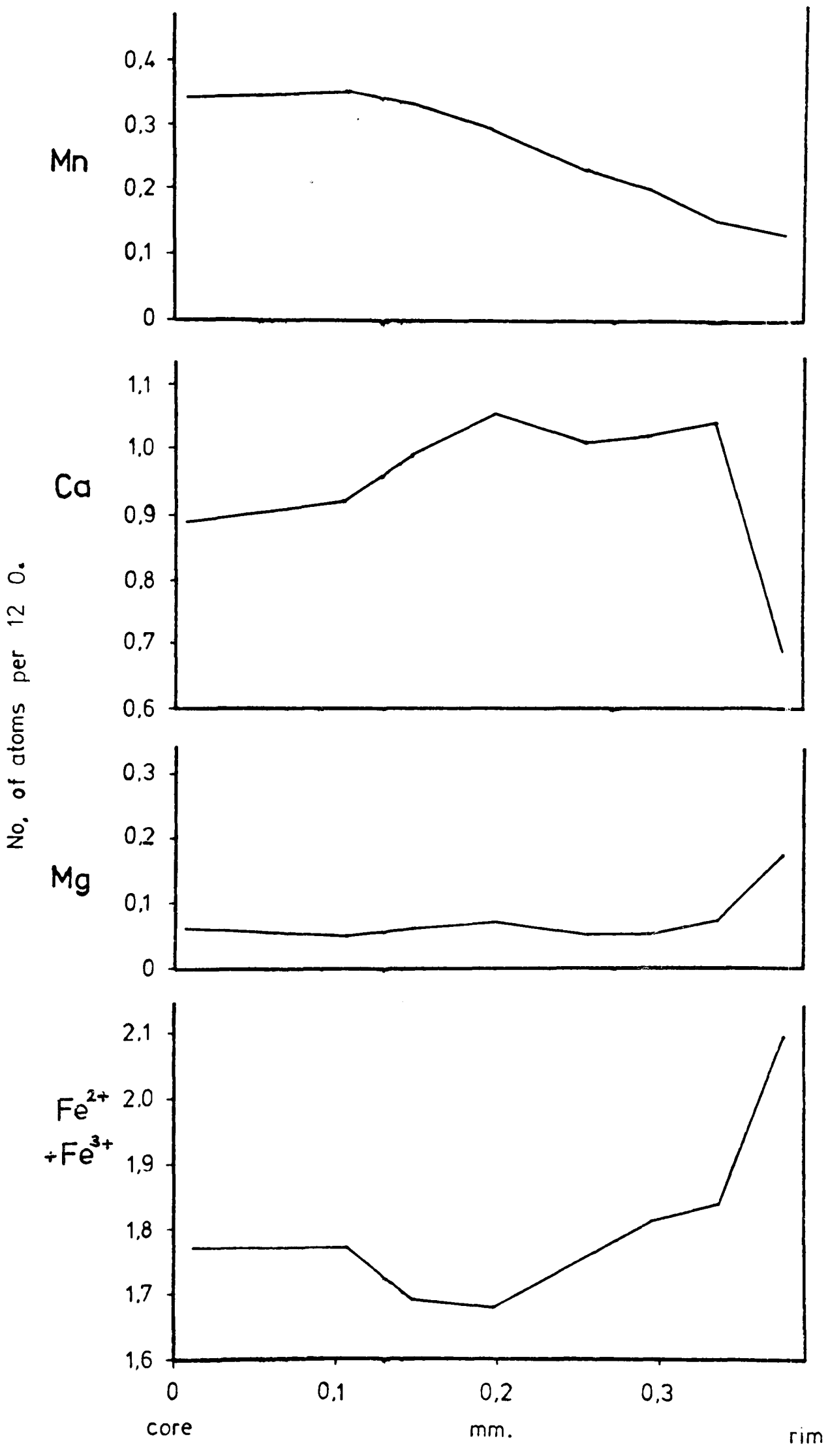



Fig. 5.4 Zoning half-profiles across an $M_a$ garnet in Inner Schieferhülle paragneiss GD 145a.

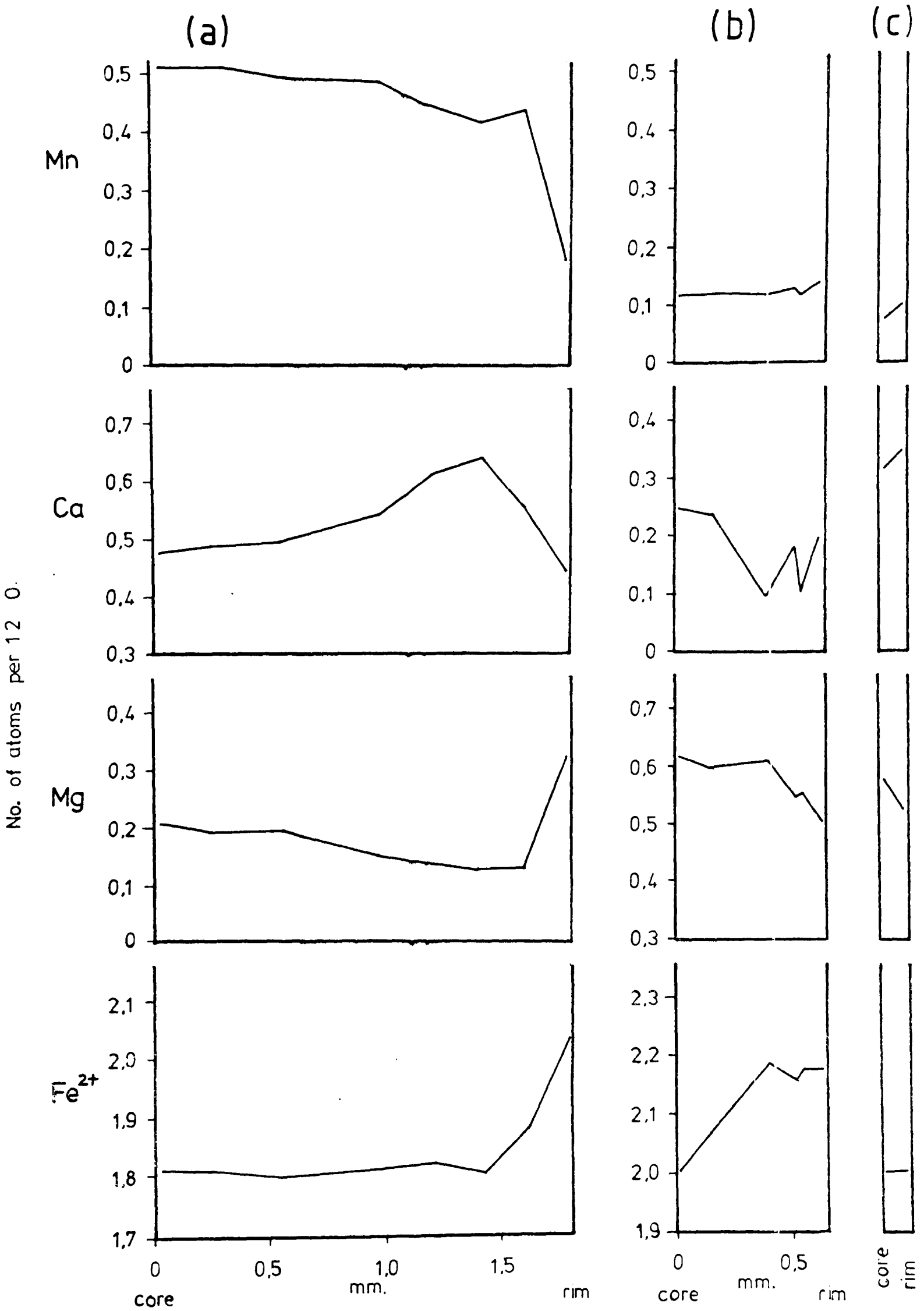



Fig. 5.5 Zoning half-profiles across three garnets: (a) $M_a$ garnet from Peripheral Schieferhülle pelite GD 18; (b) large $M_v$ garnet from Inner Schieferhülle aluminous pelite GD 209b; (c) "pin-prick" $M_a$ garnet from GD 209b. (b) and (c) have same vertical axes.

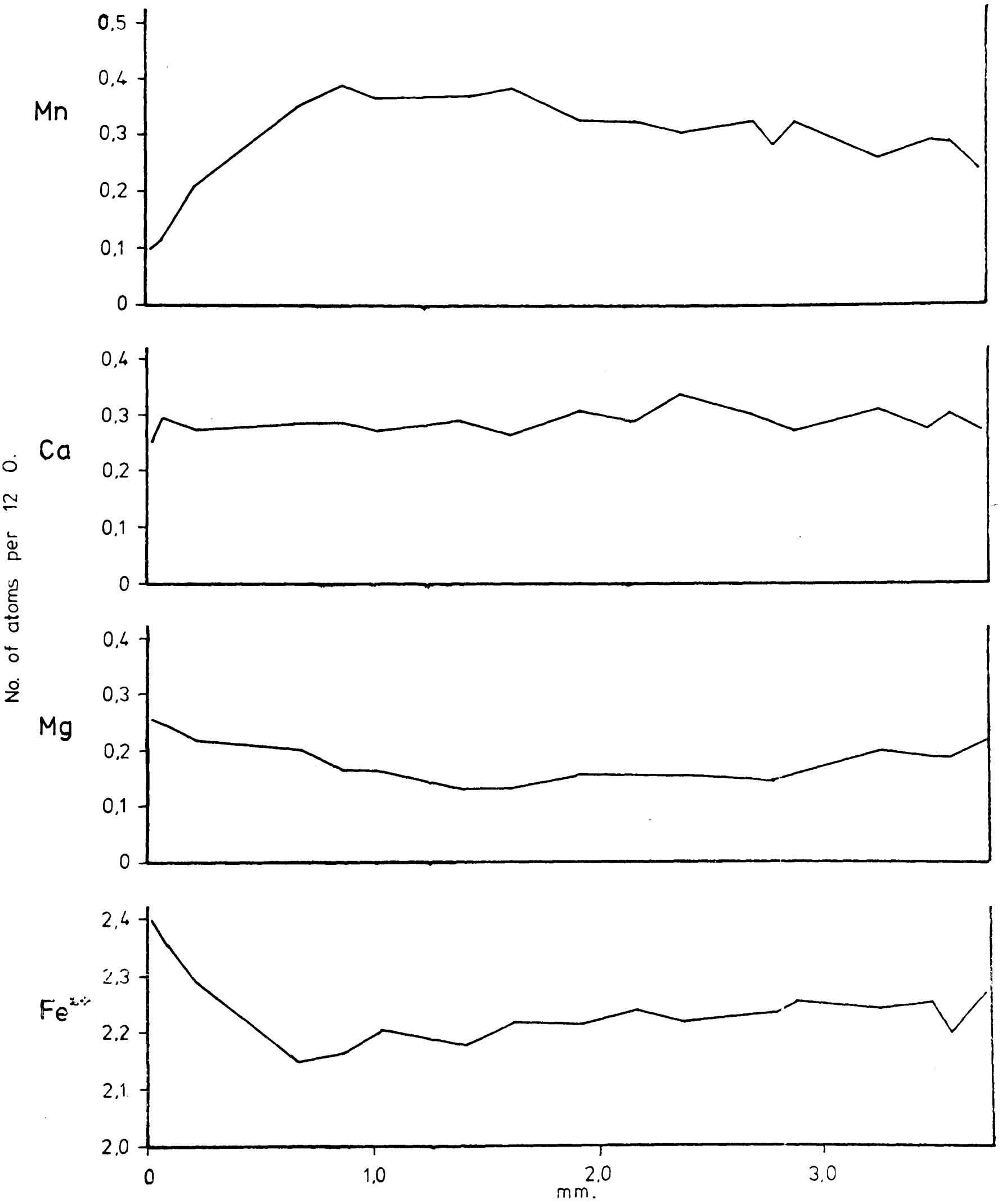



Fig. 5.6 Zoning profile across a post $S_a^2$ garnet in Peripheral Schieferhülle pelite GD 168b in a direction perpendicular to the schistosity.

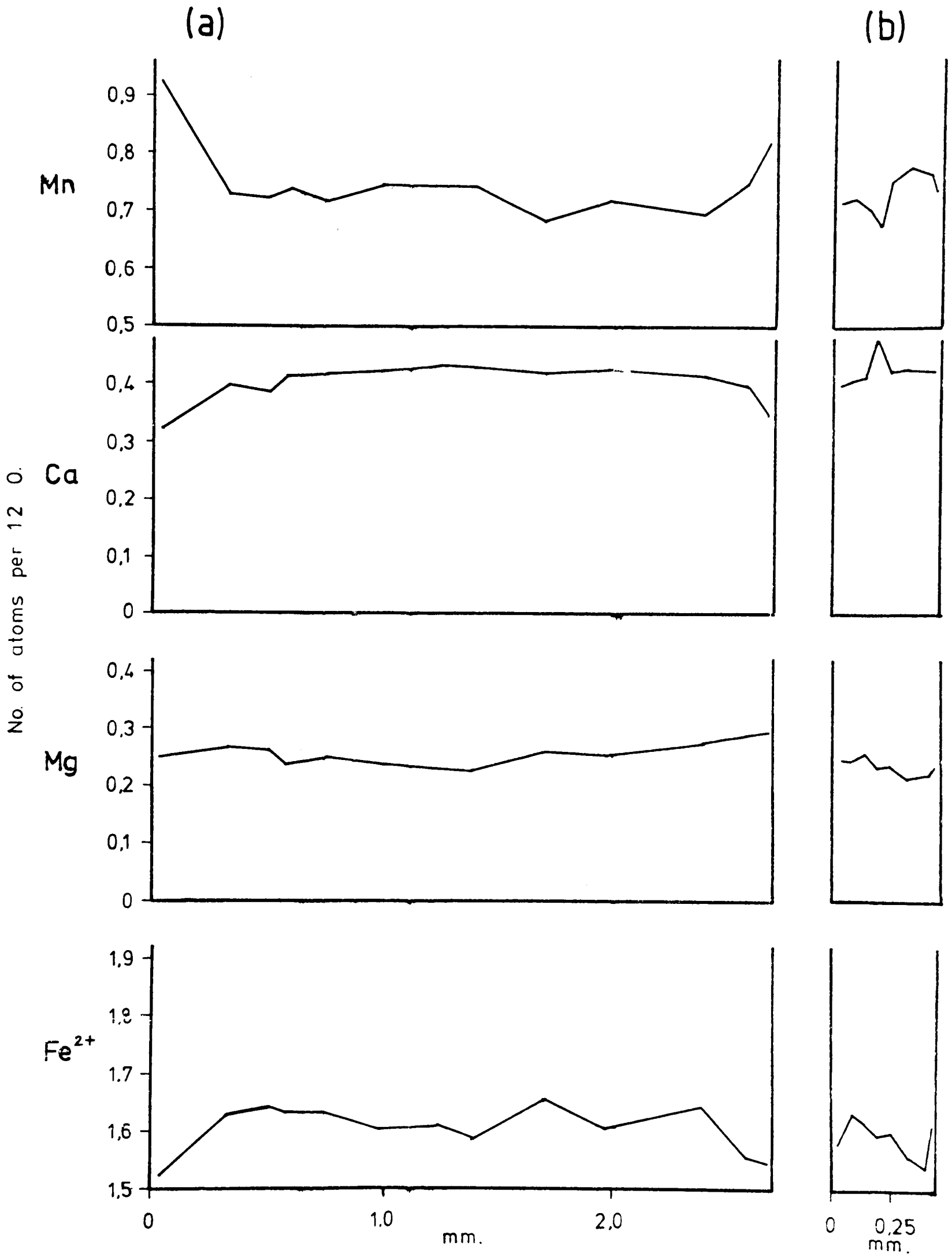
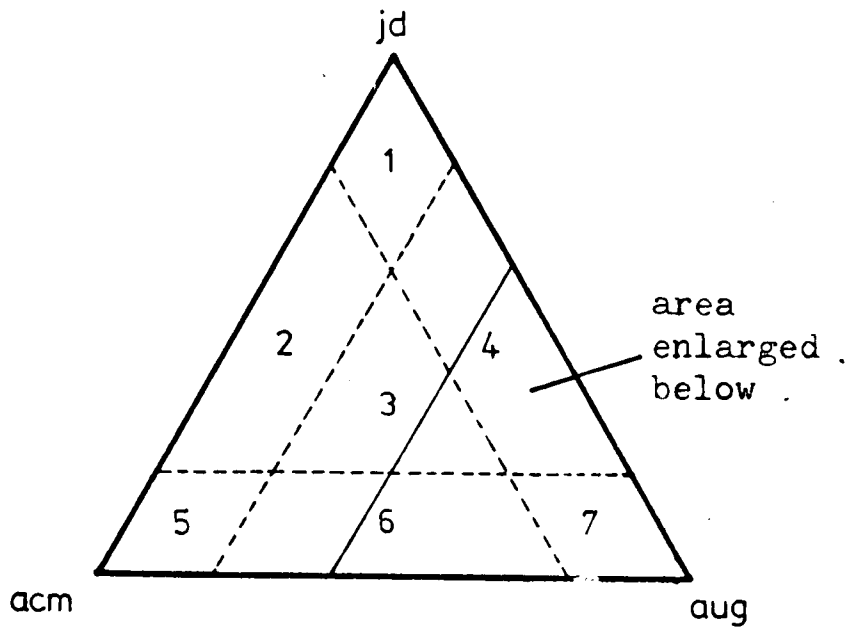



Fig. 5.7 Zoning profiles (a) parallel to $S_a^2$ (b) perpendicular to $S_a^2$ across a flat post-$S_a^2$ garnet in Peripheral Schieferhülle pelite GD 308c.




- ● $M_e$ omphacites, GD 136a.
- \+ ? $M_v$ clinopyroxenes from symplectite, GD 122.
- ○ $M_a$ clinopyroxenes, GD 1233.
- □ $M_a$ clinopyroxenes, GD 1234b.
- △ $M_a$ diopside, GD 160a.

1. jadeite
2. aegirine-jadeite
3. chloromelanite
4. omphacite
5. aegirine
6. aegirine-augite
7. augite

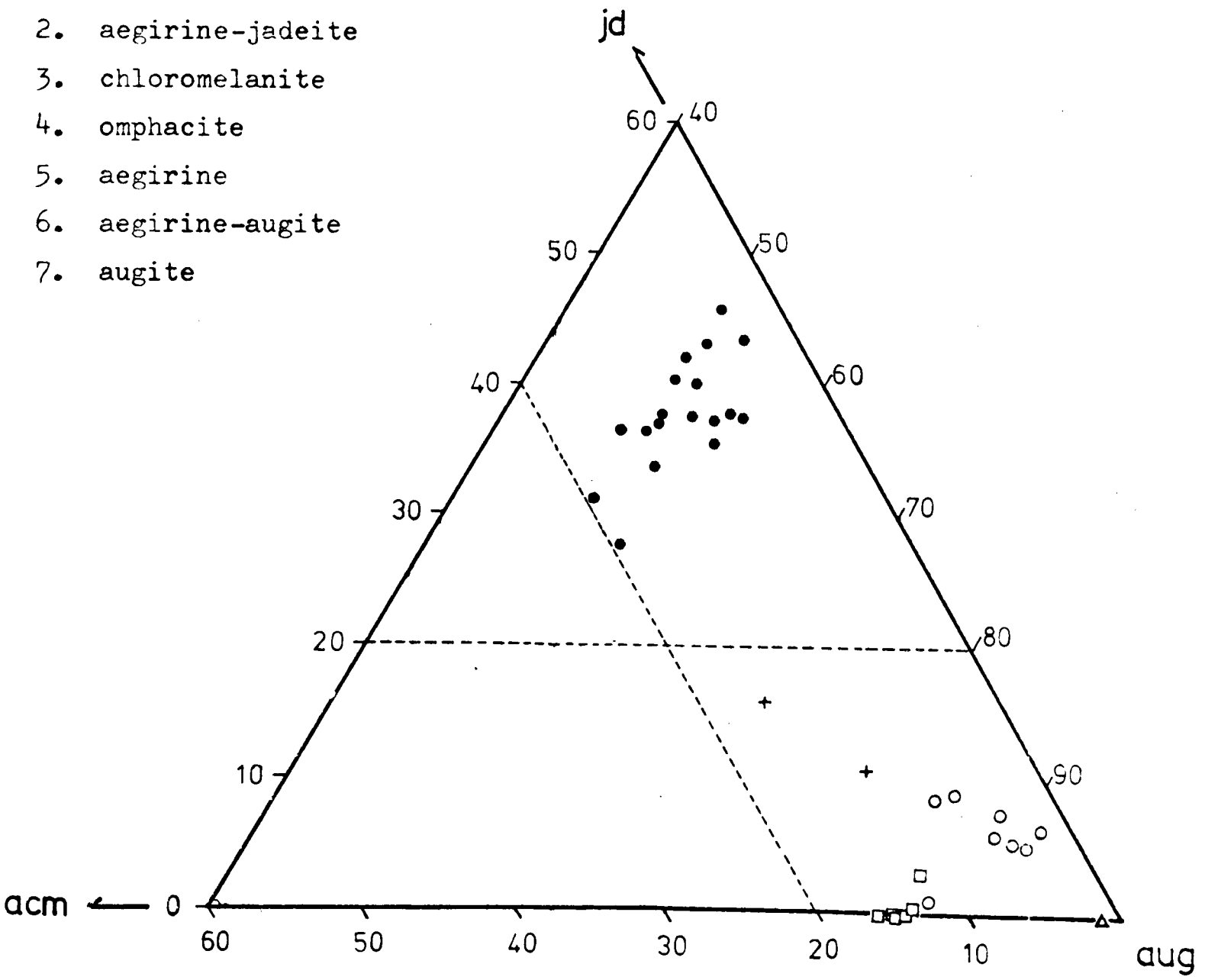



Fig. 5.8 Clinopyroxene compositions in terms of jadite, acmite and augite. (Modified from Essene and Fyfe, 1967.)

△ ? $M_v$ hornblendes, eclogitic amphibolite GD 136a.

× $M_a$ hornblende, " " GD 122.

◆ $M_a$ hornblende, feldspathic paragneiss GD 145a.

▫ $M_a$ hornblende, garbenschiefer GD 480a.

\+ $M_a$ actinolites )
o $M_a$ hornblende rims ) greenschist GD 551.

• $M_a$ hornblendes, epidote-amphibolite GD 193

† $M_a$ tremolites, siliceous dolomite GD 160a.

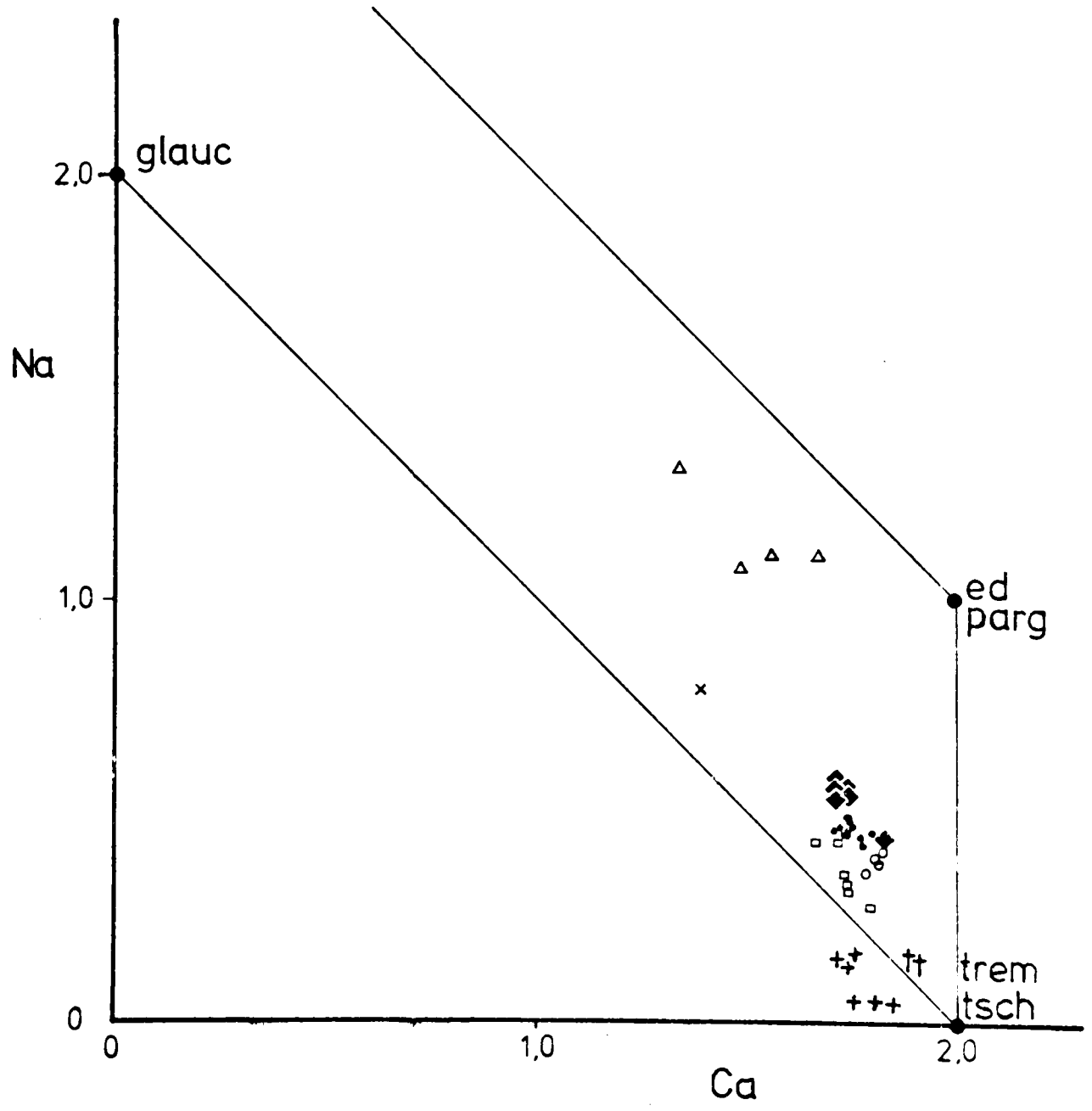



Fig. 5.9 Plot of Na versus Ca for amphiboles.

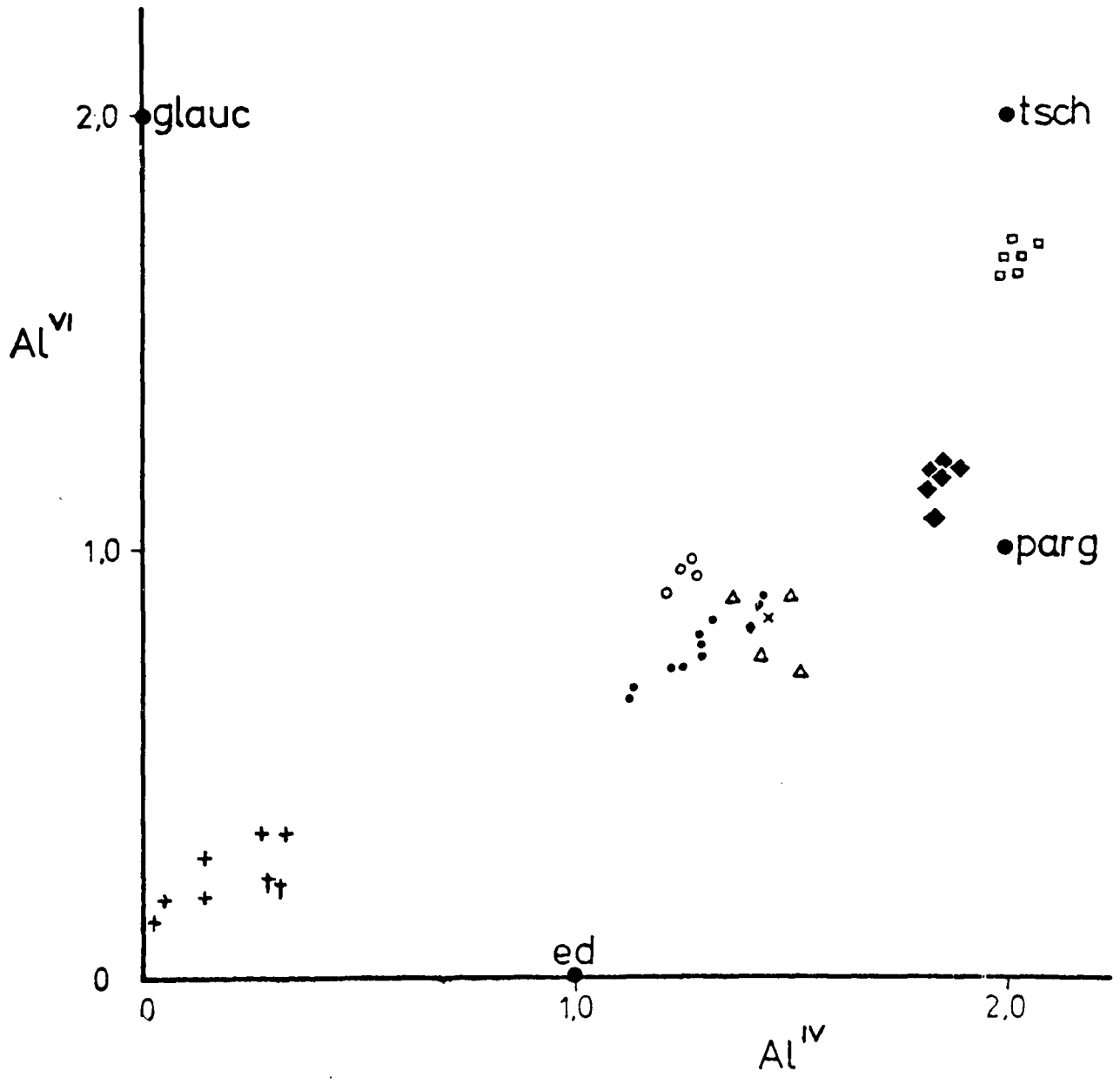
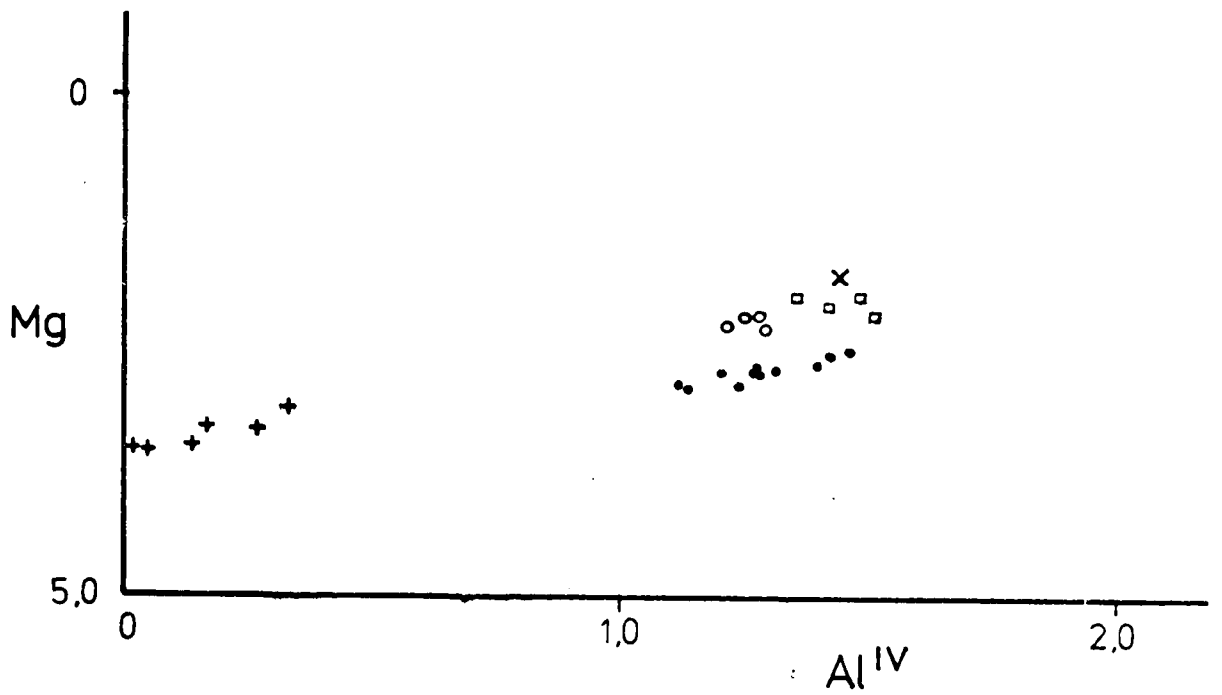



Fig. 5.10 Plot of $Al^{VI}$ versus $Al^{IV}$ for amphiboles. (Key as in fig. 5.9).



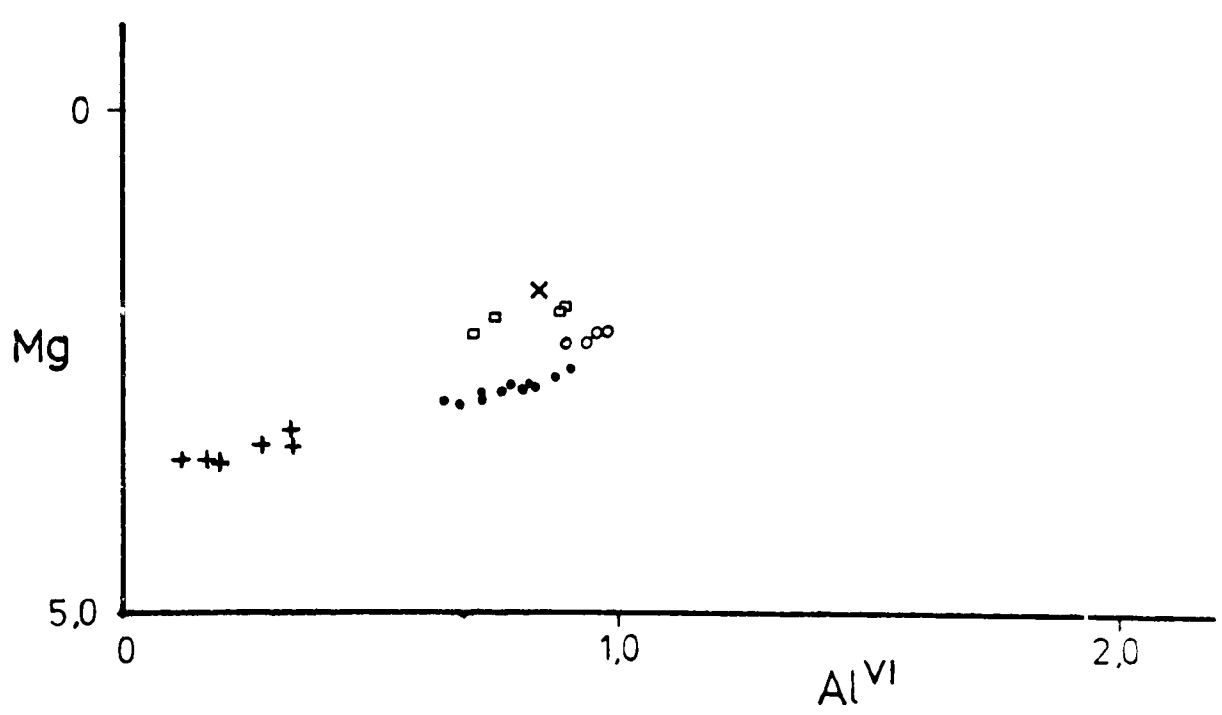




Fig. 5.11 Plots showing the degree of $(R^{3+} + R^{2+}) \rightleftharpoons Mg$ replacement as a function of $Al^{IV}$ and $Al^{VI}$ in metabasite amphiboles.

(Key as in fig. 5.9)

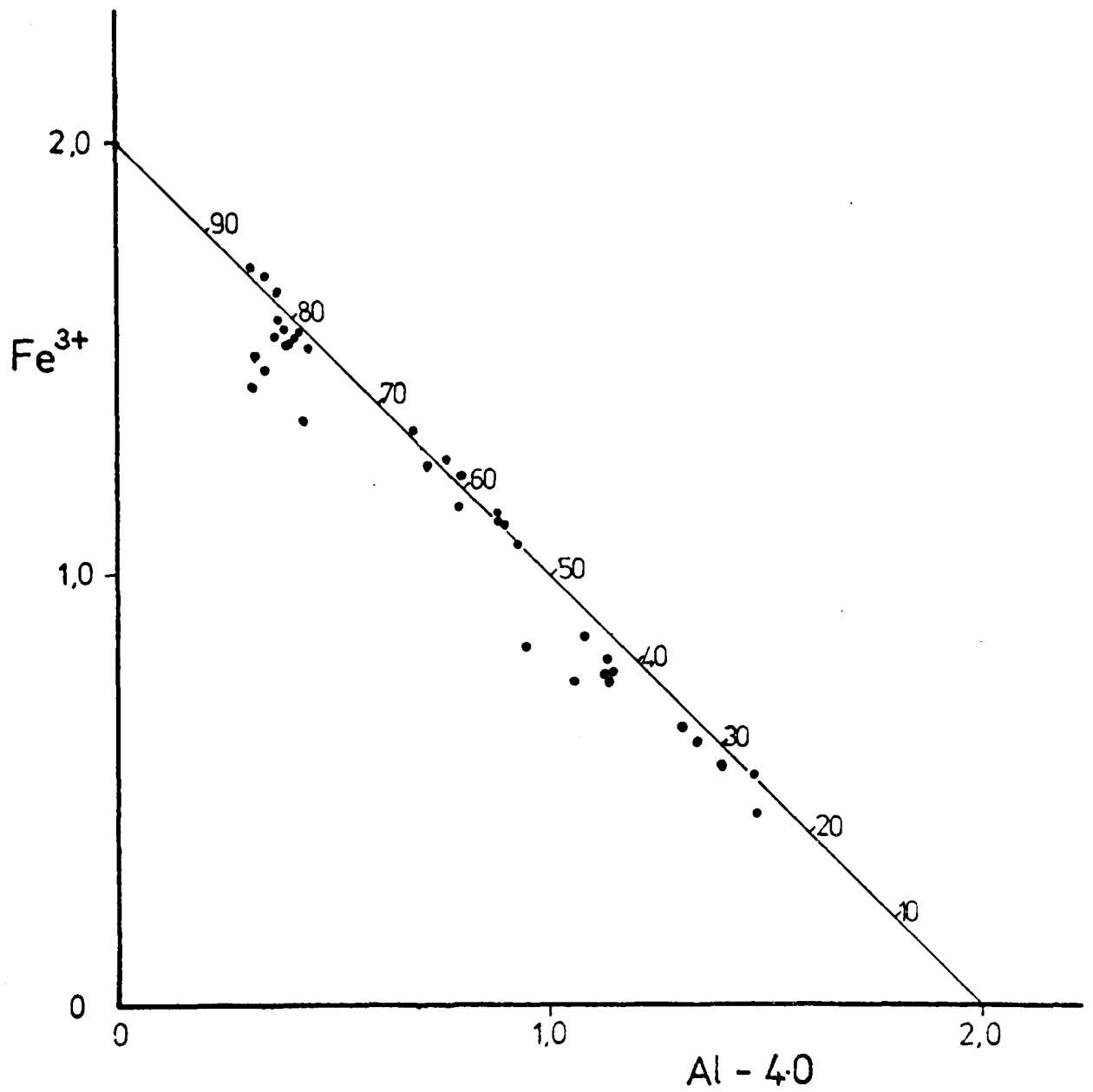



Fig. 5.12 Epidote compositions plotted in terms of $Fe^{3+}$ versus Al - 4.0. (Contoured in mole percent $Al_2Fe$ - epidote.)

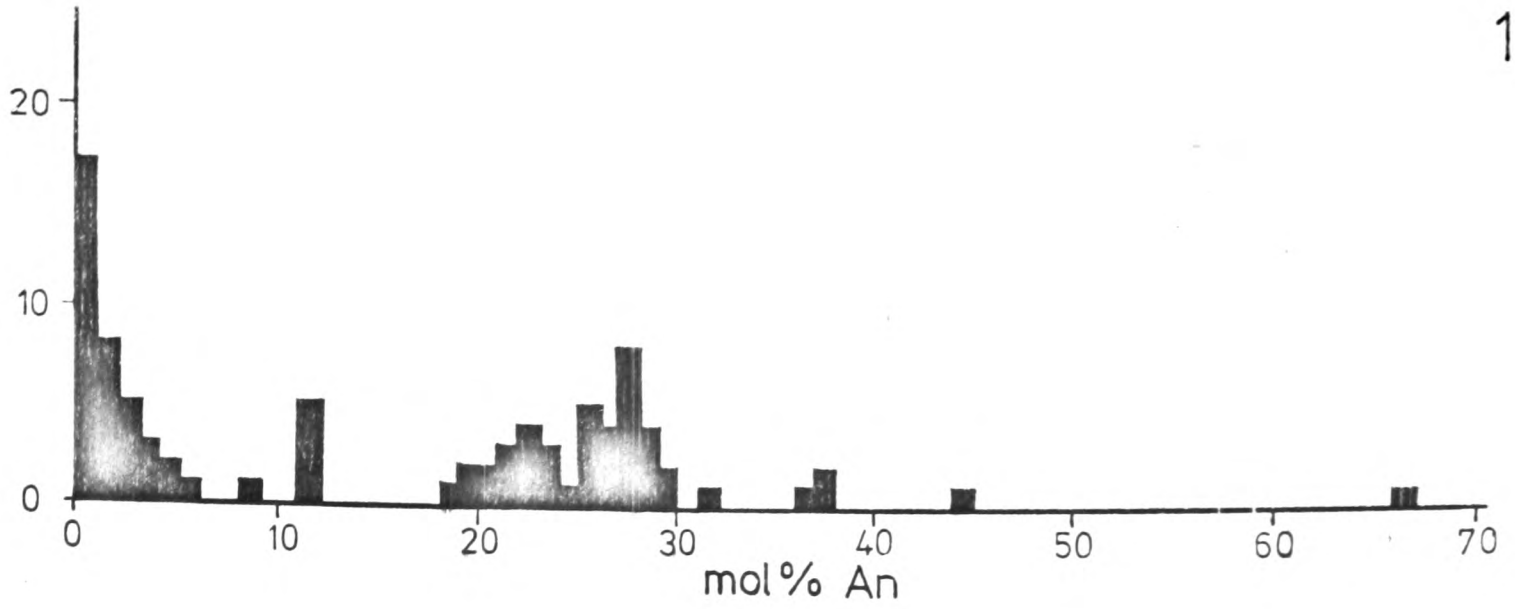



Fig. 5.13 Histogram of plagioclase compositions determined by microprobe analysis.

$$K' = \frac{100 \times K}{K+Na+Ca}$$

$$Na' = \frac{100 \times Na}{K+Na+Ca}$$

$$Ca' = \frac{100 \times Ca}{K+Na+Ca}$$

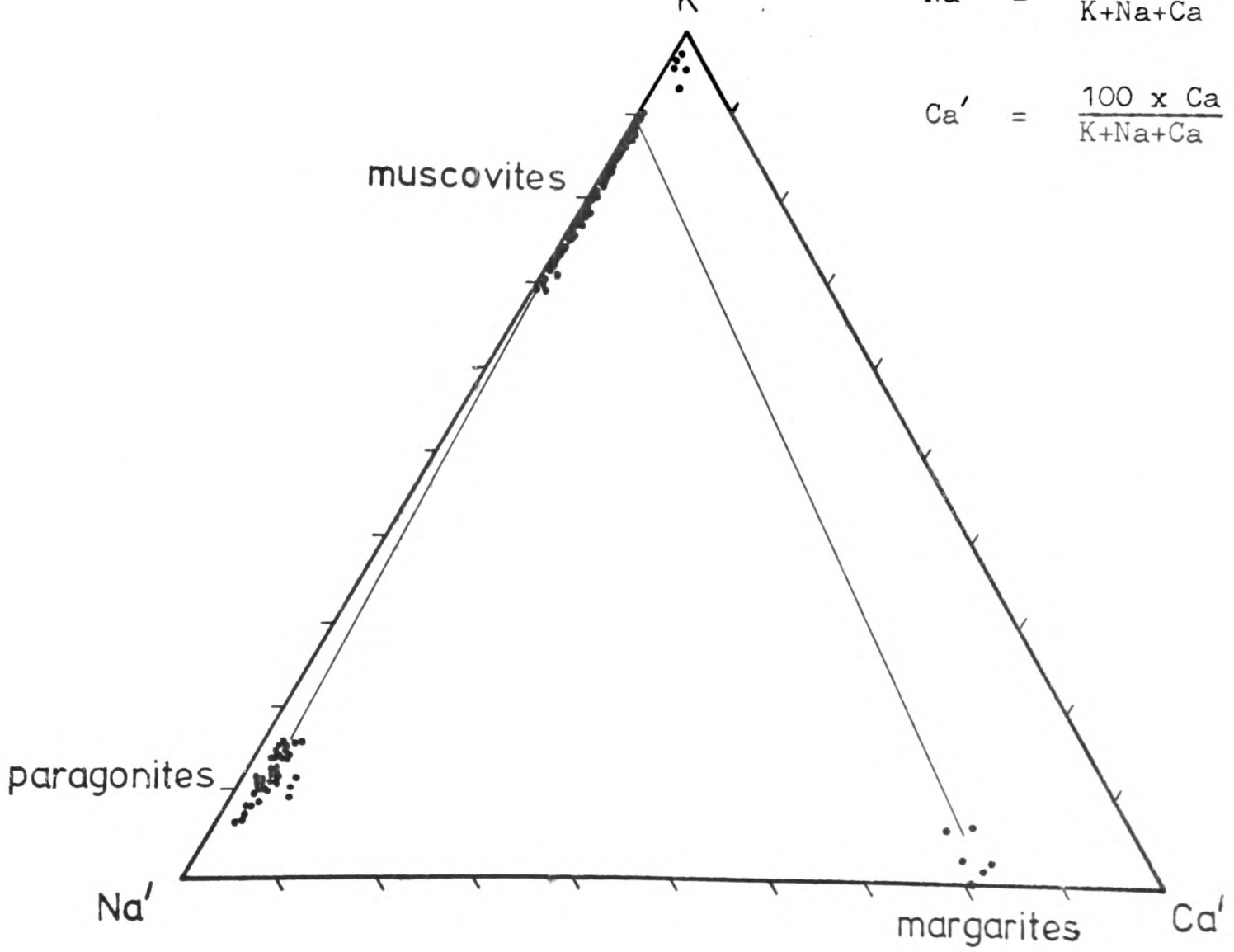
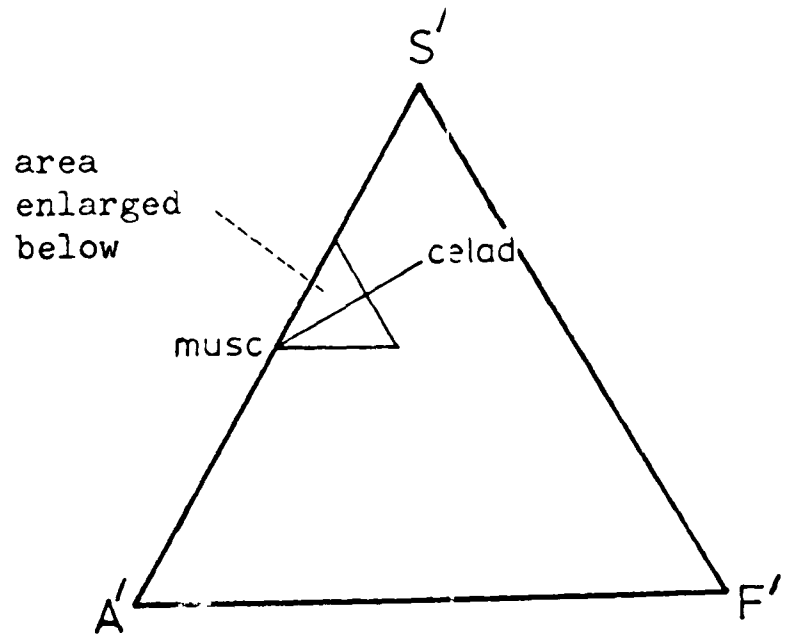



Fig. 5.14 Compositions of white micas.

$$S' = \frac{100 \times Si}{Si+Al+Fe+Mg+Mn}$$

$$A' = \frac{100 \times Al}{Si+Al+Fe+Mg+Mn}$$

$$F' = \frac{100 \times (Fe+Mg+Mn)}{Si+Al+Fe+Mg+Mn}$$



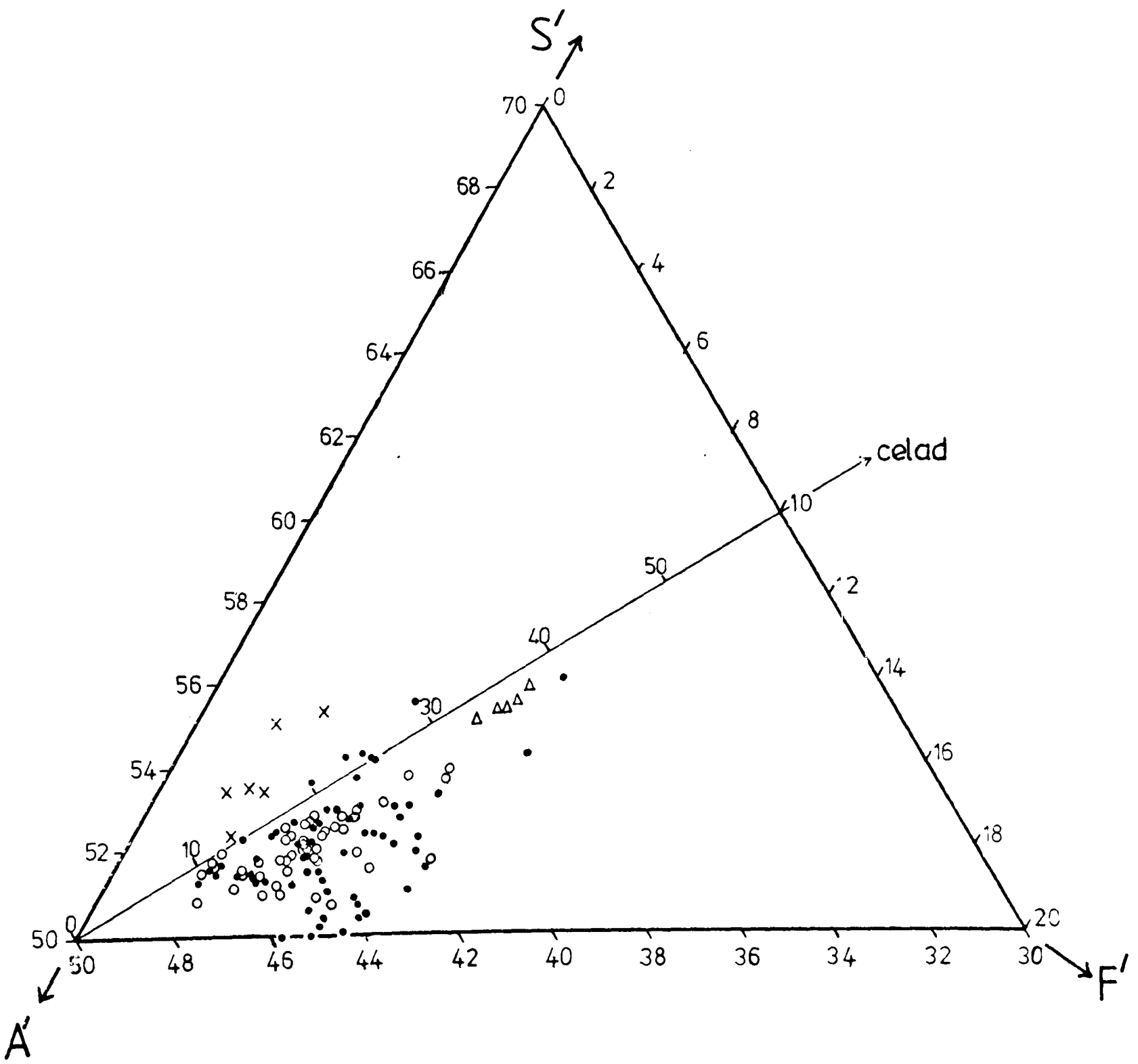
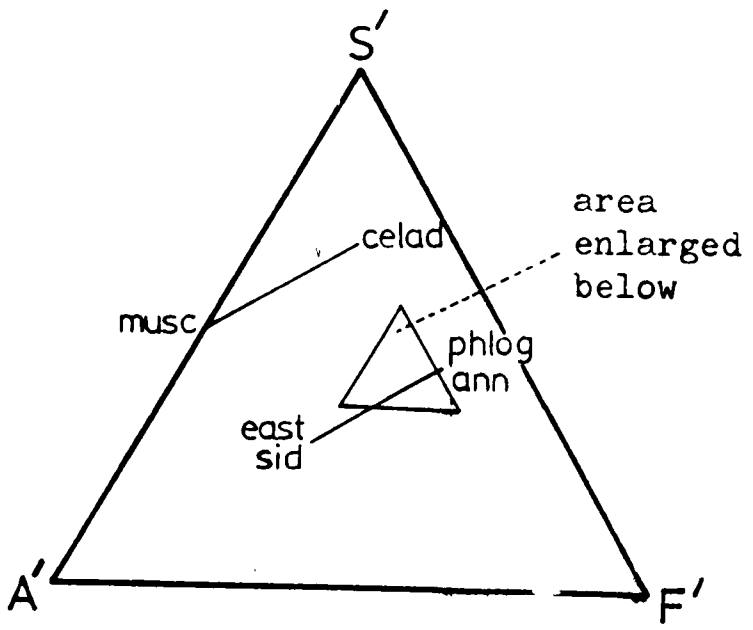




Fig. 5.15 Muscovite compositions plotted in the SAF diagram of Lambert (1959) to show degree of celadonite substitution. (Contoured in mole percent celadonite. Key as in fig. 5.16)




o Inner Schieferhülle aluminous pelites.

× Other Inner Schieferhülle mica-schists.

• Peripheral Schieferhülle mica-schists.

\+ Syenite-gneiss GD 1233.

Δ Leucogranite GD 468.

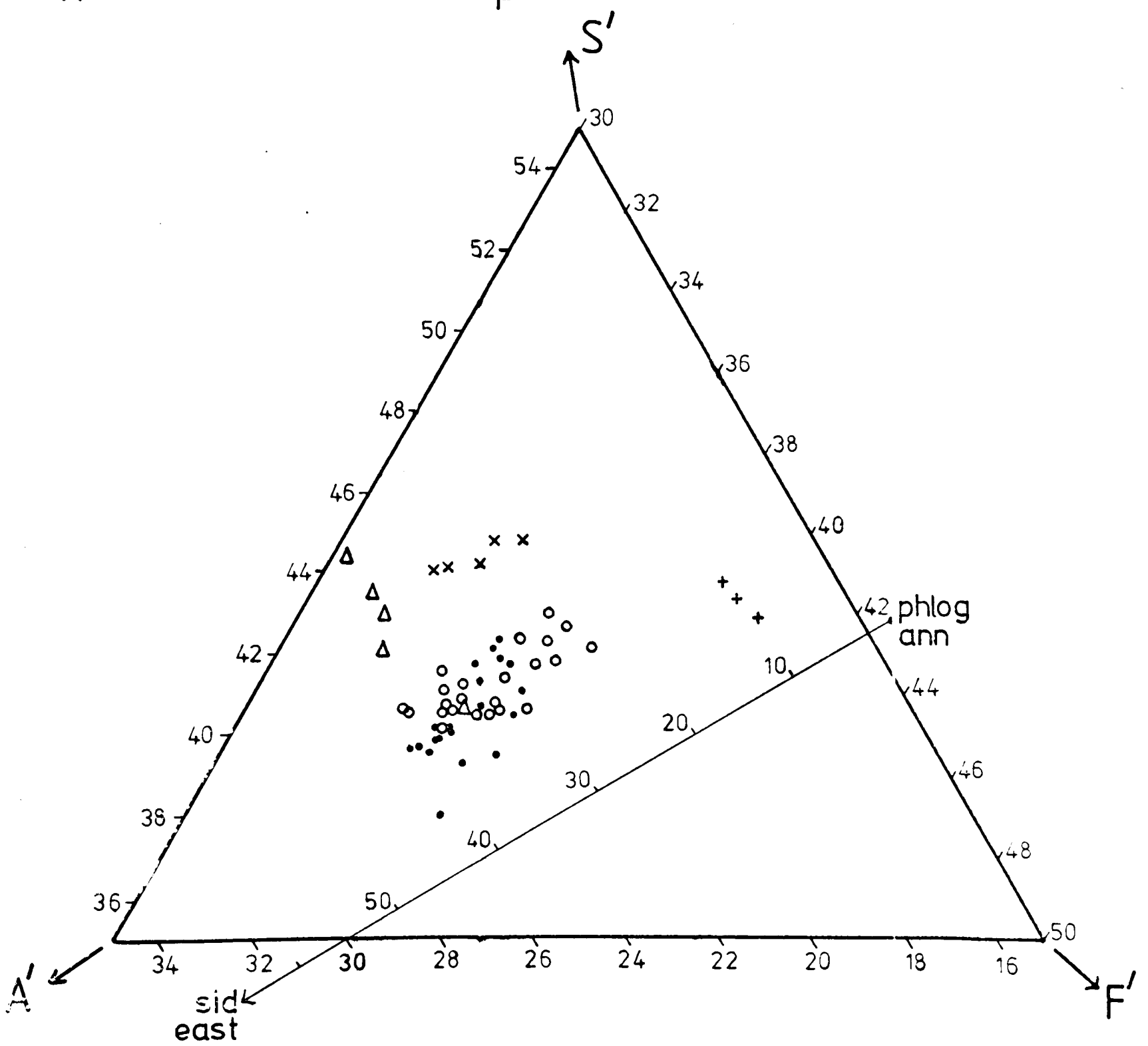



Fig. 5.16 Biotite compositions plotted in the SAF diagram of Lambert (1959). (Contoured in mole percent siderophyllite and eastonite.)

- ∘ Inner Schieferhülle mica-schists.
- \+ Peripheral Schieferhülle pelitic mica-schists.
- • " " metabasites.

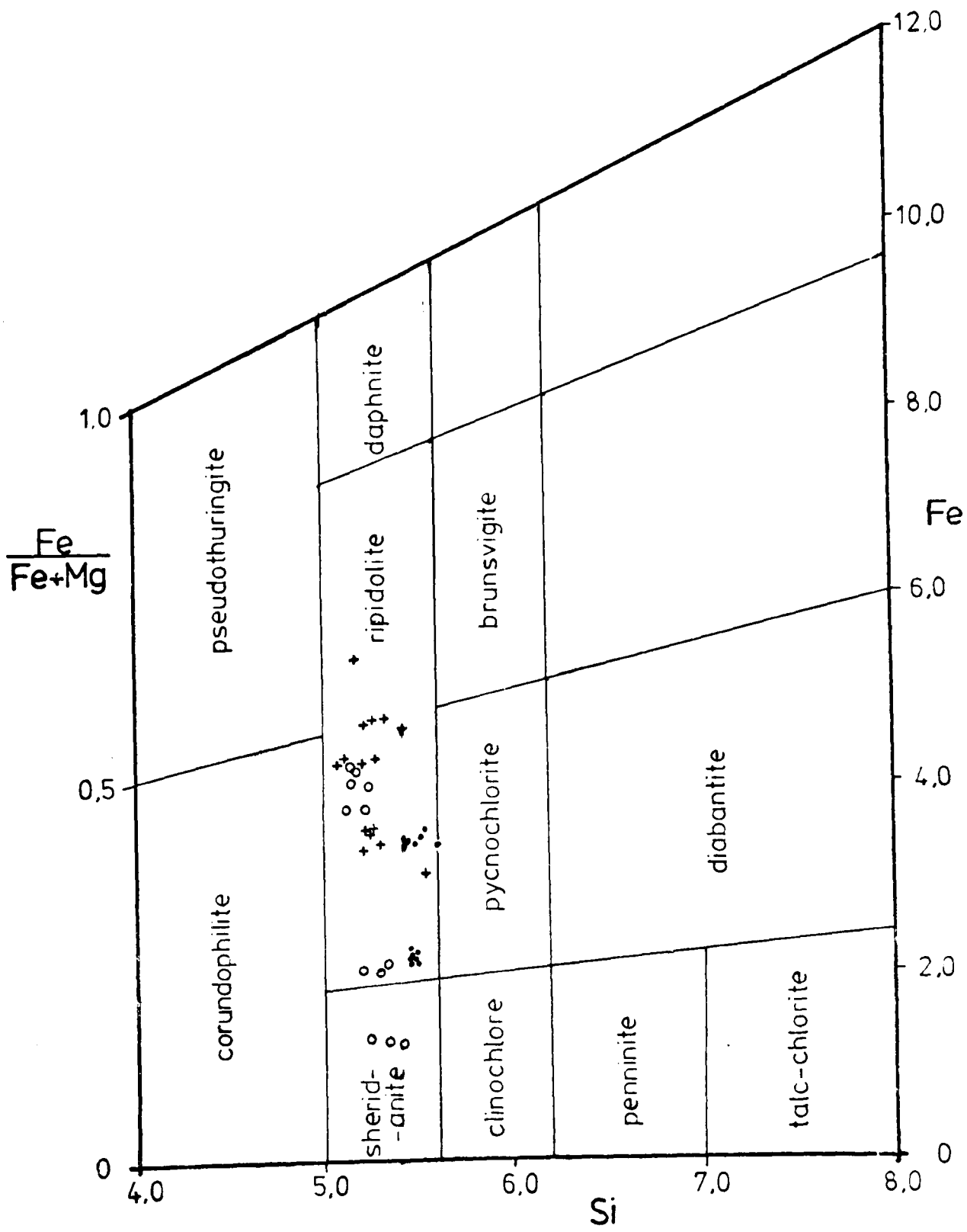
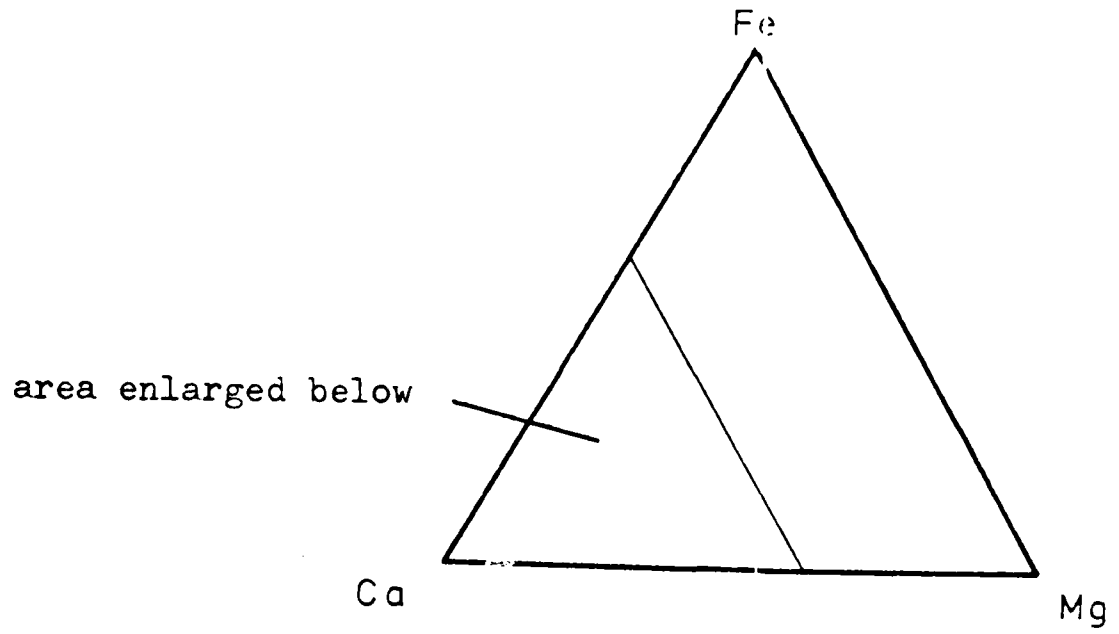



Fig. 5.17 Chlorite compositions. (Classification of Hey, 1954)



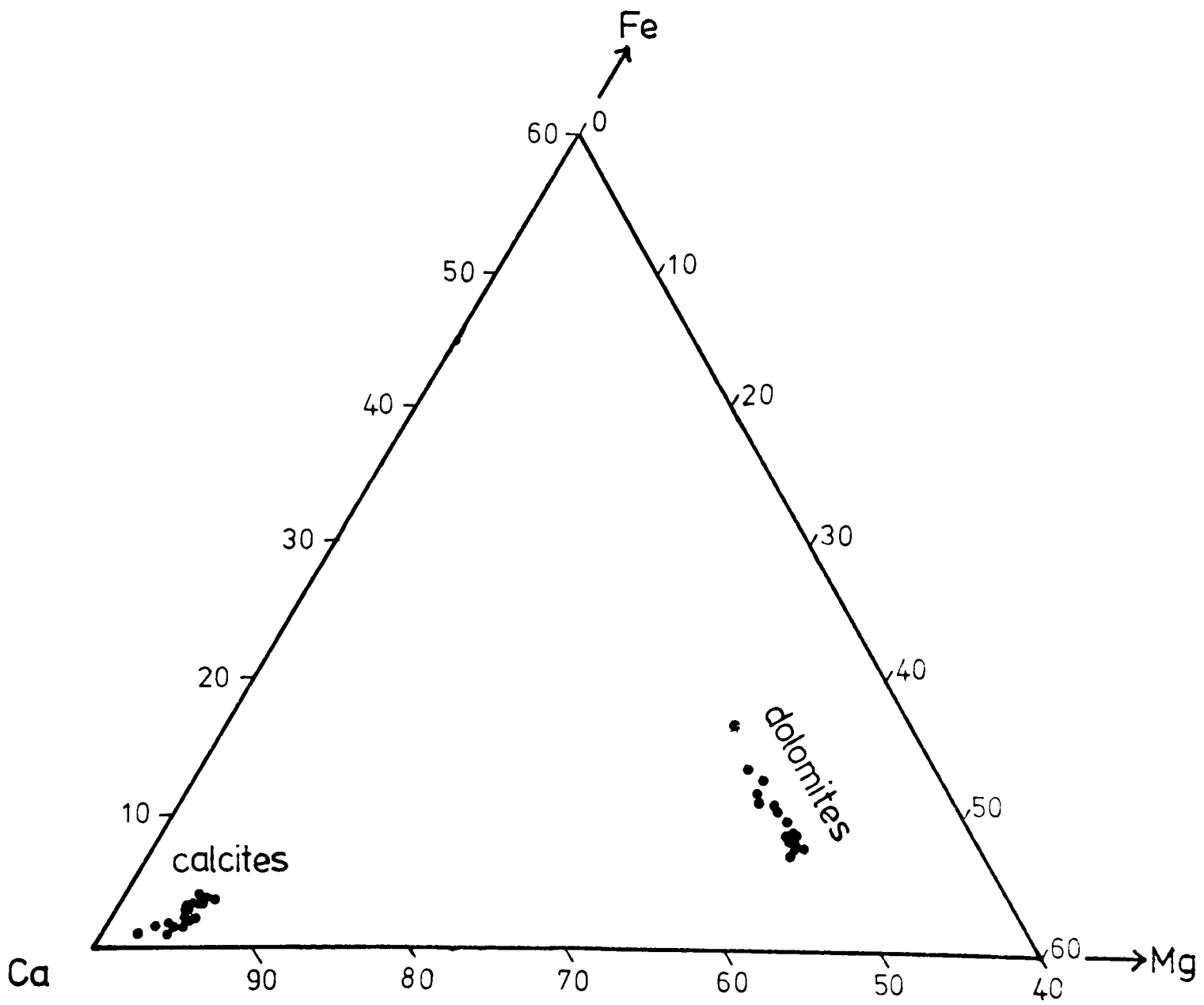




Fig. 5.18 Carbonate compositions plotted in ternary Ca-Mg-Fe.

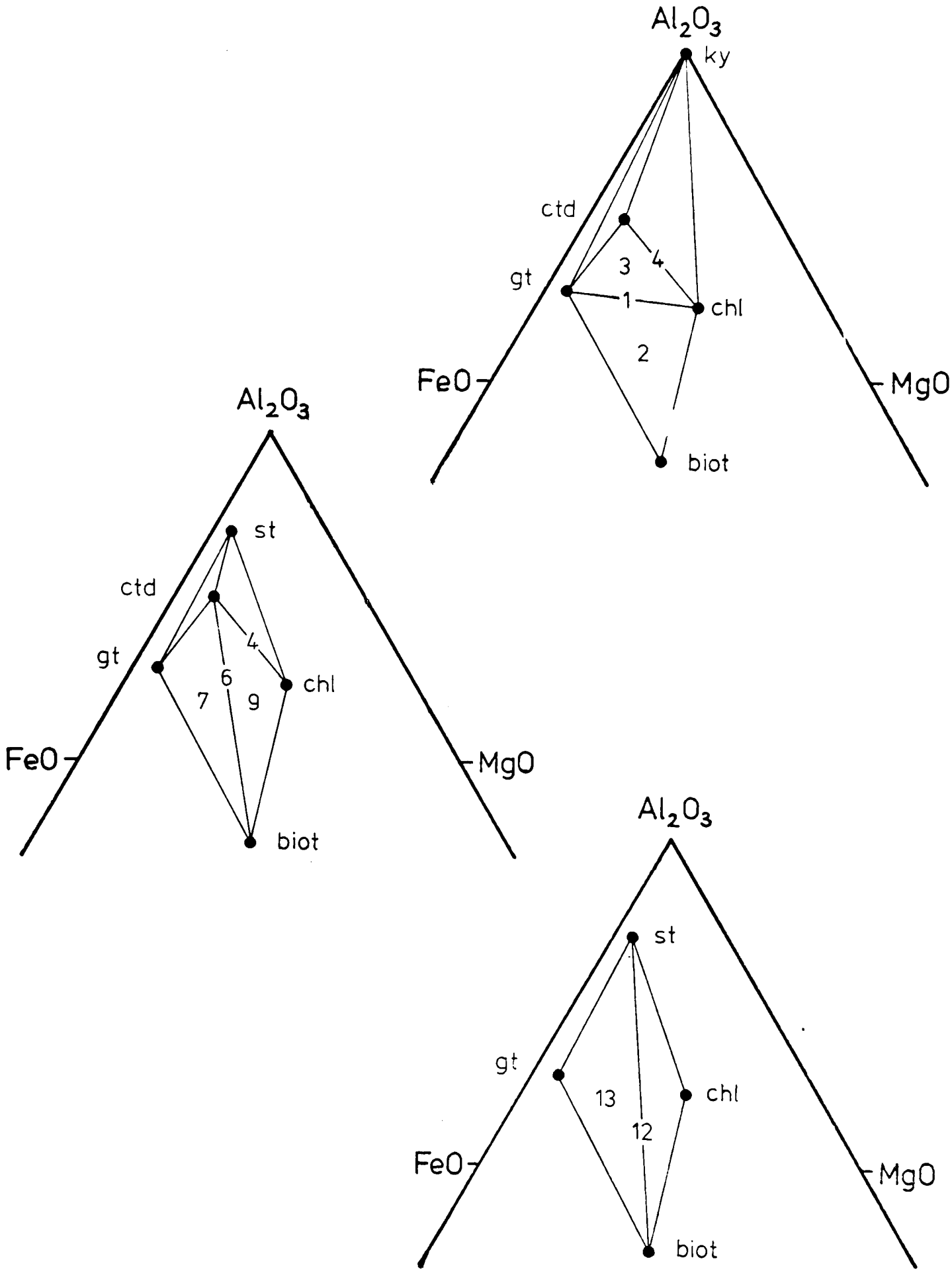



Fig. 6.1 Schematic Thompson AFM diagrams showing compatibility relationships between the high-variance pelite assemblages listed in part B(a).

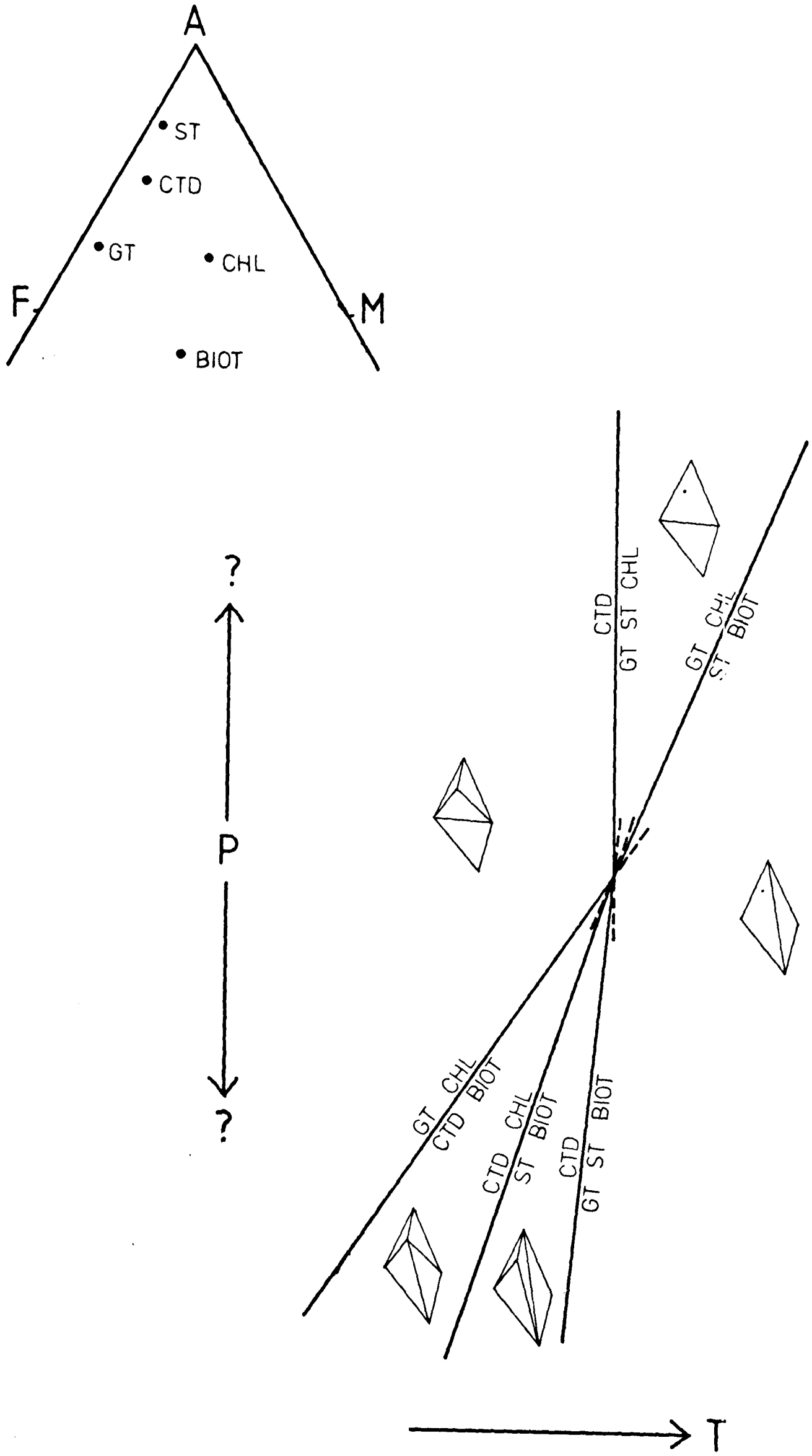



Fig. 6.2 Schreinemaker's bundle for the AFM invariant assemblage gt + st + ctd + biot + chl in musc + qz bearing pelites.

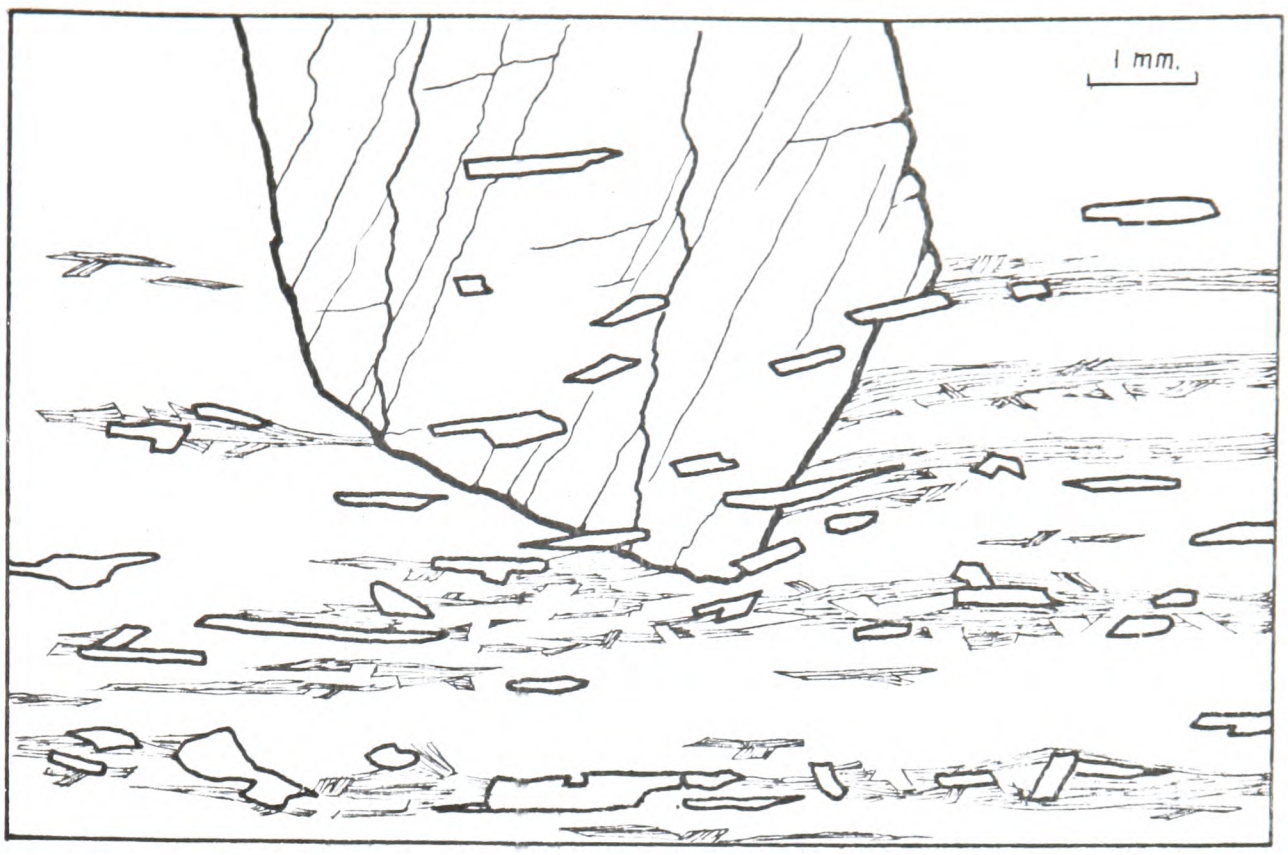



Fig. 6.3 Garnet overgrowing plates of chloritoid while replacing chlorite and muscovite in pelitic mica-schist GD 480 b.

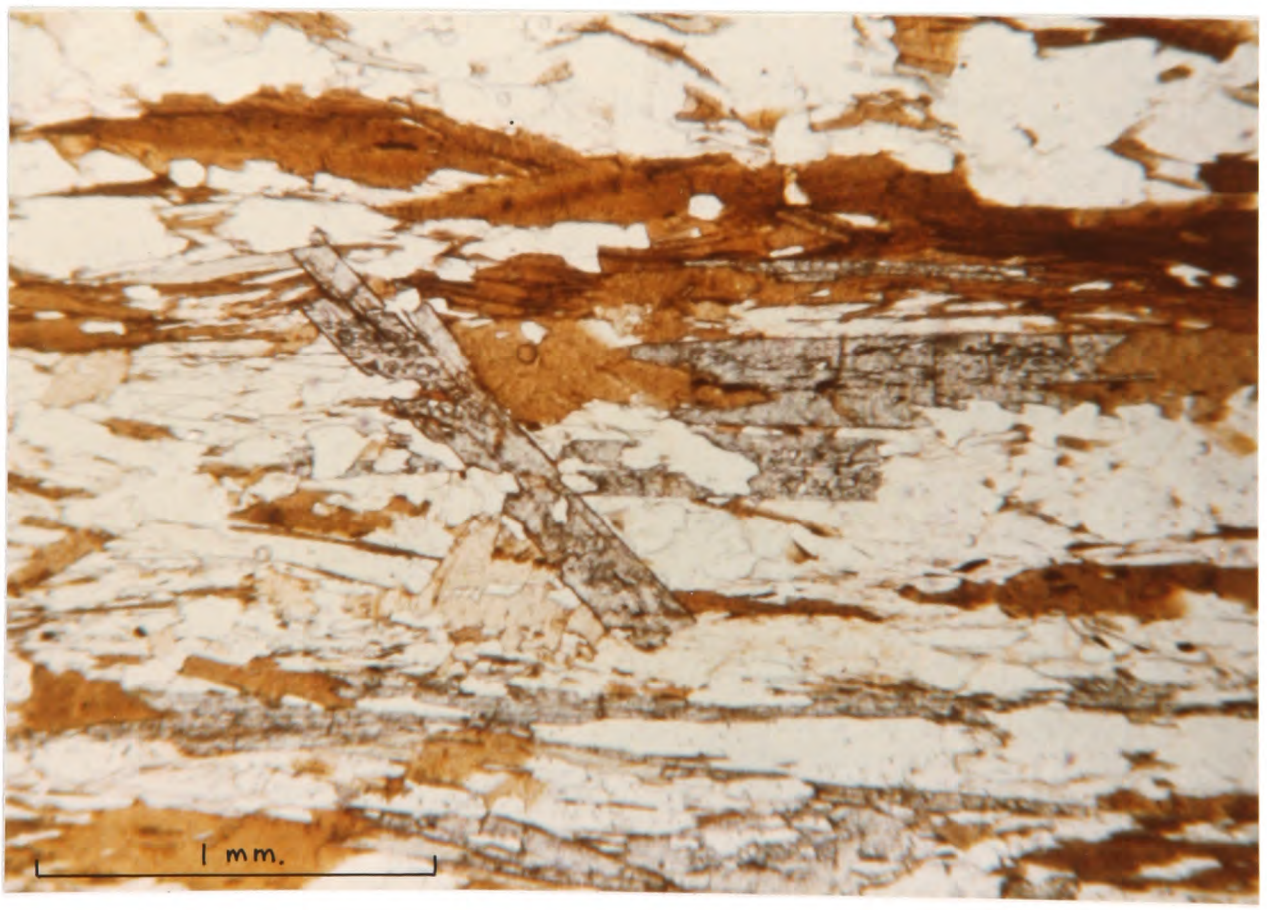
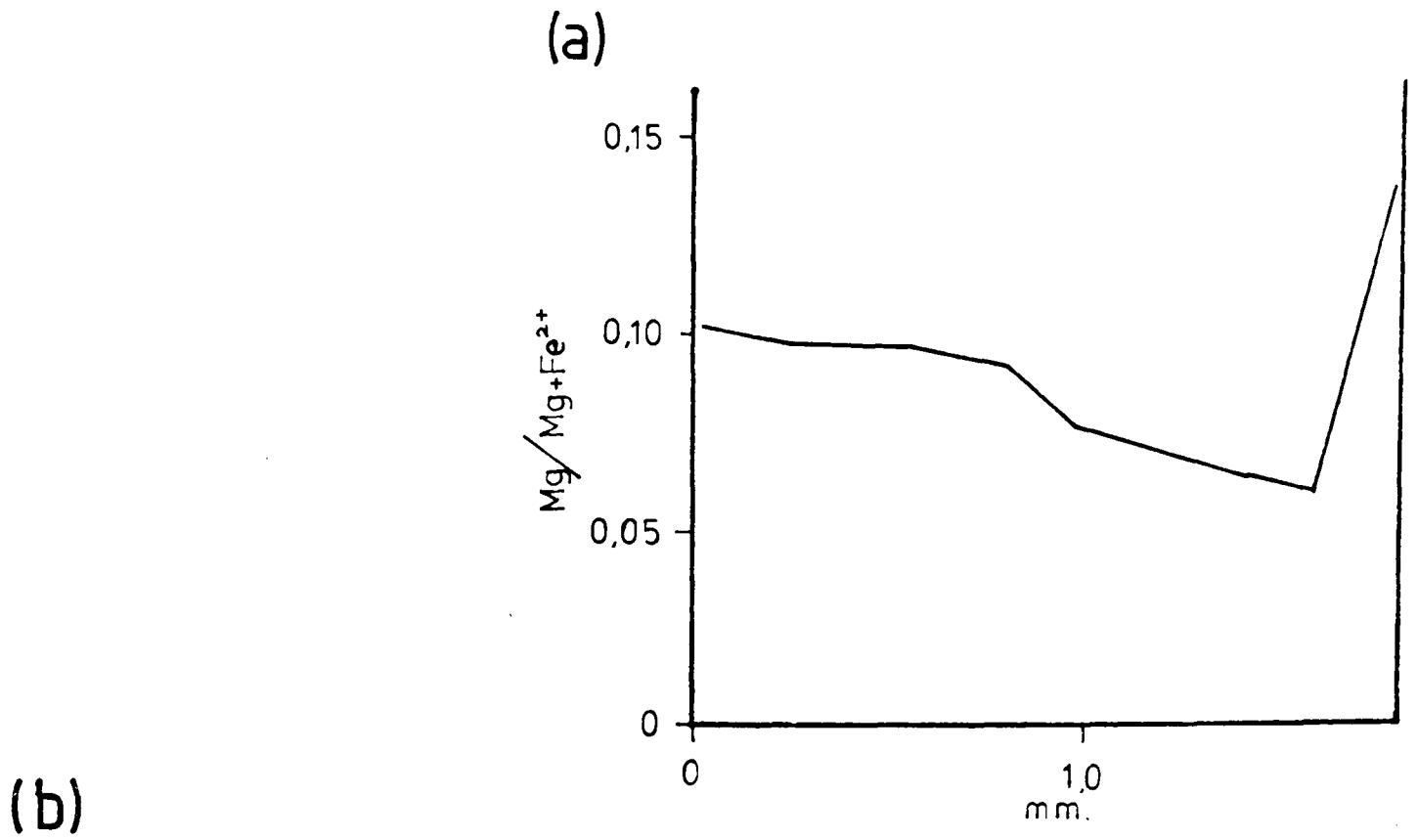
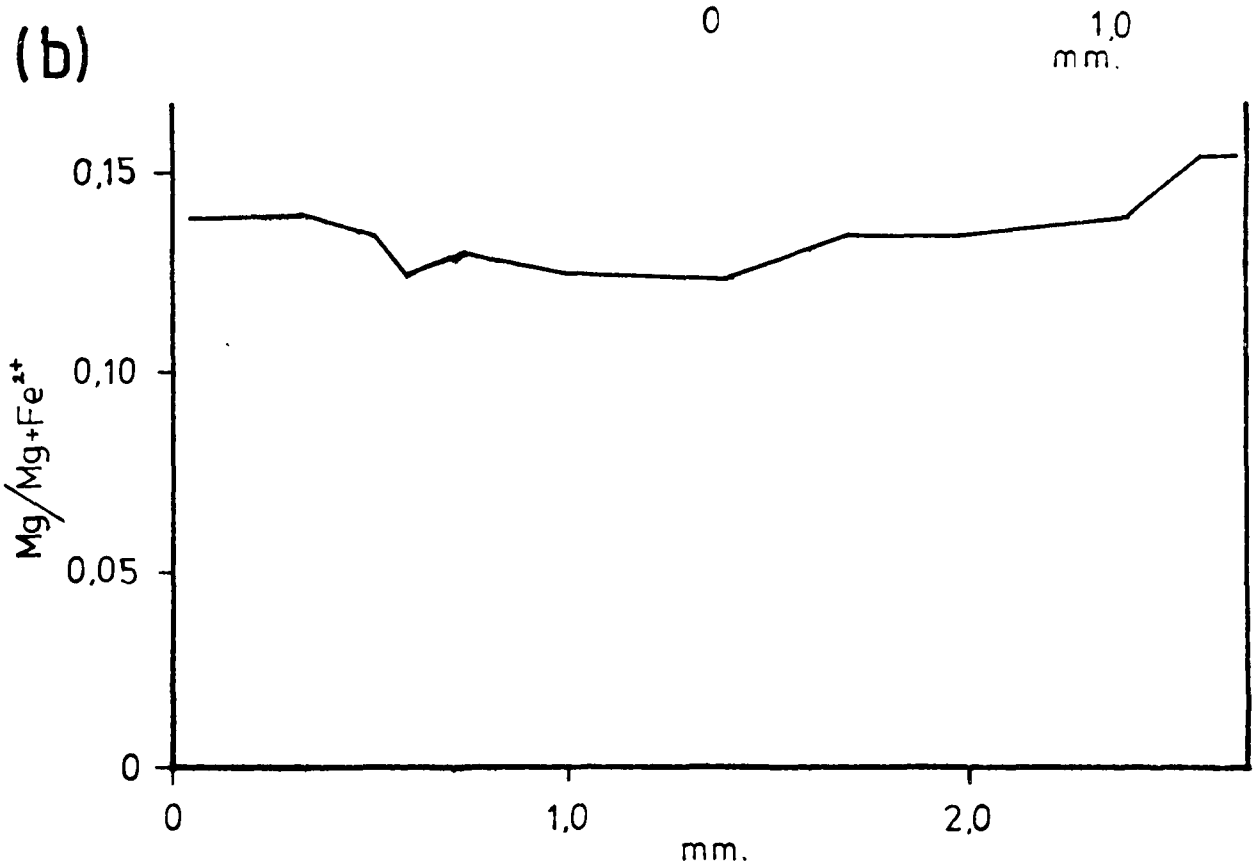



Fig. 6.4 Post $S_a^2$ chloritoid, apparently in equilibrium with biotite, in pelitic mica-schist GD 168b. Plane polarised light.



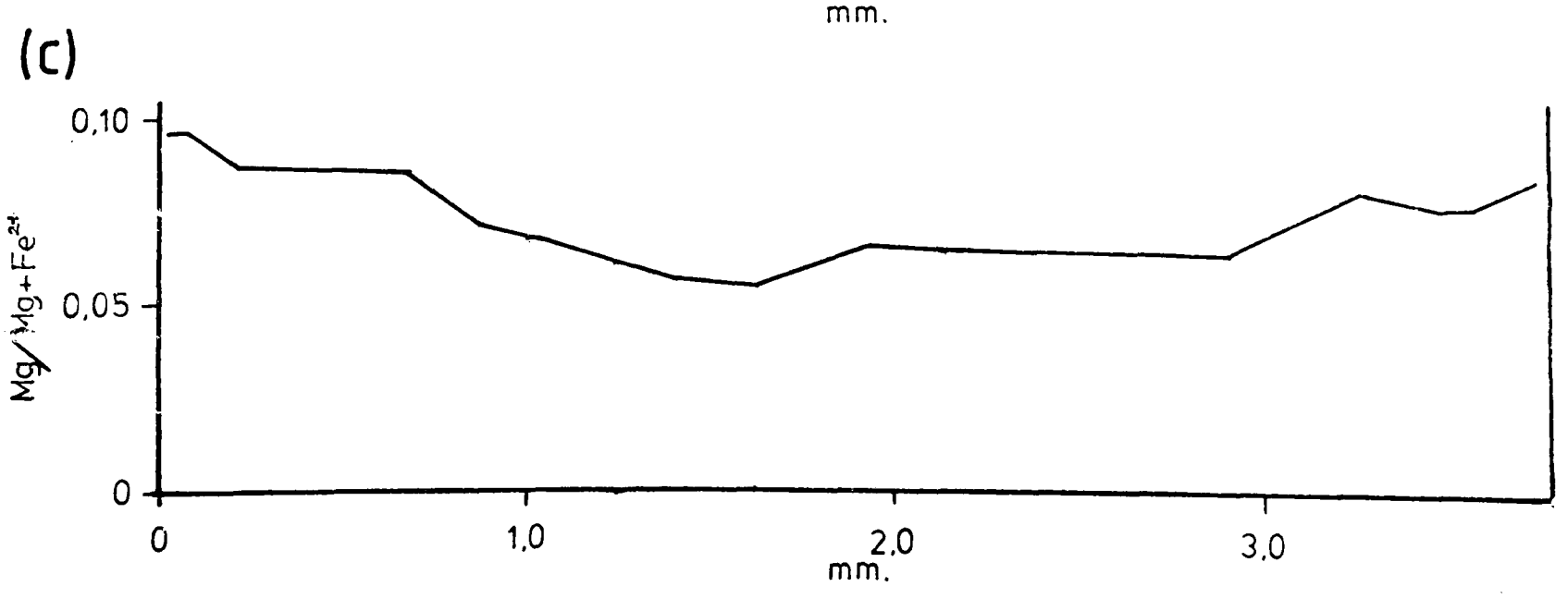




Fig. 6.5 Mg/Mg + Fe zoning profiles across garnets in Peripheral Schieferhülle pelites (a) GD 18, (b) GD 308c, (c) GD 168b.

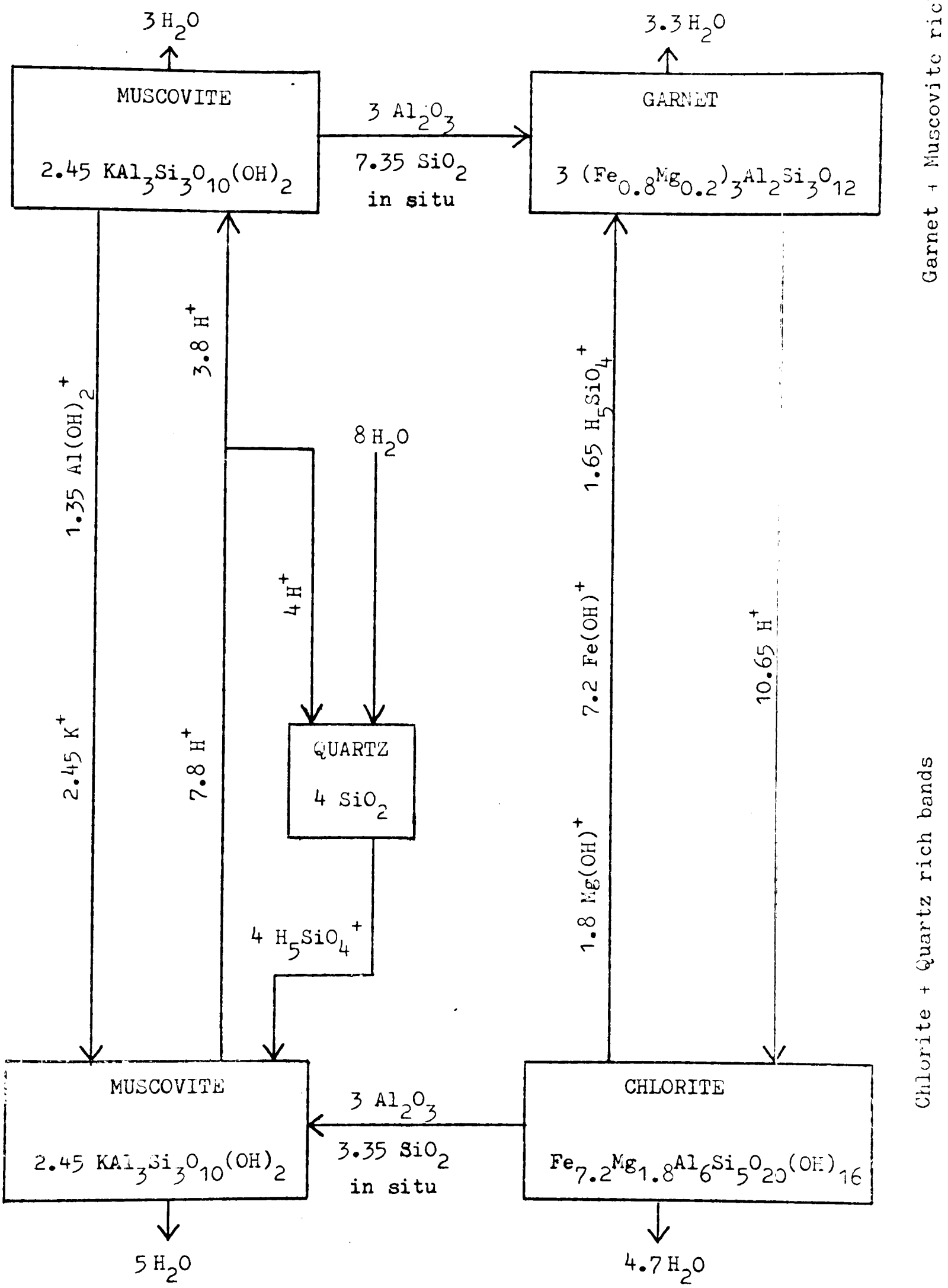



Fig. 6.6 Schematic representation of the garnet-forming reaction in GD 492.

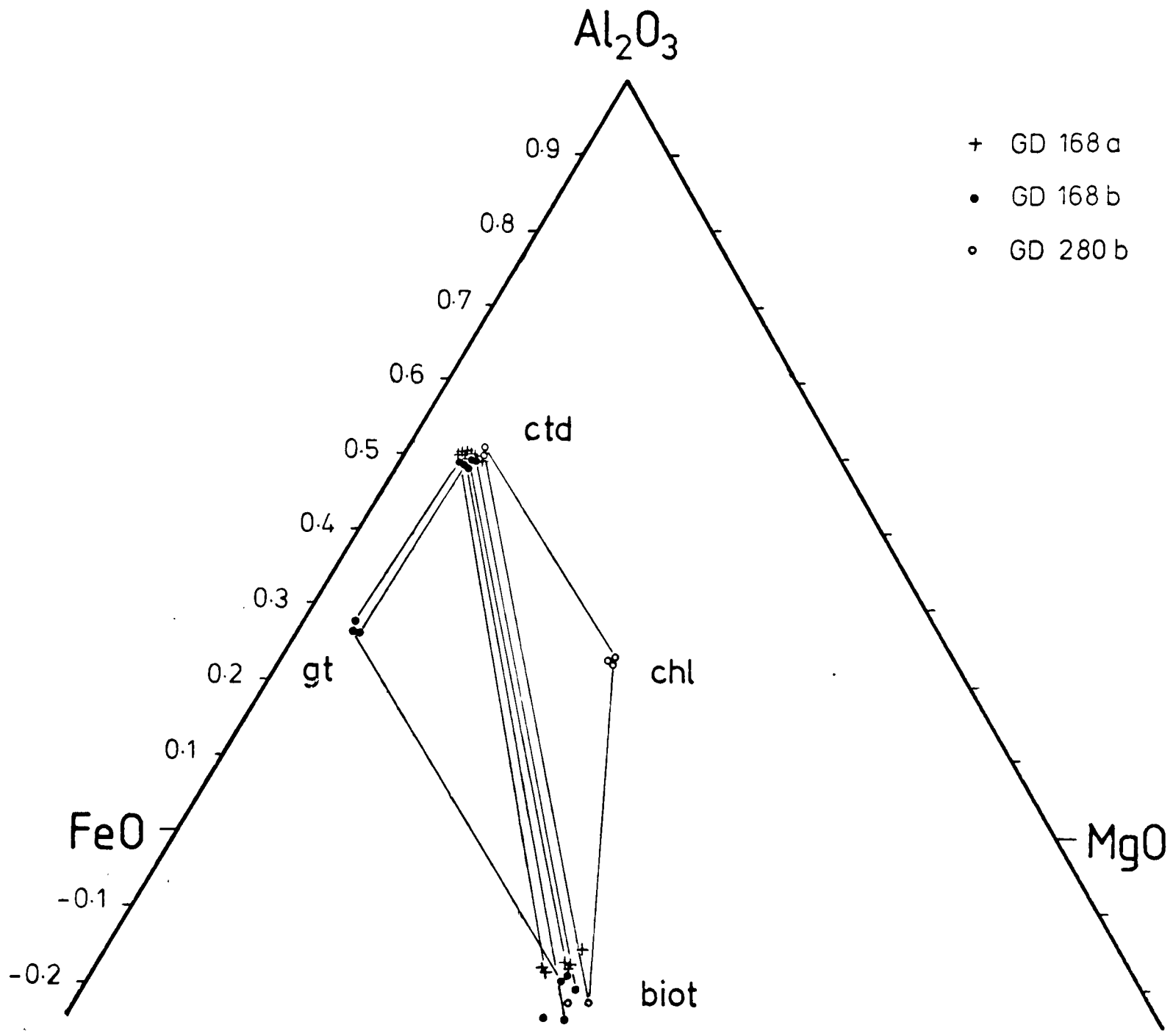



Fig. 6.7 Thompson AFM diagram for pelites from the chloritoid + biotite zone.

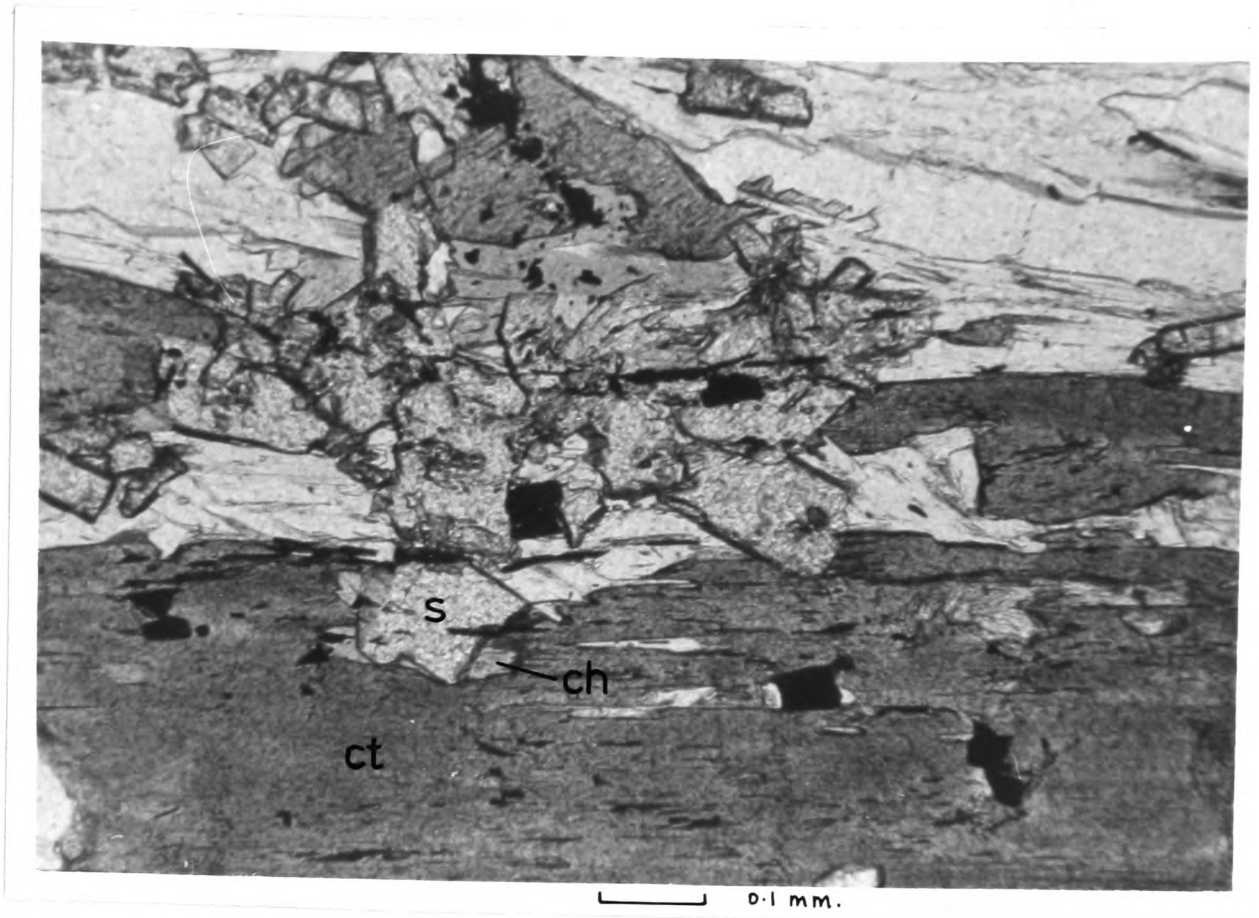



Fig. 6.8 Staurolite (s) and chlorite (ch) growing at the expense of chloritoid (ct) in pelitic mica-schist GD 308c. Plane polarised light.

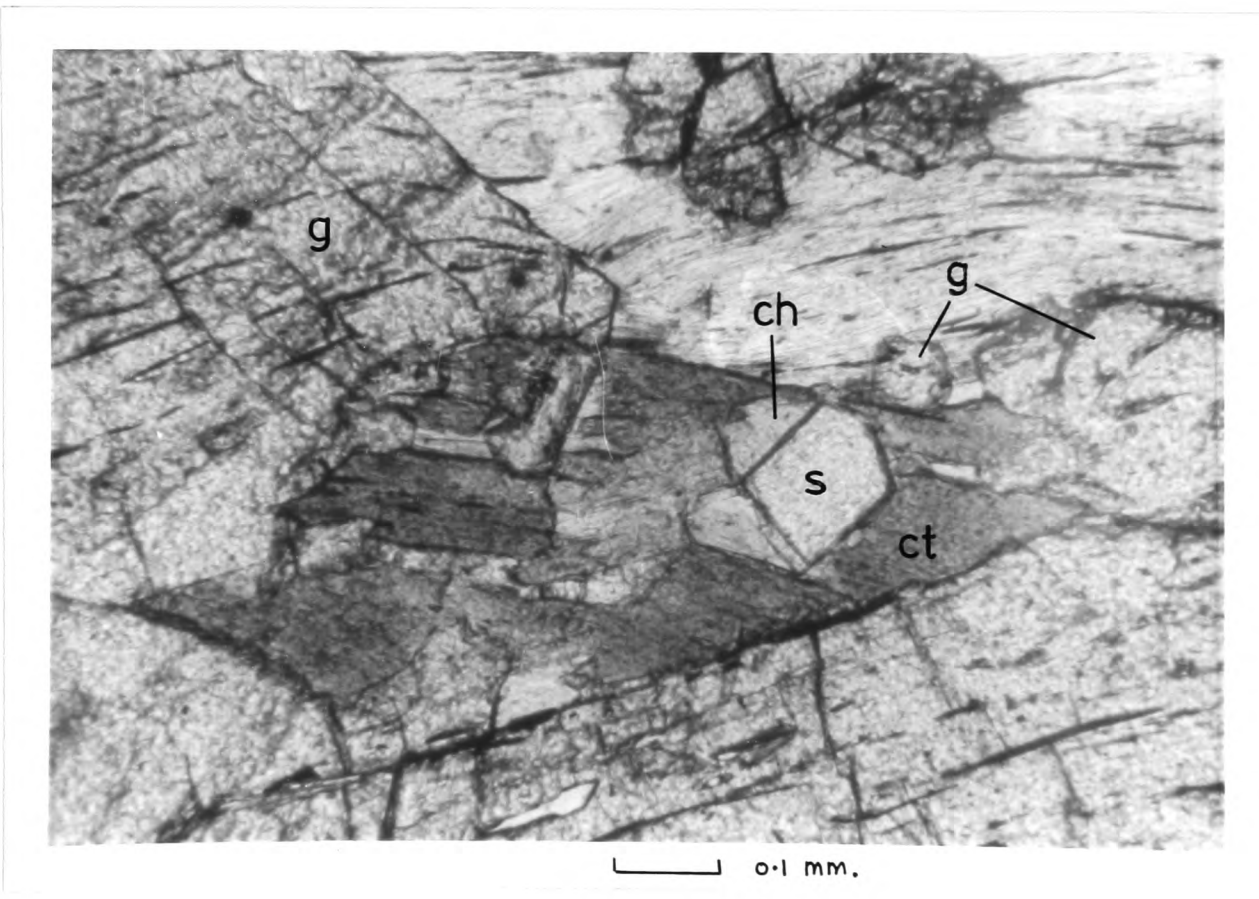



Fig. 6.9 Staurolite (s) and chlorite (ch) growing at the expense of chloritoid (ct) partially enclosed by garnet (g) in pelitic mica-schist GD 43b. Plane polarised light.

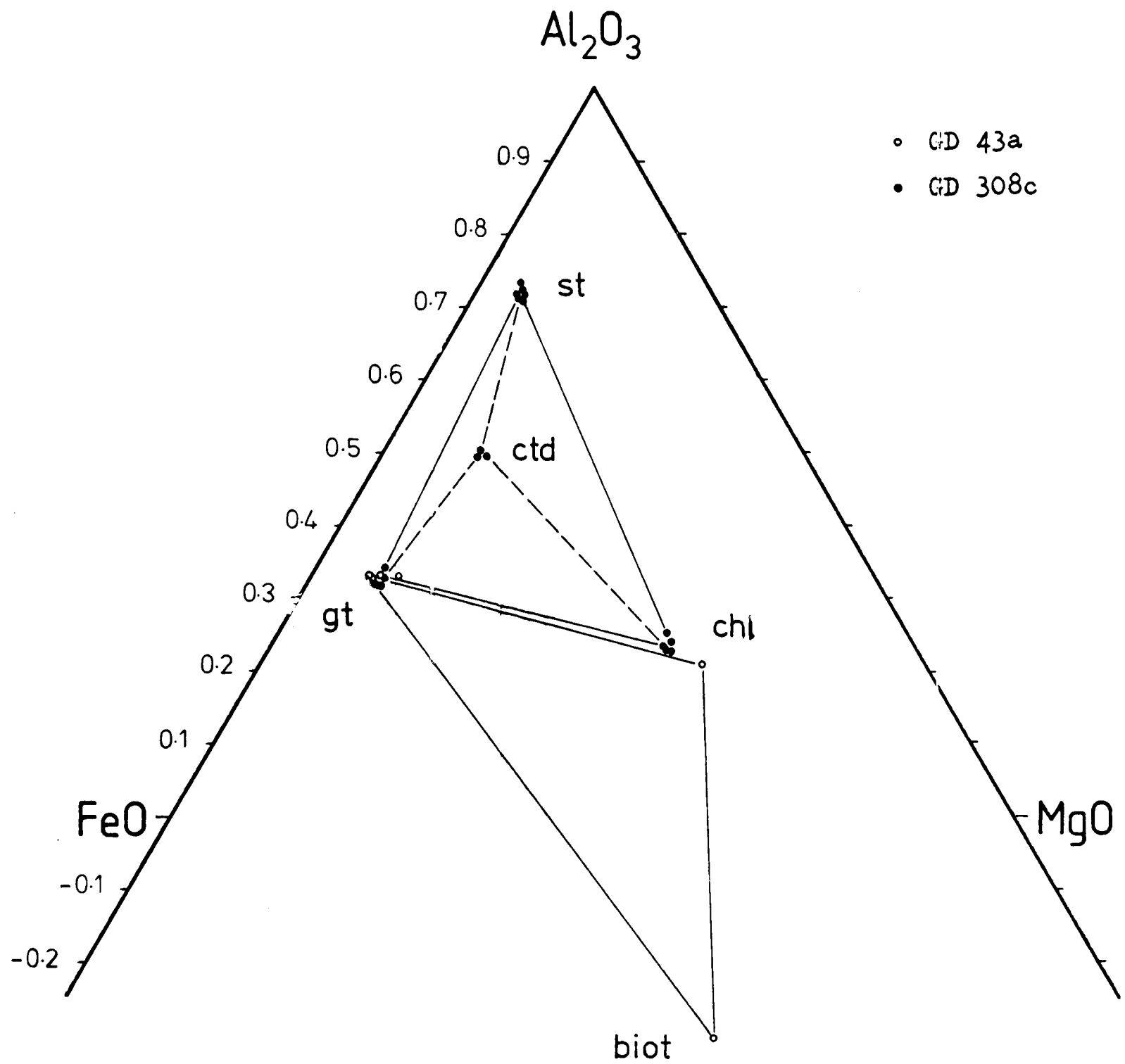



Fig. 6.10 Thompson AFM diagram for pelites from the garnet + staurolite + chlorite subzone.

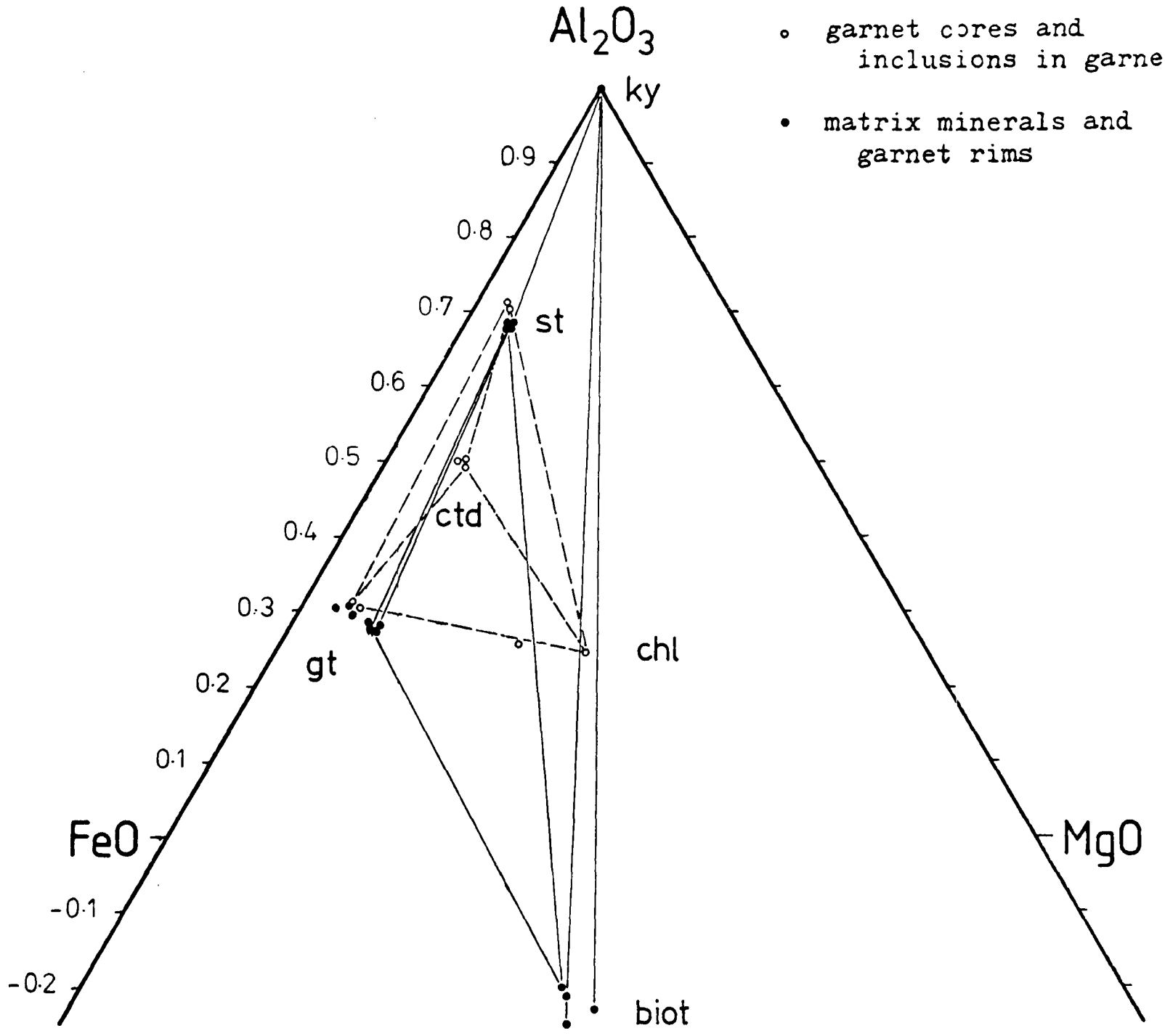



Fig. 6.11 Thompson AFM diagram for the staurolite + biotite zone pelite GD 18.

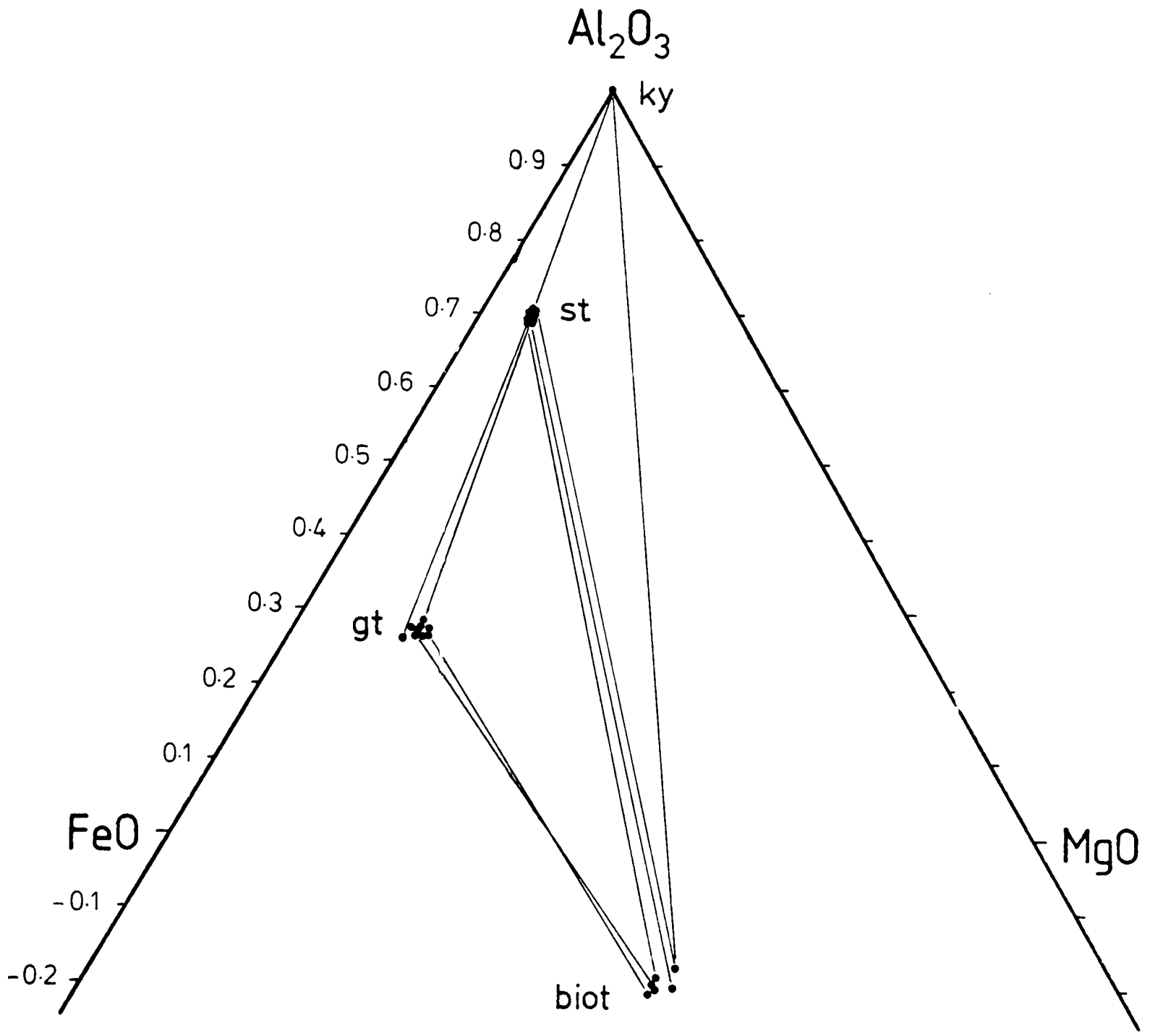



Fig. 6.12 Thompson AFM diagram for the staurolite + biotite zone pelite GD 209b.

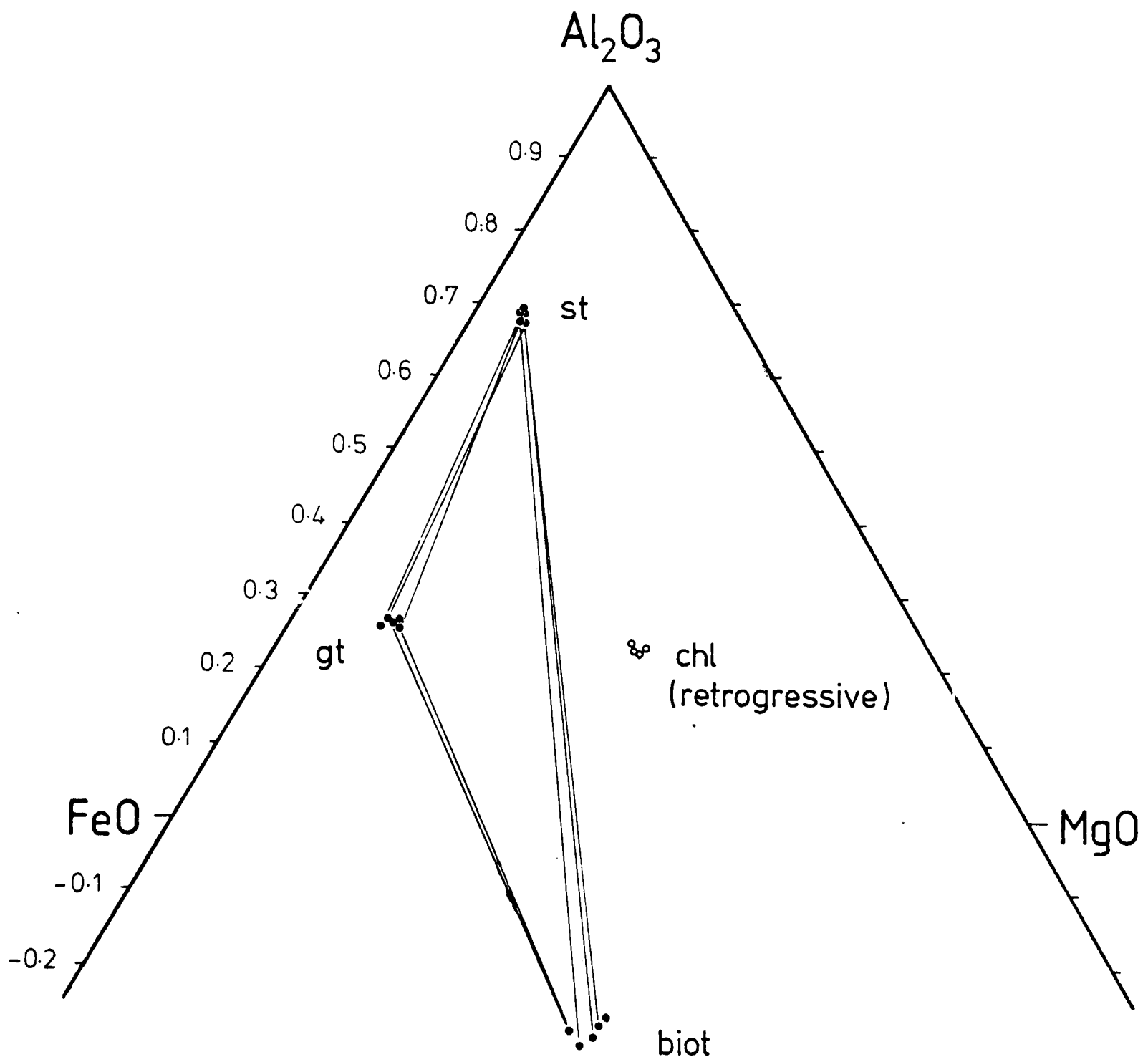



Fig. 6.13 Thompson AFM diagram for the staurolite + biotite zone pelite GD 465b.

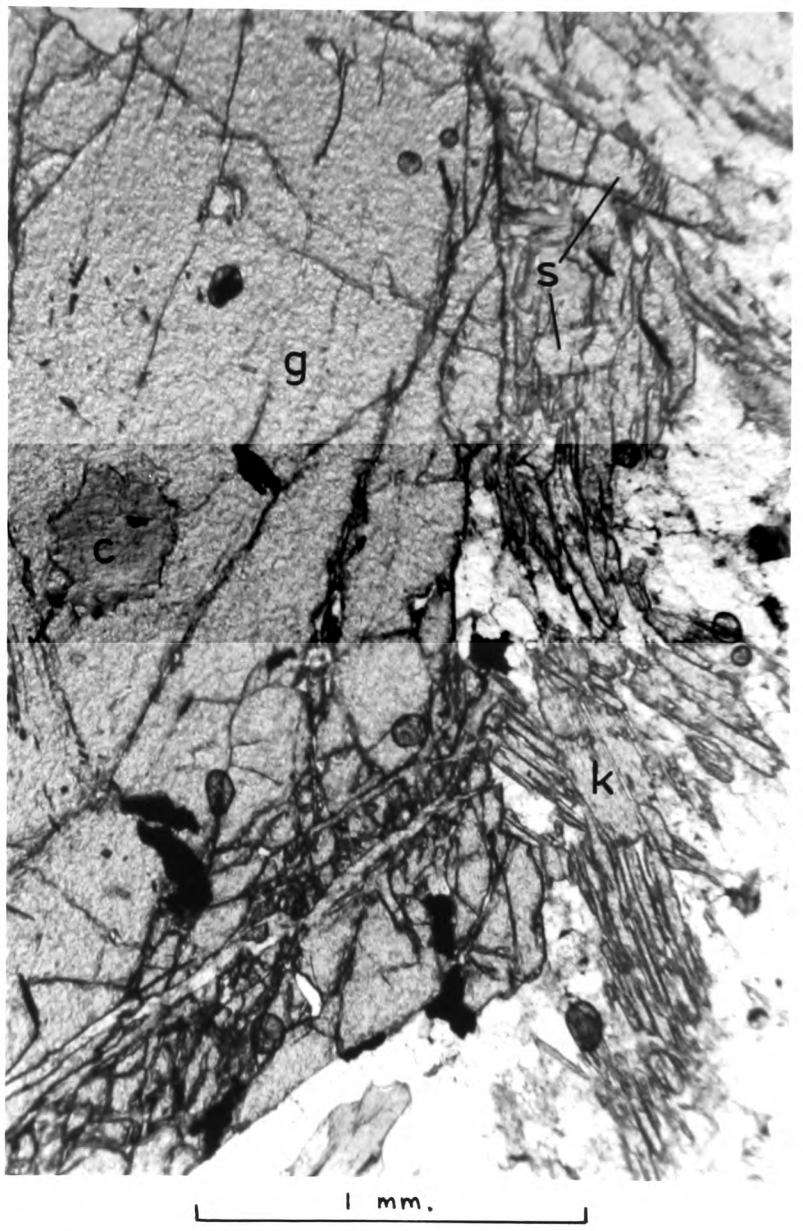



Fig. 6.14 Staurolite (s) and kyanite (k) surrounding garnet (g) which encloses chloritoid (c) in pelitic mica-schist GD 18. Plane polarised light.

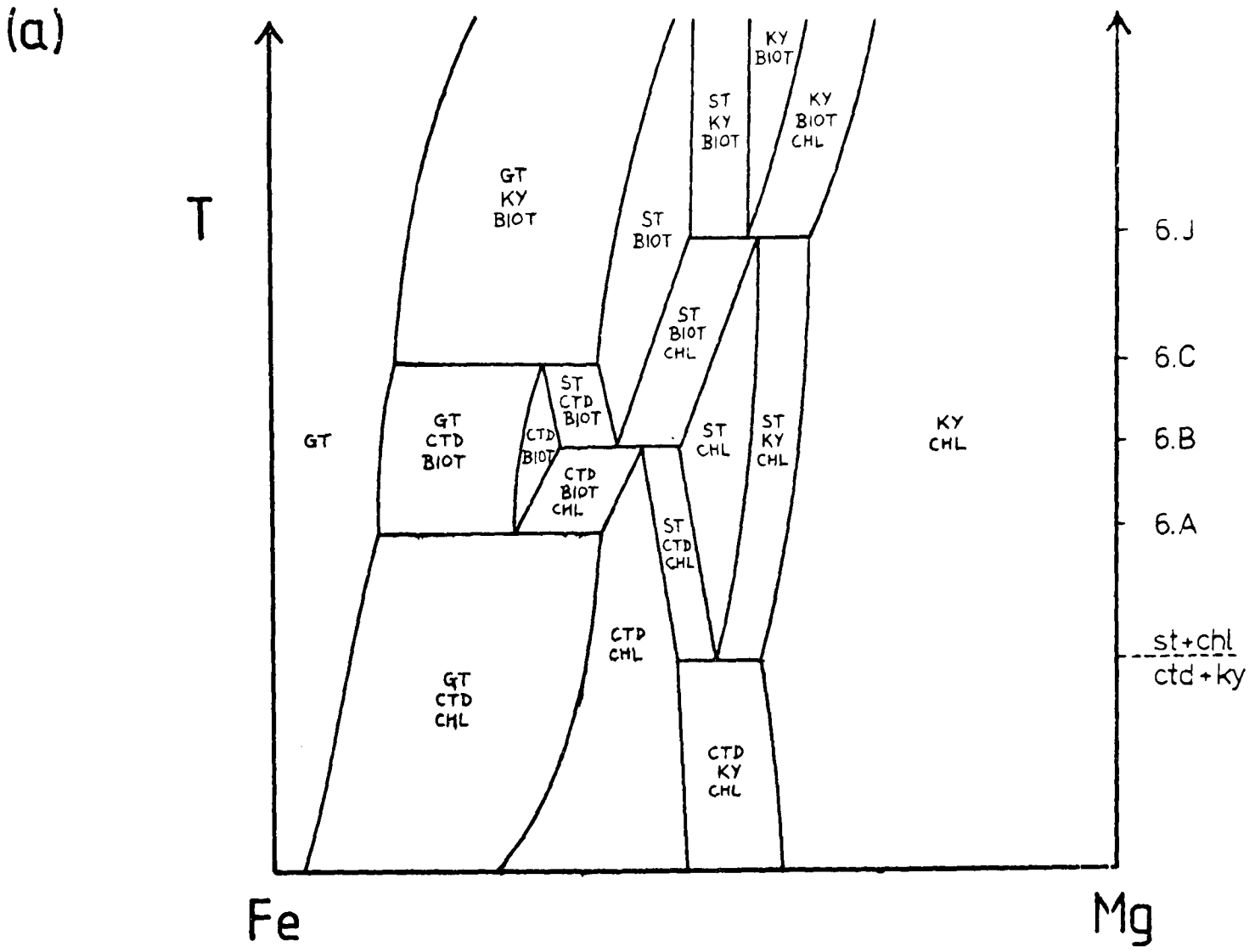



Fig. 6.15 Schematic T - X(Fe-Mg) sections in the pseudobinary system Fe-garnet - Mg-garnet for pelites of (a) the north-west Möltal, and (b) the south-east Möltal.

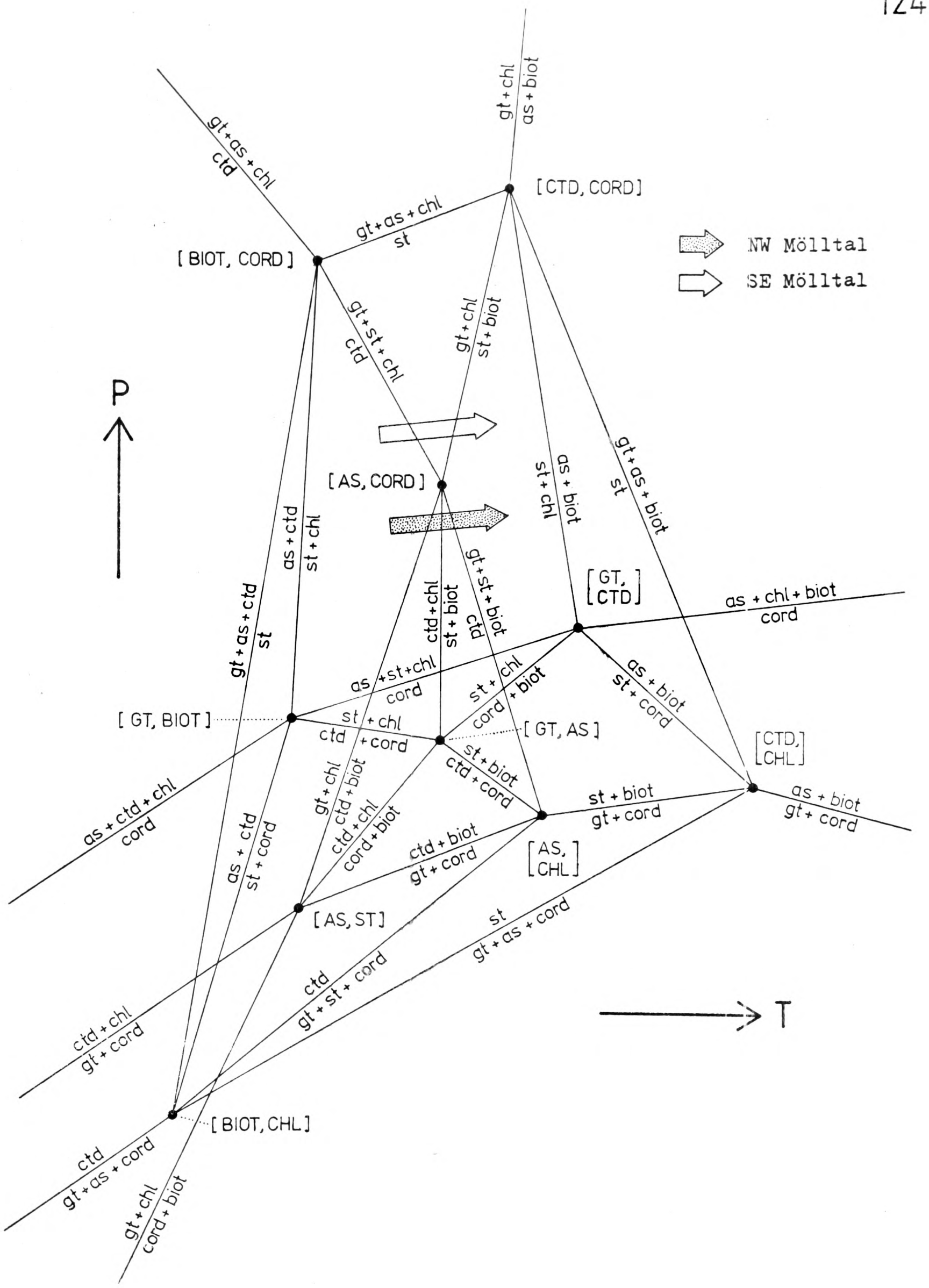



Fig. 6.16 The north-east Mölltal and south-west Mölltal facies series in relation to the preferred topology of the pelite petrogenetic grid (after Albee, 1965; Harte, 1975).

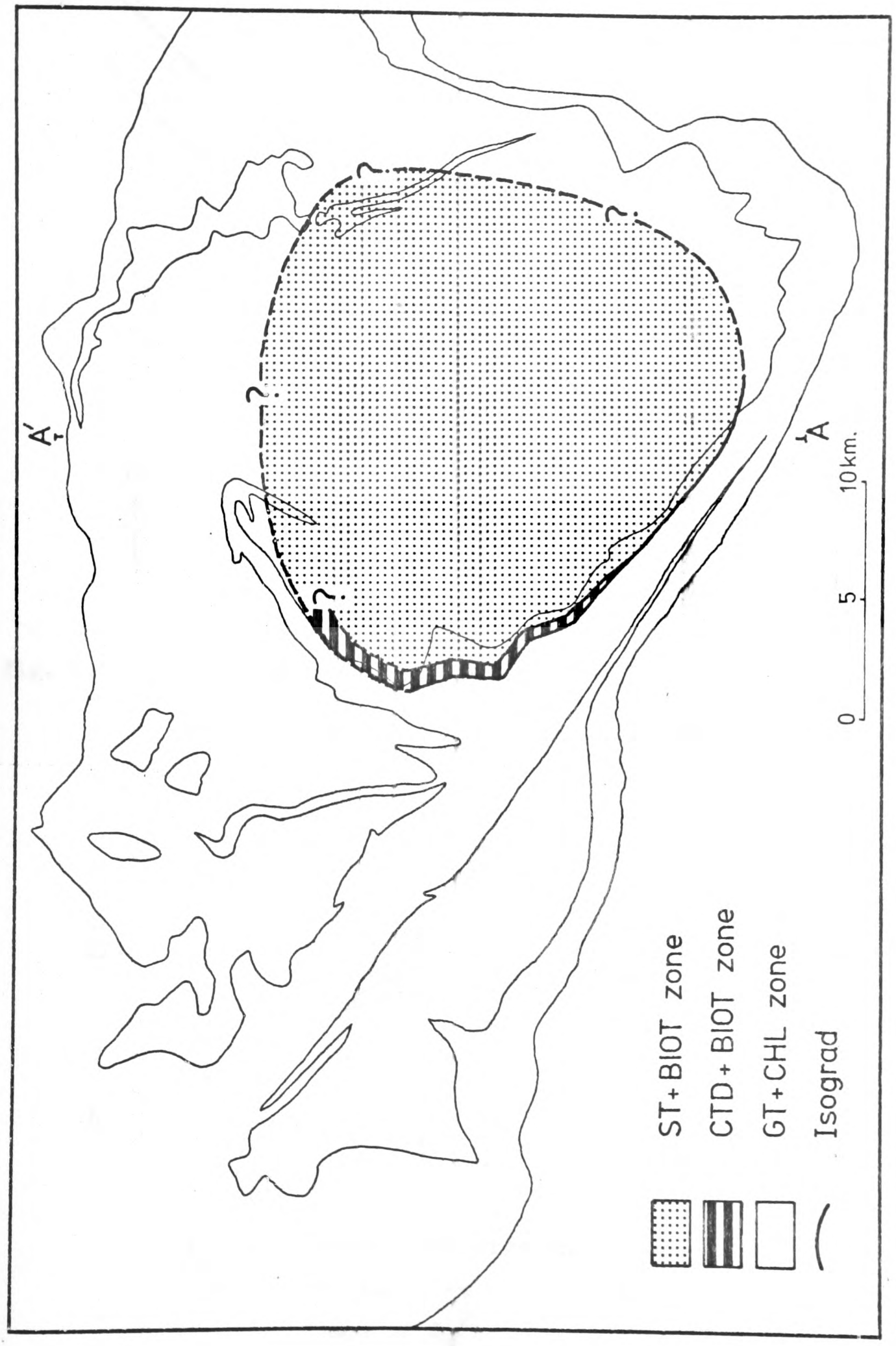



Fig. 6.17 $M_a$ metamorphic zones in the eastern Tauern window. See fig. 6.19 for section A-A'.

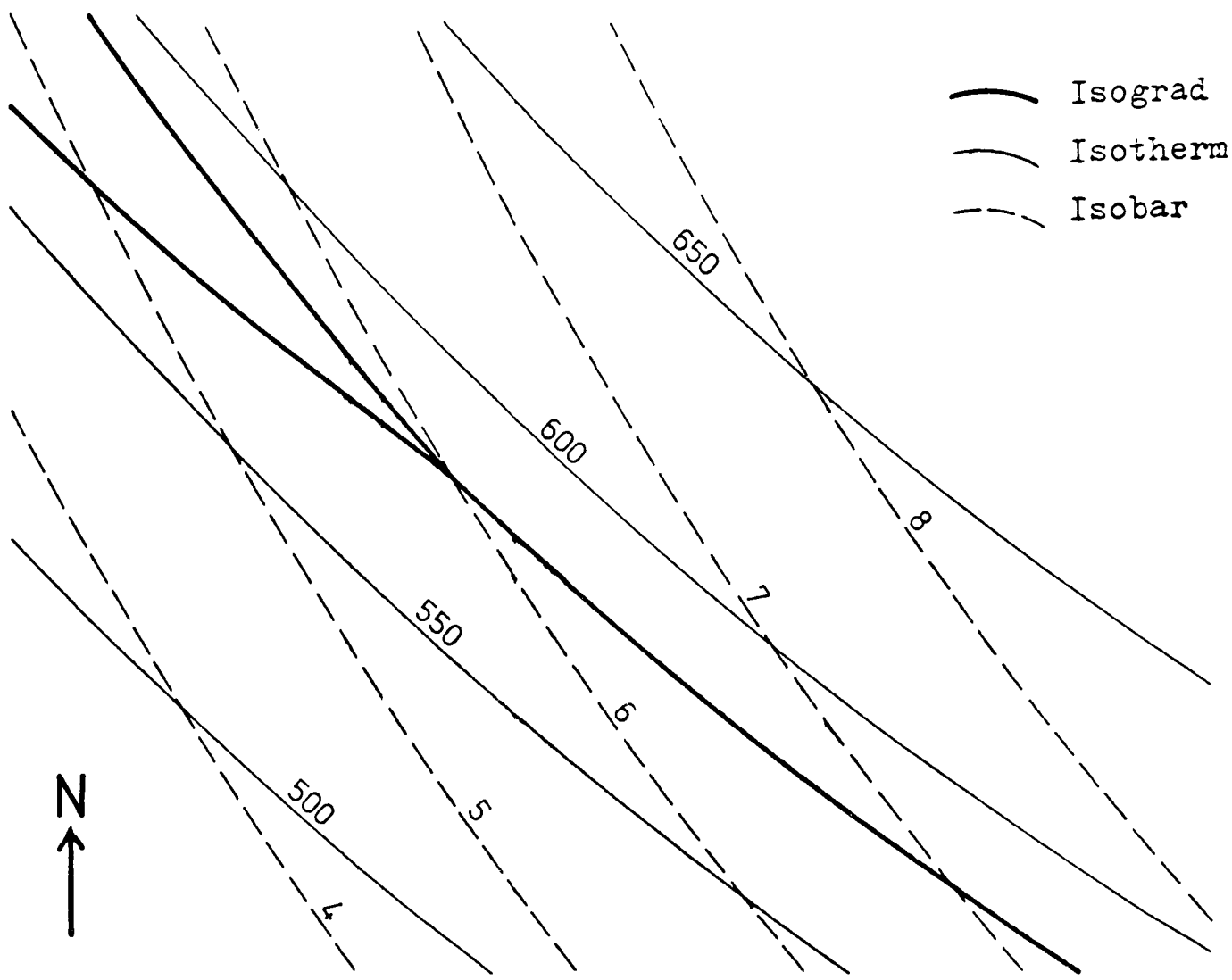



Fig. 6.18 Schematic map of the Mölltal region showing the relationship between isotherms, isobars and isograds on the erosion surface.

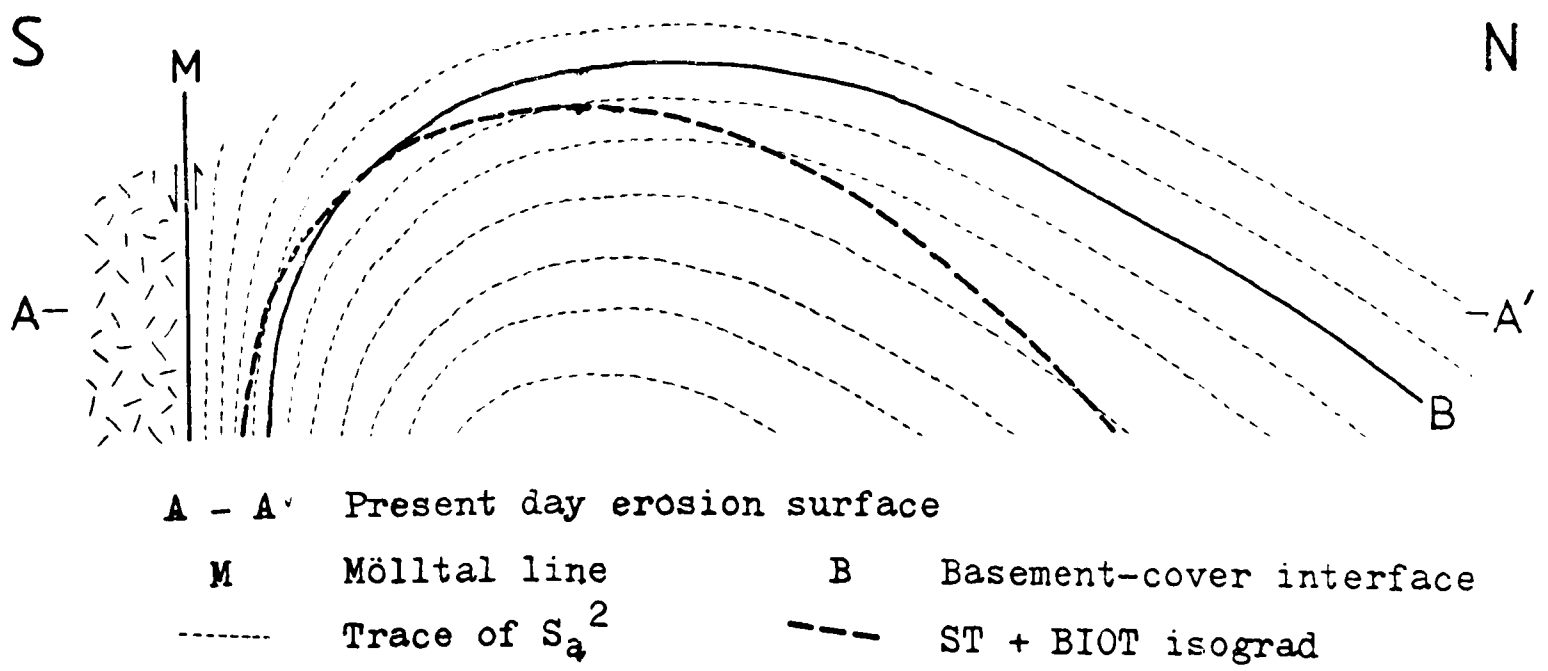



Fig. 6.19 A hypothetical north-south section through the eastern Tauern Window showing the angular relationship between the staurolite + biotite isograd and the basement-cover interface.

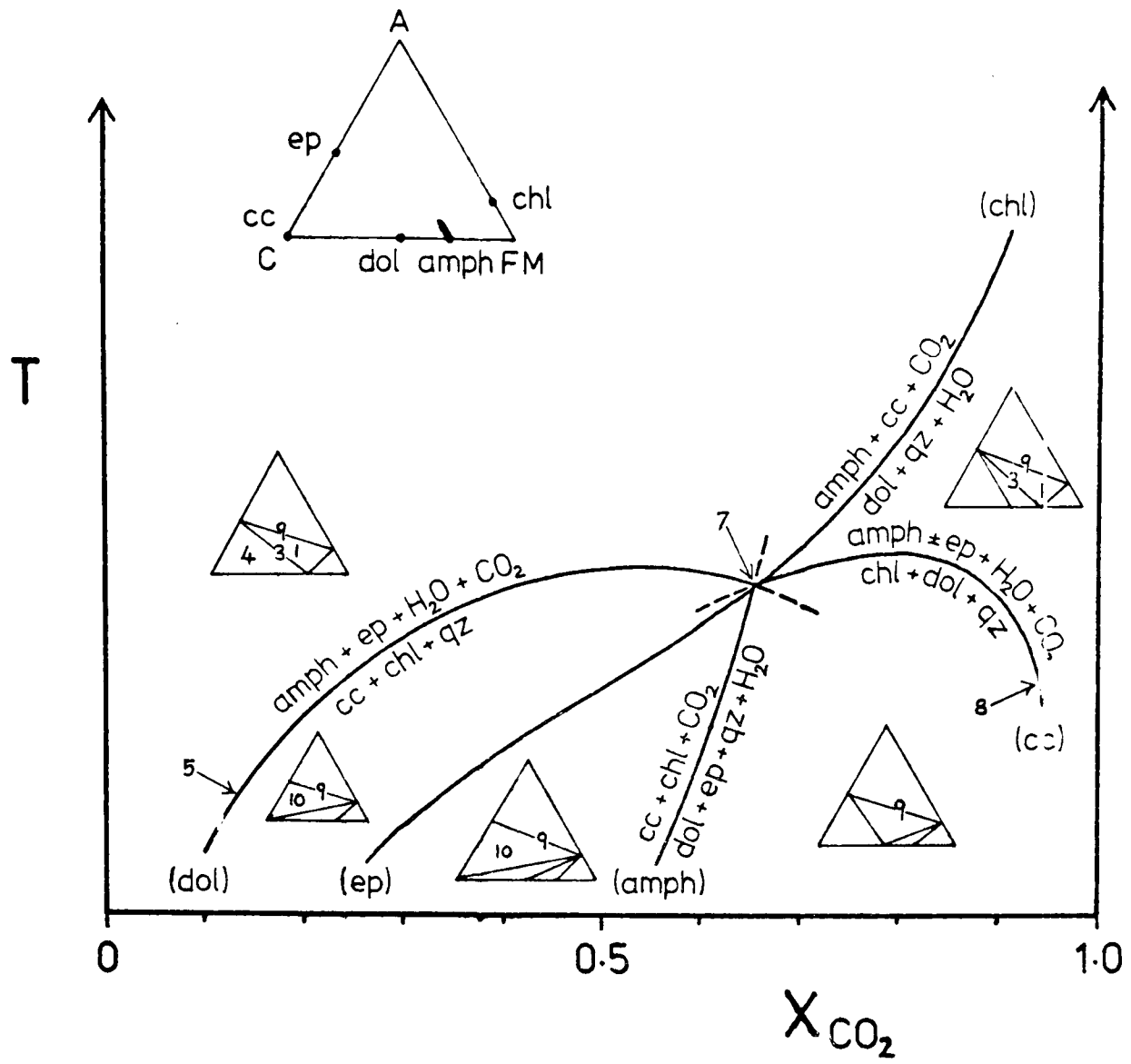



Fig. 6.20 Quartz + plagioclase bearing metabasite assemblages plotted in the schematic isobaric T - X ($CO_2$) section of Harte and Graham (1975).

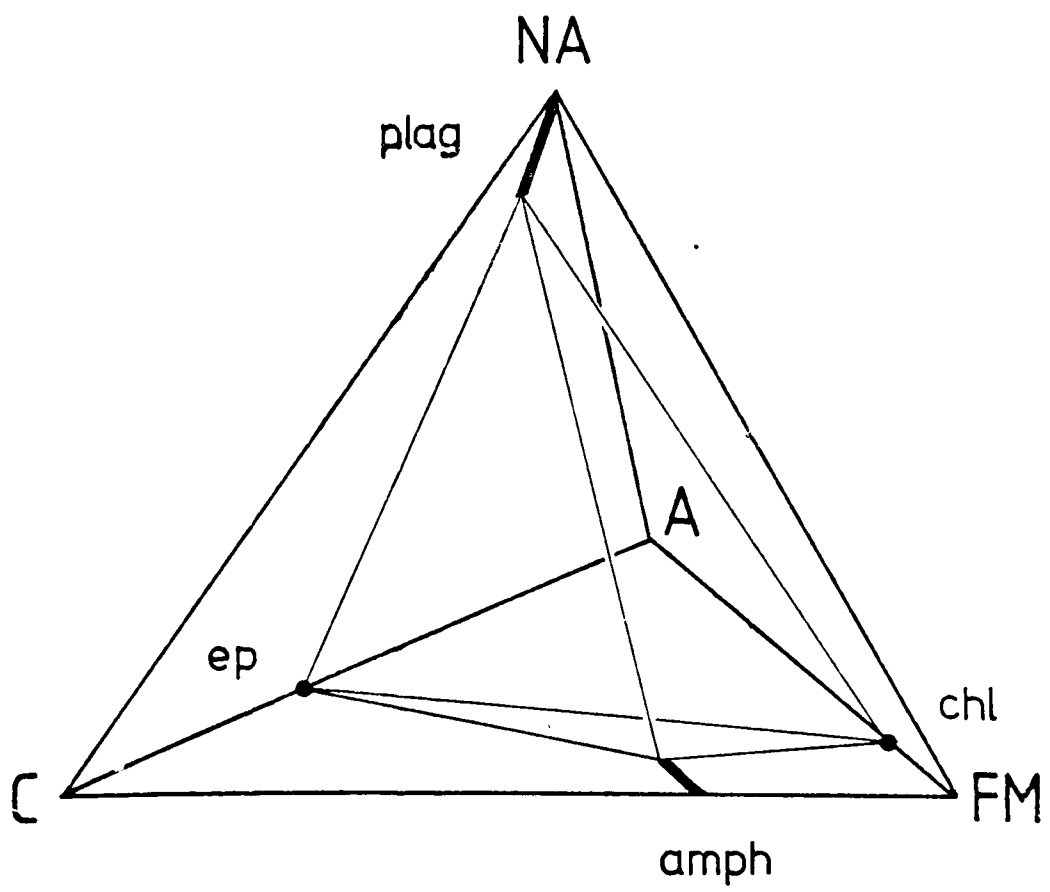



Fig. 6.21 Calcic amphibole, epidote, chlorite and plagioclase compatibility in Ernst's C-A-NA-FM tetrahedron.

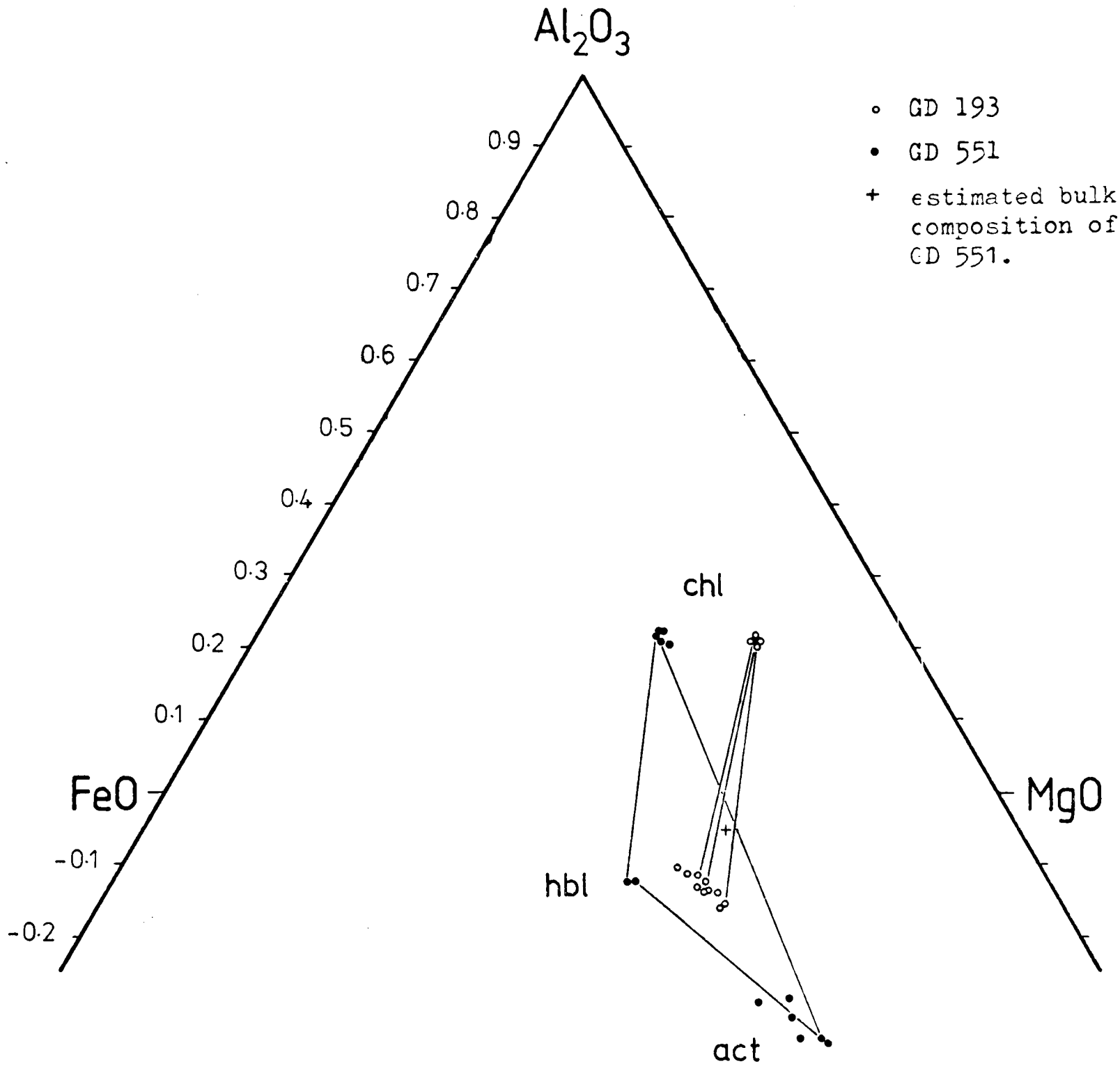



Fig. 6.22 Harte and Graham AFM diagram of two Peripheral Schieferhülle metabasites.

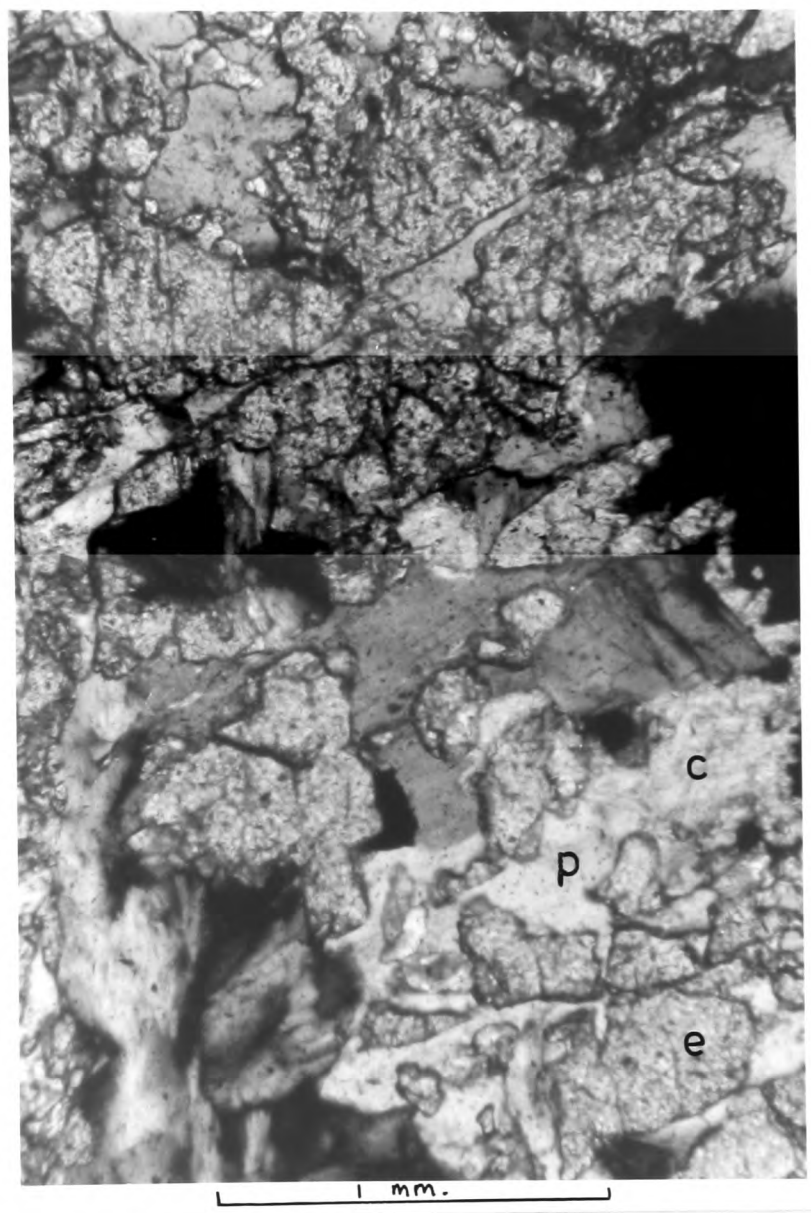



Fig. 6.23 Calcite (c) and plagioclase (p) replacing epidote (e) in epidote-amphibolite GD 482.

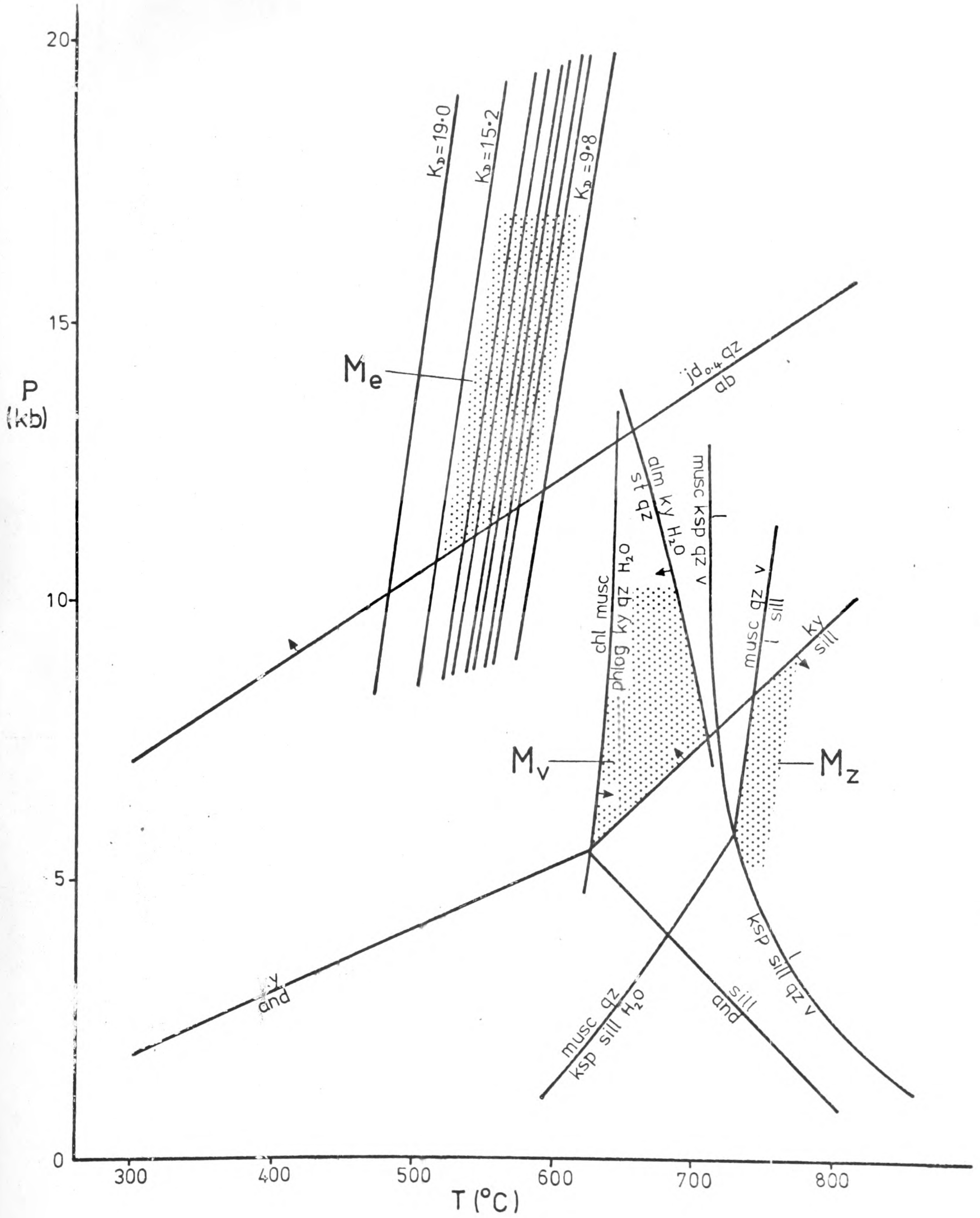



Fig. 7.1 Pre-Alpine metamorphic conditions. The arrow on a "stability limit" equilibrium curve indicates the side on which the relevant metamorphic assemblage is stable.

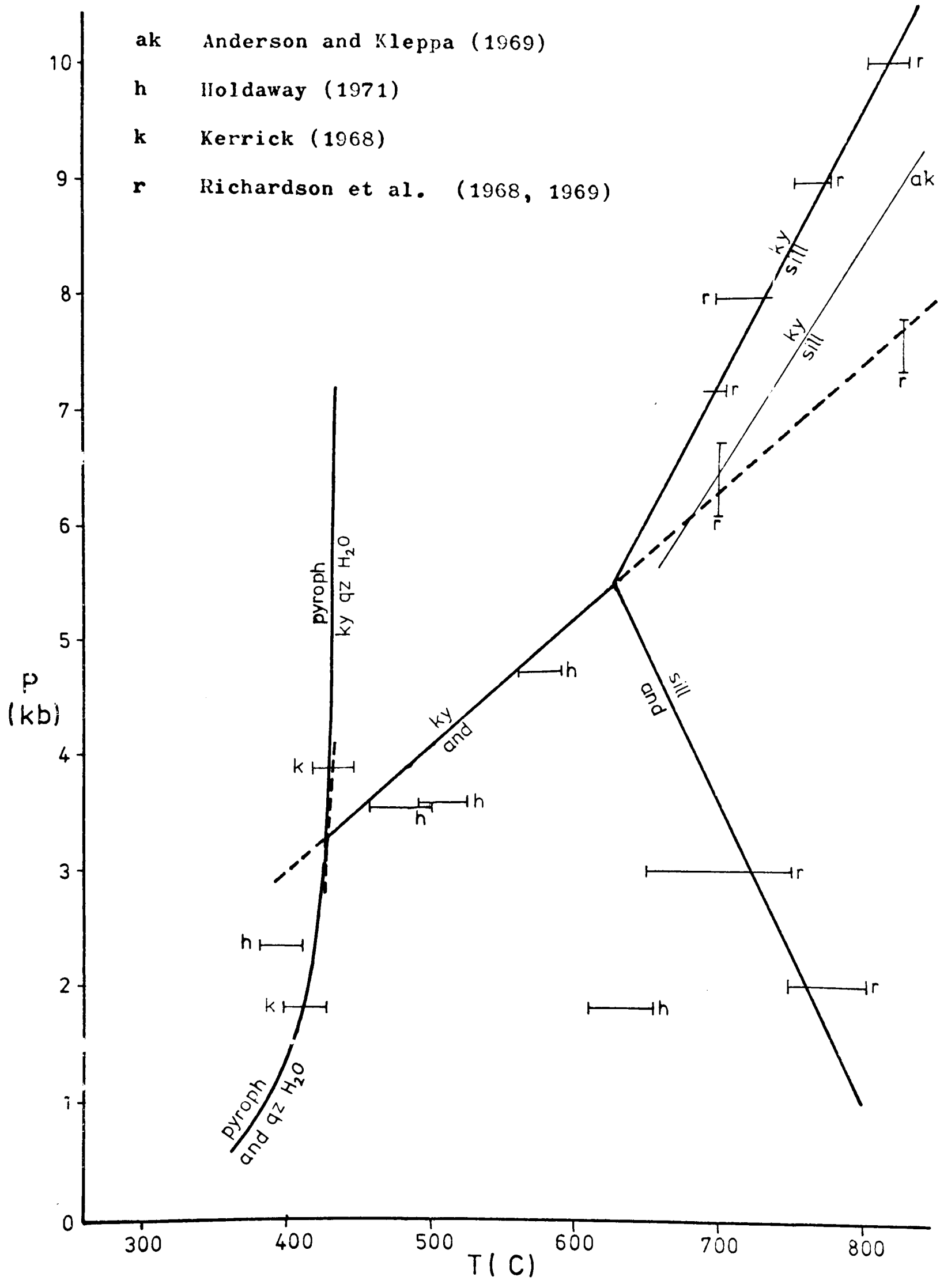



Fig. 7.2 Experimentally determined aluminosilicate equilibria.

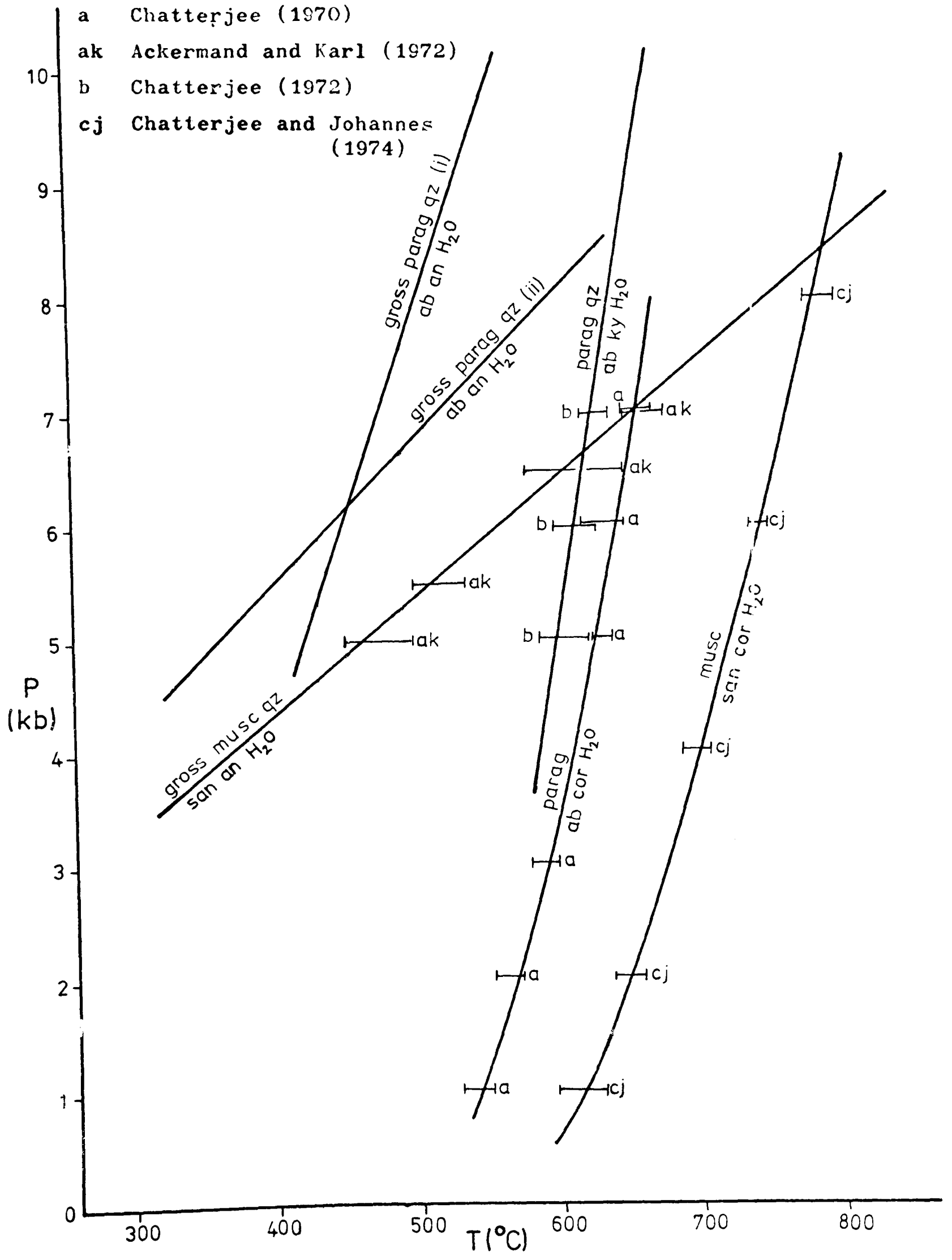



Fig. 7.3 Some experimentally reversed reactions used in the calculation of other equilibria, and the equilibrium position of reaction (7,W) calculated by two different methods (see text for explanation).

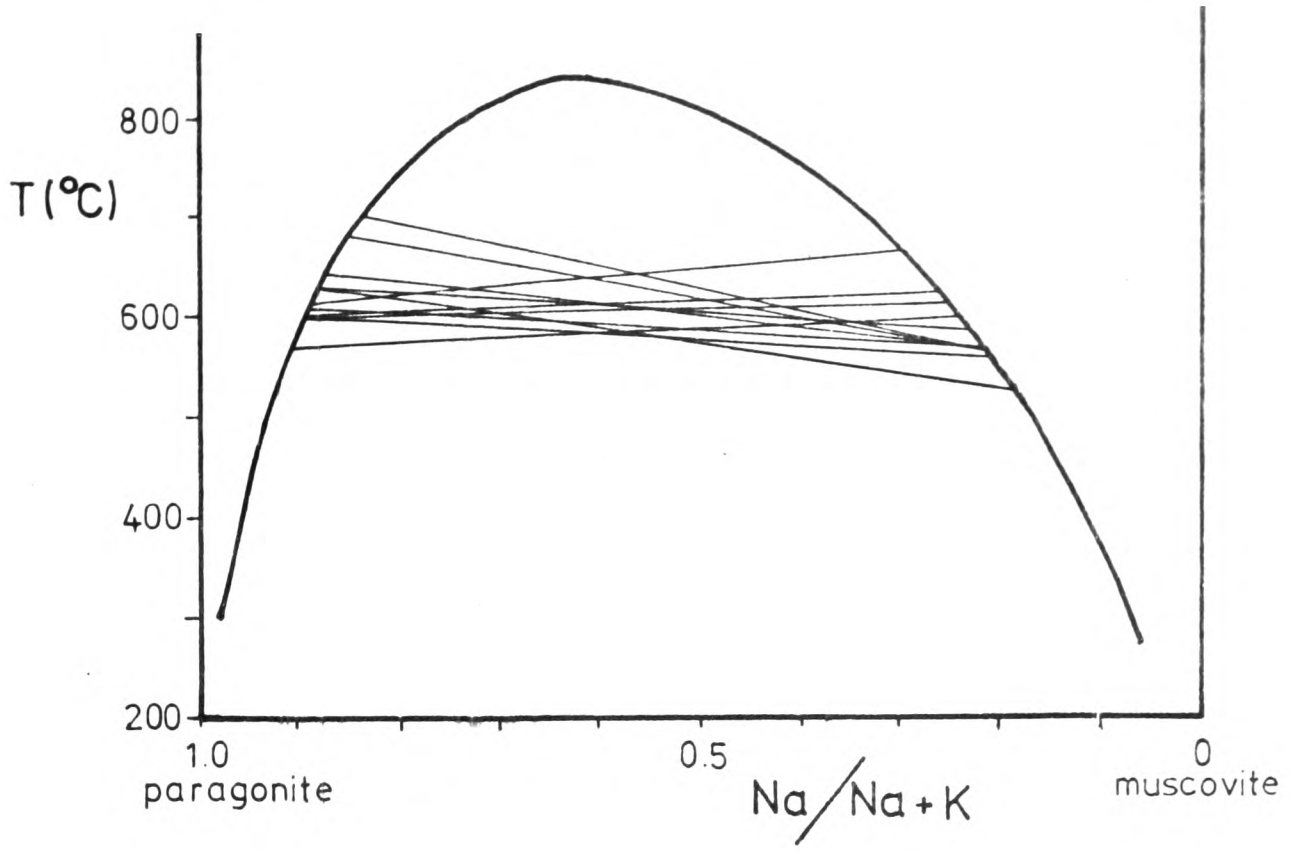



Fig. 7.4 The 2.07 kb muscovite-paragonite solvus of Eugster et al. (1972), showing tie-lines linking the compositions of coexisting micas in GD 208e and GD 465b.

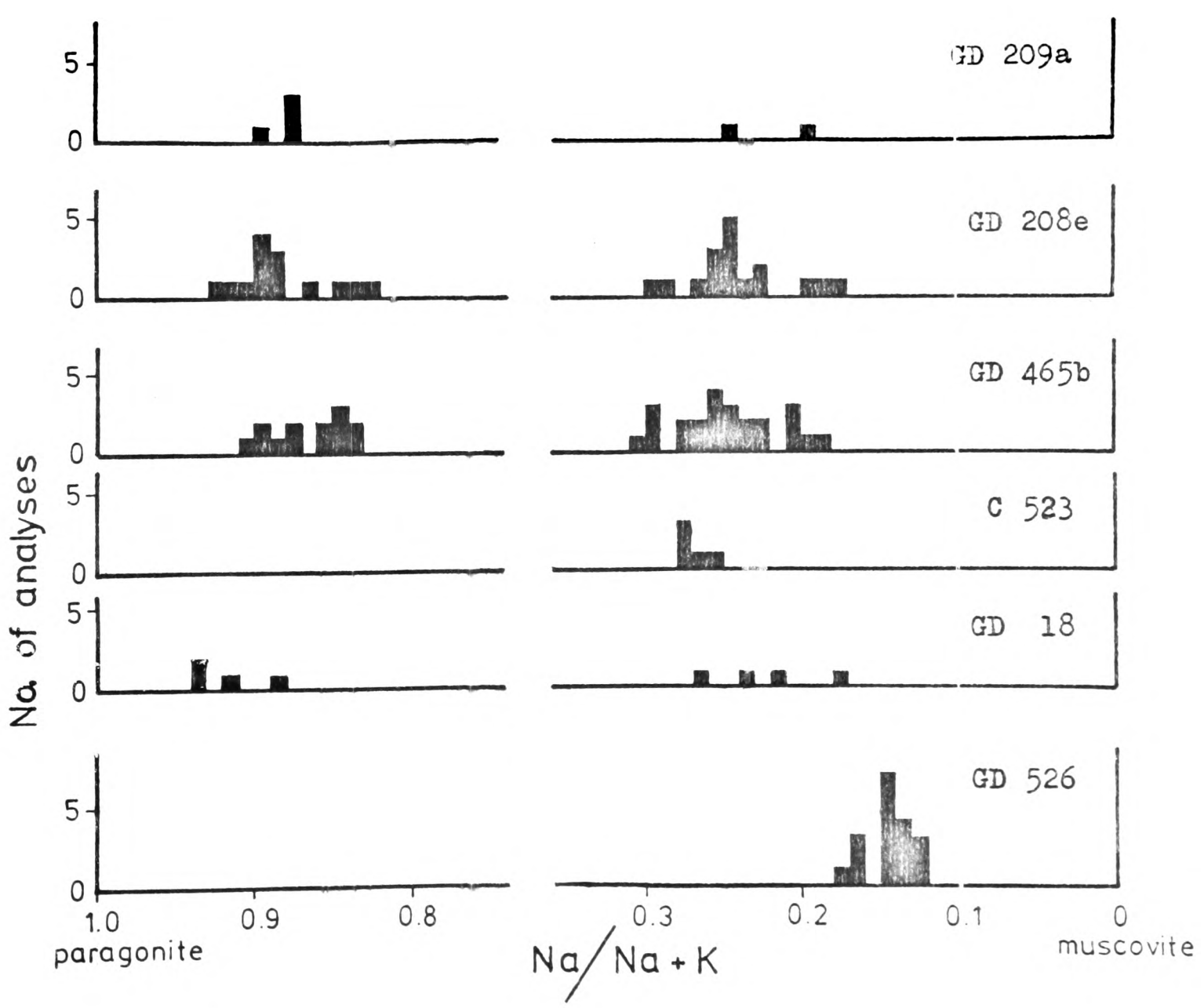



Fig. 7.5 Muscovite and paragonite compositions in various aluminous pelites. All rocks contain paragonite except C523.

Table 7.1 Average Na/Na+K values and calculated solvus temperatures for muscovites and paragonites in aluminous pelites. All rocks except C 523 contain paragonite. 90% confidence limits are given for the larger samples.

| Sample | No. of analyses | Mean $\frac{Na}{Na+K}$ | Mean T(°C) | Structural depth below base of Möltal Schieferhülle |
|---|---|---|---|---|
| PARAGONITES | | | | |
| GD 465b | 13 | 0.865 ± 0.044 | 650 ± 80 | 4 |
| GD 208e | 14 | 0.880 ± 0.052 | 620 ± 80 | $2\frac{1}{4}$ |
| GD 209a | 4 | 0.880 | 620 | $2\frac{1}{4}$ |
| GD 18 | 4 | 0.917 | 540 | 0 |
| MUSCOVITES | | | | |
| GD 465b | 24 | 0.248 ± 0.057 | 607 ± 68 | 4 |
| C 523 | 5 | 0.268 | 633 | $3\frac{1}{2}$ |
| GD 208e | 17 | 0.239 ± 0.055 | 596 ± 68 | $2\frac{1}{4}$ |
| GD 209a | 2 | 0.222 | 580 | $2\frac{1}{4}$ |
| GD 18 | 4 | 0.219 | 570 | 0 |
| GD 526 | 18 | 0.144 ± 0.024 | 460 ± 43 | MM |

MM : From the Mallnitzer Mulde

Table 7.2 Some reactions involving FASH phases. Reactions have been balanced using the mineral formulae listed at the bottom of the table.

$$3\ \text{Fe ctd} = \text{alm} + 2\ \text{cor} + 3\ H_2O \quad (7.J)$$

$$3\ \text{Fe ctd} + 2\ \text{qz} = \text{alm} + 2\ \text{ky} + 3\ H_2O \quad (7.K)$$

$$8\ \text{Fe ctd} + 10\ \text{ky} = 2\ \text{Fe st} + 3\ \text{qz} + 4\ H_2O \quad (7.L)$$

$$8\ \text{Fe ctd} + 10\ \text{sill} = 2\ \text{Fe st} + 3\ \text{qz} + 4\ H_2O \quad (7.M)$$

$$6\ \text{Fe st} + 25\ \text{qz} = 8\ \text{alm} + 46\ \text{ky} + 12\ H_2O \quad (7.D)$$

$$6\ \text{Fe st} + 25\ \text{qz} = 8\ \text{alm} + 46\ \text{sill} + 12\ H_2O \quad (7.N)$$

$$23\ \text{Fe ctd} + 7\ \text{qz} = 2\ \text{Fe st} + 5\ \text{alm} + 19\ H_2O \quad (7.O)$$

$$4\ \text{Fe ctd} + 6\ \text{qz} = 2\ \text{Fe cord} + 3\ H_2O \quad (7.P)$$

$$2\ \text{Fe st} + 15\ \text{qz} = 4\ \text{Fe cord} + 10\ \text{sill} + 2\ H_2O \quad (7.Q)$$

$$23\ \text{Fe cord} = 4\ \text{Fe st} + 10\ \text{alm} + 55\ \text{qz} + 3.5\ H_2O \quad (7.R)$$

$$3\ \text{Fe cord} = 2\ \text{alm} + 4\ \text{sill} + 5\ \text{qz} + 1.5\ H_2O \quad (7.S)$$

$$\text{ky} = \text{sill} \quad (7.C)$$

almandine : $Fe_3Al_2Si_3O_{12}$

Fe - staurolite : $Fe_4Al_{18}Si_{7.5}O_{44}(OH)_4$

Fe - chloritoid : $FeAl_2SiO_5(OH)_2$

Fe - cordierite : $Fe_2Al_4Si_5O_{18}\cdot\frac{1}{2}H_2O$

kyanite, sillimanite : $Al_2SiO_5$

quartz : $SiO_2$

corundum : $Al_2O_3$

Table 7.3 Thermodynamic data for the reactions listed in table 7.2.

| Reaction | $\Delta_f H^o_s$ (k cal) | $\Delta_f S^o_s$ (cal/K) | $\Delta V_s$ (cal/bar) |
|---|---|---|---|
| (7.J) | 301.7 | 225.1 | -0.9921 |
| (7.K) | 298.0 | 221.0 | -1.1911 |
| (7.L) | 472.9 | 397.0 | -0.8124 |
| (7.M) | 451.5 | 364.6 | -2.1984 |
| (7.D) | 965.0 | 577.0 | -7.0916 |
| (7.N) | 1063.4 | 726.0 | -0.7160 |
| (7.O) | 1962.7 | 1502.0 | -6.7679 |
| (7.P) | 323.9 | 263.8 | 1.4436 |
| (7.Q) | 196.2 | 163.0 | 5.0856 |
| (7.R) | 201.1 | -29.5 | -35.223 |
| (7.S) | 118.7 | 59.3 | -3.9932 |
| (7.C) | 2.14 | 3.24 | 0.1386 |

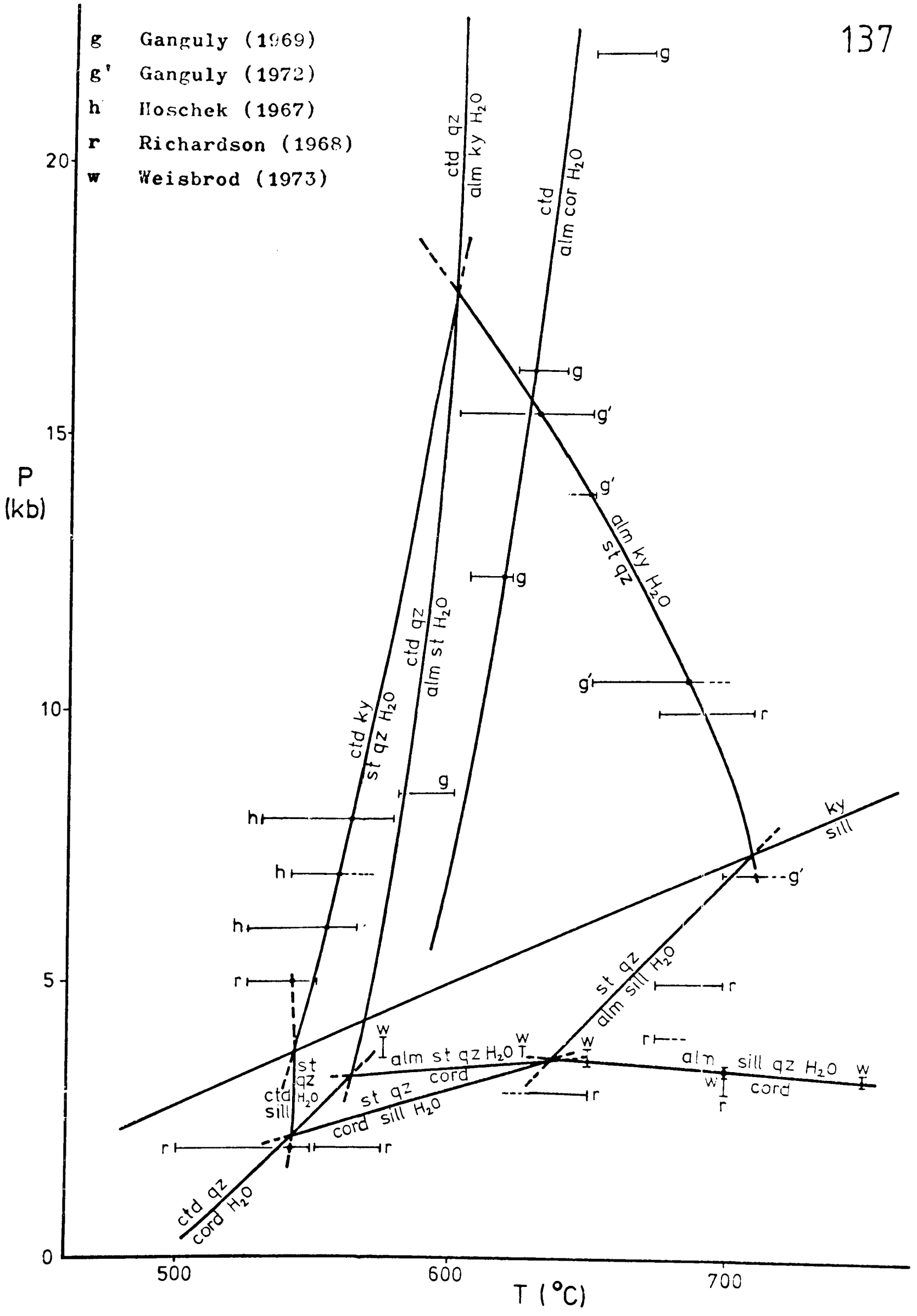



Fig. 7.6 A comparison of calculated equilibrium curves and experimental reversals for reactions involving FASH phases.

**Experimental** brackets:

b Boettcher (1970)

c Chatterjee (1974a)

n Newton (1966)

s Storre and Nitsch (1974)

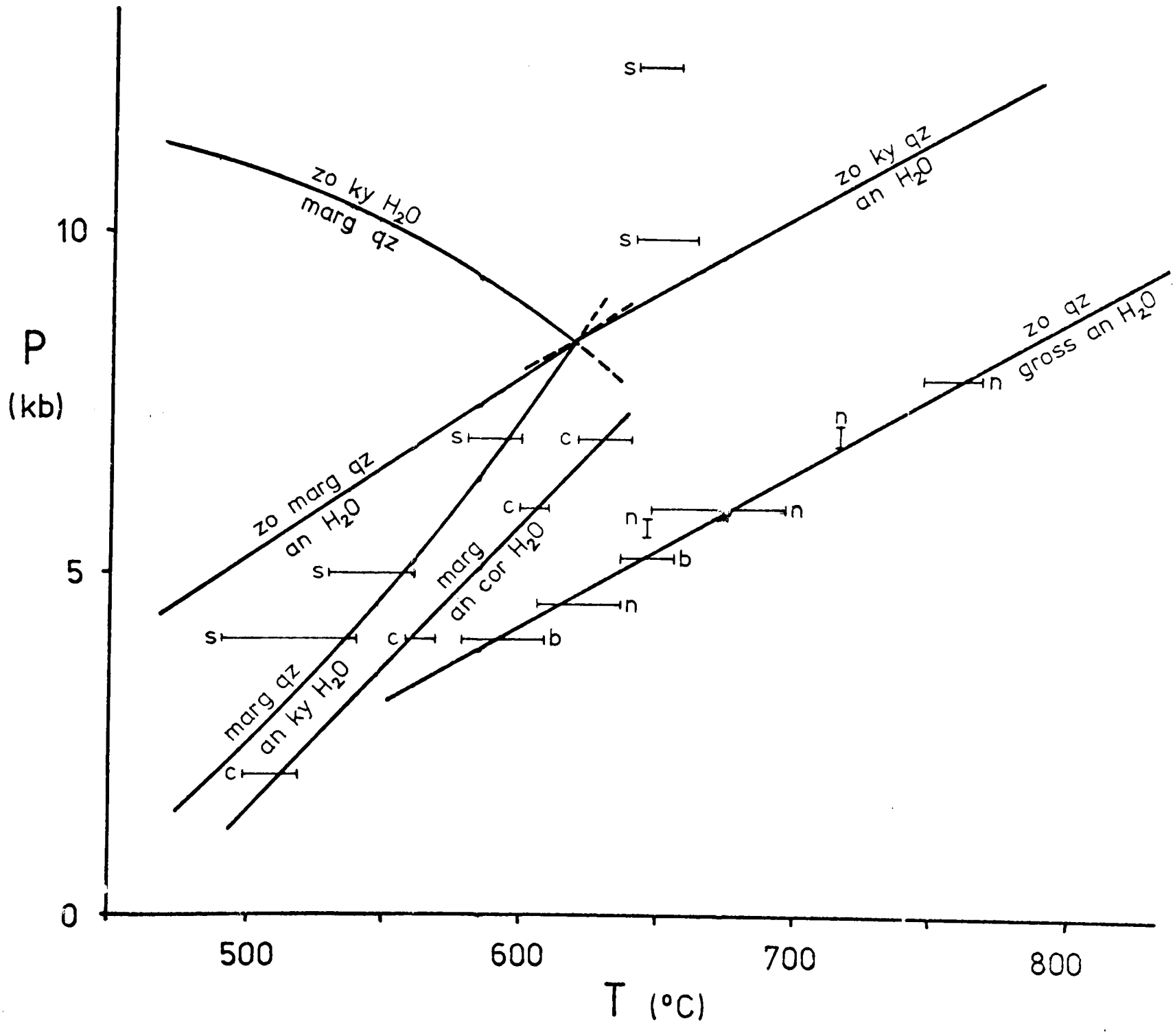



Fig. 7.7 **Calculated and experimentally determined equilibrium curves for reactions involving** CASH phases.

1-6 For individual groups of mineral grains in contact, GD 145a, $\gamma an=1.28$

7 For average mineral compositions, GD 145a, $\gamma an=1.28$

8 For average mineral compositions, GD 145a, $\gamma an=1.5$

9 For average mineral compositions, GD 43a, $\gamma an=1.28$

10 For average mineral compositions, GD 480a, $\gamma an=1.28$

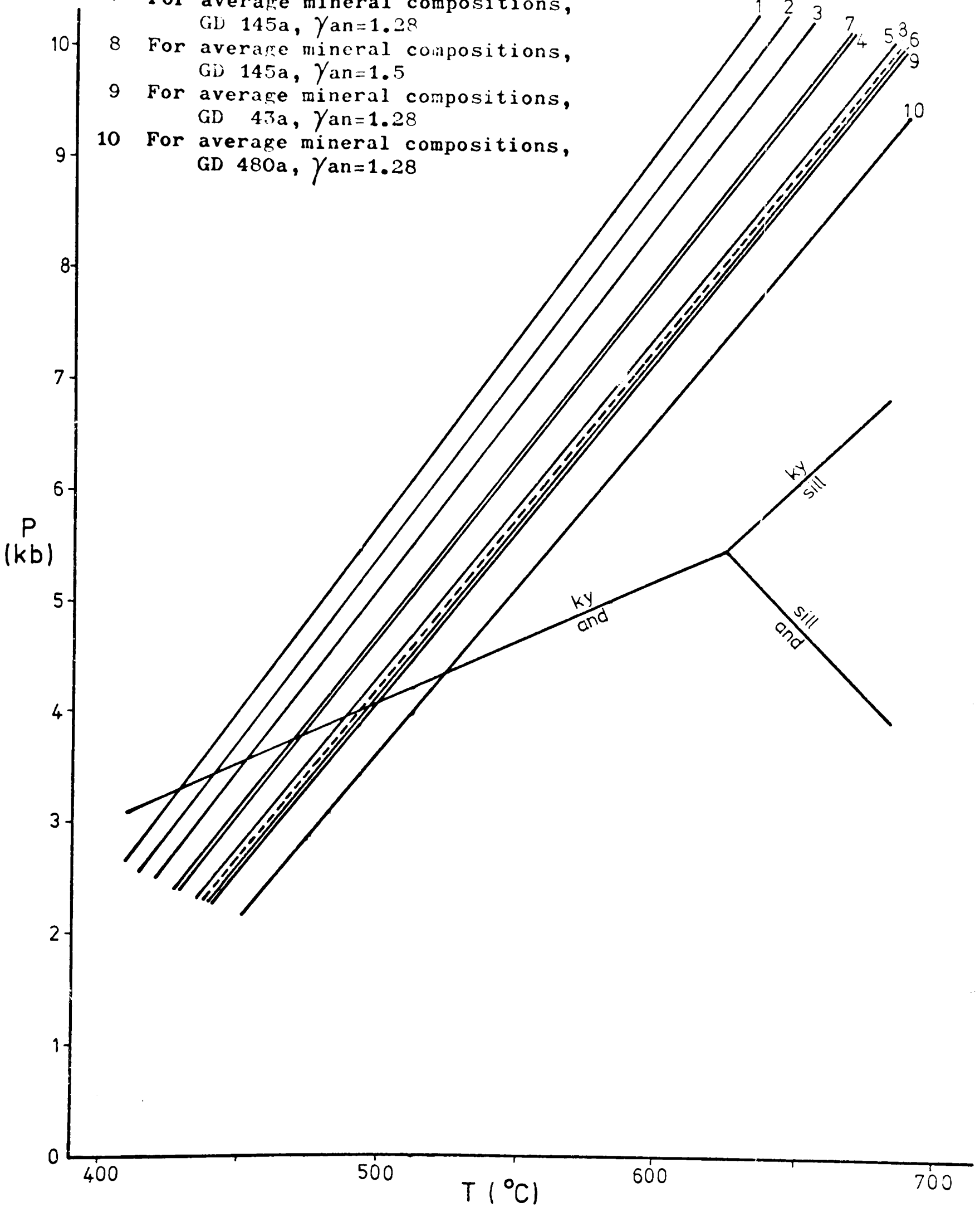



Fig. 7.8 Calculated equilibrium curves for reaction (7, T) taking into account real mineral compositions.

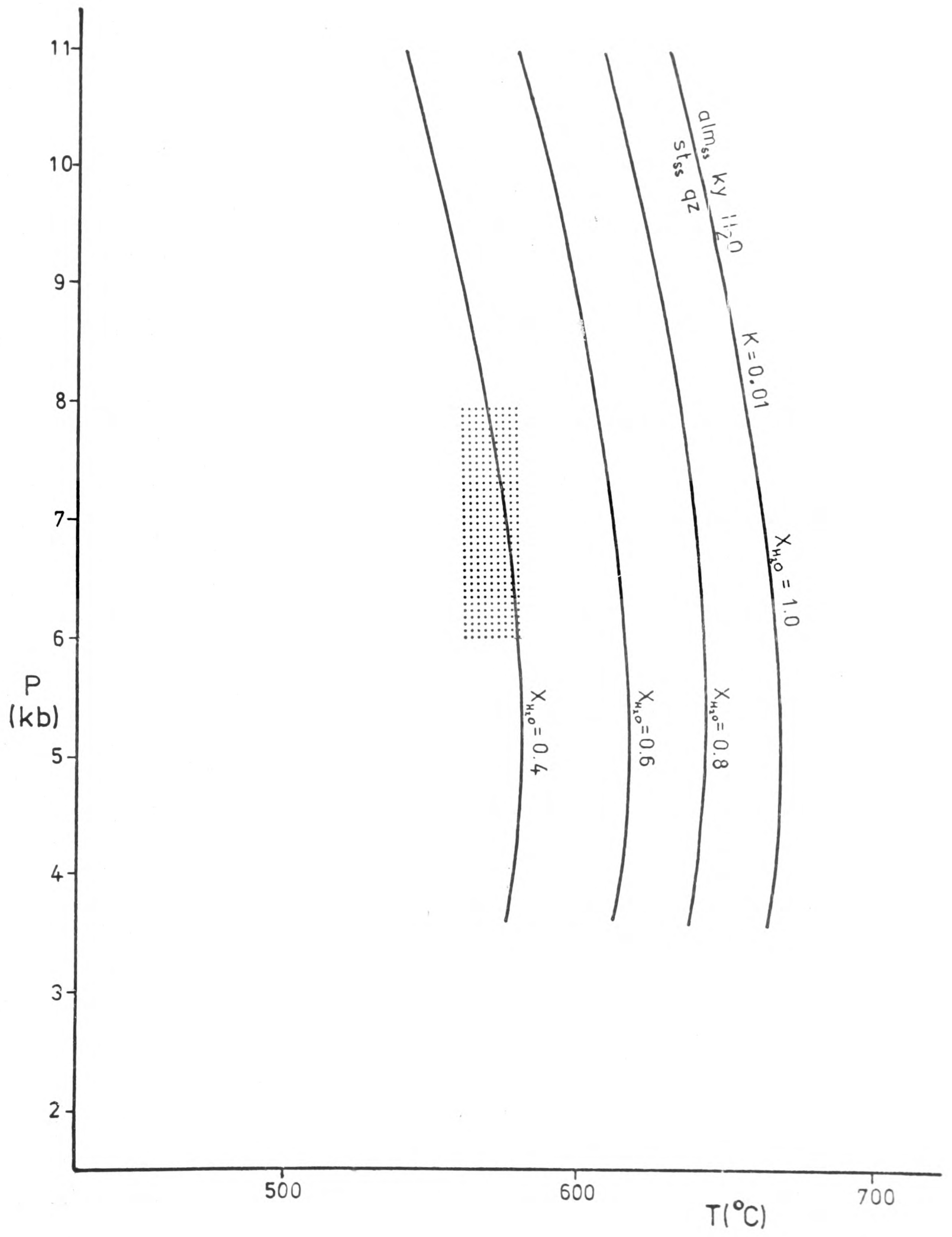



**Fig. 7.9** Calculated equilibrium curves for reaction (7,D) at different values of $X_{H_2O}$ for mineral compositions in pelite GD 18.

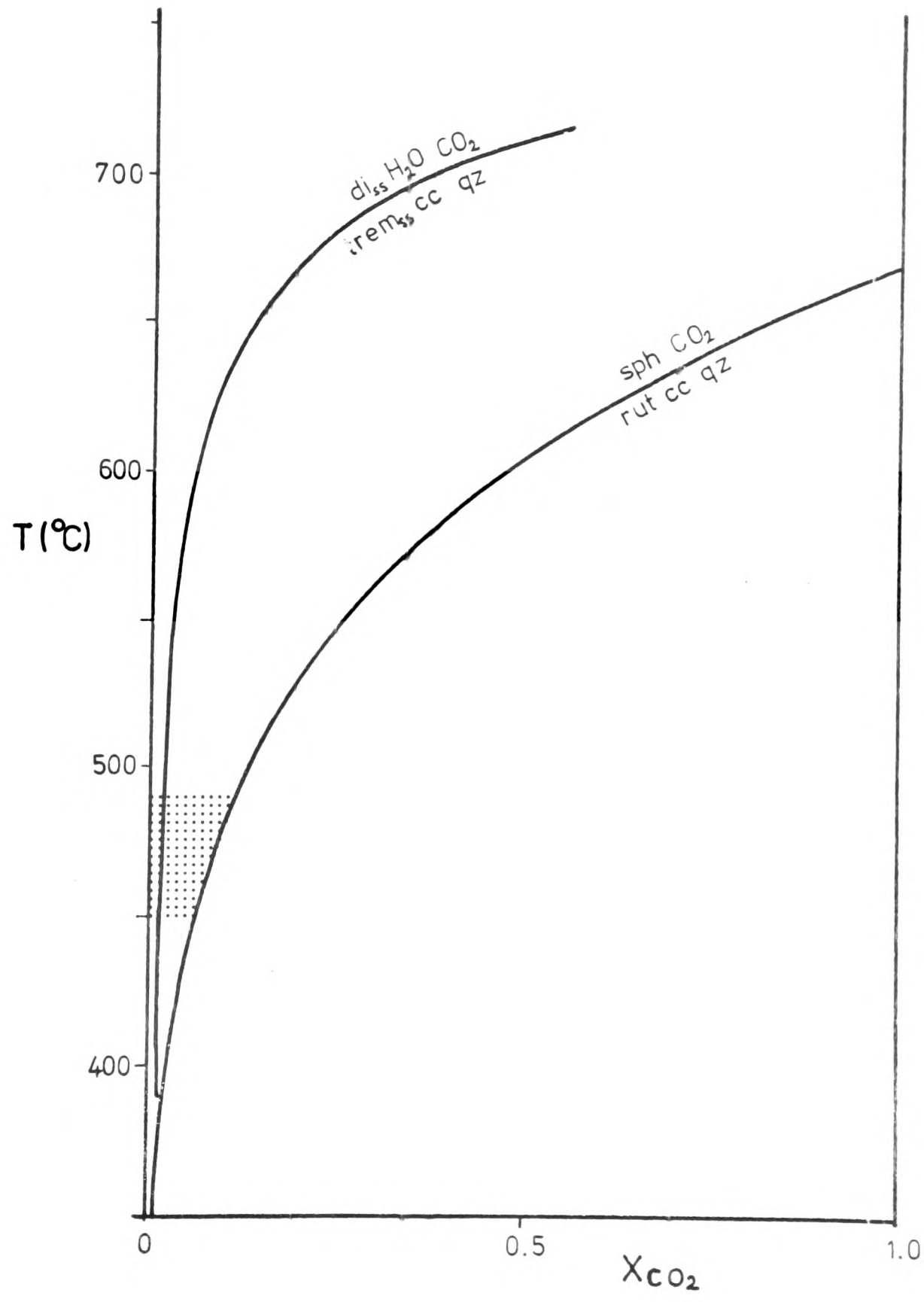



Fig. 7.10 5kb T-$X_{CO_2}$ diagram showing equilibria relevant to syenite-gneiss stability. Stippled area: estimated conditions of syenite-gneiss metamorphism.

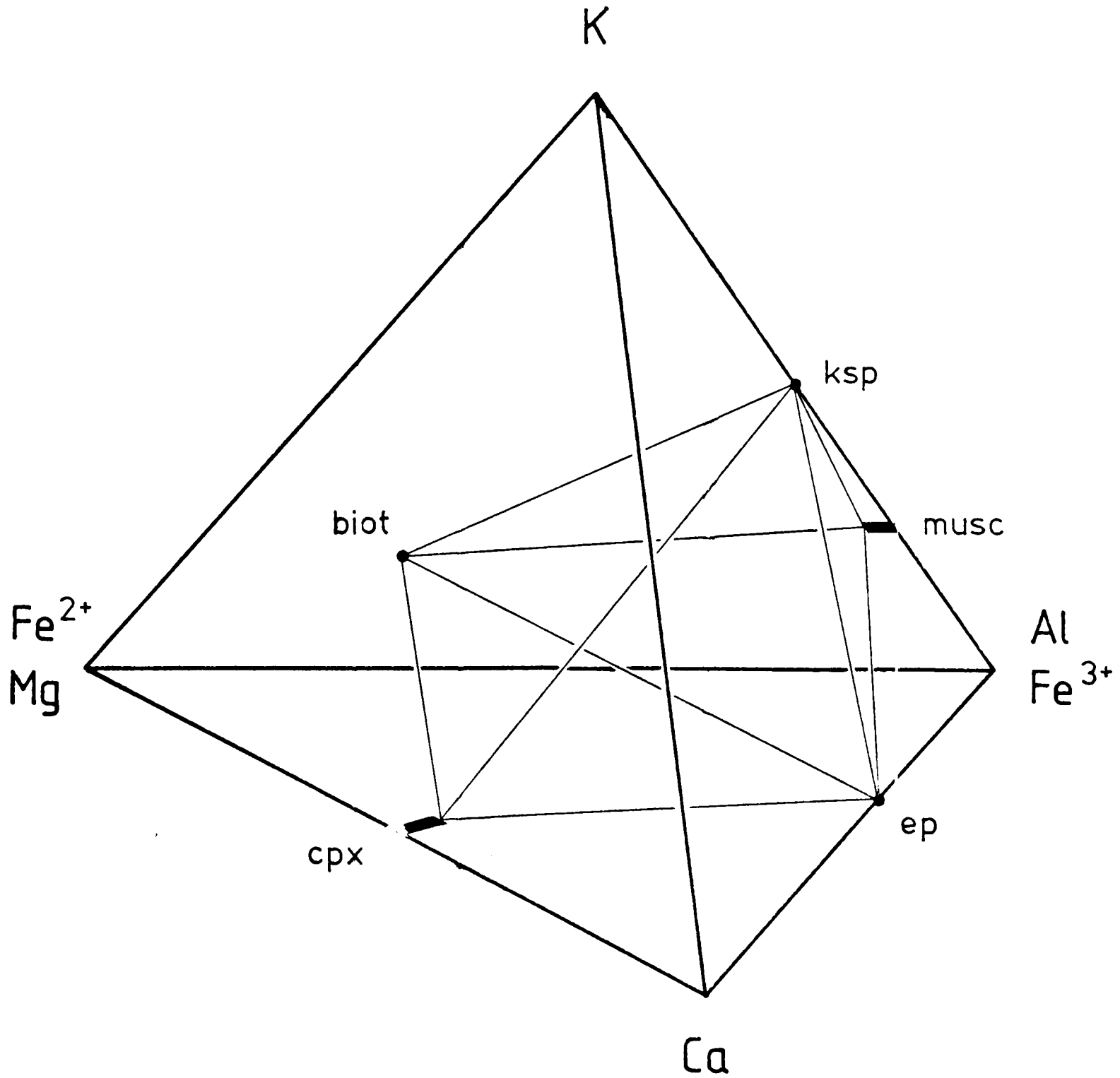



Fig. 7.11 K-(Al, $Fe^{3+}$)-Ca-(Mg, $Fe^{2+}$) tetrahedron showing mineral compatibility relationships in quartz- and albite-bearing meta-granites and meta-syenites.

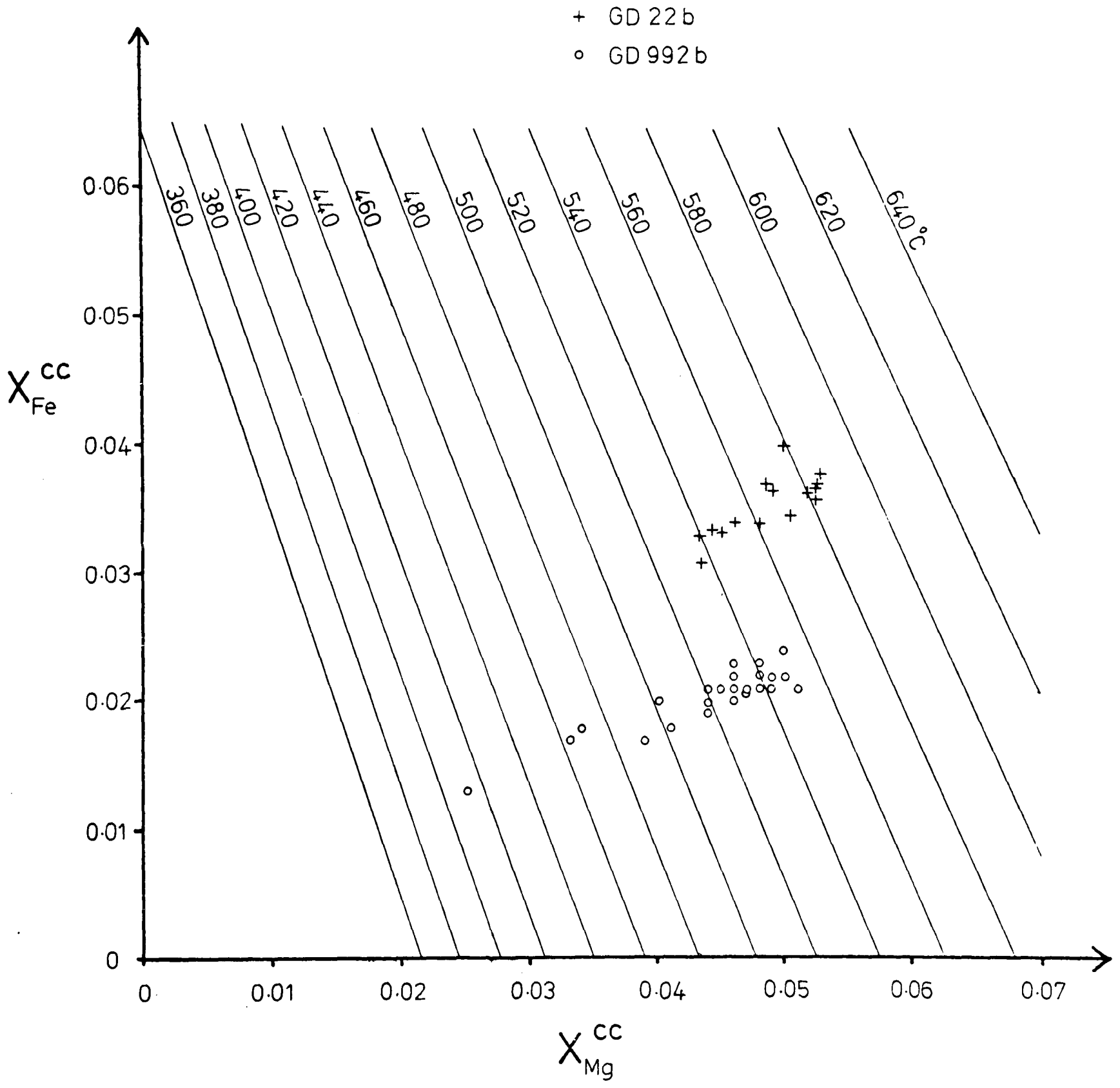



Fig. 7.12 Compositions of calcite grains coexisting with dolomite in GD 22b and GD 992b plotted in the 5kb thermometer of Bickle and Powell (1977).

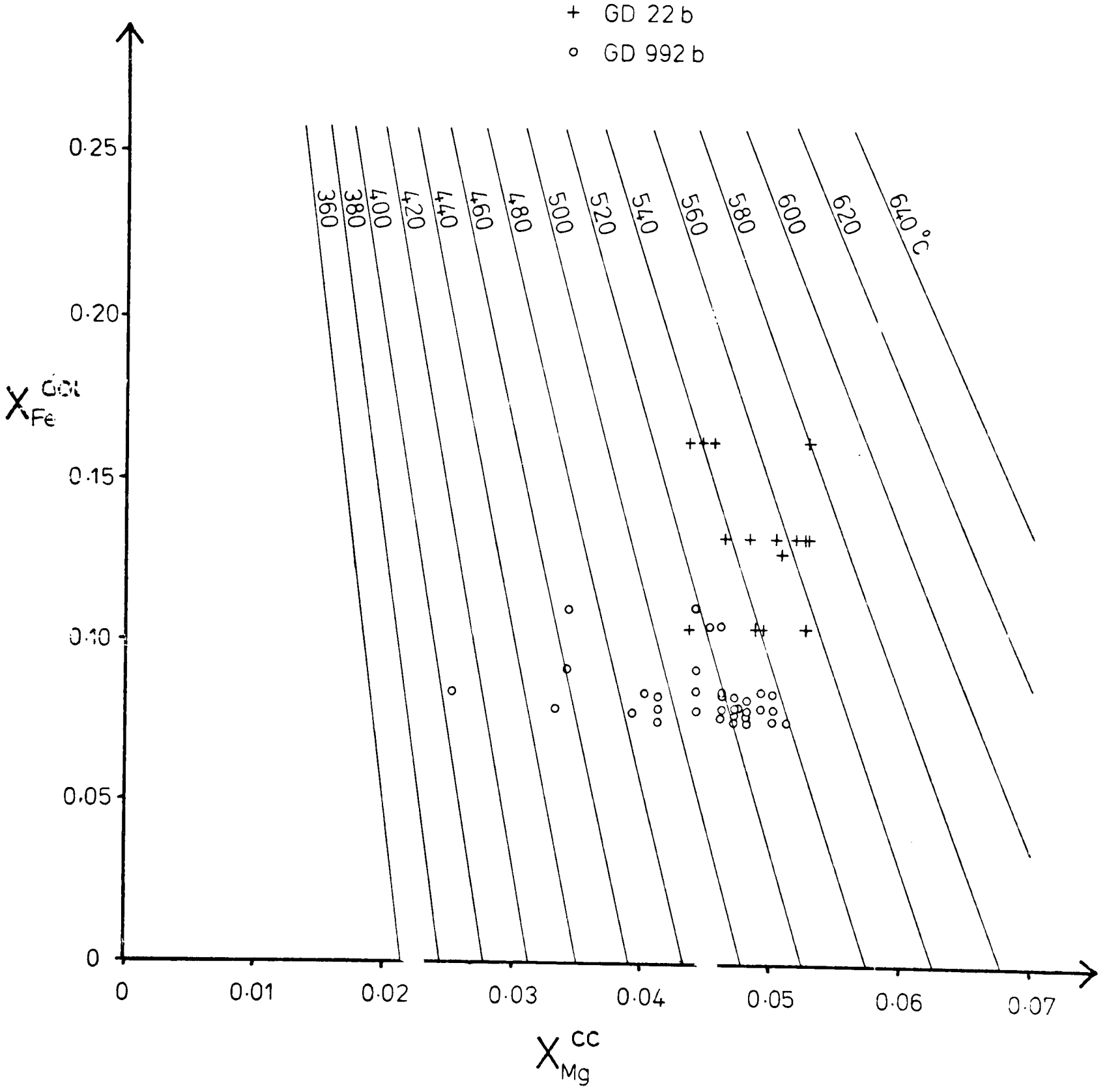



Fig. 7.13 Compositions of coexisting calcite and dolomite grains in GD 22b and GD 992b plotted in the 5kb thermometer of Bickle and Powell (1977).

1. $2zo + 5musc + 2qz = 4an + ksp + 2H_2O$

2. $musc + 4cc + 6qz = 2zo + 3ksp + 2H_2O + 4CO_2$

A: Stability field of sphene-bearing calc-schists.

B: Stability field of rutile-bearing calc-schists.

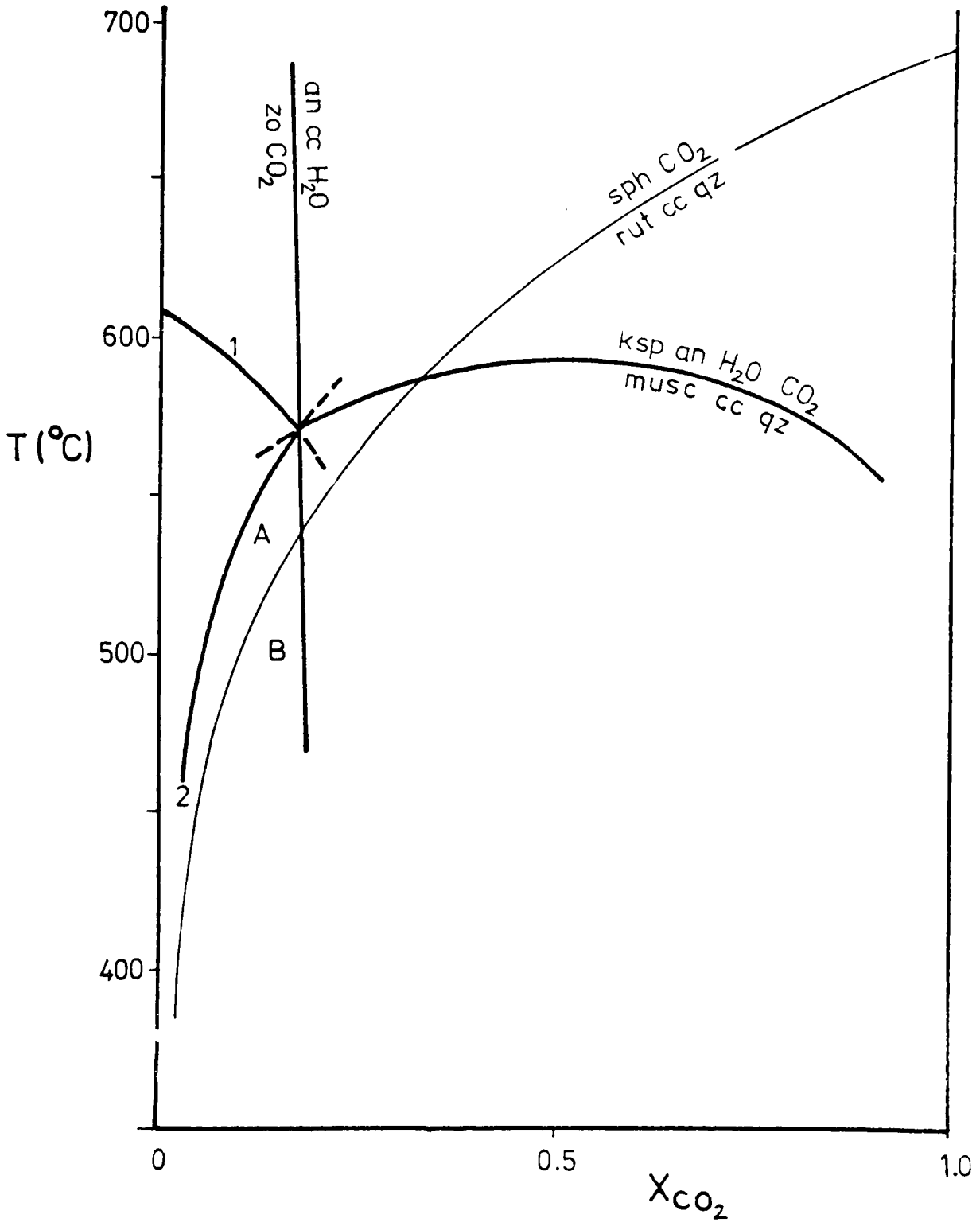



Fig. 7.14 7 kb T-$X_{CO_2}$ diagram showing equilibria relevant to calc-schist stability. The position of the invariant point and the univariant reactions radiating from it are taken from Johannes and Orville (1972).

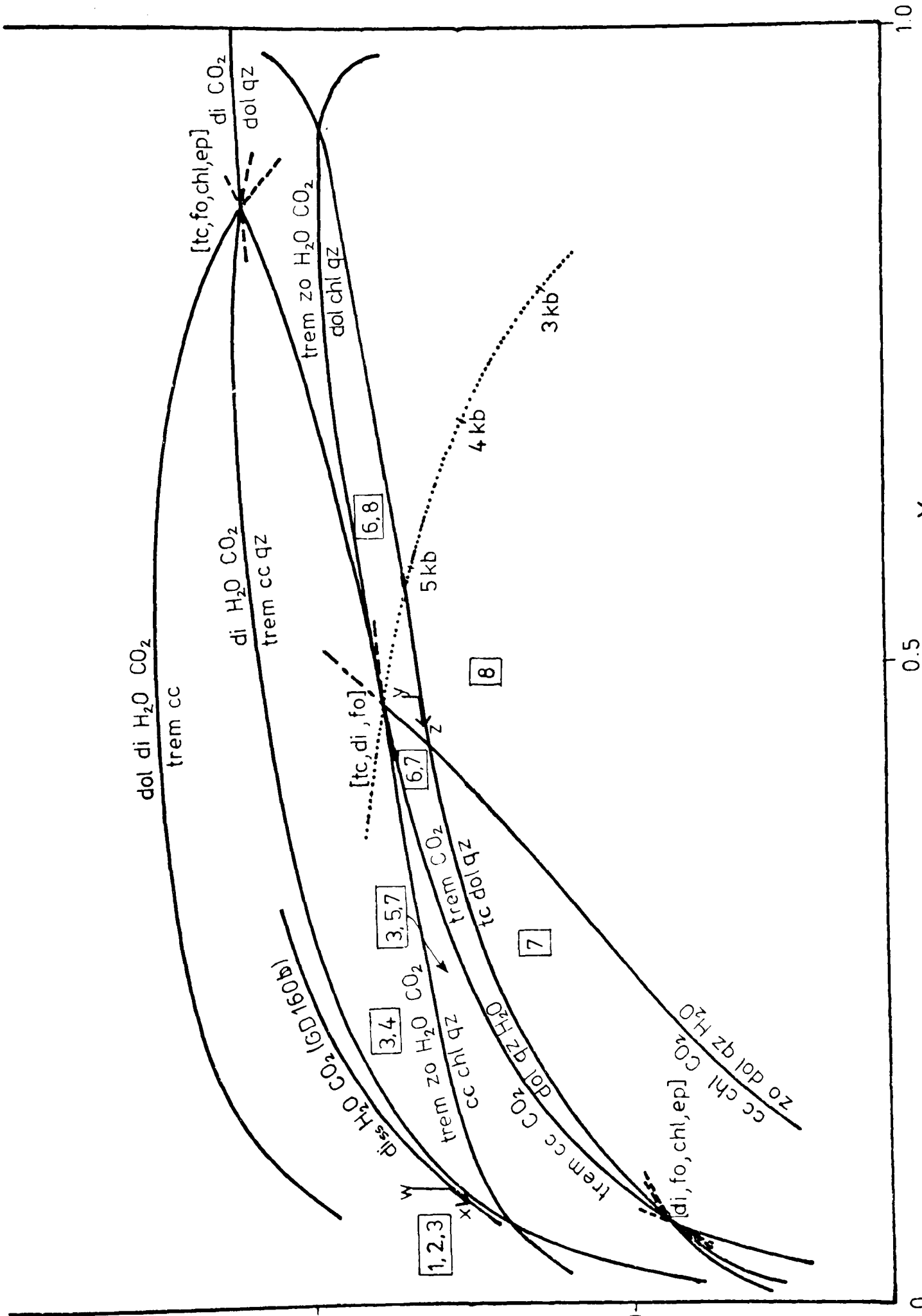



Fig. 7.15 6 kb T-$X_{CO_2}$ section for equilibria relevant to siliceous dolomites.

1. $5serp = 6fo + tc + 9H_2O$

2. $serp + mag = 2fo + 2H_2O + CO_2$

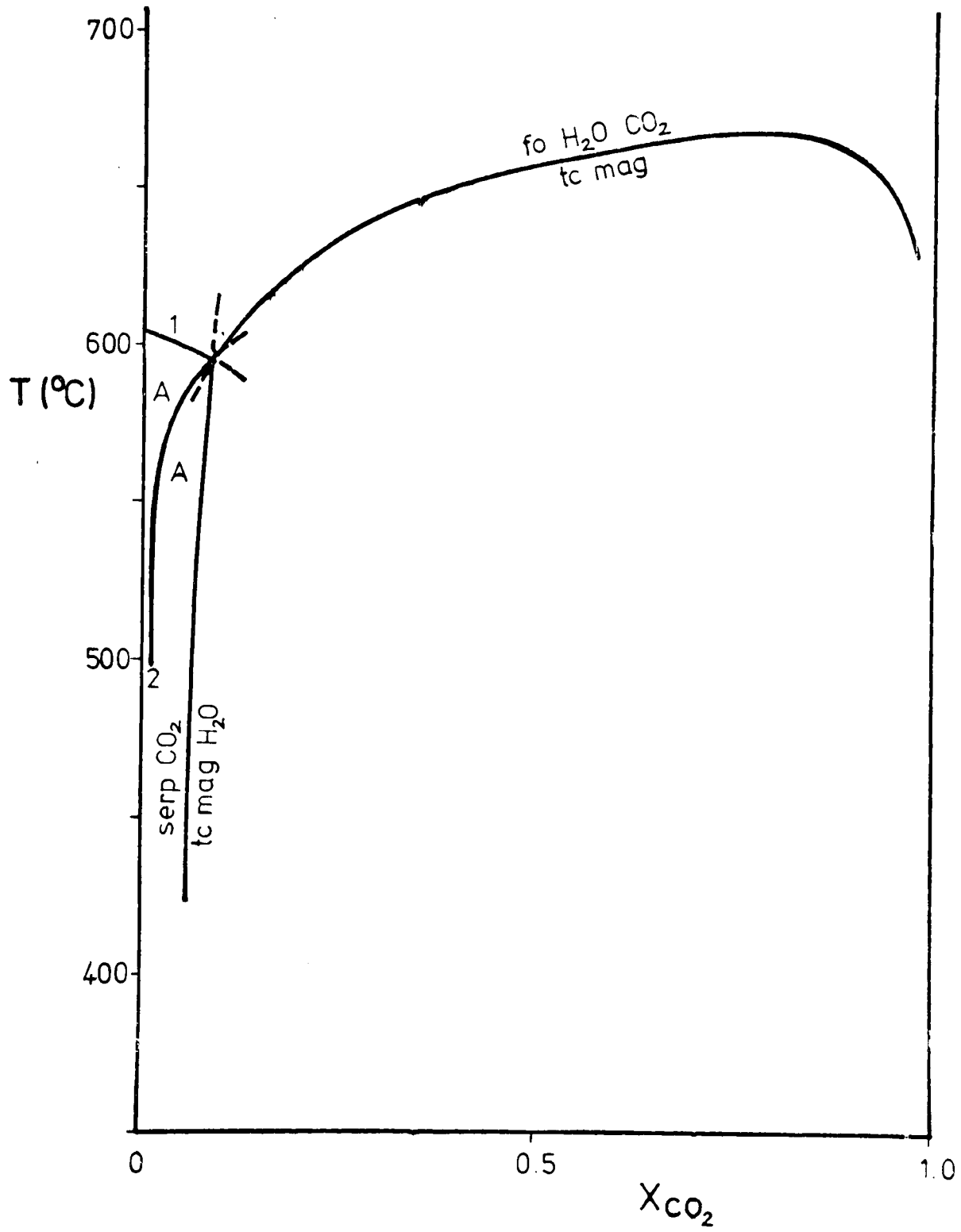



Fig. 7.16 7 kb T-$X_{CO_2}$ diagram showing equilibria relevant to serpentinites (taken from Johannes, 1969).

A : Stability field of serpentine.

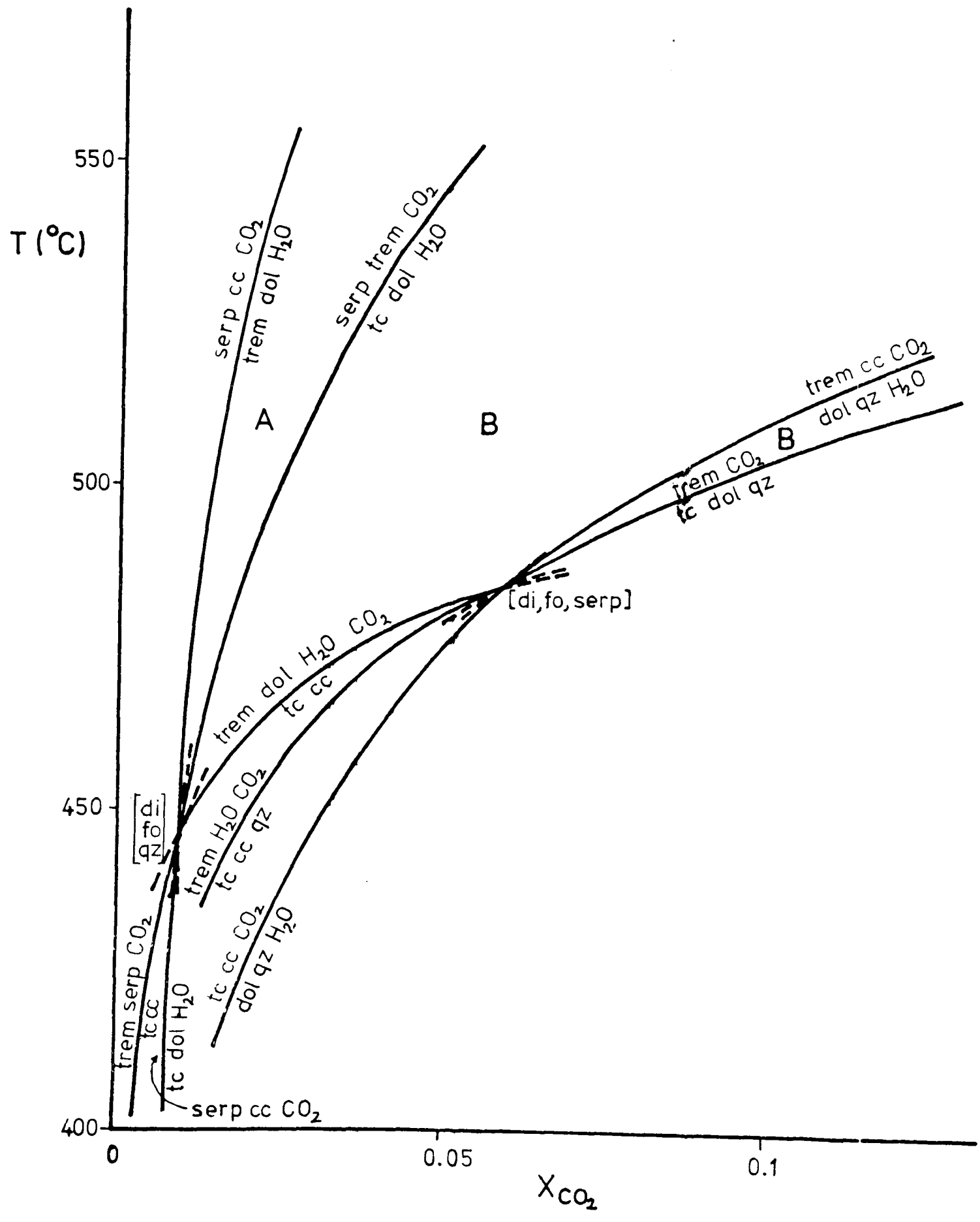



Fig. 7.17 6 kb T-$X_{CO_2}$ diagram showing calculated stable equilibrium curves for reactions involving serpentine, tremolite, talc, dolomite, calcite, quartz, $H_2O$ and $CO_2$.
A : Stability field of serp + trem + dol;
B : Stability field of trem + tc + dol.

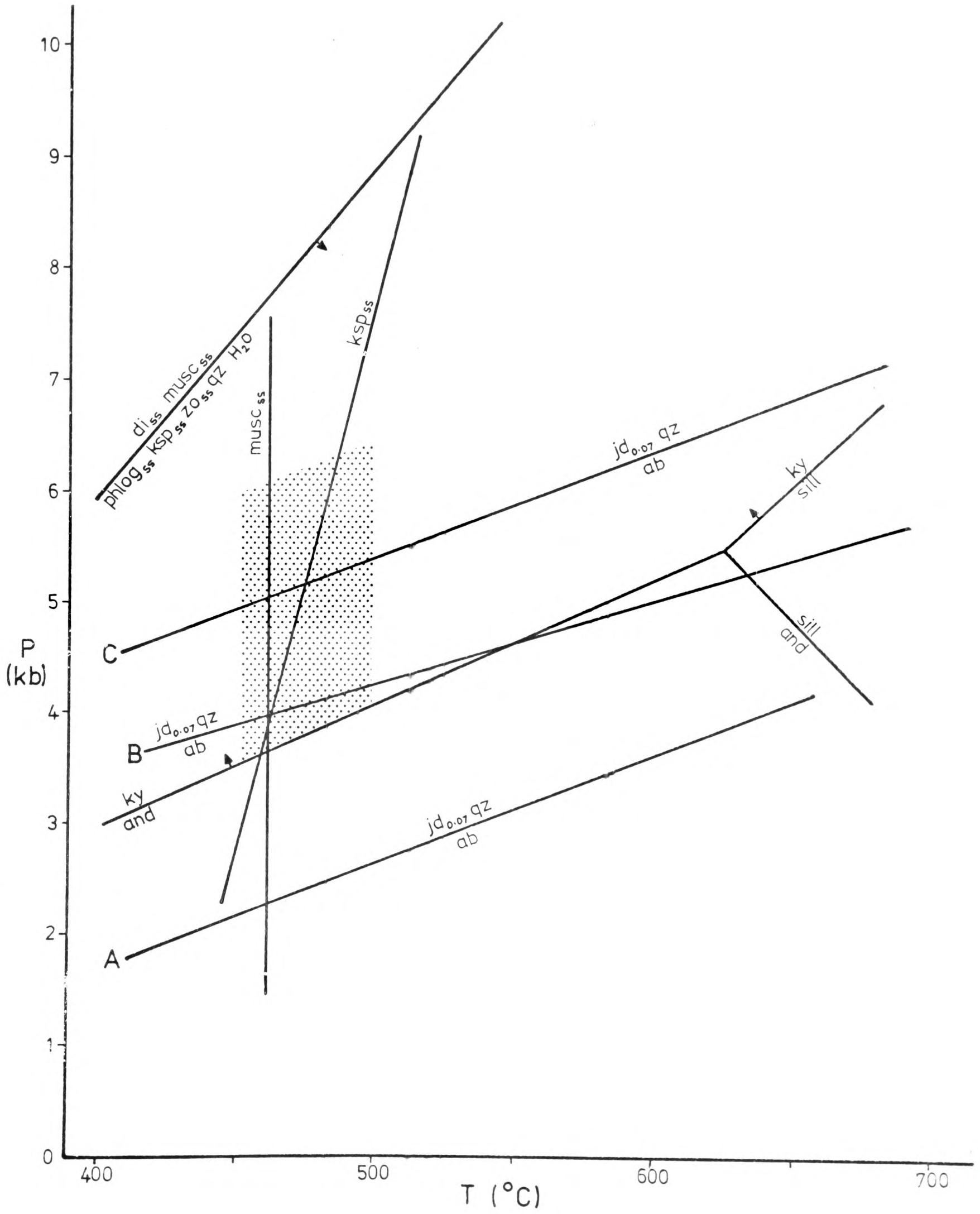



**Fig 7.18** Estimated $M_a$ metamorphic conditions (shaded) in the Romate subarea.

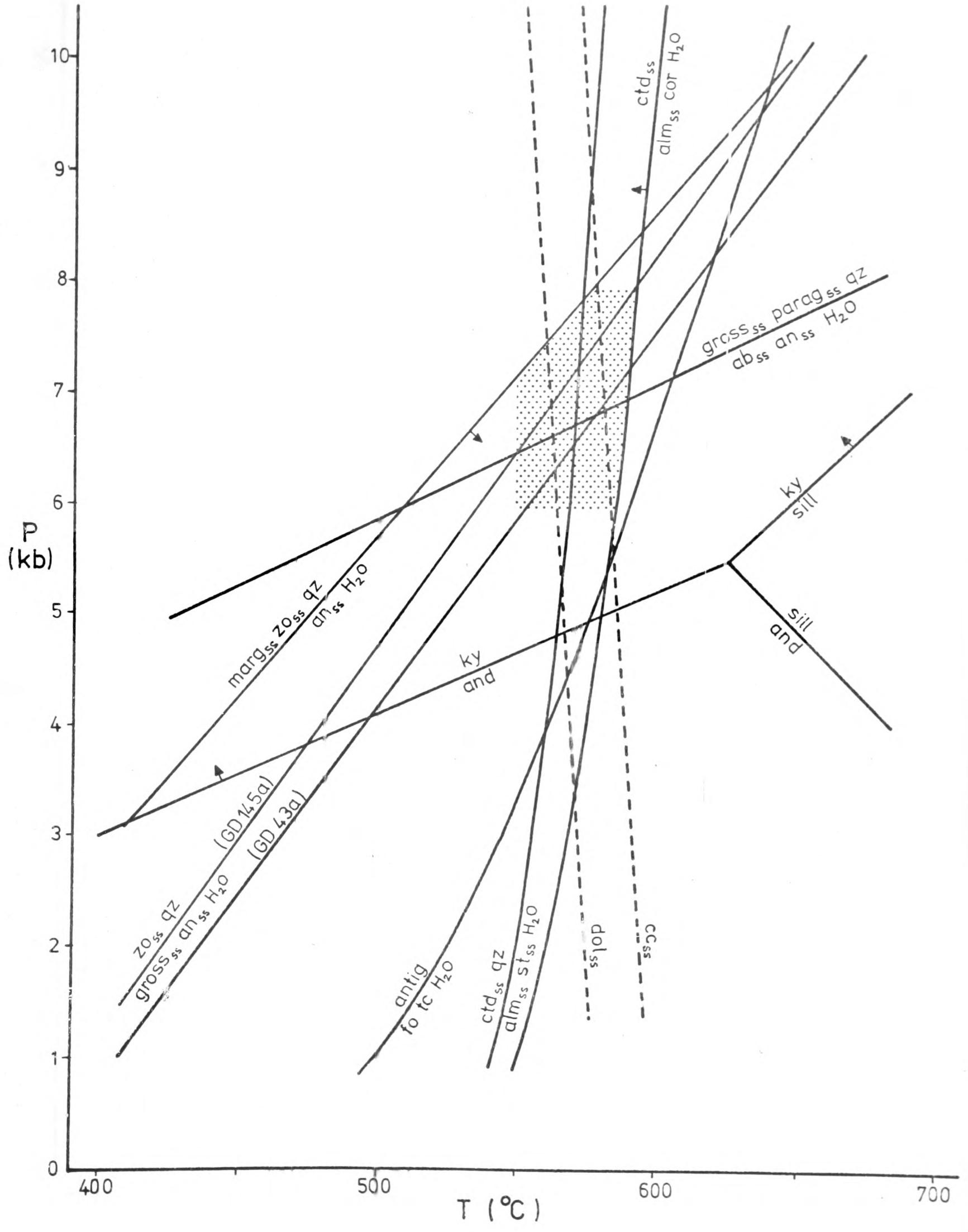



**Fig. 7.19** Estimated $M_a$ metamorphic conditions (shaded) at the structural base of the Mölltal Schieferhülle.

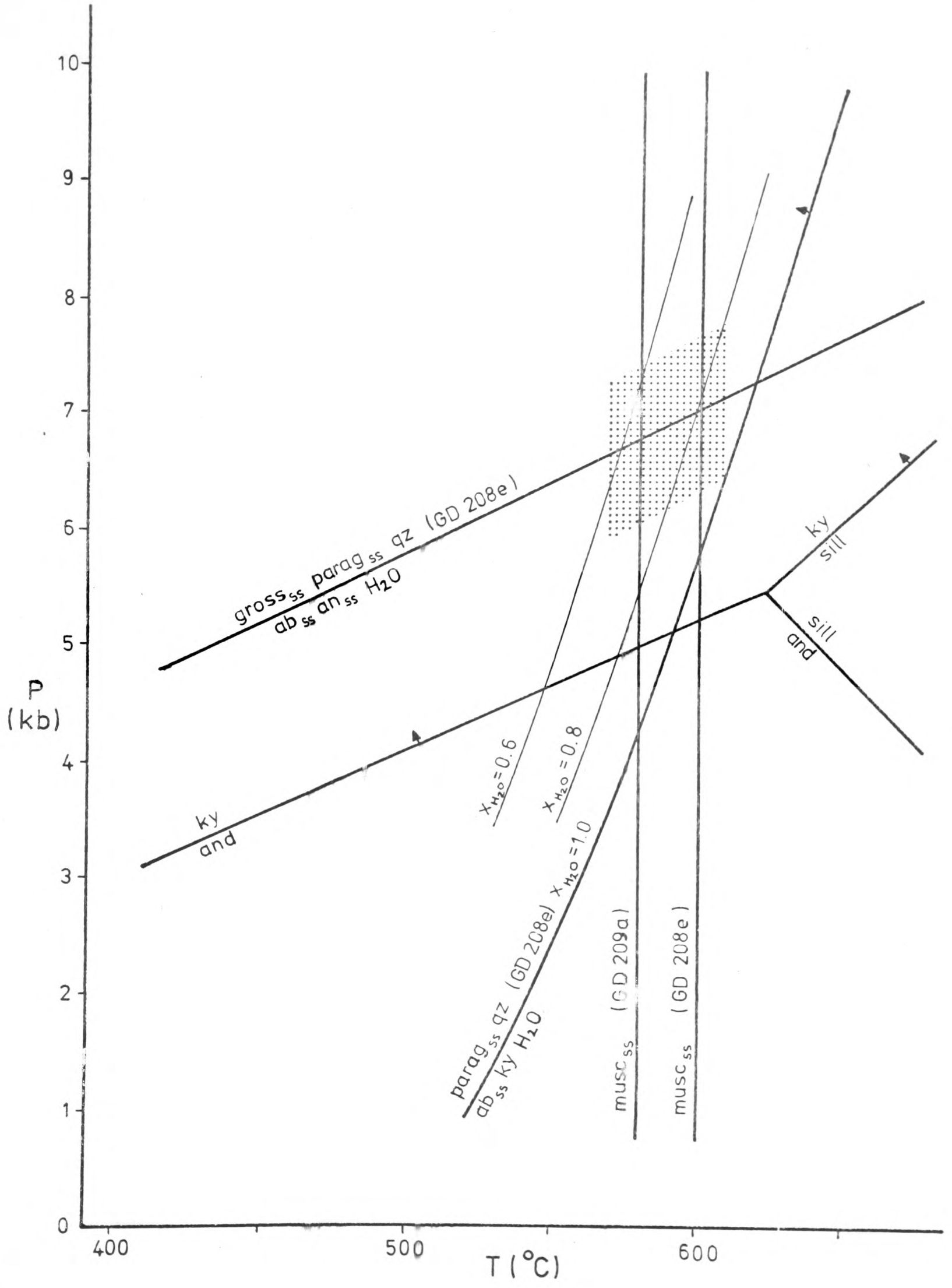



Fig. 7.20 Estimated $M_a$ metamorphic conditions (shaded) at a structural height of $2\frac{1}{2}$ km. below the basement-cover interface in the Hochalm Kern.

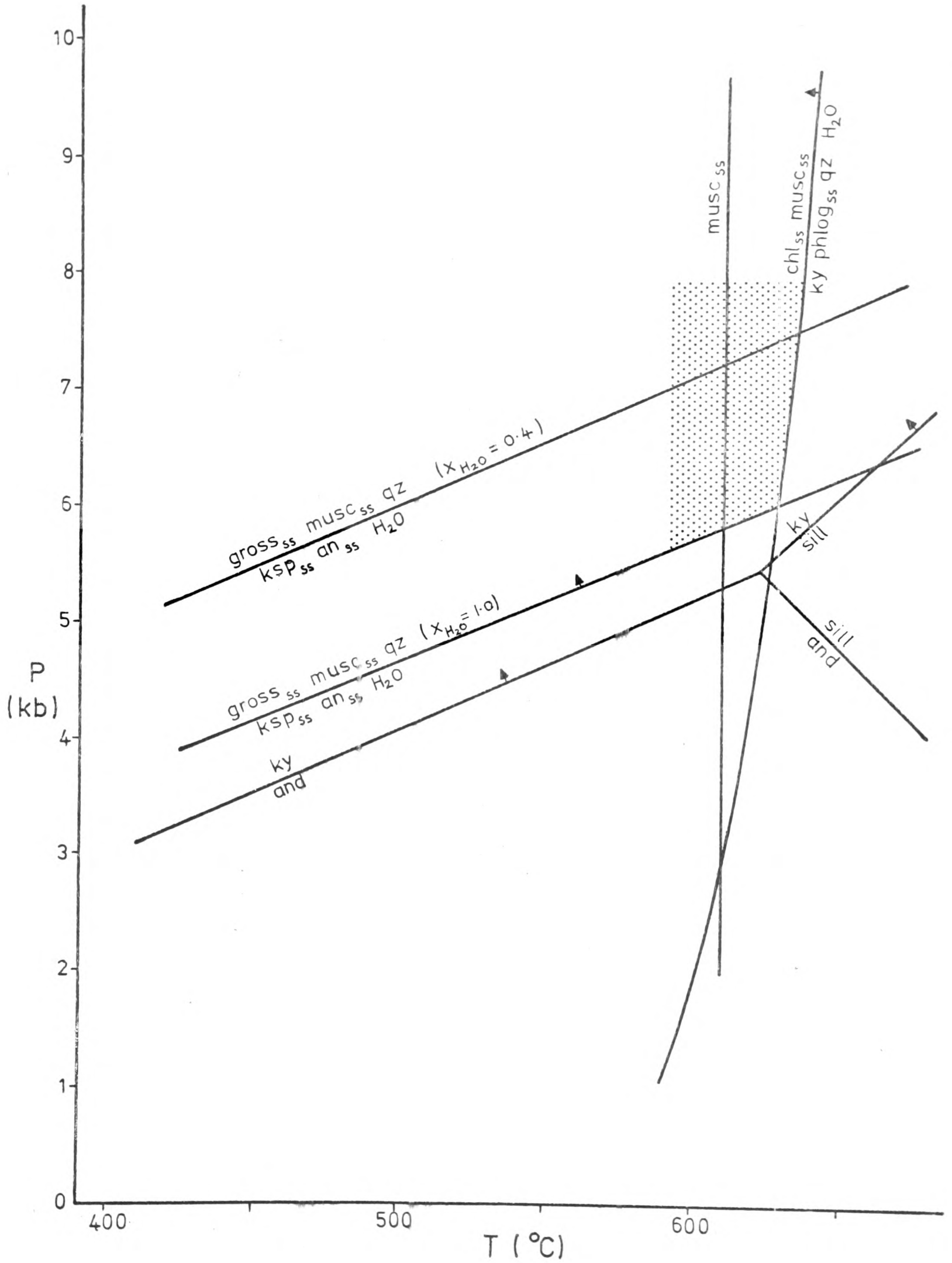



Fig. 7.21 Estimated $M_a$ metamorphic conditions (shaded) at a structural height of 3 to 4 km. below the basement-cover interface in the Hochalm Kern.

A,B Trajectories deduced by Holland (1977) for the Central Tauern on the basis of reactions involving zoned amphiboles.

C,D Possible trajectories deduced in this study for the Eastern Tauern on the basis of reactions involving CASH phases.

Estimated $M_a$ peak metamorphic conditions in the Central Tauern.

Estimated $M_a$ peak metamorphic conditions in the Eastern Tauern.

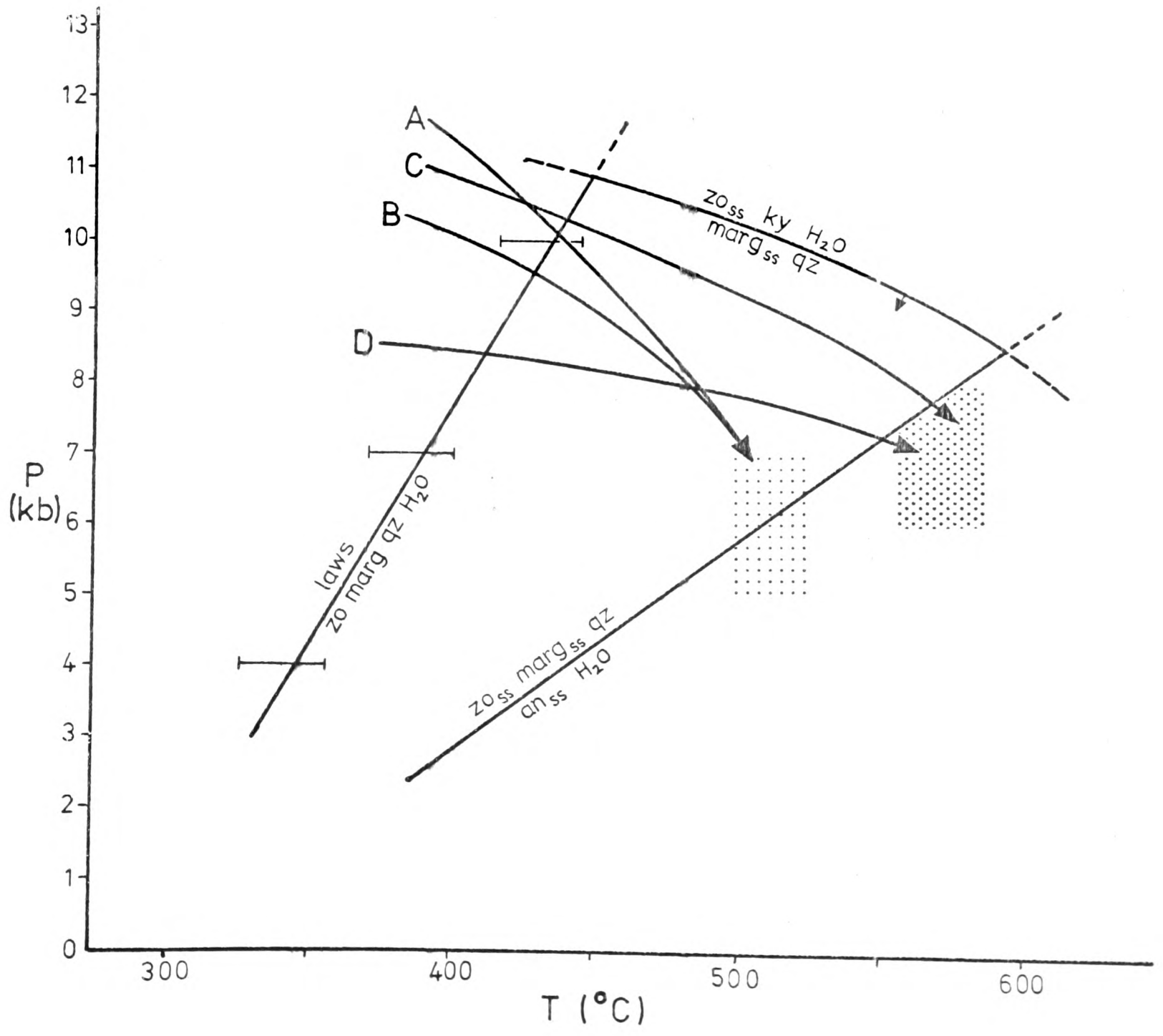



Fig. 7.22 Some possible early-Alpine P-T-time trajectories in the Central and Eastern Tauern.

**Lawsonite** - breakdown curve from Nitsch (1973).

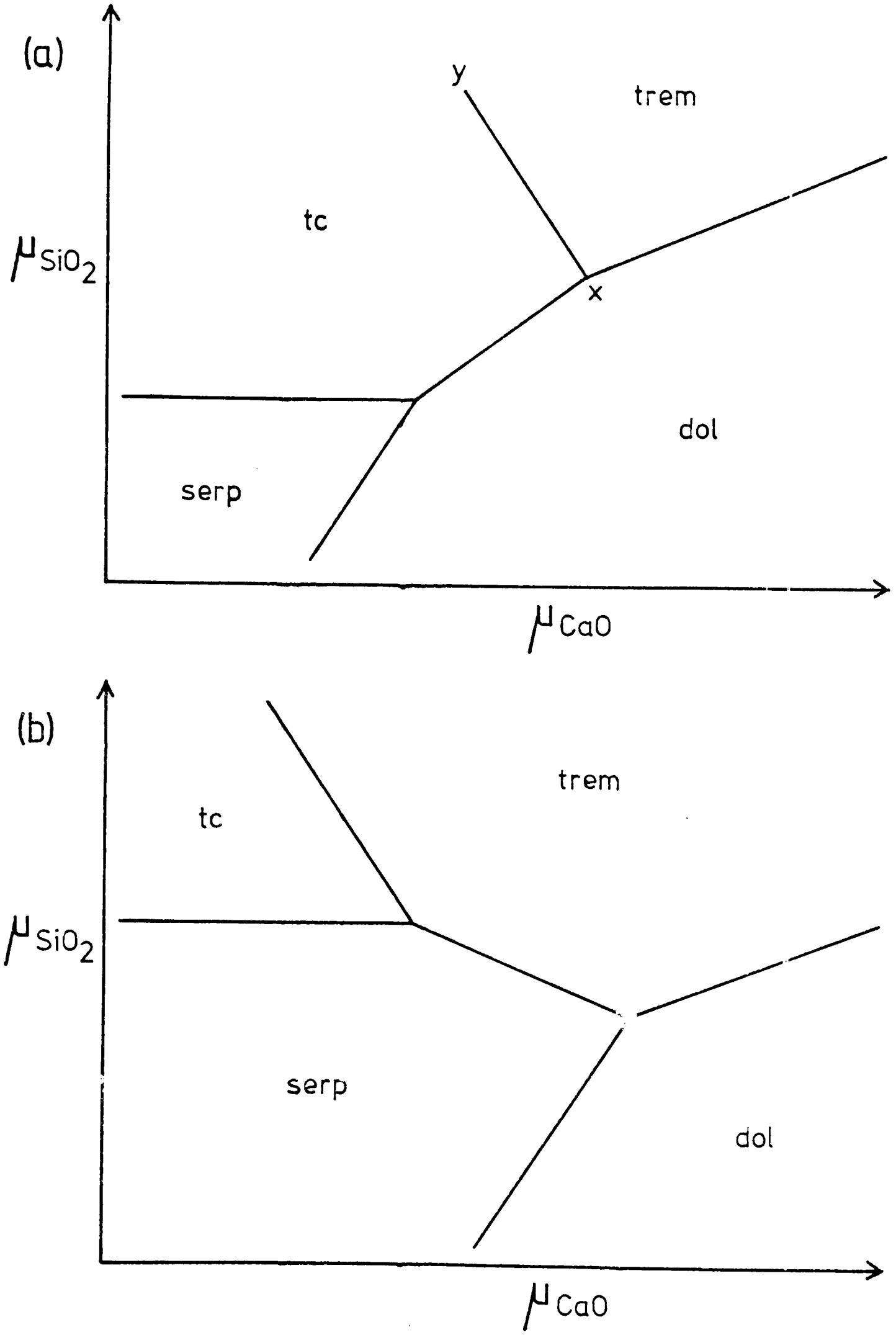



Fig. 7.23 $\mu_{SiO_2}$ versus $\mu_{CaO}$ diagrams for serpentinites and talc-schists. Topology (a) applies at slightly higher values of $X_{CO_2}$ than topology (b).

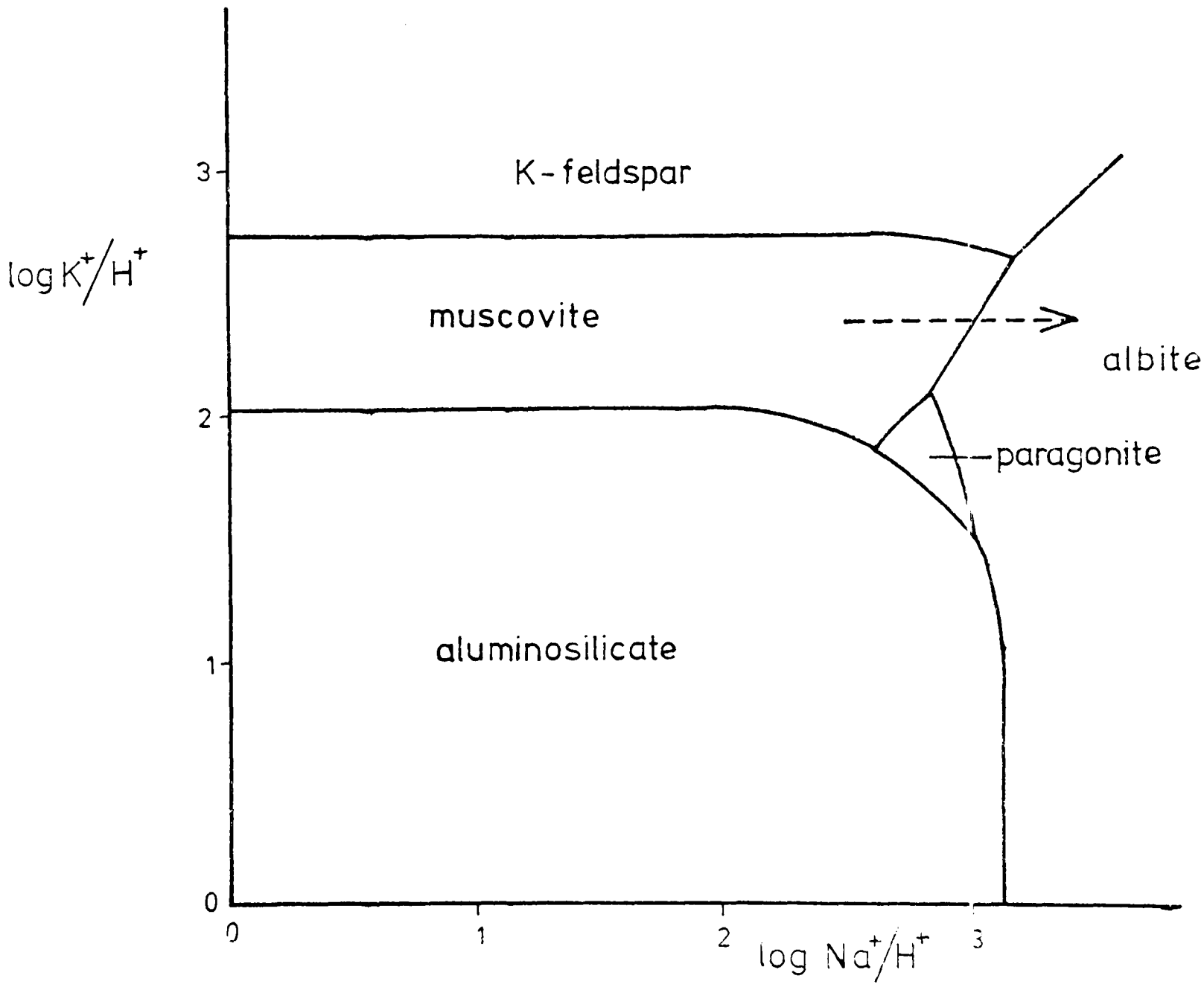
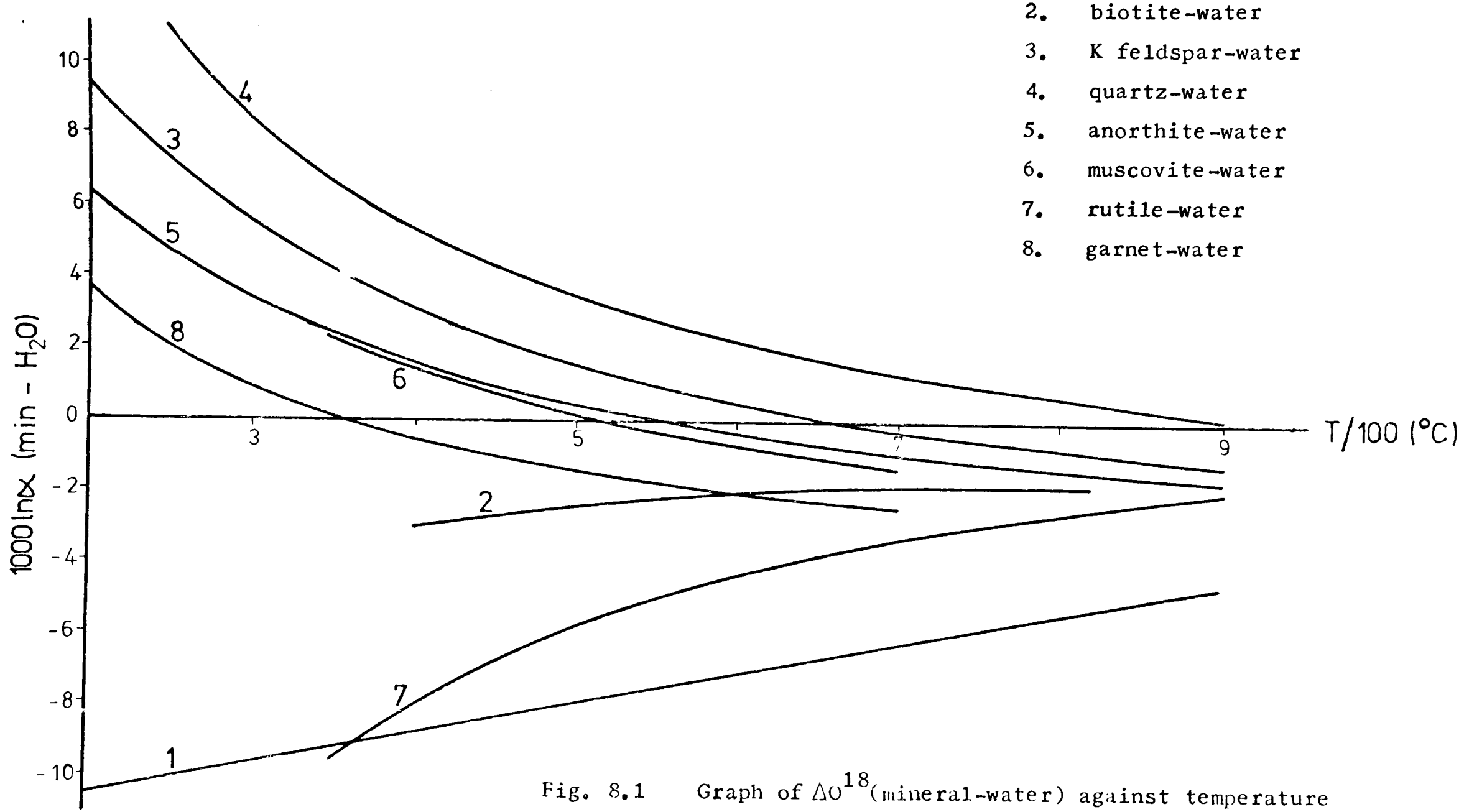



Fig. 7.24 Replacement of muscovite by sodic plagioclase in pelites explained in terms of a gradient in $Na^+/H^+$.
Stability fields from Wintsch (1975) for conditions of $T = 600^{\circ}C$, $P = 7kb$, $a_{H_2O} = 0.5$.

Table 8.1 Experimentally determined and calculated mineral-water fractionation curves.

| Fractionation | | T range | 1000 ln $\alpha$ | Reference |
|---|---|---|---|---|
| Quartz - $H_2O$ | C | 500-800°C | $4.1(10^6/T^2) - 3.7$ | Bottinga and Javoy (1973) |
| | E | 200-500°C | $3.38(10^6/T^2) - 3.40$ | Clayton et. al. (1972) |
| | E | 500-700°C | $2.51(10^6/T^2) - 1.96$ | Clayton et. al. (1972) |
| | E * | --- | $3.65(10^6/T^2) - 2.59$ | Blattner and Bird (1976) |
| Calcite - $H_2O$ | E | 0-500°C | $2.78(10^6/T^2) - 3.39$ | O'Neil et. al. (1969) |
| Muscovite - $H_2O$ | C | 500-800°C | $1.9(10^6/T^2) - 3.10$ | Bottinga and Javoy (1973) |
| | E * | 400-650°C | $2.38(10^6/T^2) - 3.89$ | O'Neil and Taylor (1969) |
| Alkali fsp - $H_2O$ | C | 500-800°C | $3.13(10^6/T^2) - 3.70$ | Bottinga and Javoy (1973) |
| | E * | 350-800°C | $2.91(10^6/T^2) - 3.41$ | O'Neil and Taylor (1967) |
| Biotite - $H_2O$ | E * | 400-800°C | † $0.0144T - 9.53x10^{-6}T^2 - 7.3$ | Bertenrath and Friedrichsen (1975) |
| Magnetite - $H_2O$ | C | 500-800°C | $-1.47(10^6/T^2) - 3.70$ | Bottinga and Javoy (1973) |
| | E | 700-800°C | $-1.60(10^6/T^2) - 3.61$ | Anderson et. al. (1971) |
| | E * | 300-900°C | † $0.00834T - 12.2$ | Bertenrath et. al. (1973) |
| Rutile - $H_2O$ | E * | 575-775°C | $-4.1(10^6/T^2) + 0.96$ | Addy and Garlick (1974) |
| Anorthite - $H_2O$ | C | 500-800°C | $1.04(10^6/T^2) - 3.70$ | Bottinga and Javoy (1973) |
| | E | 500-800°C | $2.15(10^6/T^2) - 3.82$ | O'Neil and Taylor (1969) |
| Garnet - $H_2O$ | C * | --- | † $(0.00173/T) - 4.98$ | Friedrichsen et. al. (1973) |

E : Experimentally determined. C : Calculated. * : Calibrations used in this study.
Temperatures in °K unless specified. †: Temperature in °C.

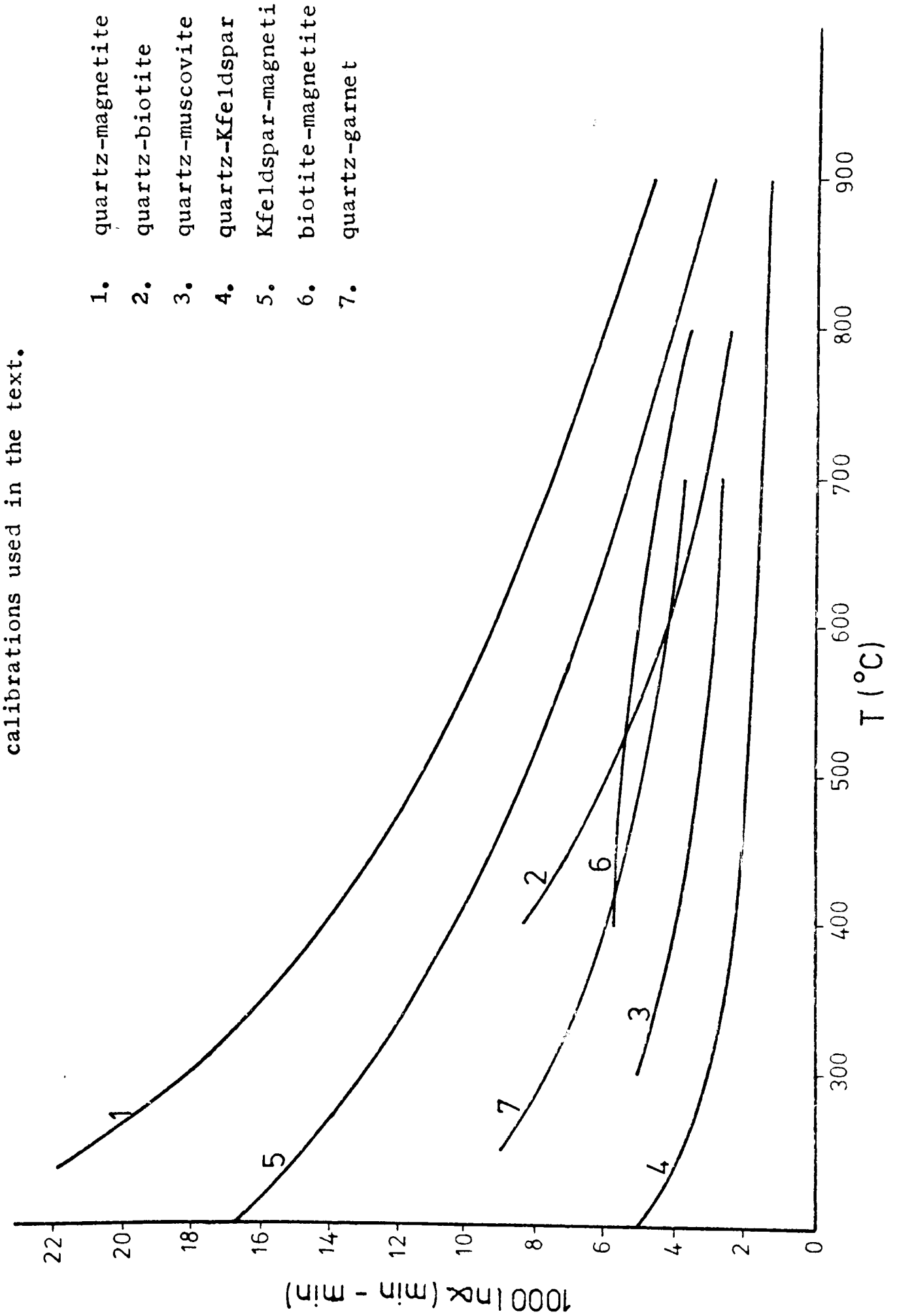


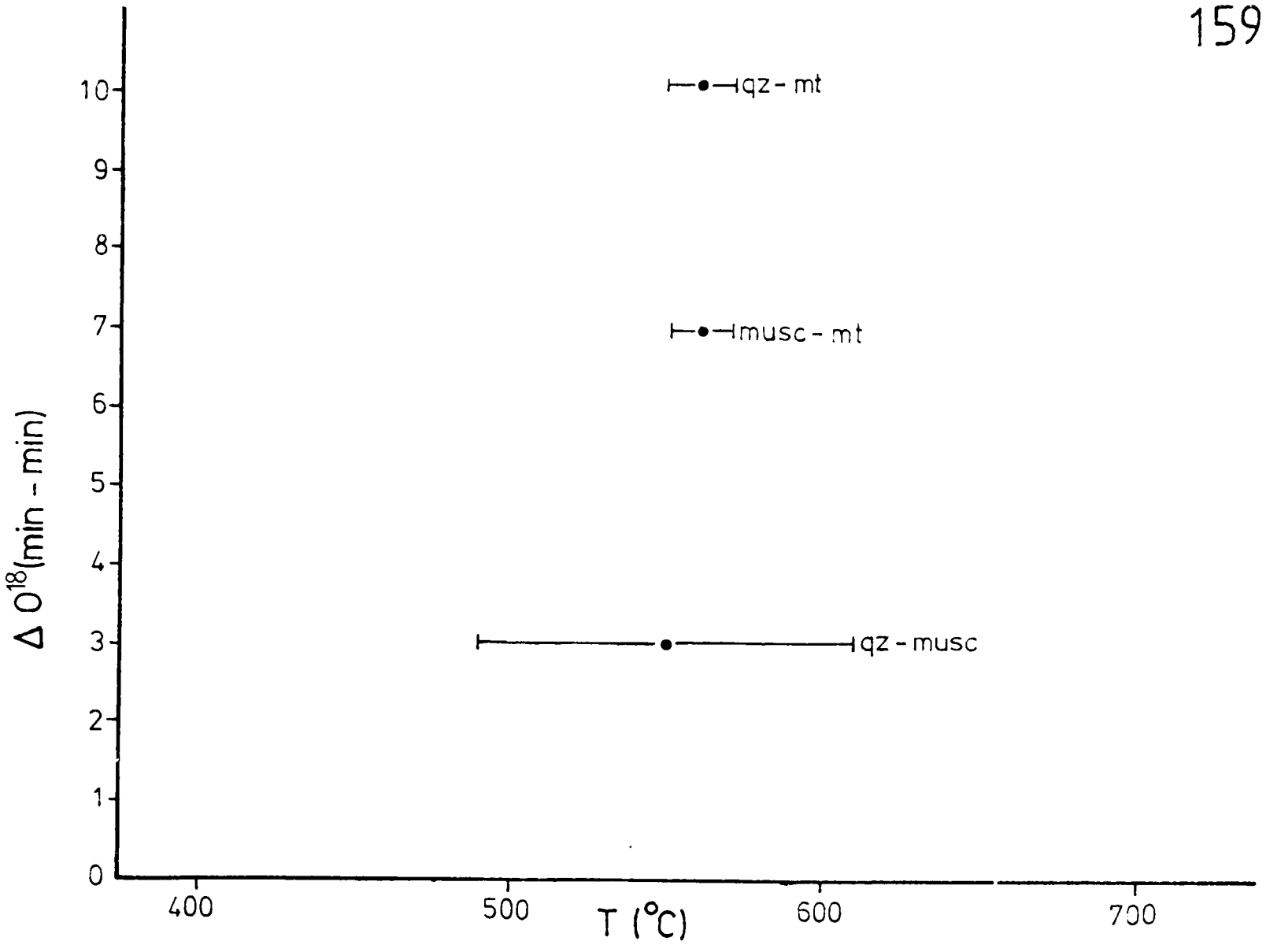

1. magnetite-water
2. biotite-water
3. K feldspar-water
4. quartz-water
5. anorthite-water
6. muscovite-water
7. rutile-water
8. garnet-water

Fig. 8.1 Graph of $\Delta O^{18}$(mineral-water) against temperature for the calibrations used in the text.

Fig. 8.2 Graph of $\Delta O^{18}_{(mineral-mineral)}$ against temperature for the calibrations used in the text.

1. quartz-magnetite
2. quartz-biotite
3. quartz-muscovite
4. quartz-Kfeldspar
5. Kfeldspar-magnetite
6. biotite-magnetite
7. quartz-garnet





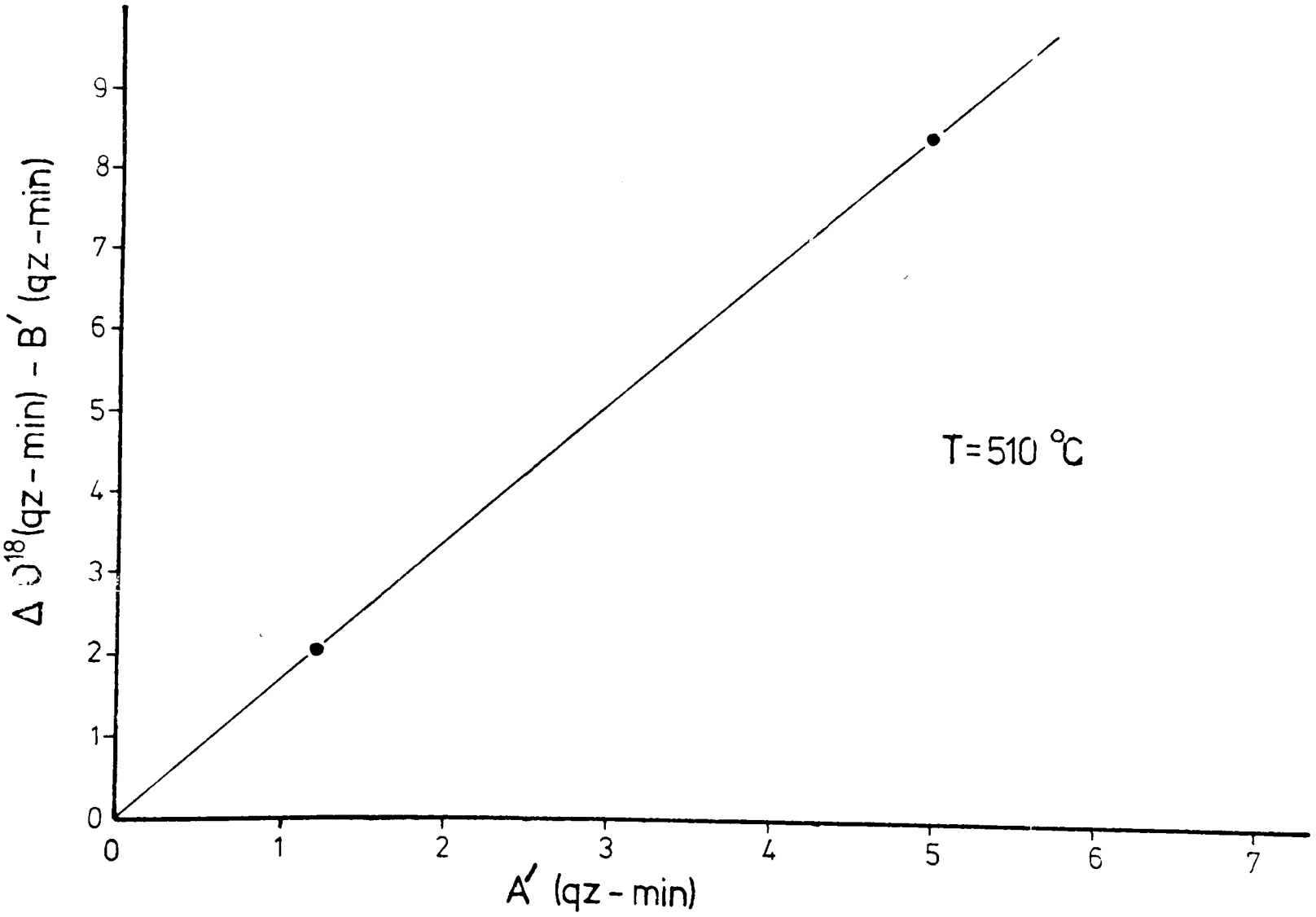
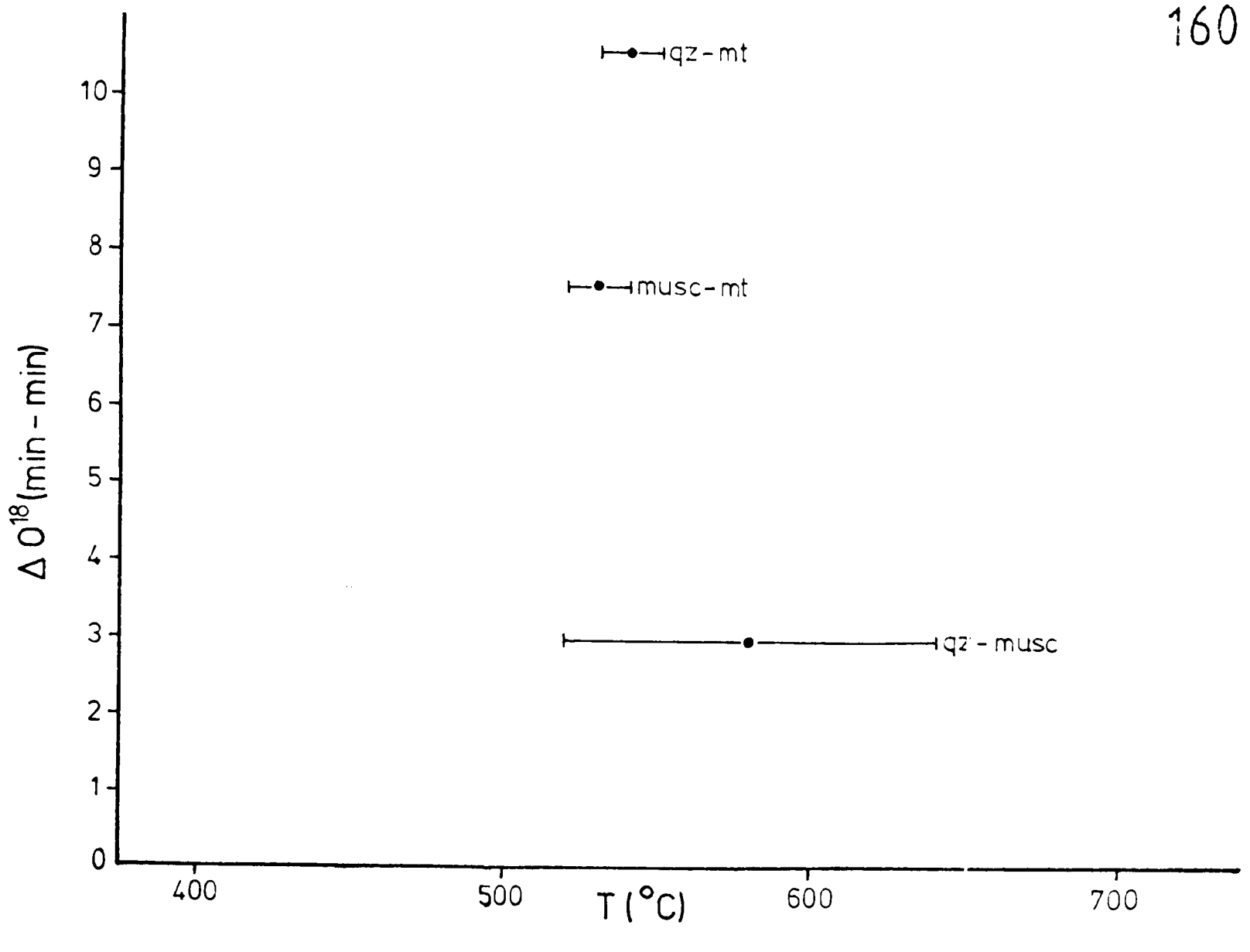




Fig. 8.3(a) Fractionation vs. temperature plot (above) and Javoy diagram (below) for isotopically well-equilibrated Inner Schieferhülle mica-schist GD 302.



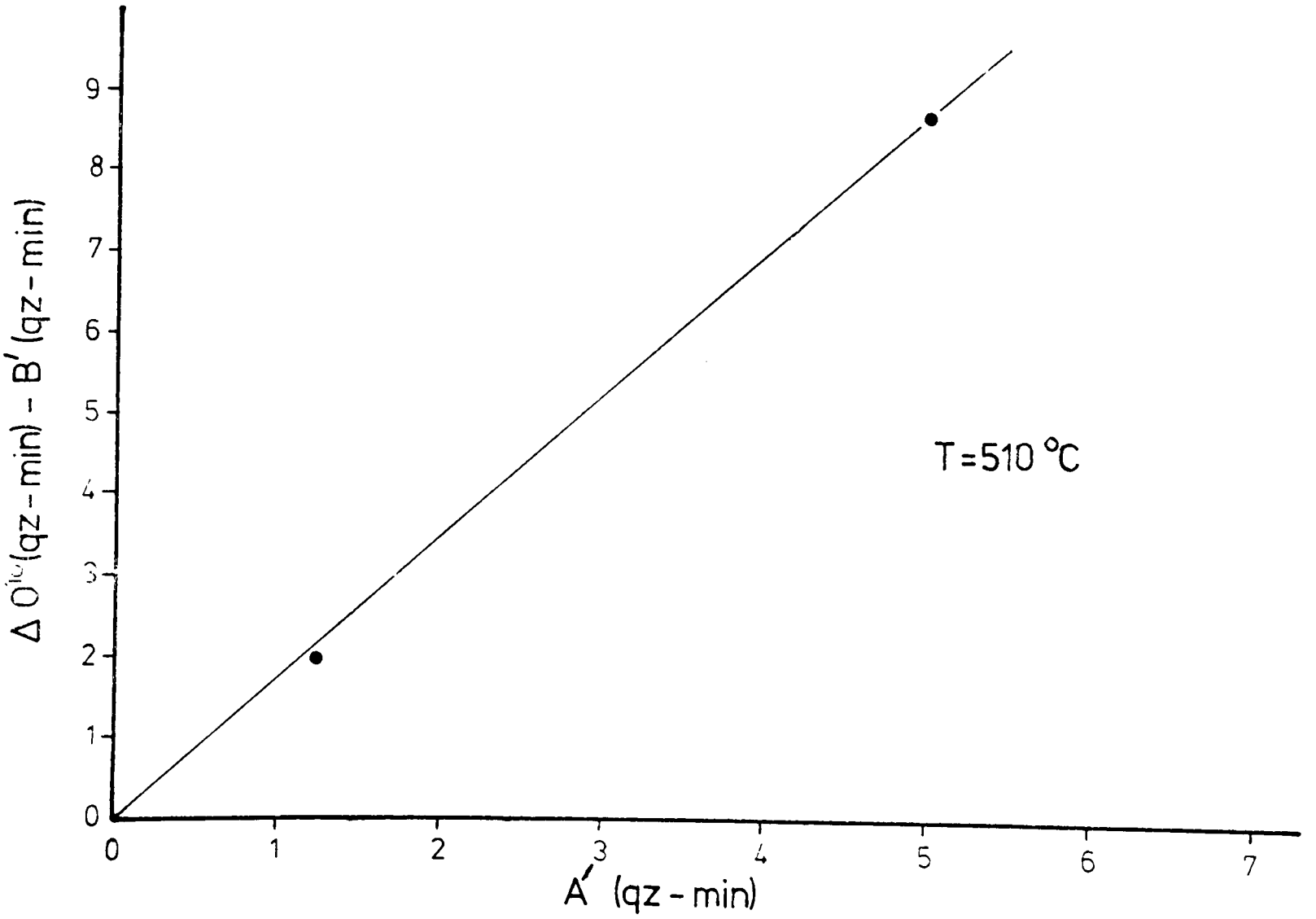




Fig. 8.3(b) Fractionation vs. temperature plot (above) and Javoy diagram (below) for isotopically well-equilibrated Peripheral Schieferhülle mica-schist GD 28b.

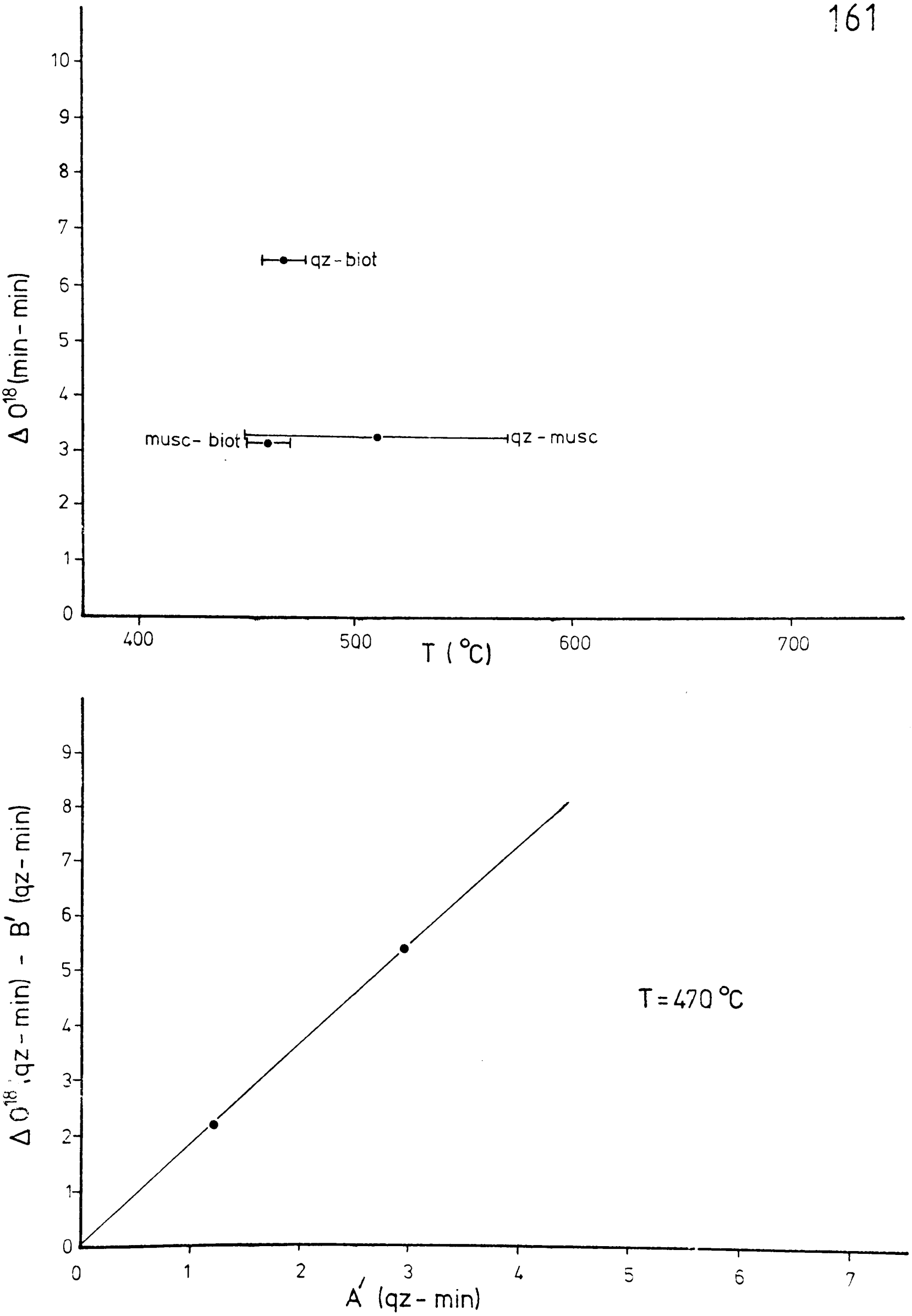



Fig. 8.3(c) Fractionation vs. temperature plot (above) and Javoy diagram (below) for isotopically well-equilibrated augen-gneiss GD 595.

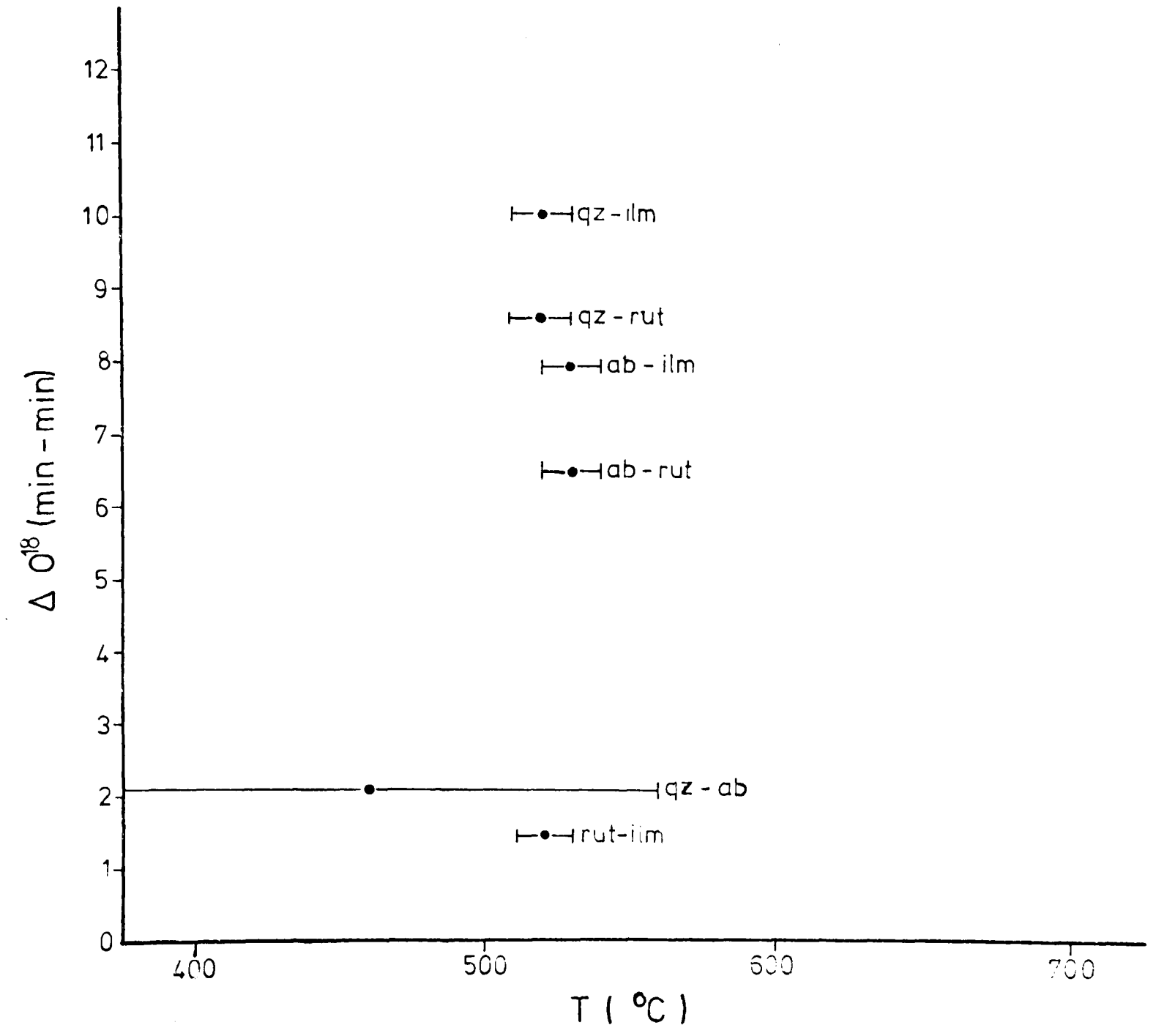
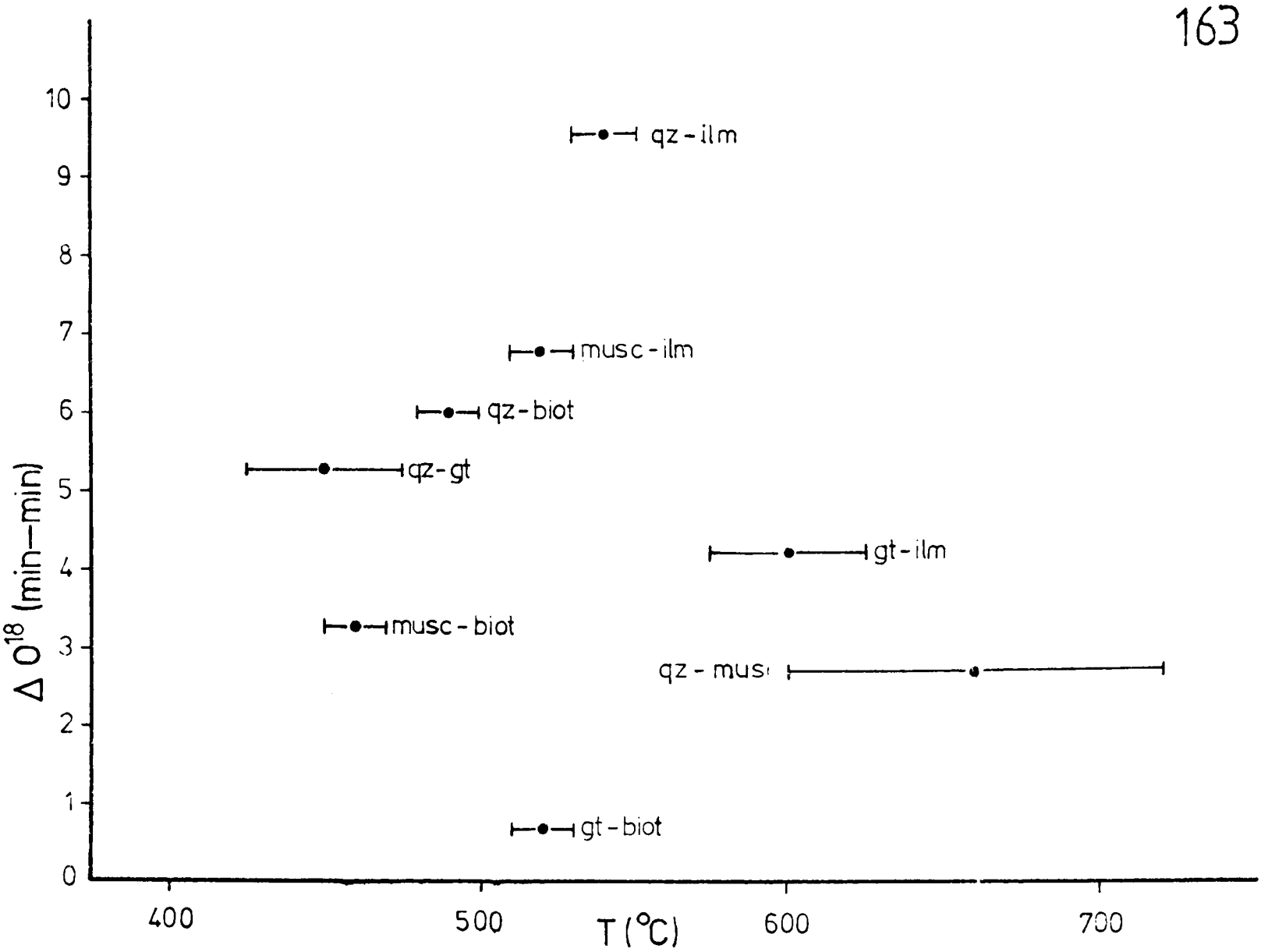



Fig. 8.4 Fractionation vs. temperature plot for combined data of vein samples AU1 and AU2.



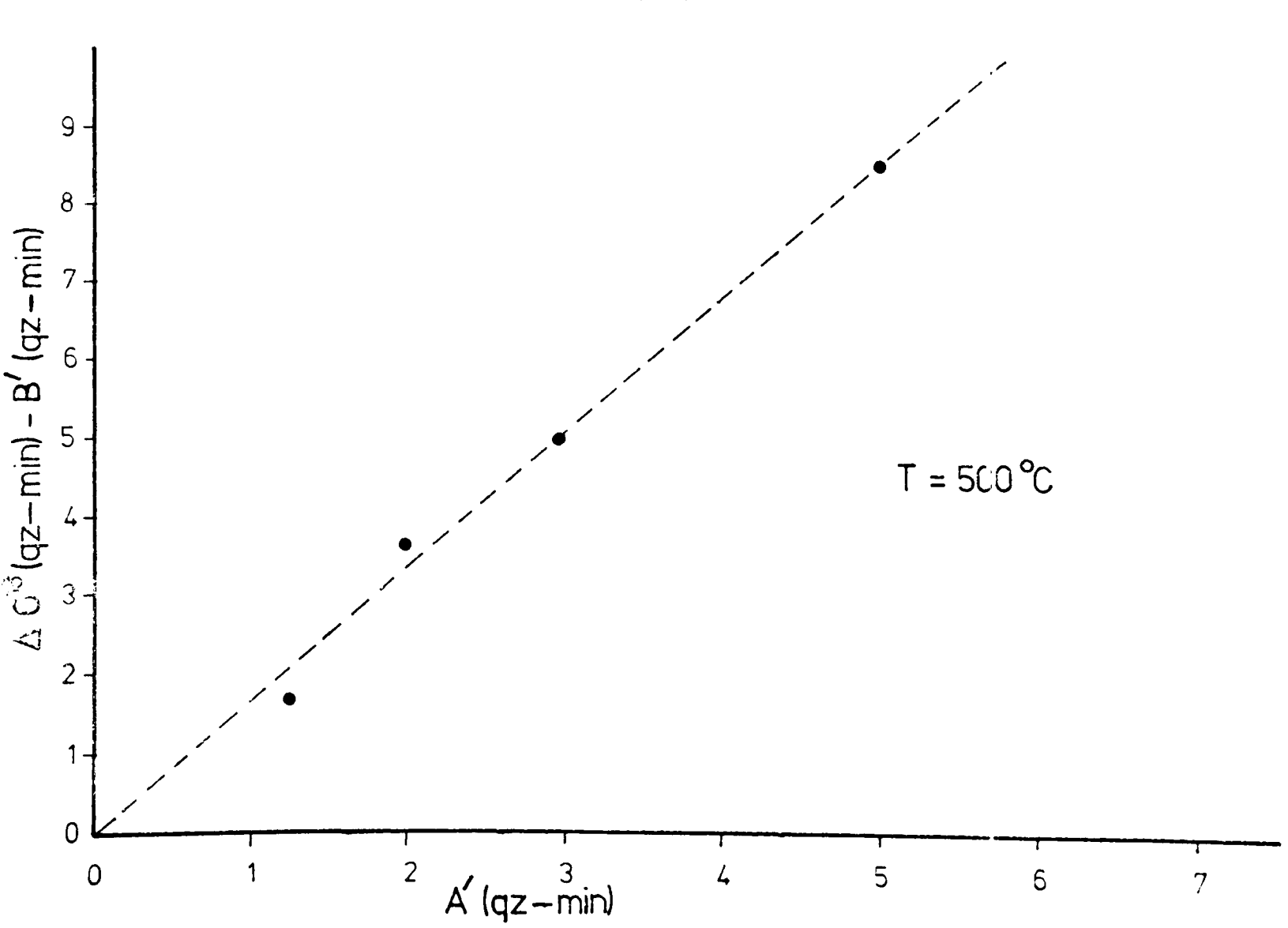




Fig. 8.5(a) Fractionation vs. temperature plot (above) and Javoy diagram (below) for isotopically poorly-equilibrated Peripheral Schieferhülle mica-schist GD 890.

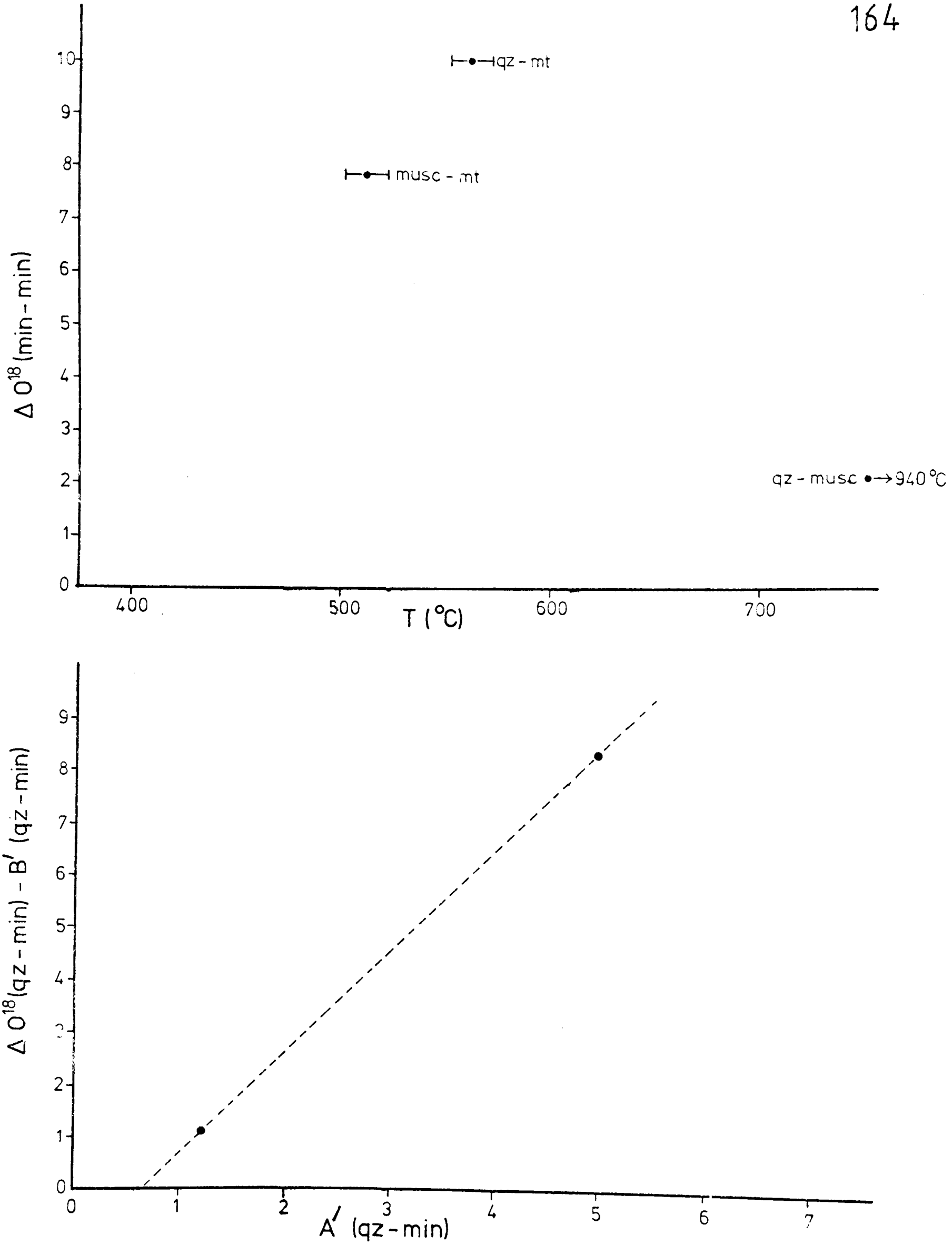
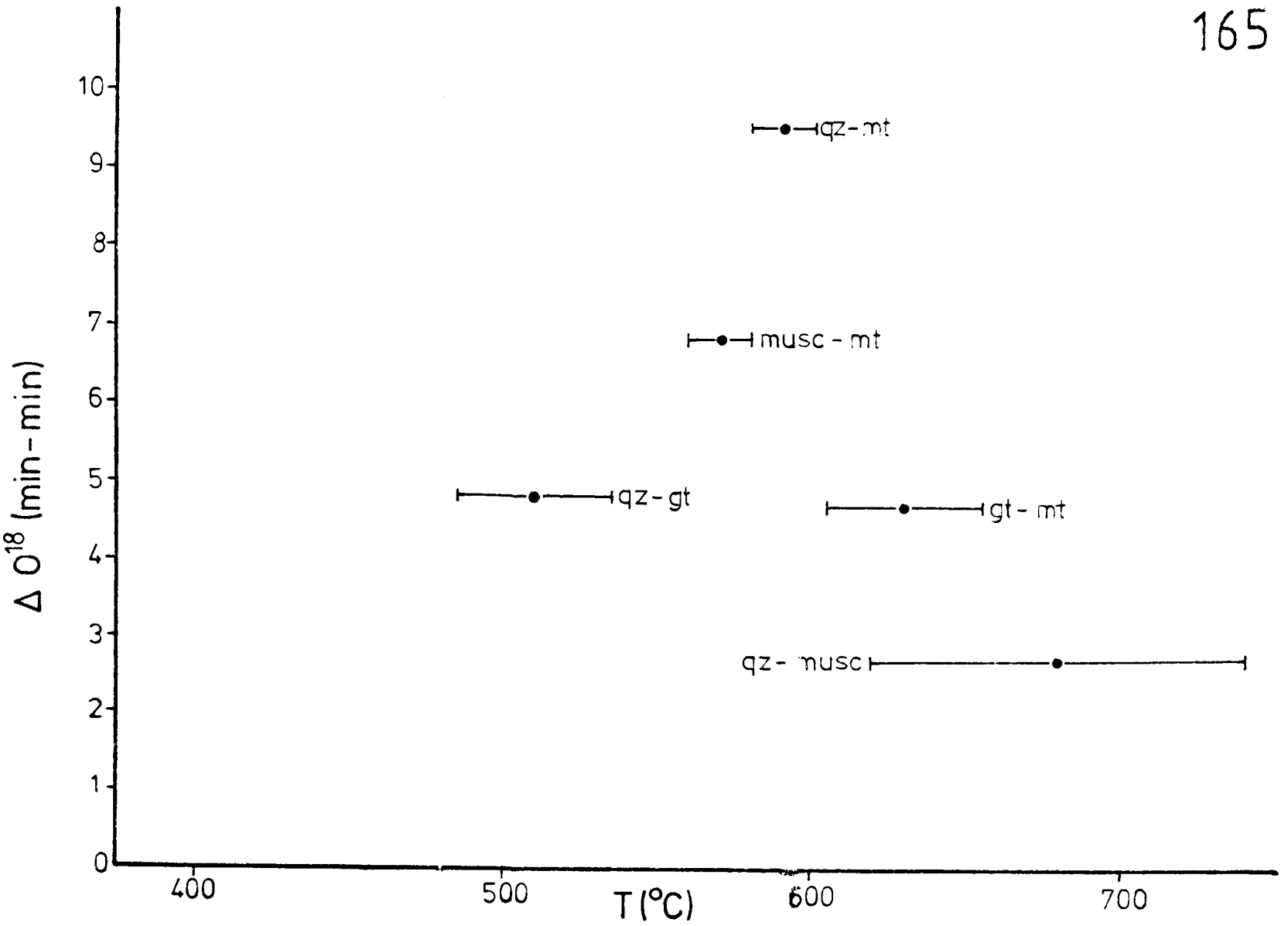



Fig. 8.5(b) Fractionation vs. temperature plot (above) and Javoy diagram (below) for isotopically poorly-equilibrated Peripheral Schieferhülle mica-schist GD 903.



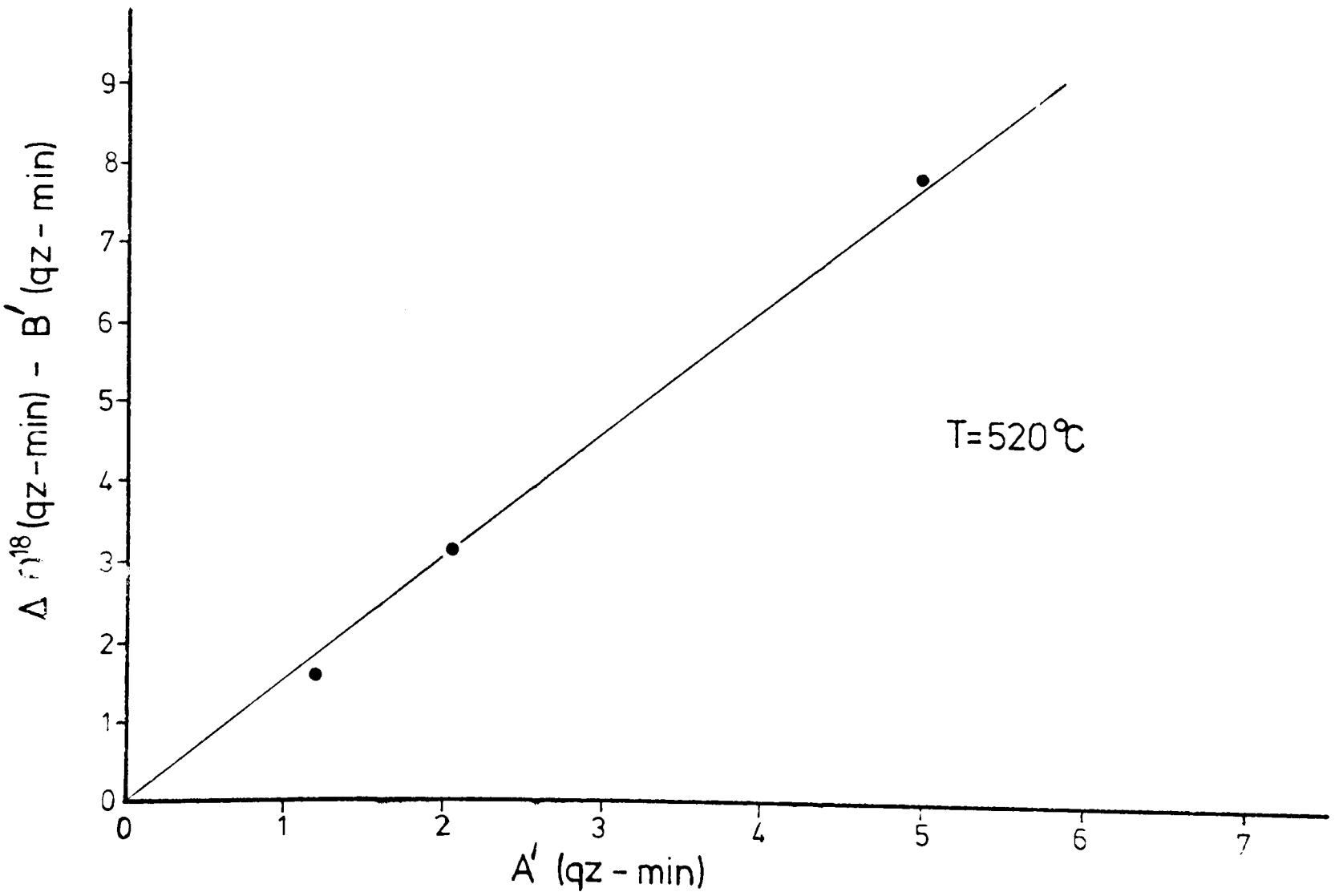




Fig. 8.5(c) Fractionation vs. temperature plot (above) and Javoy diagram (below) for poorly equilibrated Peripheral Schieferhülle mica-schist GD 234.

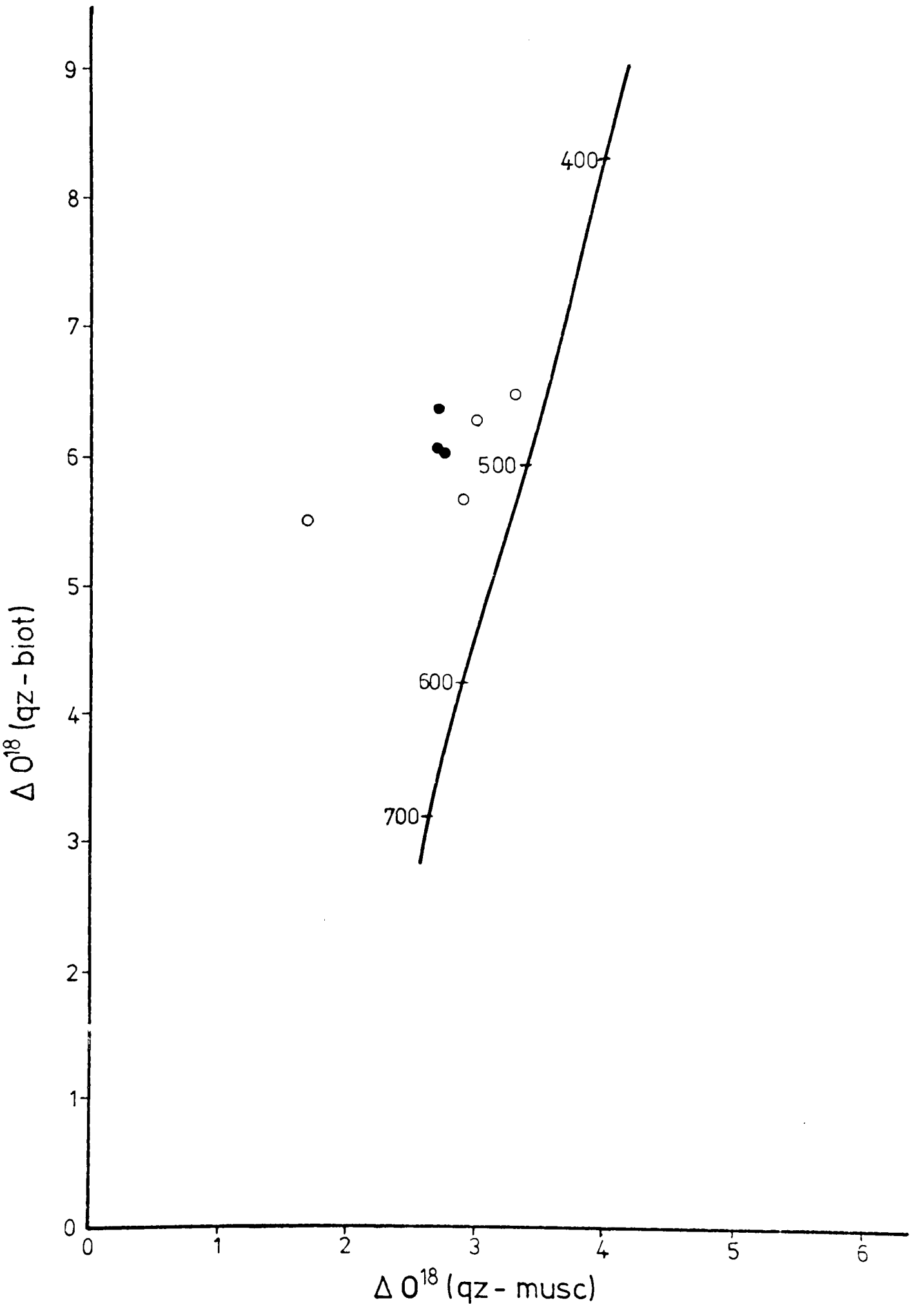



Fig. 8.6 Graph of $\Delta O^{18}$ (qz - biot) vs. $\Delta O^{18}$ (qz - musc) for Zentralgneis rocks (open circles) and mica-schists (filled circles). The line is the locus of points connecting all possible equilibrium conditions as calculated from the curves in fig. 8.2.

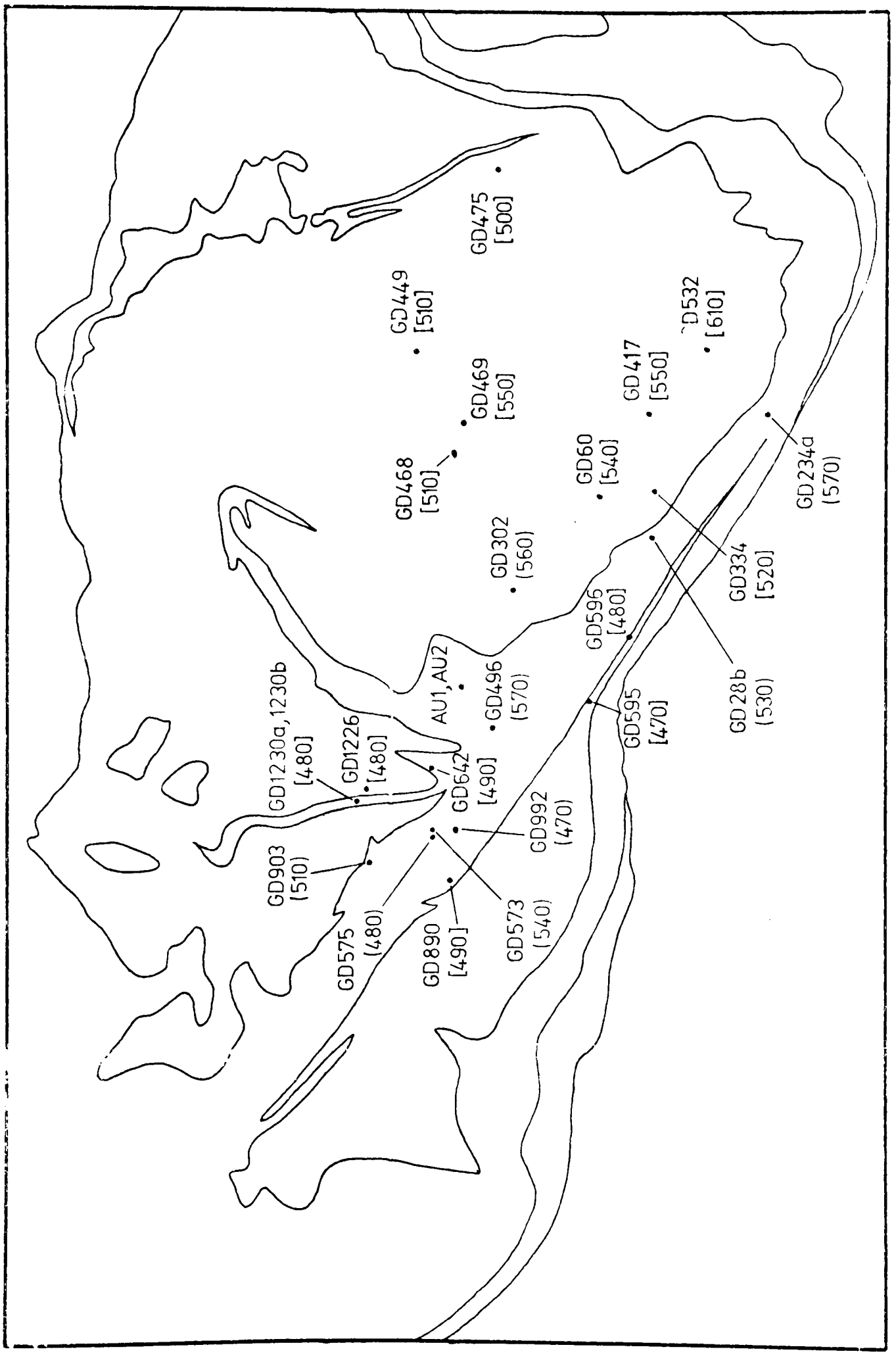



Fig. 8.7 Oxygen isotope sample localities. Temperatures calculated from quartz-biotite fractionations are shown in square brackets and those from muscovite-magnetite fractionations in round brackets.

Table 8.2 Oxygen isotopic composition of waters in equilibrium with co-existing muscovite and magnetite or ilmenite in mica-schists, quartz and biotite in Zentralgneis rocks, and all minerals in the Auernig vein samples.

| SAMPLE | "EQUILIBRIUM" TEMP. (°C) | $\delta O^{18}_{H_2O}$ (°/oo) | $\delta O^{18}_{W.R.}$ (°/oo) |
|---|---|---|---|
| AU1, AU2 | 525 | +9.7 | - |
| GD 28b | 540 | +9.7 | +10 |
| GD 234 | 580 | +12.8 | +14 |
| GD 496 | 570 | +12.2 | +13 |
| GD 573 | 540 | +12.3 | +12 |
| GD 575 | 480 | +13.1 | +12 |
| GD 890 | 530 | +12.2 | +13 |
| GD 903 | 510 | +12.2 | +13 |
| GD 992 | 470 | +16.9 | +18 |
| GD 302 | 560 | +8.1 | +7 |
| GD 642 | 490 | +8.9 | +10 |
| GD 1230a | 480 | +9.3 | +11 |
| GD 60 | 540 | +7.8 | +8 |
| GD 334 | 520 | +5.9 | +8 |
| GD 417 | 550 | +7.8 | +9 |
| GD 449 | 510 | +8.0 | +9 |
| GD 468 | 500 | +7.0 | +9 |
| GD 469 | 550 | +5.9 | +7 |
| GD 475 | 500 | +5.5 | +7 |
| GD 595 | 470 | +7.6 | +9 |
| GD 596 | 480 | +7.4 | +9 |
| GD 1226 | 480 | +6.3 | +8 |

Table 8.3 Calculated oxygen isotopic composition of waters in equilibrium with segregation quartz at various temperatures. $\delta O^{18}$ of water (musc, mt) is the composition of water in equilibrium with muscovite and magnetite at the final temperature of equilibration.

| Rock | $\delta O^{18}$ of vein quartz (°/oo) | $\delta O^{18}$ of water in equilibrium with vein quartz (°/oo) | | | | $\delta O^{18}$ of water (musc, mt) (°/oo) |
|---|---|---|---|---|---|---|
| | | 250°C | 300°C | 400°C | 500°C | |
| GD 992 | +19.05 | +8.05 | +10.55 | +13.75 | +15.6 | +16.9 |
| GD 903 | +14.25 | +3.25 | +5.75 | +8.95 | +10.8 | +12.2 |
| GD 573 | +14.4 | +3.4 | +5.9 | +9.1 | +10.95 | +12.3 |

Table 8.4 Measured whole-rock oxygen isotopic compositions.

| Sample | Lithology | $\delta O^{18}$ (°/oo) |
|---|---|---|
| | Peripheral Schieferhülle | |
| GD 50 | Calc-schist | +15.4 |
| GD 965 | Calc-schist | +18.9 |
| GD 837 | Marble | +22.7 |
| GD 18 | Pelitic mica-schist | +11.5 |
| GD 821 | Coarse-grained chloritoid schist | +17.3 |
| GD 48a | Serpentinite | + 8.6 |
| GD 48b | Actinolite rock | +10.6 |
| GD 483 | Epidote-amphibolite | + 8.9 |
| GD 551 | Greenschist | +16.45 |
| | Zentralgneis | |
| MG1 | Granite-gneiss | + 8.7 |
| MG2 | Augen-gneiss | + 8.8 |
| MG3 | Augen-gneiss | + 6.1 |
| MG4 | Quartz-phengite-schist | +11.2 |
| MG5 | Quartz-phengite-schist | +12.1 |
| MG6 | Quartz-phengite-schist | +13.6 |
| | Inner Schiefe hülle | |
| GD 649 | Graphitic quartzite | +13.5 |
| GD 1197 | Mica-schist | +11.8 |

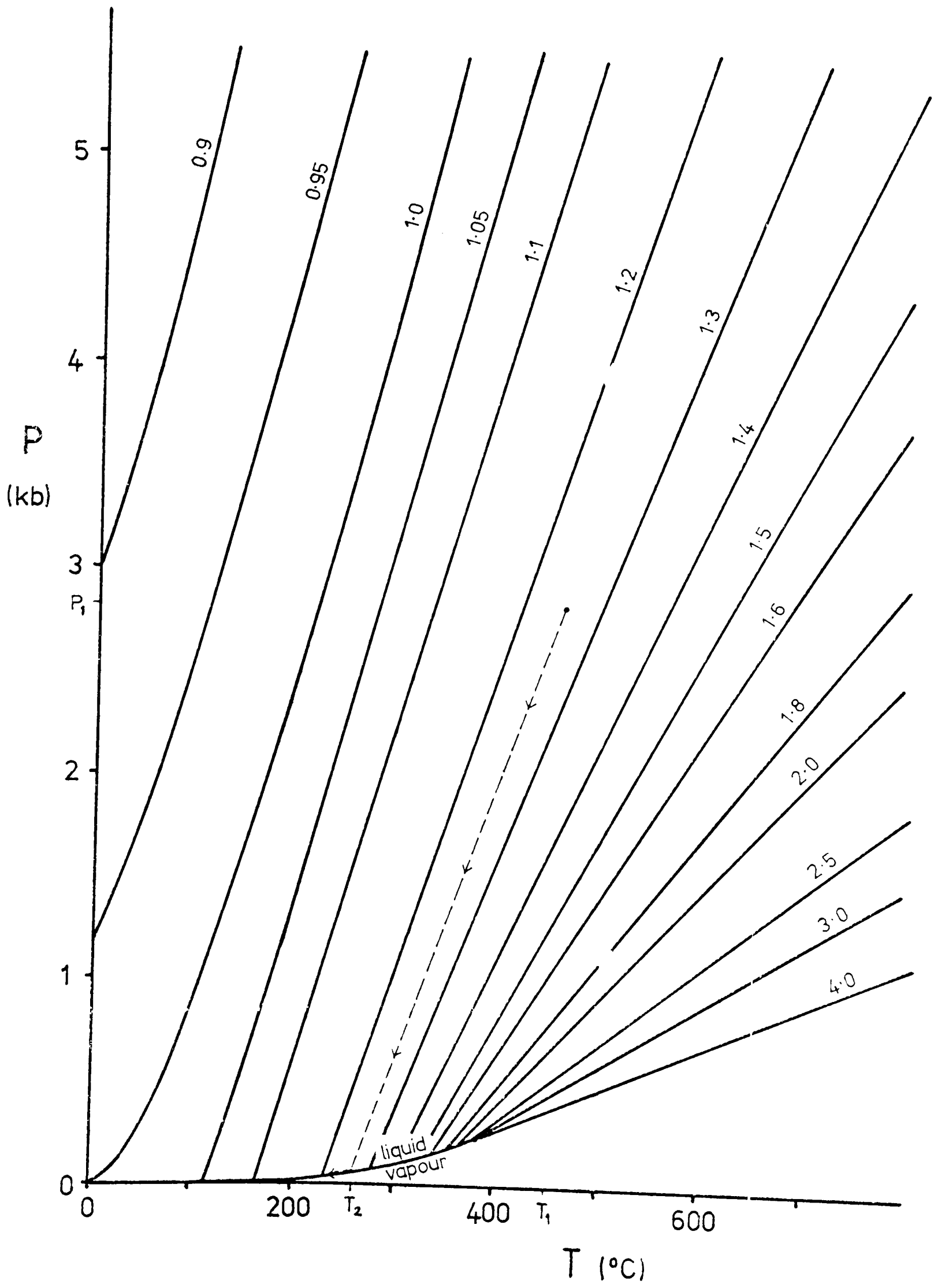



Fig. 9.1 PVT diagram for $H_2O$, from Kennedy (1950). Isochores are labelled in specific volume.

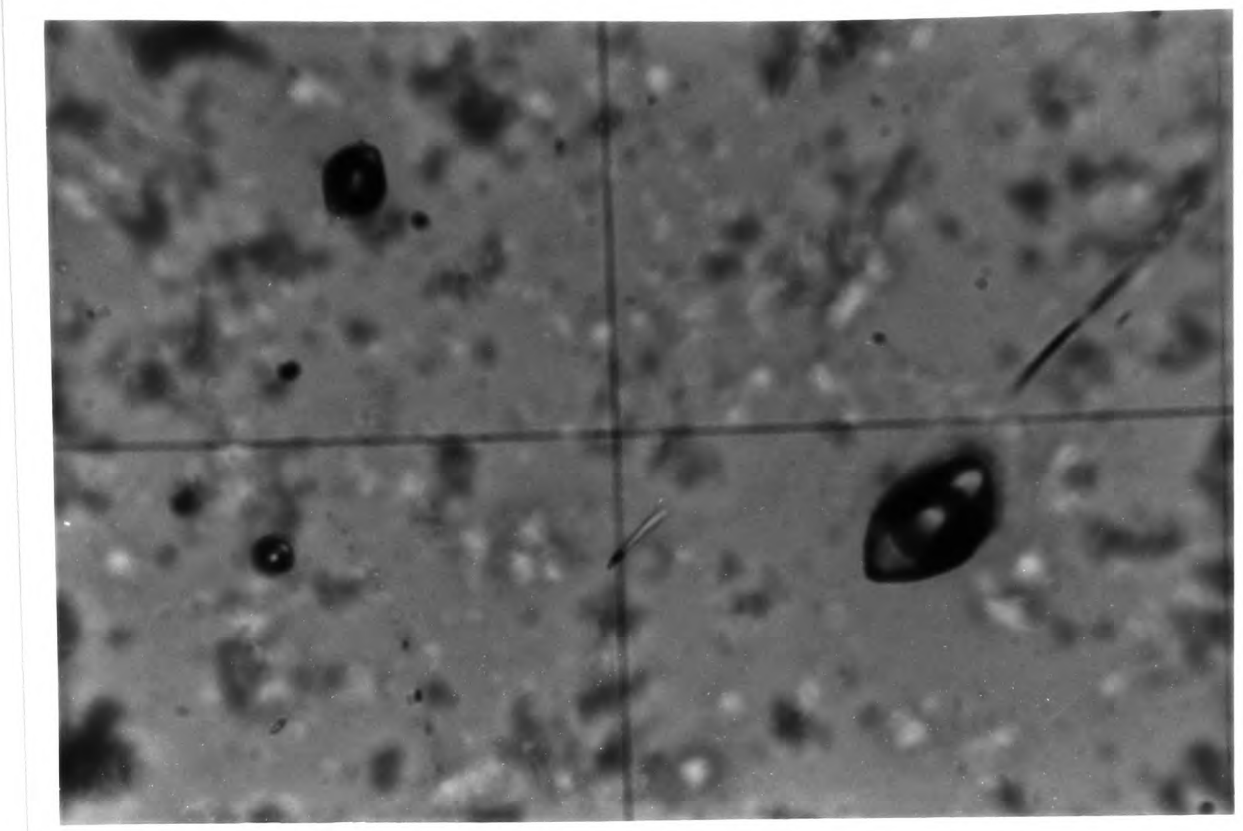


Fig. 9.2 Primary two-phase fluid inclusions in quartz from a chlorite + albite vein on Auernig.

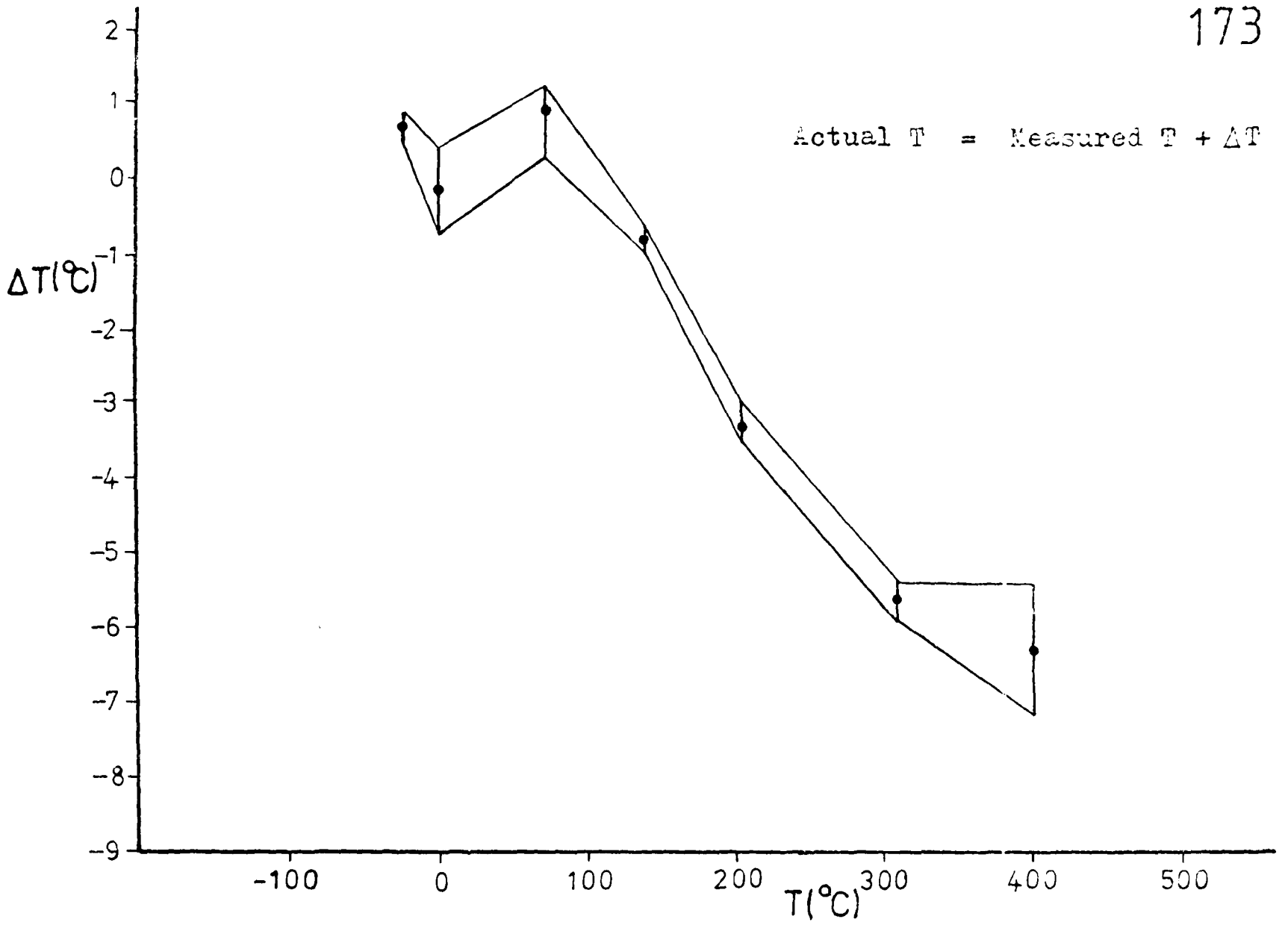



Fig. 9.3 Calibration curve for the Chaix-Meca microthermometry apparatus (May 1978).

Table 9.1 Standards used in the calibration of the Chaix-Meca apparatus.

| Standard | Melting point, T. (°C) | Mean final melting temperature (°C) | Mean ΔT (°C) |
|---|---|---|---|
| Carbon tetrachloride | -22.8 | -23.5 | +0.7 |
| Water | 0.0 | -0.2 | -0.2 |
| "Signotherm 70" | 70 | 69.1 | +0.9 |
| "Signotherm 135" | 135 | 135.8 | -0.8 |
| "Signotherm 200" | 200 | 203.3 | -3.3 |
| Sodium nitrate | 306.8 | 312.4 | -5.6 |
| Potassium dichromate | 398 | 404.3 | -6.3 |

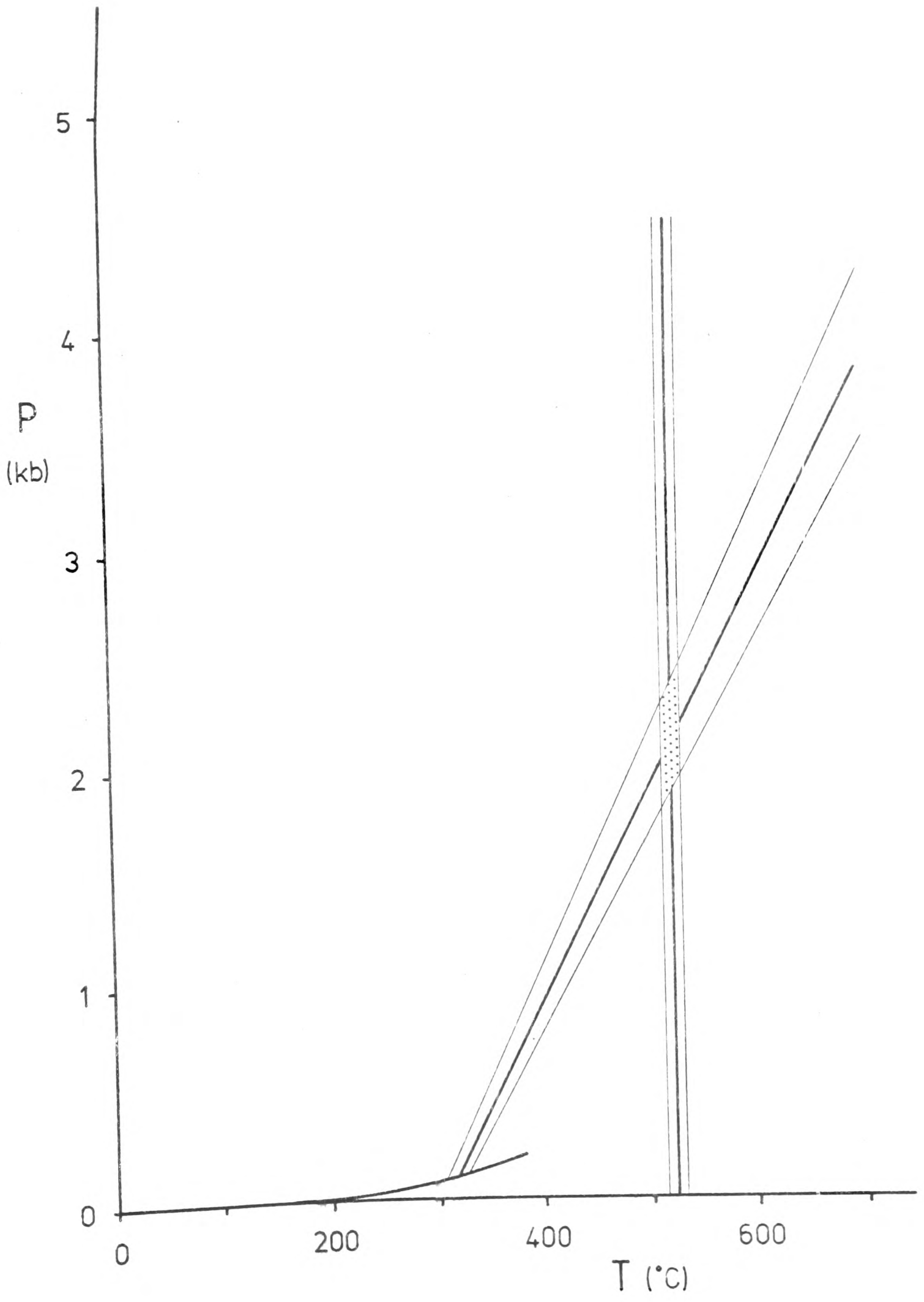



Fig. 9.4 Estimated temperature and pressure conditions (stippled) of mineral growth in a $D_a^3$ vein on Auernig. (P-independent temperature from oxygen isotope studies; P-sensitive curves from fluid inclusion studies).

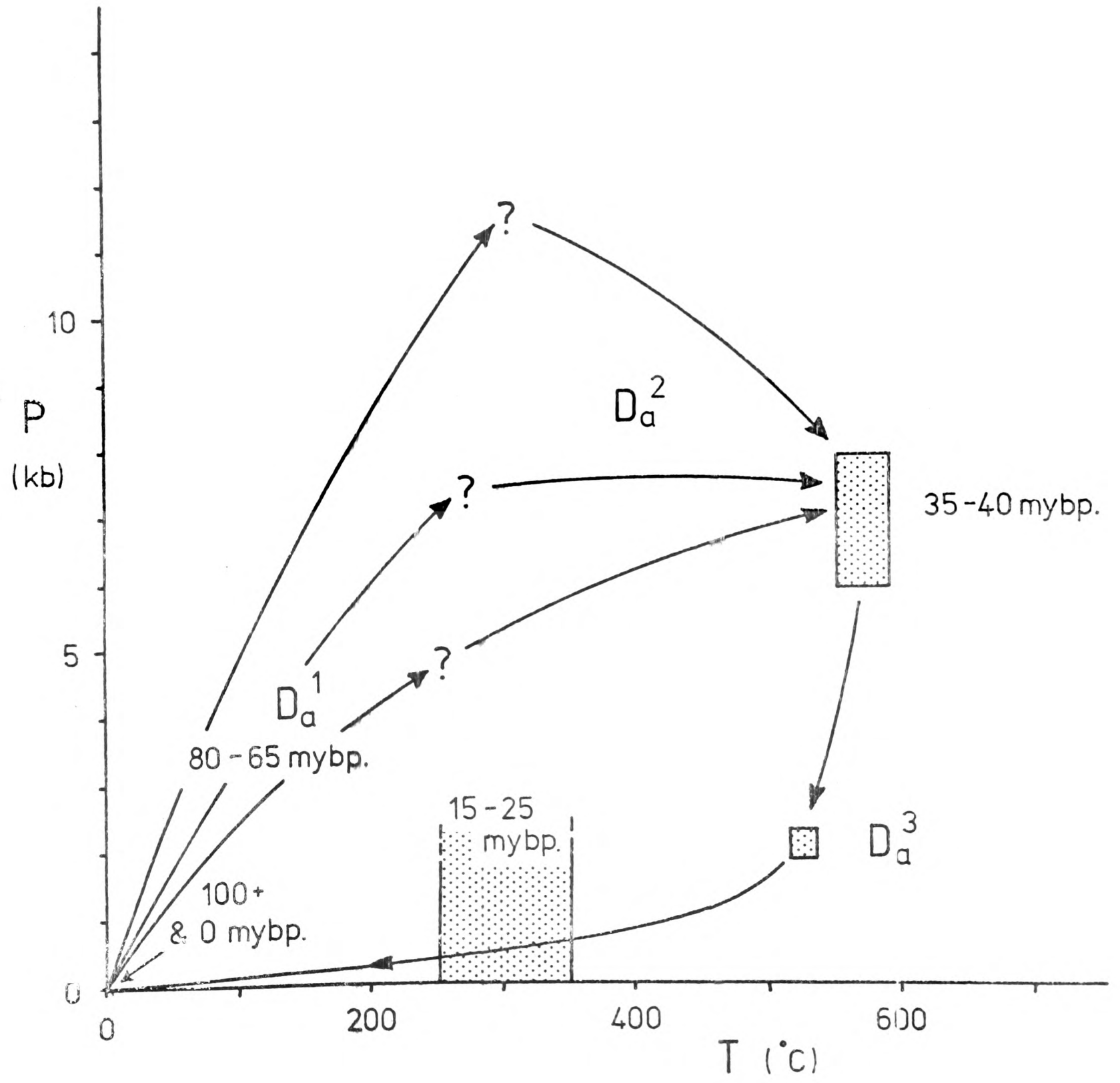



Fig. 10.1 Pressure - temperature - time trajectory for the base of the Möltal Schieferhülle during the Alpine orogeny.

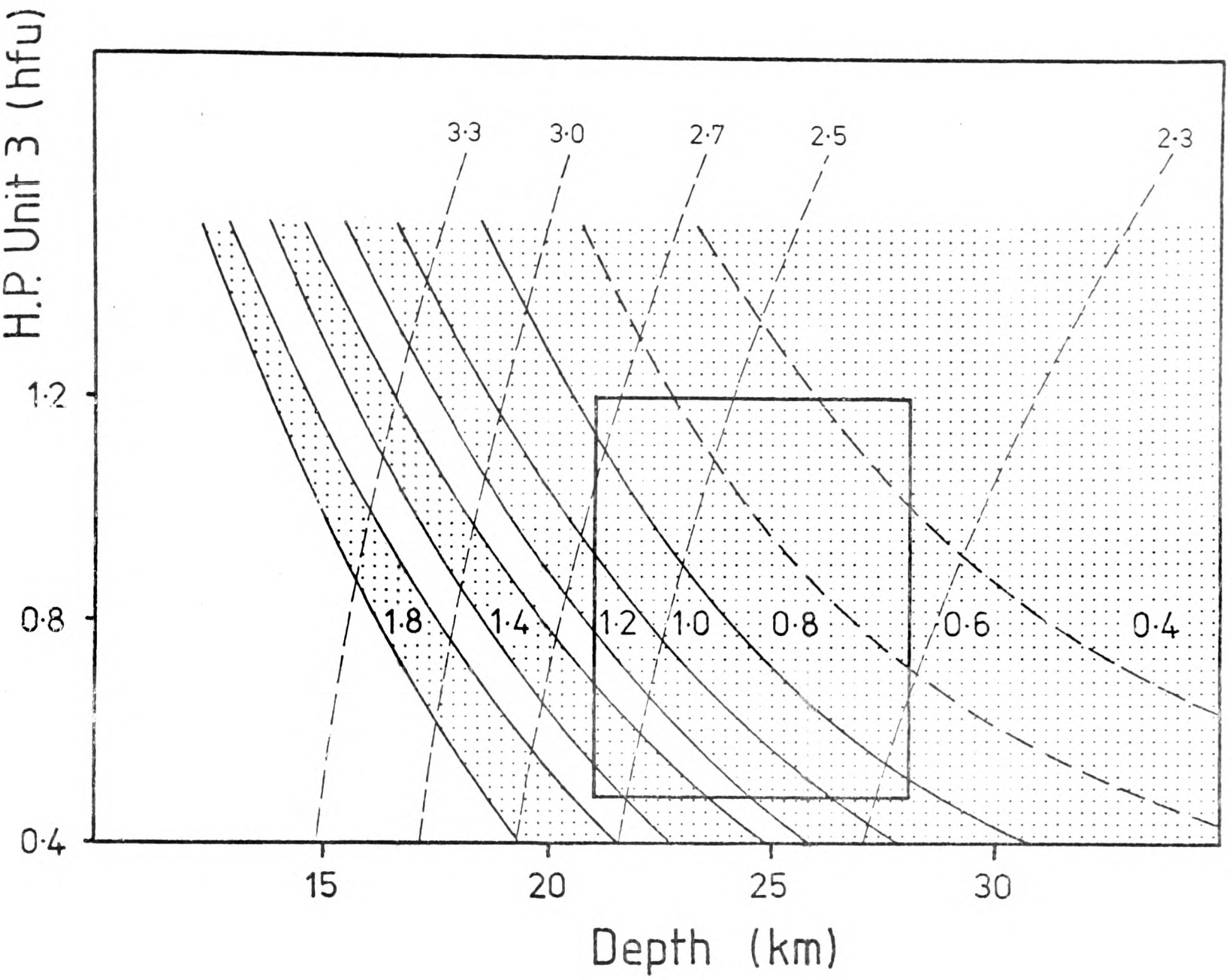



Fig. 10.2 The depth at which 550°C is reached 30 my. after the end of overthrusting plotted against total heat production in Unit 3. (Adapted from England, 1978, fig. 3). Stippled bands cover solutions of constant mantle contribution to heat flow (values given in hfu); dotted lines link conditions producing the same surface heat flow after 65 my. The box indicates the acceptable range in axis-parameters.